RSETHZ 340.311

DISS. ETHZ NO. 29839

DEEP LEARNING-BASED CELLULAR ACTIVITY RECOGNITION IN LIVE-CELL IMAGING

A thesis submitted to attain the degree of

DOCTOR OF SCIENCES
(Dr. sc. ETH Zurich)

Presented by
Alain Pulfer

MSc, ETHZ

Born on 26.09.1991
Accepted on the recommendation of

Prof. Dr. Daniel Razansky
Prof. Dr. Santiago Gonzalez
Prof. Dr. Jean-Philippe Thiran
Dr. Diego Pizzagalli

2023

ACKNOWLEDGMENTS

I am grateful to my family, for their unwavering support throughout my studies. In particular, I would like to express gratitude to my parents, my sister, my brothers, and my grandmother. I also want to extend the acknowledgments to my close friends Filippo, Giulio, Lisa, Luca, Marco, Simone, and Stefan. I also want to thank Masiar, friend and early master that inspired me in pursuing a doctorate. Finally, I want to thank Jessica, which has been a pillar in my life and a companion over the last four and a half years.

I am also indebted to all of my past and present colleagues, who taught me invaluable lessons about work and life. In order of seniority, I would like to acknowledge: Miguel Palomino, for being an early mentor figure and providing me with valuable suggestions at the onset of my PhD; Tommaso Virgilio, for all the distinguished conversations and for the wisest advices; Irene Latino, for her investment in work and her constant self-improvement; Juliana Favilene, for her beliefs and open-minded vision; Daniel Molina, for sharing many interests and introducing me to new passions; Mauro di Pilato, for his scientific enthusiasm and unparalleled humor; Joy Bordini, for her enterprising and pro-active demeanor and for making the lab hilarious; Kevin Ceni, for being a very skilled but humble computer scientist; Pau Carrillo Barberà, for his calmness and for bridging Spanish and Swiss cultures; Elisa Palladino, for her passionate involvement and support in different lab projects; Coral Garcia, for being a great scientist and for the countless off-topic conversations; Kamil Chaine, for his inexhaustible commitment and inspiring working ethic; Chiara Pizzichetti, for being a proud female scientist with unmatched cooking skills, Giacomo Ceracchetti, for his spontaneous attitude and personality; Louis Renner, for his unlimited reservoir of energy and his optimistic vision; Almudena Méndez, for her inspiring ambitions and her bright personality; Leire Franquesa, for being a skillful bachelor student which has figured her future path; Arianna Capucetti, for her scientific mastery and sensitive personality; Layla Pohl, for the brave choice of working (out at 6 a.m.) at the interface between medicine and research.

ACKNOWLEDGMENTS

I would also like to acknowledge all the collaborators which contributed to this work: Dr. Paola Antonello, Prof. Marcus Thélen, Prof. Thomas Murooka, Dr. Paul Lopez, Dr. Romaniya Zayats, Prof. Philippe Bousso, Dr. Alessandro Giusti, Prof. Luca Gambardella, Dr. Paolo Gagliardi, Lucièn Hinderling, and Prof. Olivier Pertz. Furthermore, I want to thank Dr. Diego Pizzagalli for his invaluable mentorship and guidance, which have helped me to grow both professionally and personally.

Lastly, I would like to express my gratitude to Prof. Daniel Razansky for his supervision at ETHZ and for being available and open to discuss, to Prof. Jean-Philippe Thiran, for kindly accepting to examine my thesis with a short notice, and to Prof. Santiago Gonzalez, for his dedicated mentorship and the countless teachings over the course of my studies.

This thesis is dedicated to Roberto.

ASTRATTO

Nel corso degli ultimi due decenni, la microscopia a due fotoni è diventata una tecnologia di riferimento per lo studio in tempo reale delle interazioni tra le difese immunitarie e diversi patogeni *in vivo*. Tuttavia, nonostante la sua rilevanza, sussiste una scarsità di strumenti analitici dedicati a questa piattaforma, con tecniche quantitative prettamente basate sull'analisi di traiettorie cellulari. Pertanto, la mia tesi di dottorato ambisce a colmare tale lacuna contribuendo allo sviluppo di nuove tecniche analitiche di dati generati *in vivo*. L'obiettivo principale di questo lavoro è lo sviluppo di strumenti per il riconoscimento dell'attività cellulare (RAC) al fine di distinguere e quantificare diversi comportamenti legati al sistema immunitario e alla morte cellulare. Per raggiungere tale obiettivo, ho sviluppato architetture di intelligenza artificiale (IA) progettate per l'analisi del linguaggio e dei video. Contestualmente, ho curato e reso pubblici i dati necessari per applicare tali tecniche di IA. Infine, a conferma della loro fruibilità, ho fornito una validazione biologica degli strumenti RAC nel contesto del sistema immunitario. In conclusione, questa tesi di dottorato presenta un approccio pionieristico per determinare il comportamento cellulare in dati di microscopia. In futuro, lo sviluppo di strumenti CAR consentirà la previsione e la caratterizzazione di attività cellulari complesse, contribuendo all'avanzamento della ricerca fondamentale e agevolando lo sviluppo di strategie terapeutiche.

ABSTRACT

Over the past two decades, two-photon intra-vital microscopy (2P-IVM) has emerged as the gold standard technology for the real-time investigations of interactions between host immune defenses and pathogens. However, despite its significance, analytical tools dedicated to this platform remain scarce, with quantitative measurements primarily relying on cell trajectory analysis. The aim of this doctoral thesis is to address this gap by providing a comprehensive analysis of data generated *in vivo*. The main objective of this work is the development of novel cell activity recognition (CAR) tools to distinguish and quantify cellular behaviors related to the immune system and cell death. To achieve this goal, I explored the application of deep learning architectures designed for natural language processing and computer vision tasks. Simultaneously, I curated and made public datasets for the application of supervised learning techniques. Finally, I provided a biological validation confirming the usability of the generated CAR tools in the context of the immune system. In conclusion, this doctoral thesis presents a pioneering approach to measuring cellular behavior. In the future, the development of CAR tools will enable the prediction and characterization of complex cellular activities, contributing to the advancement of fundamental research and therapeutic strategies.

CONTENTS

ABBREVIATIONS

A

AI: Artificial intelligence

APC: Antigen presenting cells

AR: Activity recognition

AUC: Area under the curve

B

BC: B cells

C

CAR: Cellular activity recognition

CNNs: Convolutional neural networks

CTL: Cytotoxic T lymphocytes

CV: Computer vision

D

DC: Dendritic cells

DL: Deep learning

E

Eos: Eosinophils

F

FOV: Field of view

FPR: False positive rate

G

GC: Germinal center

H

HAR: Human activity recognition

HEV: High endothelial venules

I

IF: Inter follicular

IL: Interleukin

L

LNM: Lymph node macrophages

LN: Lymph node

LSTM: Long-short-term memory

M

MP: Multiphoton

MP-IVM: Multiphoton intravial microscopy

MSD: Mean squared displacement

N

Neu: Neutrophils

NLP: Natural language processing

NK: Natural killers

O

OF: Optical flow

P

PCD: Programmed cell death

PLN: Popliteal lymph node

R

ROC: Receiver operating curve

ROI: Region of interest

RNN: Recurrent neural network

S

SCS: Subcapsular sinus

SNR: Signal to noise ratio

SVM: Support vector machine

T

TC: T cells

TNF: Tumor necrosis factor

TPR: True positive rate

U

UVPR8: UV inactivated PR8

V

vAbs: Virtual antibodies

INTRODUCTION

1. Live-cell imaging

Live-cell imaging[1] is a powerful technology that revolves around the visualization of living cells in real-time using microscopy techniques. This approach offers several advantages over traditional static acquisitions, enabling researchers to observe the motility of cells in response to different stimuli and across various experimental conditions. For this reason, live-cell imaging provided a deeper understanding of dynamic biological processes such as chemotaxis, cell division and cell death among others. Due to these highlights, this imaging platform is an essential asset in the toolkit of modern cell biologists.

Among the existing imaging platforms, fluorescence microscopy is one of the most employed for cellular investigations[2]. One of the reasons is the specificity of the technology, which allows the specific visualization of different cell types, organelles and physiological structures. This is possible due to the usage of fluorescent dyes[3] that bind specifically target cellular structures or molecules within the cell. The labeled cell is then excited with excitation light to emit fluorescence light that is captured by a detector to generate the corresponding image.

Wide field fluorescence microscopy is a technique in which the imaged sample is entirely excited. The main drawback of this platform is that it generates considerable amount of scattered light, ultimately leading to blurred images and photodamage of the fluorophores. By contrast, confocal fluorescence microscopy[4] utilizes a pinhole, or spatial filter, to reject out-of-focus light. This precaution translates into smaller airy disks that ensure sharper images and less background noise. In addition, the sample is not entirely excited, as the excitation laser only targets punctual regions at a time while scanning the sample in a raster pattern. This ensures that only light emitted from the focal point is collected, further reducing scattering and enhancing the quality of the image. Detrimental to these advantages, confocal microscopy is affected by lower acquisition speed, which is inherently limited by the scanning acquisition process.

Spinning disk confocal microscopy[5] represents a leap forward that overcame the limitations associated with point-scanning. This technology employs multiple pinholes placed on a rotating disk, as opposed to a single one, and multiple emissions lasers excite different focal points of the sample in correspondence of the different pinholes.

Consequently, this technique can effectively reduce scattering without excessive loss of acquisition speed. This enables the capture of extremely fast-lived processes like cell division[6] and microtubules re-arrangement[7] among others.

One drawback of the afore mentioned techniques is the gradual loss of fluorescence from the fluorophores, a phenomenon known as photobleaching[8] which inherently affects all fluorescence-based imaging platforms. Another limitation of classical fluorescent microscopy pertains the reduced ability to penetrate tissues due to scattering and absorption.

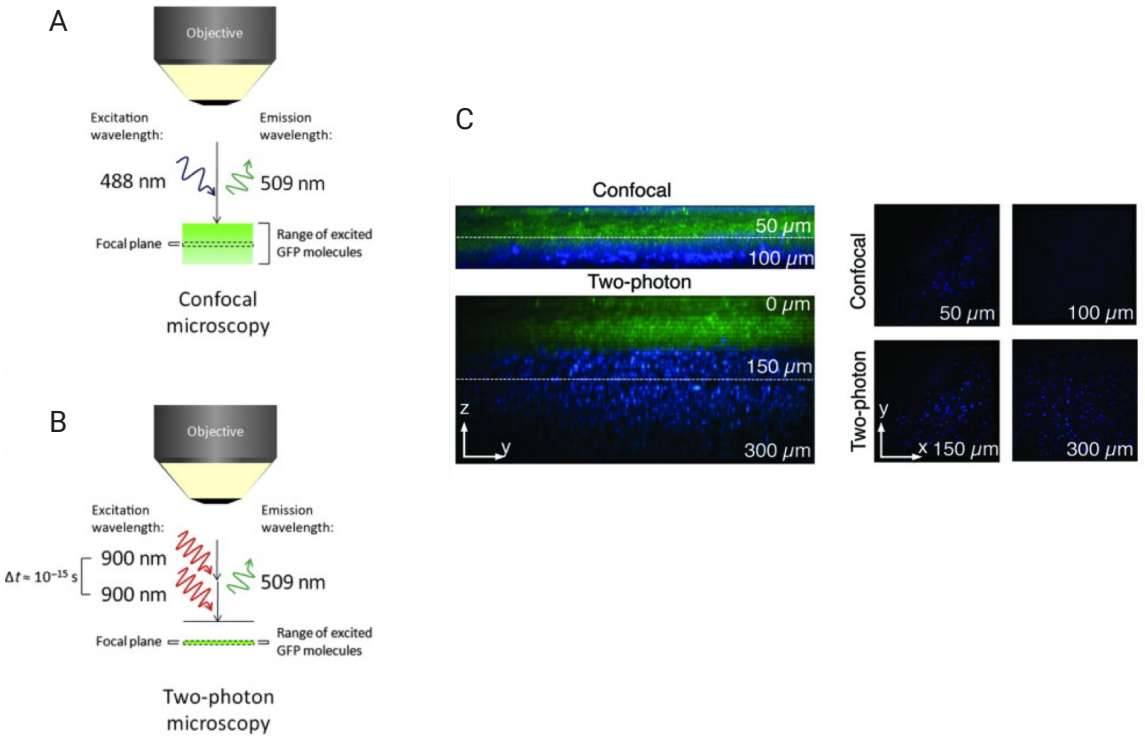

Figure 1. Comparison of linear and non-linear excitation in confocal and two-photon microscopy. ***A.*** *Confocal microscopy employs a single photon with lower energy to excite a fluorophore that will emit a second wavelength of higher energy.* ***B.*** *2-Photon excitation employs two consecutive excitation wavelengths in the near infrared spectrum to generate the same emission wavelength as confocal microscopy but with reduced scattering and excitation volume.* ***C.*** *2-Photon microscopy enables in depth imaging compared to confocal microscopy. Adapted from*[7]

Multi-photon microscopy (MP), primarily developed for neurological investigation, has emerged as a solution to contain and mitigate the problems associated with traditional fluorescence imaging. MP microscopy, as opposite to confocal microscopy, employs a pulsed laser that emits two or more high energy photons in the near-infrared range (Fig. 1B), leading to their simultaneous absorption by a specific fluorophore and the subsequent emission of a photon with higher energy. By utilizing two lower energy excitation photons instead of a single one, MP produce less scattering while enabling for deeper tissue penetration compared to confocal microscopy (Fig. 1C). Moreover, by reducing scattering and confining absorption to a defined area, MP-IVM significantly reduces phototoxicity and photobleaching. For these reasons, MP has become a popular investigation tool, enabling a plethora of studies in the domain of neurology, developmental biology, immunology, and tumor biology.

1.1. In vitro live-cell imaging

Live-cell imaging is a powerful approach that offers a unique opportunity to study living cells in real-time. This technique combines advanced microscopy and imaging technologies to capture both static snapshots and time-lapse sequences of living cells while preserving their viability and functionality. Unlike traditional fixed-sample imaging, which provides static information, live-cell imaging enables researchers to delve into the dynamic and ever-changing processes within cells. This includes observing cell growth and division, tracking cell movements, and studying intricate cell-to-cell interactions. By gaining insights into these dynamic cellular behaviors, researchers can unravel critical biological processes and better understand complex dynamics at the cellular level. Live-cell imaging encompasses two main modality with respective advantages and disadvantages; *in vitro* and *in vivo*.

Live-cell imaging *in vitro* permits a tight control of the environment and the standardization of experimental protocols. Cells growing on a glass or plastic dish are maintained in a stable environment with several adjustable parameters that include temperature, oxygen levels, pH, and content of the growing media among others. This allows for highly reproducible results. In addition, *in vitro* live-cell imaging enables researchers to study cells from a wide range of organisms, and to apply techniques that would not be possible *in vivo*. For instance, cell manipulation by transfection or gene editing is easier

compared to *in vivo* settings. At the same time, experimental costs and ethical limitations are reduced due to not using animals.

Therefore, *in vitro* imaging is a versatile technique prone to capture several biological insights, such as chemotaxis[9,10], cell-to-cell interactions, and 3D organoids[11]. *In vitro* imaging aims to mimic the physiological conditions encountered in living tissues, allowing to model and represent intricate biological systems[12]. However, these systems have not achieved yet the fidelity required to depict complex cellular interactions encountered in physiological conditions.

1.2. In vivo live-cell imaging

The main advantage of *in vivo* live-cell imaging, is the ability to study cells in a physiological environment in tissues, and organs, including cell-to-cell interactions. Accordingly, *In vivo* imaging provides information that cannot be fully appreciated in culture due to the inherent lack of physiological conditions, such as the presence of vessels and the interactions between multiple key players of the immune system. Amongst the microscopy platforms suitable for *in vivo* studies, multiphoton intravital microscopy (MP-IVM) is one of the most commonly employed[13] due to the aforementioned technical advantages. The application of MP-IVM typically involves a step of cell labelling, followed by animal surgery and image acquisition.

For cell labelling different methods are available, including the adoptive transfer of cells from transgenic animals expressing a fluorophore-tagged protein, *in vitro* labeling with fluorescent dies, or the injection of fluorescently labeled antibodies that specifically bind to the cells of interest[14,15]. After labelling, the next step to perform MP-IVM is selecting the proper surgical model to enable the exposure and immobilization of the relevant organ[16–18] (Fig. 2A). Surgical models for long-term acquisition of organs and tissues can vary in complexity and invasiveness, and they can include the gut[19], brain, spinal cord[20], and tumors[21,22] amongst others[23,24].

After surgery, the anesthetized animal is transported to the microscope where image acquisition is performed with MP-IVM (Fig. 2B). Resulting acquisitions typically consists in 4D imaging data over time (Fig. 2C), which can be successively analyzed with software tailored for the quantification of cell motility and morphology (Fig. 2D).

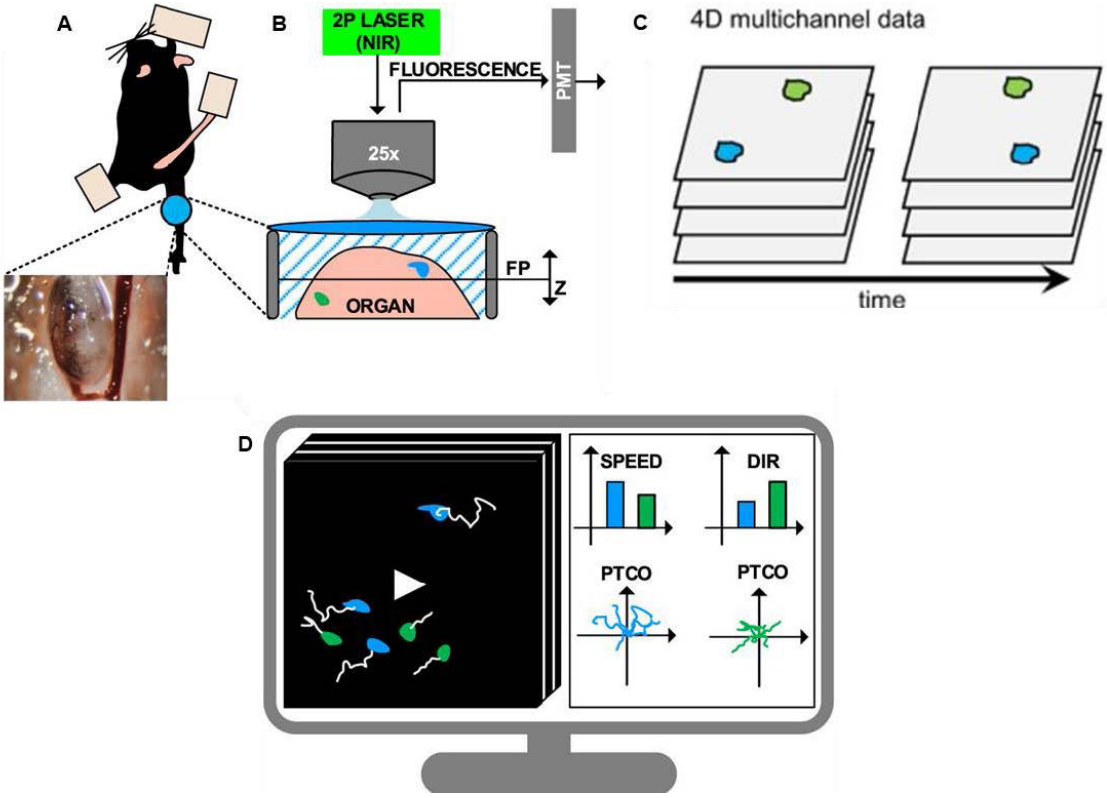

Figure 2. Pipeline for intravital imaging acquisitions. A. *Depiction of a surgically exposed lymph node in an anesthetized mouse.* ***B.*** *2-Photon acquisition of the exposed organ.* ***C.*** *Representation of the generated acquisitions accounting for multiple focal planes and channels.* ***D.*** *Subsequent analysis of the imaging data with a dedicated imaging analysis software. Adapted from*[25,26].

2. Quantitative analysis for live-cell imaging

Intravital 2-photon datasets are especially rich in information due to the presence of multiple simultaneously imaged, chemical cues, cell types or vascular systems. Therefore, the resulting analysis process is extended and complex, posing serious challenges to its interpretation. For this reason, in comparison to other techniques such as flow cytometry, live-cell imaging has for long been considered a qualitative addition to biological research. The quantitative aspect of this platform were implemented with the development of new methodologies that enabled the estimation of cell abundance, morphology, and motility. At present, two common quantitative strategies cell are commonly used, namely tracking-based and pixel-based.

2.1. Track-based analysis

Over the last two decades, the analysis of live-cell imaging revolved around the quantification of cellular motilities, which was successively used as an experimental readout. For instance, cells moving in a specific direction may indicate chemotaxis, while cells moving randomly could imply a surveillance function. These motility measures are typically calculated from cell trajectories presented in the form of spatial-temporal coordinates and a unique identifier (x, y, t, ID). This information includes a range of motility parameters that can be instantaneous (calculated at a specific point in the trajectory) or average (calculated over the entire trajectory). Accordingly, parameters such as speed, directionality, and arrest coefficient describe multiple motility states and behaviors[27,28] , which in turn can be associated with precise biological functions[27]. For this reason, motility parameters computed from tracks can help identifying population of cells involved in different biological functions. Moreover, these measurements are also helpful to assess wheatear distinct experimental conditions affect cell motility. However, track based analysis present some limitations. For example, cell tracks only capture the information related to the spatial coordinates of the cells, neglecting changes in cell morphology over time. Additionally, track-based measures can be highly biased depending on the quality, duration, and temporal resolution of the trajectories[28]. Therefore, accurate and comparable tracks are fundamental to produce reliable derived measurements.

Cell tracking can be performed manually, by labelling the centroid of individual cells,

or automatically, by algorithmically detecting or segmenting the cells and connecting their centroids based on heuristic or optimization strategies. The second option is the fastest, but a series of limitations hamper the automatic generation of tracks in live-cell imaging. For instance, the high plasticity of cells often leads to tracking errors[28]. Additionally, high cell density can hinder the distinction of individual cells. Lastly, technical such as varying signal-to-noise ratio or moving specimen might affect the overall experimental readout, particularly *in vivo*[29,30]. Therefore, automatic tracking does not always guarantee reliable results, as available algorithms are not exempted from errors[31]. Consequently, human annotation remains the most reliable way to minimize tracking errors and improving the reliability of derived measurements used to infer cell migration and general motility[32]. Nonetheless, this procedure is time-consuming and prone to individual operator bias. Consequently, researchers face the decision to choose between more reliable and time-consuming manual tracking, or faster but less accurate automatic tracking. Ultimately, this tradeoff is an incentive for the improvement of cell tracking algorithms[33] and the development of track-free analyses.

2.3. Pixel-based analysis

Pixel-based techniques can extract meaningful information from microscopy data without the need for tracking. These methods primarily focus on processing the intensity values of the image to gain insights on the abundance and spatial distribution of fluorescent signals. In turn, this information allows to estimate the total abundance of cells, as well as the occurrence of certain biological processes labeled with fluorescent markers, such as apoptosis. Moreover, signal colocalization can determine the degree to which two fluorescent signals overlap in the same location. At the cell level, this measure can indicate an interaction such as a cellular contact[34], a cell scanning for antigens[35], or a phagocytic ingestion among others[36].

Another common technique based on pixel intensities is optical flow (OF)[37]. OF estimates the displacement of individual pixels between consecutive frames of a time-lapse relying on two assumptions: 1) pixels should retain similar photometric properties between frames, 2) and they should perform small spatial displacements[38]. In live-cell imaging, this information provides insights into the motility of objects, allowing estimating their directionality, speed,

and shape without the limitations associated with tracking procedures. However, OF methods do not always apply to live-cell imaging conditions. One reason is that the assumption of constant pixel intensity is not met, due to fluctuations in fluorescence emission over different regions of the specimen and across time points. Moreover, the sampling rate of microscopy acquisition significantly influences the measured displacement of cells between frames. Consequently, time-lapses acquired with larger sampling rate might not respect the assumption of small object displacements between consecutive frames.

A general limitation of pixel-based techniques is the need for extensive parameter adjustment, which hampers their applicability to varying imaging settings. For this reason, although pixel-based techniques are generally effective and straightforward to apply, they can suffer a lack of generalizability that prompted researcher to develop novel and more robust methods. A notable example is Ilastik[39], a semi-supervised classifier for segmentation that enables users to interactively define pixels of interest to improve the outcome of the predicted foreground. This approach represent a significant improvement in the field and a step toward the mainstream applicability of pixel-based analysis. However, as the availability of imaging data rapidly increases, there is a concrete need for further methodological advancement to effectively extract and process imaging data. To this end, modern computer vision (CV) and activity recognition (AR) techniques can reveal promising strategies, especially in treating time-lapses data.

3. An overview of computer vision and activity recognition

Computer vision is a discipline of computer science that aims to enable computers to extract and process the visual information contained in natural images and movies[40]. One of the goals of the field was the algorithmic understanding of visual data analogously to how human vision perceive and interpret real-world information. To achieve this goal, early attempts in the field focused on the engineering of spatial features based on the hypothesis and understanding of human vision. The casual discovery that neurons in cats activate upon seeing simple lines[41,42] laid the basis for a hierarchical model of vision in which low-level features enable the understanding of high-level features such as objects or sceneries[43,44].

Hence, early work in CV focused on the development of algorithms that could extract simple low-level features, such as lines or corners, to progressively build a higher-level understanding of natural images. These features were extracted with the aid of image filters, namely 2D matrixes with numerical entries capable of finding correspondences of simple shapes within the image. This approach established the birth of feature extraction and pattern recognition[45], which successively enabled the task of image classification. By engineering different filters, vision researchers could extract multiple descriptors from natural images. Successively, by quantifying the occurrence of these descriptors, they could classify the content of the images. For instance, early face detectors would employ rudimental image filters to highlight horizontal lines representing the eyes and the mouth[46,47] (Fig. 3A). Such filters, applied in a cascade sliding-window fashion, allowed to effectively detect faces within images depicting multiple individuals (Fig. 3B).

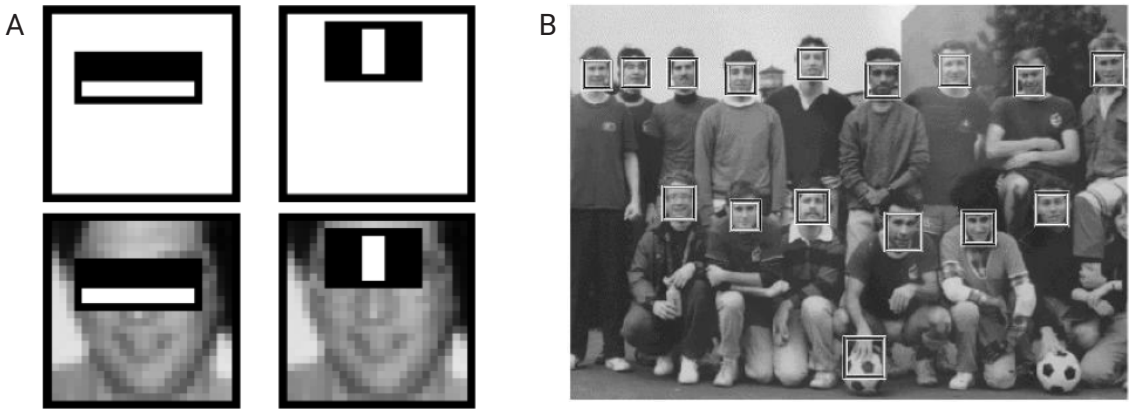

Figure 3. Simple face-detector based on spatial filters A. *Representative kernels of the Viola-Jones face detector to identify key facial features.* ***B.*** *Subsequent application of the Viola-Jones algorithm to detect all faces in a group picture. From*[46].

The aforementioned approach is also popularly known as "bag of words"[48], words referring to individually engineered features (Fig. 4). For example, to distinguish an image depicting a face from an image depicting a bicycle, a different occurrence of the words, or features, "nose", "eye", "mouth", "wheel" and "pedal" are expected in the two images. After engineering several filters, the occurrence of the extracted words was compared with reference populations of images of known content and label, such as "faces", "cars" or "mountains". Reference image populations had known statistical distributions of words, which were compared with the words occurrence of novel images to establish their label.

This strategy had a large consensus in the vision community, finding successful application in the most disparate image classification tasks. However, two bottlenecks were present at the time. Firstly, manually engineering several image descriptors was not sustainable in the long term, as their number would inevitably grow with the class labels and complexity. Moreover, manually engineered features often relied on hypothesis and intuition, offering no guarantee of being adequate and inevitably leading to a trial-and-error process. Secondly, traditional statistical and probabilistic inference approaches required large sample sizes and did not guarantee optimal results in high-dimensional non-convex spaces.

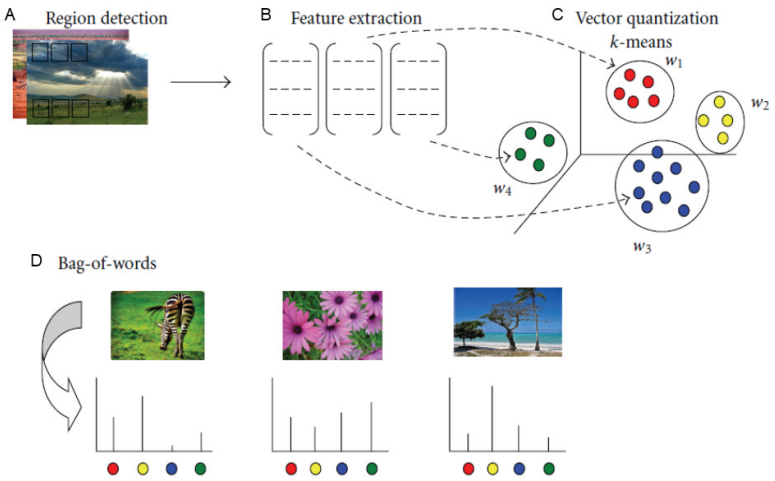

Figure 4. Representative steps of a bag-of-words classification algorithm. A. *Region from Input images are extracted.* ***B.*** *Each region is processed to create a feature vector.* ***C.*** *Feature vectors are grouped by similarity in clusters, or words, to build a dictionary.* ***D.*** *The occurrence of individual words in an image is the hallmark used to attribute a label. Adapted from* [48].

It is with the advent of machine learning techniques, and more specifically with support vector machines (SVM)[49], that CV made a major leap forward. SVM enabled to learn separating boundaries in a high-dimensional space from few samples, having the upper hand over traditional statistical approaches. However, the selection of optimal features remained a trial-and-error approach that often required several iterations before achieving satisfying results. While SVM improved the classification step, feature engineering remained a large barrier for computer vision practitioners[50]. Therefore, computer vision required more robust methods to extract features from images.

3.1. Modern computer vision and deep learning

Deep learning elegantly addressed the two previously mentioned issues encountered in CV, namely the extraction of features from natural images and their classification. The advent of convolutional neural networks[51] (CNNs) offered an apparent solution to the challenge of feature engineering by enabling the algorithmic optimization of spatial filters used for feature extraction. The application of CNNs to natural images generated a feature map that was optimized for both the extraction of relevant features and for their subsequent classification. Accordingly, gradient descent optimization ensured that the features extracted were sufficiently informative to achieve a high classification accuracy, sparing countless time from the manual engineering of non-effective features. At the same time, the algorithmic optimization of the decision layer of CNNs bypassed the need for adjusting the hyper-parameters of traditional discriminative approaches, such as SVM or random forest. Therefore, feature extraction and classification were finally merged into a unique end-to-end step that made feature engineering and traditional ML classifiers less appealing (Fig. 5).

The subsequent shift in the CV paradigm brought tremendous advantages for practitioners, and CNNs quickly became of the main building-blocks of most DL architectures for vision-based tasks. In modern computer vision, several key tasks constitute the foundation of the field. These mainly include image classification, object detection[53–55], and object segmentation, each serving a distinct purpose. Image classification is the simplest task and it involves assigning a class label to entire images based on their content (Fig. 6A). Object detection, on the other hand, is more chal-

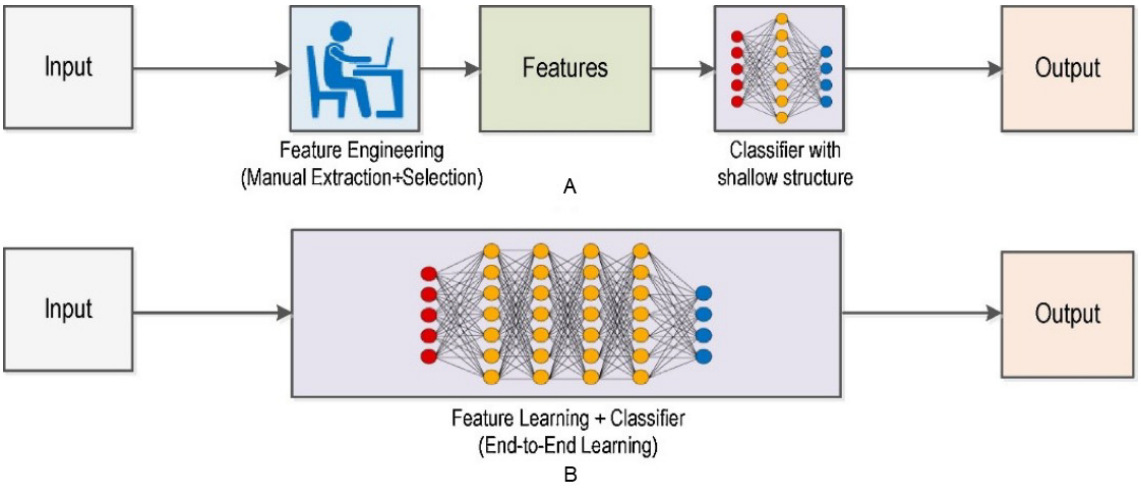

Figure 5. Comparison between classification algorithms using manual-engineered or deep-learning-based features. A. *Traditional classification algorithms includes the explicit design of manually-engineered feature that are subsequently classified.* ***B.*** *In deep learning, feature learning and classification steps are merged, enabling the automatic and optimal identification of features. From* [52].

lenging than classification, as it entails predicting the spatial coordinates of target objects within an image along with their class label (Fig. 6B). This is typically achieved by estimating the bounding boxes coordinates framing each object of interest. Object segmentation adds another layer of complexity, as it presuppose a pixel-level generation of masks for individual objects or regions of interest within images (Fig. 6C). Lastly, semantic segmentation merges the idea of object detection with object segmentation. This is achieved by associating each pixel in the predicted semantic foreground with a specific semantic category (Fig. 6D). Hence, this task is more fine-grained than standard segmentation, as it assigns a label with a unique identifier to each predicted segment.

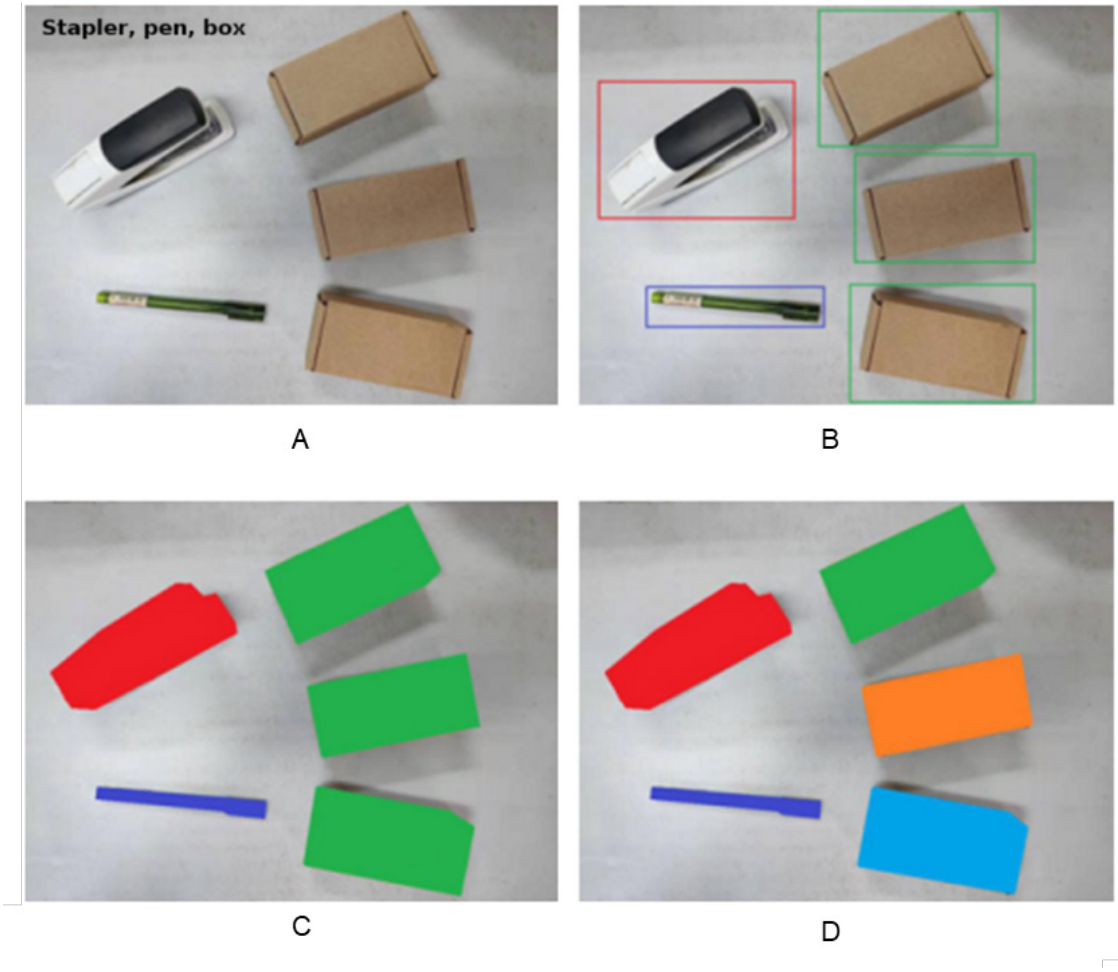

Figure 6. Depiction of four common tasks in modern computer vision. A. *The classification task consists in attributing a label to the whole image based on its content. B. Object detection involves the spatial detection of individual objects within the image and their classification.* ***C****. Semantic segmentation involves labeling each pixel in an image with a corresponding class label for the object of interest, e.g. "pen", "stapler", "box".* ***D.*** *Instance segmentation, in addition to label each pixel with a corresponding class, provides distinct instances for multiple objects belonging to the same class. From*[53].

3.2. Computer vision in bio-imaging

In the past decade, the field of CV has gained significant interest from the biological and microscopy communities. CV algorithms have successfully tackled the complex visual features present in live-cell imaging data, leading to astonishing results in medical imaging[56]. Notably, CNNs have outclassed human physicians in classifying histological tissues, proving useful the screening various pathological conditions[57,58] (Fig. 7A). Moreover, when applied in a sliding window fashion, CNNs have facilitated the detection of target cells, tissues or organelles within specific regions of the images[59] (Fig. 7B). Therefore, these advancements have found large application in digital pathology, where they proved instrumental for the classification, detection and segmentation of cells and tissues.

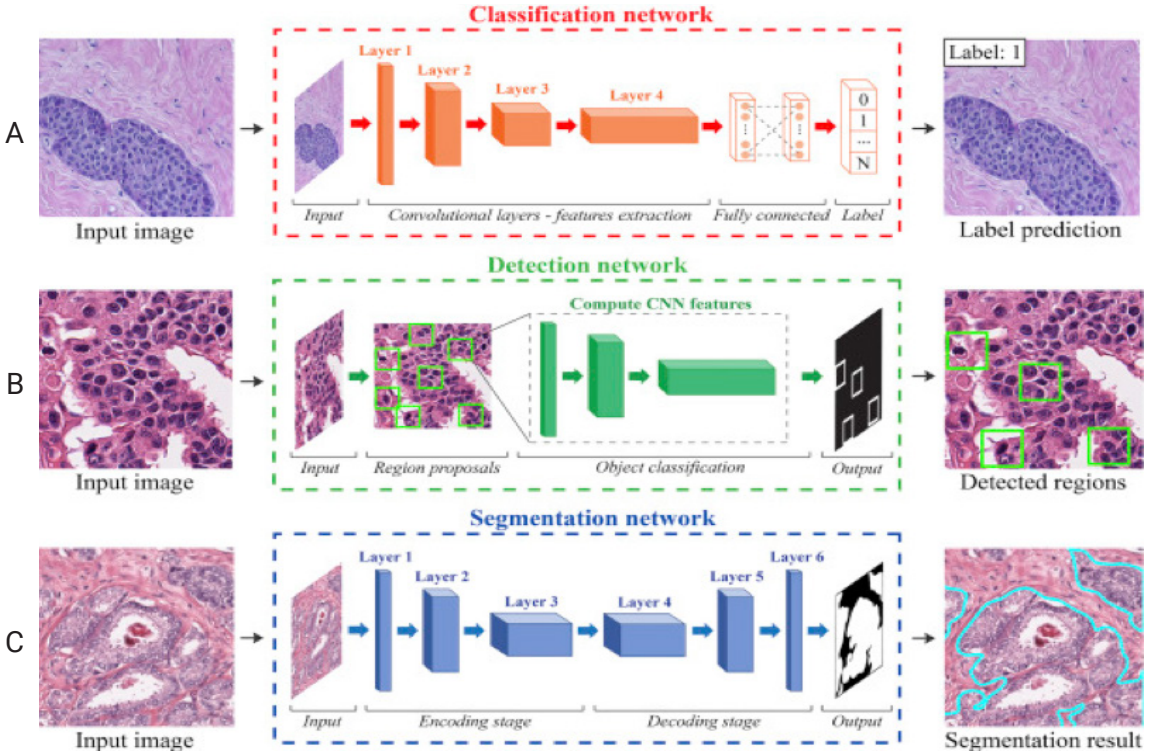

Figure 7. Common deep learning applications in digital pathology. A. *Classification network applied to predict the label of histological tissues.* ***B.*** *Detection network locates cells of interest within histological tissue.* ***C.*** *Segmentation network highlights the contour of regions of interest in histological tissues. From* [60].

The recent advent of auto-encoder architectures, such as the U-net[61], has made a substantial impact in the practical application of CV to bio imaging. This architecture, specifically designed for biological use, offered robust and accurate object segmentation based on supervised annotations (Fig. 7C). In addition to the coordinates of the target objects predicted by traditional detectors, auto encoders provide the shape of the object too. Moreover, auto-encoders have the technical advantage of accessing the entire image compared to region proposal detectors, resulting thus in more efficient training due to the need of fewer samples. This offered researchers novel opportunities to analyze live-cell imaging data and effectively quantifying the occurrence of a cell population of interest, the presence of anomalous cells, as well as highlighting internal cell structures and organelles. In addition, auto encoders generally improved all existing routines relying on cell segmentation as a pre-processing step, most notably cell tracking and lineage analysis among others.

The popularity of auto-encoders architectures arose in every field of bio imaging, including medical imaging, digital pathology, microfluidics, and live-cell imaging. However, regardless of the milestones achieved, current CV applications for live-cell imaging mostly addressed the static aspect of acquisitions (classification, detection, segmentation), neglecting the temporal information embedded within consecutive frames. Therefore, to access this information, there is a concrete need for techniques that explicitly address the temporal insights of live-cell imaging. In this regard, approaches based on activity recognition might reveal beneficial in several live-cell imaging contexts.

3.3. Human activity recognition

Activity recognition (AR) is the process of automatically identifying and understanding the actions of individuals, animals, or objects from various sensory data such as images, videos, audio record or motion data. AR involves the development of algorithms and techniques that enable to recognize and understand distinct activities based on features and patterns encountered in the sensor data. Typically, this involves a combination of techniques to extract relevant features from sensor data, such as motion patterns. Successively, these features can be used to train a model capable to recognize specific activities performed by a subject.

Among the different types of AR, human activity recognition (HAR) focuses on identifying and understanding the motility patterns of humans to predict their behavior[62,63]. HAR is typically divided in four distinct steps[62–64]. At first, sensory indicators of human activity are collected for an interval of time with dedicated monitoring devices (Fig. 7). These can include motility data such as video records, motion sensors, and geographical position among others. Alternatively non-motility data can include the web history, the activity performed on electronic devices, as well as body parameters recorded with smart watches.

Successively, the collected sensory data are processed to be suitable for the training of a predictive model. Finally, the trained model is deployed on novel and unseen sensory data to infer the activities performed by humans (Fig. 8).

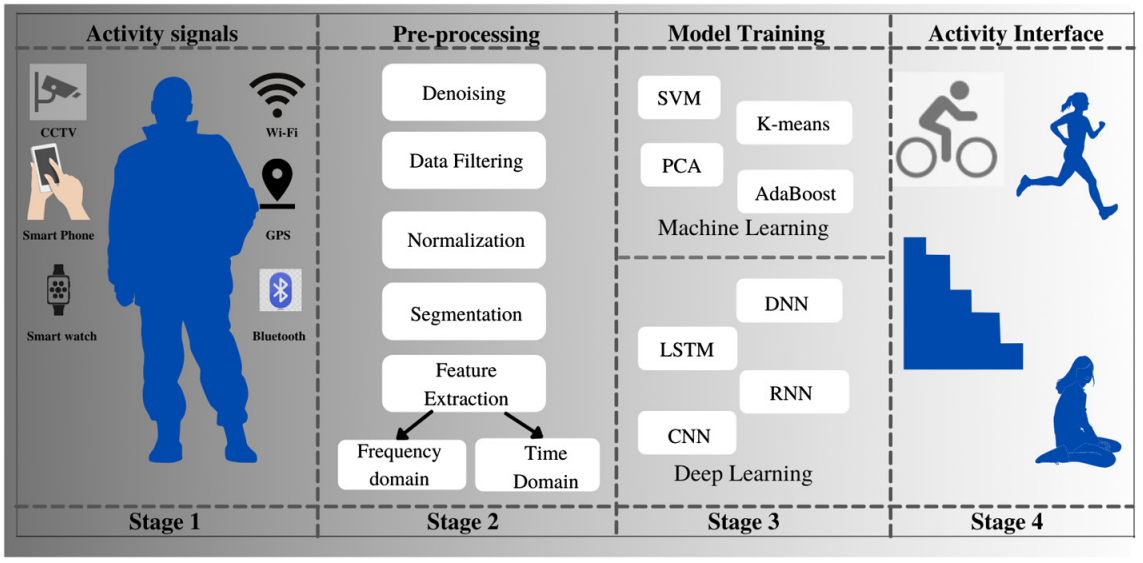

Figure 8. Steps for human activity recognition. *Sensory data representative of human activity are collected using a digital device. After processing the data to extract key features, the latter are used to train a discriminative model to distinguish human activities. Finally, the trained model is deployed on novel sensory data to infer human activity. From* [65].

The applications of HAR are several and can include monitoring of sport actions, surveillance from camera records, law-enforcement, appropriate urban conduct, and commercial surveys among others. At present, HAR plays a crucial role in several tasks that contemplate processing of real-world information, and its use is expected to increase with the growing availability of sensory data.

3.3. Video-based activity recognition and related challenges

One of the main research topic in computer vision is video-based activity recognition[66], which involves the analysis and understanding of human activities encoded within a video sequence. The assumptions underlying this technique is that spatial information of human activities is encoded within static frames, whereas the temporal information is captured by the changes occurring between consecutive frames. Therefore, video-based activity recognition requires the processing of both spatial and temporal features with dedicated techniques. However, the complex nature of video data can pose several challenges. Among these are temporal modeling, which entails understanding how activities evolve over time as well as identifying their temporal dependencies. Temporal modelling can prove difficult as it involves various sub-routines such as motion detection, tracking changes in morphology, and discerning interactions between objects and individuals. Furthermore, video data can exhibit high dimensionality, spanning diverse lengths, high resolutions, and wide-fields of view, thus demanding computationally intensive processing. The variability in viewpoints and camera angles further complicates matters, as these variations alter the appearance of the same activities. Camera motion, such as zooming or shaking, can introduce visual artifacts, intensifying the difficulty of activity recognition. Finally, occlusions and clutter often obscure activities in realistic settings, with subjects of interest potentially obstructed by other objects and leading to a loss of information.

To address these challenges, advanced machine learning and computer vision approaches are required, particularly those with demonstrated robustness in real-world movie scenarios. However, the design and benchmarking of such techniques would be impractical without the availability of extensive curated datasets for activity recognition. Consequently, researchers have begun crafting dedicated datasets comprising standardized clips depicting various

human activities categorized by classes[67] (Fig. 9). These datasets often encompass several of the aforementioned challenges, such as changing viewpoints, dynamic backgrounds, and varying quality and lighting conditions.

Figure 9. Activities sample from UCF101 dataset. *Image gallery depicting human activities sampled from the UCF101 dataset. From*[68] .

3.4. Deep learning architectures for video-based activity recognition

As previously discussed, video-based AR requires robust approaches for the extraction of spatial-temporal features as well as for their classification. Early attempts of AR in computer vision were based on the classification of the optical flow between consecutive frames or digital filters, among other manually engineered features. However, current research focuses on end-to-end DL networks capable of extracting and classifying the spatial-temporal information contained in movies. Following, we report the main DL architectures that have been used for video-based activity recognition:

Traditional 2D CNNs operate at the frame level to extract spatial features from each frame[69]. While this approach does not capture temporal relationships per se, temporal information can be represented by aggregating the feature vectors of each frame. Common aggregation techniques include averaging, max pooling, or using CNNs in conjunction with sequence modeling architectures like LSTM[70].

Similar to 2D CNNs, 3D CNNs simultaneously extract spatial and temporal filters using a 3D kernel applied to the x, y, and time dimensions[68]. With this approach, the entire video is treated as a volume and passed directly into the architecture, eliminating the need for additional preprocessing steps.

Recurrent Neural Networks (RNNs) were initially designed to process sequential data in natural language processing (NLP) tasks. These networks evaluate sequential entries while retaining memory of previous entries, allowing to capture complex and distant time relationships within the time series. Recently, RNN architectures have been applied to model temporal dependencies in video tasks[71]. To increase their effectiveness, these architectures are often preceded by modules for spatial feature extraction, such CNNs stacked on top of the recurrent architecture (e.g., CNN-LSTM).

Similarly to RNNs, transformers[72] were also developed to treat sequential data in the context of NLP. However, a major difference is that these architectures rely on attention mechanism rather than memory. The entire input sequence is processed at once, and attention heads learn to understand which part of the sequence holds significance in order to make correct inference. Similarly to RNNs, transformers are combined with spatial feature extractors and produce hybrid models (CNN-Transformer).

Finally, multiple-Stream networks[73] were devised to address a limitation of CNNs, which cannot directly extract temporal features. To overcome this aspect, double-stream networks introduced two types of inputs. The first input consists of the unchanged RGB sequence of frames, while the second input is a sequence of optical flows capturing temporal changes between frames. These inputs are independently processed by CNNs, and their outputs are combined through temporal aggregation. Variations of these architectures include the incorporation of additional streams and the stacking of DL architectures (e.g., Two-Stream-CNN-3DCNN, Two-Stream-CNN-LSTM). Multiple-Stream networks do not represent an entirely new class of architectures but rather a modification of existing architectures by extending the input sources.

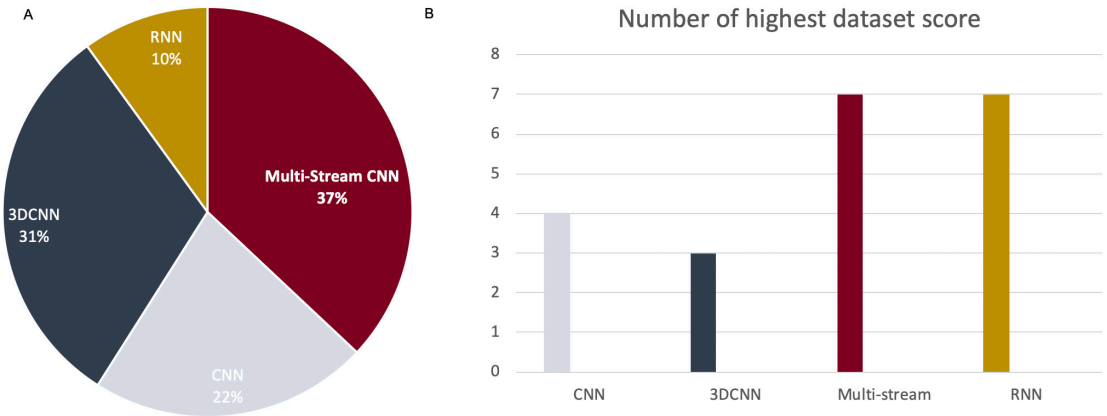

Figure 10. Prevalence of deep learning architectures in computer vision. *A. Pie-plot showing the percentage usage of deep learning architectures for computer vision tasks until 2021. B. Bar plot showing the number of times that a deep learning architecture achieved the highest accuracy on an activity recognition dataset. Data elected and extracted from[74] and subsequently re-plotted.*

These architectures offer different approaches to address the challenges of video-based activity recognition, including capturing spatial information and modeling temporal dependencies. Vision researchers often explore combinations of networks to improve performance and meet specific requirements of recognition tasks. However, it is important to note that, at present, no architecture is universally superior to others. On this matter Ullah and colleagues[74] emphasized that different architectures may perform better or worse depending on the dataset characteristics, as each dataset can present unique content that might be better grasped by a specific network[74]. For instance, Multi-stream networks, 3D CNNs, and recurrent networks all achieved the highest benchmark score in at least one kinetic datasets for AR[74] (Fig. 10). Therefore, in light of these evidences, computer vision practitioners should conduct a thorough and comprehensive evaluation to determine the most suitable network for a particular activity recognition task.

3.5. Video-based cellular activity recognition

AR has well-established applications within the human social infrastructure, and recently it has captured the interests of other fields, among which the scientific community. In this regard, AR has been used to monitor the stress levels and well-being of experimental mice in a cage, or to keep track of the behavior and migratory patterns of animal herds. These promising applications are laying the basis to expand the usage of AR to other scientific fields, including live-cell imaging.

In the context of live-cell imaging, AR techniques could produce tremendous advantages to automatically monitor the behavior of cells. Analogously to human, cells can display characteristic morphological phenotypes associated with distinct activities[26]. For instance, migrating cells can undergo a unique locomotion pattern, also referred as amoeboid migration. Conversely, the morphology of cells at rest is rounded and constant. Cells also exhibit morphological hallmarks when undergoing mitotic division, cell death, antigen scanning, and extravasation among others. Thus, simple morphological features can enable the application of cellular activity recognition (CAR) to differentiate and classify distinct cellular behavior. In this context, CAR strategies could provide an understanding of the dynamic processes occurring in live-cell imaging on par with fluorescent reporters. For instance, any cellular activity that yields a

distinctive morphological phenotype could be automatically detected in a label-free manner. Processes like cell death, immunological synapses, cytotoxic interactions and others could be measured without specific staining nor the use of transgenic animals, thus reducing experimental manipulations, costs, and times. Moreover, CAR could obviate to common problems related to manual annotation and cell tracking[25], reducing the bias due to subjective annotation and processing time. In turn, these aspects could enable robust and high-throughput analysis of live-cell imaging data.

Despite the clear advantages of CAR, however, its usage might be hampered due to the intrinsic challenges and complexity of live-cell imaging. Similar to HAR movies, live-cell imaging data present occlusions due to overlapping cells, clusters, and non-cellular structures. In addition, live-cell imaging data present higher dimensionality than standard RGB movies, as they often capture multiple focal planes encompassed in four-dimensional time-lapses (x, y, z, channels, time). Moreover, the presence of specific imaging artifacts, such as photo bleaching, signal intensity variation and poor contrast, further exacerbate the challenges associated with imaging platforms. Fort these reasons, although video-based HAR revealed effective in capturing human activities, the application of HAR algorithms to address CAR is not necessarily straightforward.

For instance, in video-based HAR, the use of two-stream architectures resulted in the highest accuracy across various kinetic datasets[74]. However, the transposition of these architectures to CAR might be hampered in live-cell imaging. This arises from the inherent assumption of small luminescence changes in optical flow, which is not necessarily respected in live-cell imaging due to large variations in the signal intensity. Therefore, vision researcher should carefully consider all the related challenges that are specific to live-cell imaging prior to establish a CAR strategy. To do so, researchers should have access to curated datasets encompassing multiple cellular activities. However, at present tailored kinetic datasets encompassing various cellular activities are non-existent. Therefore, generating and curating these datasets should be a priority for establishing the field of CAR.

4. Cellular activities displayed by the immune system

The immune system is a complex network of organs and cells tasked to defend the organism against potential threats such as viruses, bacteria, parasites and cancer cells. In such a system, innate immunity represents the first line of defense against unwanted pathogens[75]. This defense comprehends effector cells that, upon recognizing evolutionary conserved antigen regions, are responsible for directly clearing potential threats by phagocytosis[76] or induced killing. The second line of defense of the immune system is the adaptive response, in which cells specialized for antigen recognition produce specific antibodies that binds to pathogen and orchestrate their disposal in a selective manner.

A natural biological response triggered by the immune system in response to injury or infection is inflammation. Inflammation is a protective mechanism aimed at removing harmful stimuli and initiating the healing process by grouping the main actor of the innate and adaptive response at the site of inflammation while enhancing their activity. The process is complex and characterized by high cell dynamism which involves changes in the behavior of cells both at the site of inflammation as well as at distant organs[77,78]. in this process, Immune cells are key players that relocate into infected or injured tissues and orchestrate the immune response by releasing pro inflammatory signals and mediators that initiate a cascade of immune reactions[79–83].

To better characterize this complex set of interactions, researchers are interested in studying the behavior of individual immune cells participating in the process. To this end, fluorescent microscopy and cytometry techniques are employed to identify and characterize distinct cellular population based on the presence of specific fluorescent markers. This generates a landscape of immune players, their activation state and their function at a given time-point. However, one downside of these techniques is the finite number of fluorophores per panel, which in turn limits the number of cell populations and activation states that can be detected simultaneously.

To obviate the aforementioned limitations, CAR in live-cell imaging would enable multiplexing of distinct cell actions without constraints imposed by the finite panel. In turn, fluorescence channels would remain available for capturing other cell types of interest. However, the successful application

of CAR for the study of the immune system requires the explicit definition of cellular activities in association with a clear and characteristic morphological phenotype. Currently, this relationship is not always addressed in the literature, as from a biological perspectives cell populations are rather characterized in a mechanistic way and from a biochemical perspective.

Therefore, to enable the application of CAR in immunology, we curated a review of immune cellular activities and related motility patterns[26]. In our work, we considered the immune response to be a hierarchical set of actions performed by single cells or a group. To this end, we reported from the literature all actions displayed by immune cells in different organs during key inflammatory processes (Table 1), providing a consensus definition for each action and its biological relevance during inflammation. In the next paragraphs we directly cite the main activities displayed by immune cells as reported in our review article[26].

4.1. Patrolling

Patrolling is an action associated with random-like movement and extensive monitoring of tissues (Fig. 11A–B)[84]. Patrolling-like cells exhibit long tracks in a confined area, which results in low directionality. The speed of patrolling-like cells varies according to the cell type, conditions, and anatomical site. For instance, patrolling-like monocytes exhibited a speed of 36 um/min in the endothelium of carotid arteries and 9 um/min in the mesenteric venules[85], while patrolling-like B cells exhibited a speed of 6 um/min in the lymph node follicles.

Patrolling-like cells are pivotal in the initiation of the inflammatory process, as they are capable of efficiently monitoring large areas and promptly responding to the presence of antigens.

Maximize antigen encountering. Patrolling-like behavior in immune cells was interpreted as a strategy to maximize antigen encountering in different tissues. The endothelium of blood vessels is continuously monitored by innate immune cells displaying a patrolling-like behavior. Amongst these, monocytes promote the recruitment and activation of neutrophils, and initiate a local neutrophil response via secretion of proinflammatory cytokines[84–87]. Neutrophils within the blood vessels lumen instead were described with a patrolling-like behavior within the lumen of blood vessels and associated with an increased capacity for being recruited to the inflammation site[88,89].

More recently, tissue-resident eosinophils have also been reported to display a patrolling-like behavior in the vasculature of different organs, which became more prominent in response to inflammatory stimuli[90].

In the LN, patrolling-like B cells continuously survey subcapsular macrophages and follicular dendritic cells in order to identify antigens that are either presented on a cell surface or suspended in the environment[91]. Moreover, within the germinal centers (GC), patrolling-like B cells exhibited a probing, dendritic morphology that confers them a larger surface area and therefore a greater opportunity for antigen encountering (Fig. 11C, ii)[91]. Similarly, NK cells were reported to maintain a patrolling-like behavior during priming, suggesting that the patrolling-like pattern is an efficient strategy for sensing and integrating cytokine signals in the vicinity of multiple DC[92]. In the same context, patrolling-like of T cells was also reported as a strategy to avoid obstacles in densely packed microenvironments[93].

Tumor immunosurveillance. Within the tumor microenvironment, patrolling-like monocytes were also associated with immune surveillance, promptly detecting tumor material, establishing interactions with metastasizing cells, and promoting recruitment and activation of natural killer (NK) cells in lung carcinoma[94]. Similarly, within the lymph node (LN), NK cells exhibit a patrolling-like pattern while searching for cognate targets and transformed cells (Fig. 11C, iii)[95].

4.2. Directed migration

Directed migration is an action associated with cells displacing along straight trajectories. These cells typically exhibit long tracks with high confinement ratio and possibly high speed (Fig. 11 D–E) depending on the cell type, the conditions, and the microenvironment.

In an inflammatory context, cells undergo directional migration in response to chemotactic cues and inflammatory signals, as well as when influenced by anatomical structures. Generally, directional migration is described as a strategy to rapidly reach a specific target, which also plays important roles in recruitment, tissue repair and cleaning, and antigen presentation[96,97].

Response to chemotactic gradients. One of the best-characterized processes associated with directional migration is chemotaxis. This involves the polarization and displacement of cells towards the source

of a chemotactic gradient (Fig. 11F, i). For instance, neutrophils perform directed migration towards injured, infected, or inflamed areas[98–100], where their presence is relevant for tissue repairing, microbial clearing[101], amplification of the inflammatory response[102] and shaping of the adaptive immune response[103]. Even macrophages perform directed migration in interstitial tissue in response to bacterial infection or tissue injury[104].

Influence of anatomical structures on the directed migration. Tissue architecture can influence cell movements, conferring properties of directed migration. The most compelling case of this is the transportation of cells via the bloodstream[105,106]. More recently, transportation of immune cells via lymphatics[107,108] was also reported, and is associated with a strategy for rapidly reaching lymphoid tissues[96].

Directed migration of immune cells was also reported in tumor microenvironments. For instance, CD8+ T cells exhibited a directed migration pattern along collagen fibers in a model of ovarian carcinoma (Fig. 11F, ii)[109]. Moreover, the architecture of the LN was reported to influence the recruitment of B and T cells, which displayed directional migration to relocate precisely in their respective areas[110].

4.3. Arresting

Arresting is a cell action characterized by confined trajectories and speed below a predefined threshold (Fig. 11G–H)[110]. The migration of immune cells typically involves alternating cycles of "stop-and-go"[111], and during the inflammatory process, motile cells change their behavior into arresting to perform a variety of functions, including signaling and activation.

Communication and signaling. Effective intracellular communication requires arresting. Notably, both B cells and T cells undergo an arresting phase prior to interacting with DC during priming[112]. This step is essential to maximizing the contact duration and to inducing signaling.

Killing. The formation of stable contacts between a cytotoxic cell and its target is one of the best-characterized biological processes during which cytotoxic cells arrest. For instance, CD8+ T cells arrest during the formation of the cytotoxic synapses with target tumor cells and resume their migration after killing the target[113,114].

Adhesive interactions during recruitment. During recruitment from the blood stream,

several types of leukocytes form adhesive interactions with stromal cells, leading to a decrease in motility and eventually to their arrest[110] (Fig. 11 I). This coincides with findings from recent studies that show that T interacting with lymphatic capillaries cells were commonly arrested[34].

Cell activation. In neutrophils, arresting was associated with the oxidative burst[115], which is a state in which reactive oxygen species are generated. This occurs both during phagocytosis and in response to soluble antigens In contrast, Beuneu and colleagues[92] reported that NK cells do not arrest while being activated by DC. However, NK cells were reported to arrest in the medullary part of the LN[116] following influenza vaccination. Although the arrested NK cells were forming stable contacts with macrophages, this behavior was not associated with NK-mediated lysis. Therefore, it may suggest an alternative activation pattern.

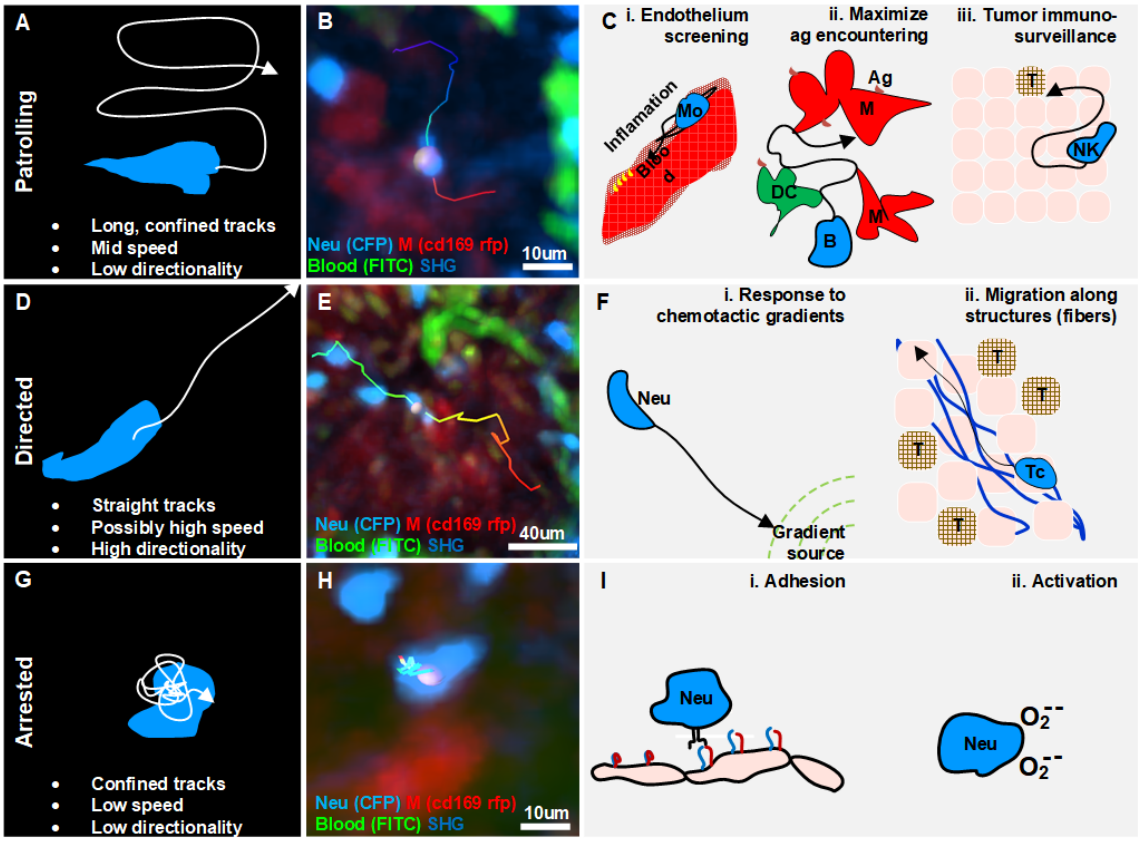

Figure 11. Gallery of actions displayed by individual immune cells. A. *Illustration of a patrolling-like cell, with the characteristic long track in a confined area, which is associated with mid-speed and low directionality (high confinement).* ***B.*** *MMP-IVM micrograph showing a patrolling-like neutrophil (light blue) migrating between macrophages (red) in the subcapsular sinus of a lymph node following infection.* ***C.*** *Illustration of biological cases of patrolling-like behavior, including (i) a monocyte (Mo) screening the endothelium of blood vessels, (ii) a B cell surveying antigen-presenting cells in the lymph nodes (M: macrophages, DC: dendritic cells), and (iii) a natural killer (NK) cell during immune-surveillance in tumor microenvironments (T).* ***D.*** *Illustration of a cell migrating directionally, with the characteristic straight tracks associated with high directionality and possibly high speed.* ***E.*** *MMP-IVM micrograph showing a neutrophil (light blue) exhibiting directed migration towards the subcapsular sinus area of a lymph node following infection.* ***F.*** *Illustration of biological cases of directed migration including (i) a neutrophil (Neu) directed towards the source of a chemotactic gradient, and (ii) a T cell (Tc) moving with directed migration while following collagen fibers (blue structures) in the tumor microenvironment (T).* ***G.*** *Illustration of an arrested cell with the characteristic folded track, which is associated with a low speed and high confinement.* ***H.*** *MP-IVM micrograph showing a neutrophil (light blue) arresting in the proximity of a macrophage (red) in the subcapsular sinus area of a lymph node following infection.* ***I.*** *Illustration of biological cases of arresting including (i) a neutrophil (Neu) during an adhesive interaction with an epithelial cell layer, and (ii) a neutrophil arresting during the production of reactive oxygen species. Adapted from our review*[26].

4.4. Contact formation

Within the immune system, a cellular contact is defined by the formation of an immunological synapse[117]. During contact formation, the distance between membranes of cells decreases up to a distance of 15 nm to 100 nm[118]. Cells forming contacts may exhibit an arrested behavior, or maintain a patrolling-like behavior according to the duration and type of the contact. Cellular contacts are a form of cell-to-cell communication that enables the formation of clusters between the proteins on the surface of two distinct cells (Fig. 12A–C)[119,120]. Although contacts are continuously formed and disrupted between migratory and resident cells in physiological conditions, certain contacts of immune cells are pivotal for inflammatory processes[116,121].

Immunological synapses. One of the best-characterized cases of contact formation between immune cells is the immune synapse that occurs between DC and T cells (Fig. 12C, i). DC play a crucial role in initiating the immune cell response as they scan the surrounding environment in search of antigens to capture and present to naive T cells[122]. The interaction between T cells and DC follow a series of steps characterized by varying contact durations. At first, T cells engage many short-lived contacts with the surrounding DC, reducing their overall motility due to the multiple interactions[123]. Upon successful encounter between T cells and antigen-presenting DC, long-term and stable contacts occur, and T cells remain arrested. This leads to the activation of T cells, which finally recover motility and proliferate. In an OT-I model, a comparison between antigen-specific CD8+ T cells and polyclonal CD8+ T cells revealed that antigen-specific cells significantly decreased their speed in response to the formation of stable interactions with DC[124]. By contrast, polyclonal CD8+ T cells maintained a constant speed[124]. This finding is in agreement with the T-DC model, where different phases of the T cell-DC interaction were associated with different contact durations[125]. Additionally, contacts between T cells and DC can occur in non-lymphoid organs and compartments, such as the lymphatic capillaries of the ear skin[34].

NK cells form short-term contacts with DC by recognizing cytokines on the surface of DC in addition to soluble signals. In contrast with *in vitro* observations, where long-lasting contacts between NK cells and DC were observed, *in vivo* acquisitions in the LN revealed that NK cells maintain a motile behavior during their activation[126]. This yields

to the formation of brief contacts with the duration of 1–3 min, suggesting an efficient strategy to sense and integrate cytokine signals in the vicinity of multiple DC.

Cytotoxic synapses and lysis. Cytotoxic T leucocytes (CTL) can establish cytotoxic synapses with other cells, which eventually leads to cell death (Fig. 3C, ii)[127]. Cytotoxic synapses formed by CD8+ T cells (Fig. 12C, ii) rely on a shared molecular mechanism with CD4+ T cell immunological synapses.[127] However, CD8+ T cell synapses appear to be more stable and efficient in killing the target[128]. Two known killing mechanisms involve the binding of FasL to Fas, resulting in the induction of apoptotic death by caspase activation[129]. The second mechanism involves Ca^{2+} dependent release of perforin and granzymes, yielding to the activation of alternative apoptotic pathways[129]. The latter mechanism was reported to be faster since it does not require specific receptors to be activated[127]. Common targets of CTL are virus-infected or transformed cells. However, CTL killing efficiency was reported to be affected by the affinity for its ligand[123,127].

NK cells are also able to form contacts intended to lyse target cells through degranulation. Within the LN, NK has been observed to form contacts with B cells to eliminate major histocompatibility complexes mismatched targets[95]. Additionally, in the context of tumor microenvironment, NK-mediated lysis was reported to occur either by establishing contacts of long duration with a single NK or via multiple short contacts with several NK[92].

4.5. Swarming

Swarming is an action in which a collectivity of cells, called swarms, cluster in a defined space or move towards a common target in a coordinated manner (Fig. 12D–E)[130]. Swarms have been classified according to their size and duration[130]. Transient swarms with fewer than 150 cells are reported to last up to 40 minutes. Larger swarms, meanwhile, can include more than 300 cells and can persist for hours[130].

The swarming process has been primarily described in neutrophils, which form cell aggregates in inflamed and injured tissues. Notably, duration and swarm size were positively correlated with the severity of the tissue damage or infection, with extended lesions recruiting thousands of neutrophils involved in swarms that persisted for days[131,132]. Cell death, known to induce recruitment of phagocytic cells[27,133,134], is

regarded as one of the triggers of swarm formation.

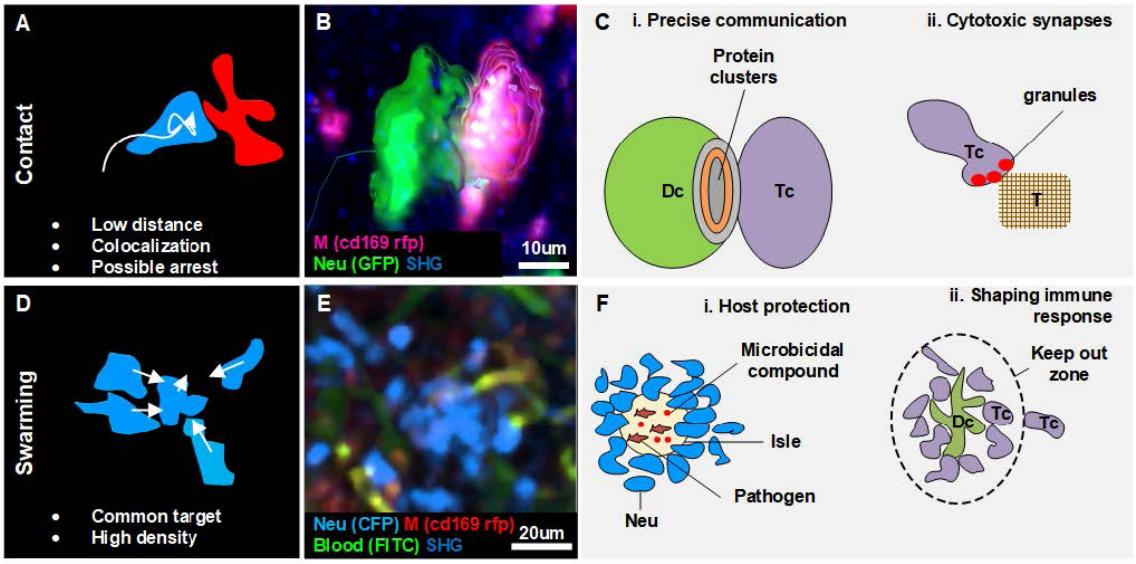

Figure 12. Gallery of actions displayed by two or a collectivity of cells. A. *Illustration of the morphodynamics of contact formation between two cells, characterized by a low distance and the possible overlap of colors.* ***B.*** *MP-IVM micrograph showing a neutrophil (green) establishing contact with a macrophage (violet). 3D reconstructions are shown to highlight the shape of the cells during the formation of the contacts.* ***C.*** *Illustration of biological cases of contact formation including (i) a T cell (Tc) forming an immunological synapse with a dendritic cell (Dc) with a cluster of proteins in the contact area, and (ii) a T cell (Tc) accumulating cytotoxic granules in contact with a tumor cell (T).* ***D.*** *Illustration of the morphodynamics of swarm formation, characterized by cells moving towards a common target, resulting in the accumulation of cells in a confined area (high density).* ***E.*** *MP-IVM micrograph showing a neutrophil swarm (light blue) following infection in the subcapsular area of a lymph node.* ***F.*** *Illustration of biological cases including (i) a swarm of neutrophil (Neu) to contain pathogens in an isle enriched with microbicidal compounds, and (ii) a swarm of T cell (Tc) accumulating around an antigen-presenting dendritic cell (Dc) to prevent the other Tc from interacting with the Dc. Adapted from our review*[26].

Two key functions are associated with the swarming process: host protection and tissue remodeling[131,132,135], both described below.

Host protection. Swarm formation was reported in infection models as a strategy to contain pathogens and protect the host[136]. To this end, swarms lead to the confinement of pathogens in isles where microbicidal compounds concentrate (Fig. 12F, i)[131]. Moreover, neutrophil swarming was observed to contain bacteria spread[135] and limit the growth of fungi *in vivo*[137]. Eosinophils were also observed performing swarms throughout the parenchyma in the lungs in different infection models. Amongst these, during parasitic infections, swarms of eosinophils were maintained for several days[138].

Tissue remodeling and shaping the immune response. Neutrophil swarming was also reported in the context of sterile inflammation. Sterile photo burning[100] and needle damage[98] caused neutrophils to form abrupt and long-lasting clusters of large dimensions, suggesting a role in tissue remodeling and repair.

Additionally, the formation of swarms can alter the cellular structure of immune organs. For instance, swarms formed by neutrophils were reported to disrupt the network of resident SCS macrophages in parasitic infection models[131,139,140]. Considering that SCS macrophages are important for containing the spread of pathogens[141,142] and for activating adaptive immunity[99,141] the alteration of this cell layer by swarms might influence the overall immune response. Interestingly, other cell types, such as NK cells, were also observed to form swarms in the SCS area of the LN and to interact with resident CD11b+ cells. The accumulation of NK cells in the SCS area was linked to the function of promoting self-activation by the encounter with specific APC[143]. Other cell types such as T cells were reported to form swarms around APC following immunization. Since most of the interactions in the swarms were maintained over time[122], it has been proposed that swarms may keep newly arrived T cells at the boundaries of the swarm, limiting their interaction with DC (Fig. 12F, ii)[122].

Table 1. *Summary of the actions described in different inflammatory conditions, organs, and cell types. Adapted from our review[26].*

Condition	Organ	Cell type	Reported actions
Acute inflammation	Kidneys	Monocytes	Patrolling-like [144]
		Monocytes neutrophils	Contact formation [144]
Chronic inflammation	Liver	NKT	Directed[145] Patrolling-like[145] Swarming[145]
Hypersensitivity	Lymphatics	T	Arrested[34] Patrolling-like[34] Swarming[34]
		T DCs	Contact formation[34]
		DCs	Arrested[34] Patrolling-like[34]
Induced	Vasculature	Monocytes	Patrolling-like [84,87,146]
	LN	NK	Contact formation[147] Patrolling-like[147]
		T cells	Contact formation[147]
		NKs	Patrolling-like[95]
		NKs B	Contact formation[95]
		B	Arrested[123]
		T	Arrested[92] Patrolling-like[35]
		T DCs	Contact formation[35,125,148–150]
	Skin	Neutrophils	Directed[132] Swarming[132]
	Lungs	Eosinophils	Directed[90]
Infection	Spleen	Neutrophils	Directed[151] Patrolling-like[151]
		DCs	Swarming[151]
		T	Arrested[151]
		Monocytes	Swarming[151]
	Skin	Neutrophils	Directed[152] Swarming[115,135]
		Eosinophils Macrophages	Contact formation[153]
		Eosinophils	Arrested[153] Directed[153]
	Lungs	Neutrophils	Patrolling-like[115] Swarming[115]
	LN	Neutrophils	Arrested[140] Directed[140] Swarming[130]
		NKs DCs	Contact formation[126]
		NKs	Arrested[126]

Inflammation	glomerulus	Monocytes	Patrolling-like[144]
Injury	Skin	Neutrophils	Directed[98,154] Swarming[98,154]
Steady state	Vasculature	Monocytes	Patrolling-like[84,87]
	Skin	Eosinophils	Patrolling-like[153]
		Eosinophils macrophages	Contact formation[153]
	LN	T	Patrolling-like[155,156]
	Lungs	Eosinophils	Patrolling-like[90]
Sterile inflammation	CNS	Monocytes	Patrolling-like[86]
	Liver	Neutrophils	Directed[157] Swarming[157]
Tumor	Lung	Monocytes	Patrolling-like[94]
Vaccination	LN	Neutrophils	Arrested[27] Directed[27] Patrolling-like[27]Swarming[27]
	Vasculature	Monocytes	Patrolling-like[85]

5. CAR to quantify programmed cell death

5.1. Programmed cell death

Another promising application for CAR strategies is the detection of cellular activities with an evident phenotype, such as programmed cell death (PCD). PCD refers to the mechanism by which cells actively orchestrate their disposal to benefit the organism. One of the best characterized form of PCD is apoptosis, a key process involved in several biological functions to maintain body homeostasis. Accordingly, every day damaged or dysfunctional cells undergo apoptosis to accommodate new healthy cells. This clearing mechanism ensures a balanced turnover and correct functioning of the tissues. Moreover, the removal of infected cells, or cells that sustained DNA damage, is a crucial mechanism of host defense that counteracts the insurgence of pathogens and tumors. Consequently, misregulation of apoptosis may result in severe pathological conditions, including cancer, infectious diseases and autoimmune disorders.

From a morphological perspective, apoptosis display specific hallmarks that make it unique. At a late apoptotic stage, cells undergo shrinkage, chromatin condensation, membrane blebbing and the formation of apoptotic bodies[158]. In response, phagocytic cells are locally recruited by the release of "eat me" signals, and they are successively responsible for clearing the remaining apoptotic bodies, resulting in the conclusion of the process.

This sequence of events is specific to apoptosis, making it a distinctive signature for the process. Hence, video-based CAR methods have the potential to facilitate the analysis of *in vitro* and *in vivo* time-lapses by automatically identifying apoptotic events based on motility and morphological patterns. Notably, the morpho-dynamics of apoptotic cells share similarities to the movements exhibited during various human activities. Therefore, we anticipate that CV-based tools will prove successful to achieve robust CAR for detecting multiple apoptotic cells in live-cell imaging. This achievement will consequently benefit several experimental fields, including toxicology and immunotherapy.

5.2. Advantages and disadvantages with respect to fluorescent probes

The usage of apoptotic reporters[159] is pivotal to gain insights into the adverse effects

of various substances on cellular health and survival. Fluorescent markers that activate during the onset of apoptosis provide a means to quantify apoptotic cells in real time, enabling to monitor changes in cell viability and proliferation induced by specific substance. In turn, this permits to evaluate the toxicity of different compounds and facilitates the screening of potential drugs that inhibit or induce apoptosis.

In line with the scope of fluorescent reporters, algorithms designed for apoptosis detection can deliver real-time quantification of cell death, offering potential advantages over traditional fluorescent probes. One such advantage is label-free detection, as CV and DL methods can operate on unlabeled cells[160], eliminating the need for fluorescent reporters and additional experimental setups. This non-invasive approach has the potential of reducing artifacts associated with fluorescent labeling[161], experimental costs and manipulation time.

DL algorithms are also suited for high-throughput processing, enabling the analysis of large data batches. This feature proves especially beneficial in high-content screening assays for apoptosis, where DL-based detection could reduce experimental variability due to labeling efficiency, probe selection, and photobleaching. Additionally, DL methods can decrease subjectivity in analysis by eliminating biases stemming from individual interpretation or judgment, such as when operating manual labeling of apoptotic. In this case, by automating the analysis process, DL minimizes the reliance on human labeling, thereby enhancing objectivity. Lastly, by leveraging the capabilities of neural networks, DL holds the potential to uncover novel morphological insights and temporal patterns associated with apoptosis, contributing to a deeper understanding of the mechanisms.

5.3. Therapeutic perspectives in toxicology and tumor therapy

The successful implementation of automated apoptosis detection holds great potential for the future of therapeutics that induce or inhibit apoptosis. From a toxicology standpoint, the algorithmic quantification of apoptotic cells serves as an experimental readout providing valuable information about the toxicity of distinct compounds and their ability to elicit apoptosis. Additionally, these methods could also be employed to uncover novel inhibitors of cell death, and due to the capability of measuring apoptosis over time, they could enable a

detailed characterization of dose-response dynamics for different compounds.

In addition to toxicological assays, automated apoptosis detection might play a crucial role in monitoring tumor treatments, where the therapy typically aims to kill a specific cell population. Accordingly, the apoptotic count can be regarded as a detailed readout of the effectiveness of the therapy. This can be especially relevant for treatments that induce targeted apoptosis in tumors, such as apoptotic-inducing agents[162,163] and chimeric antigen receptors T cells (CAR-T)[164]. At present, measuring the efficacy of several anti-tumor therapies relies on measuring changes in the host life span. Arguably, the host survival remains the most indicative parameter to assess the efficacy of the therapy. However, this approach offers little insights on the fate of individual cells and the dynamics of tumor killing.

Solid tumors exhibit significant heterogeneity and diverse microenvironments[165], which can differentially impact the infiltration of cytotoxic cell populations, including T and CAR T cells[22]. As a result, the immunotherapy efficacy can display large variability. To address this issue, it is crucial to gain a comprehensive understanding of the spatial interactions between tumors and the immune system. By doing so, we can successively understand and overcome the limitations of current therapies. Consequently, there is an urgent need for tools capable of assessing individual interactions between immune cells and tumors.

Existing molecular probes for detecting apoptosis provide a cumulative measure of cell death but lack spatial and temporal resolution. While the cumulative signal from these probes can estimate the total number of apoptotic events, it is not possible to determine their specific spatial coordinates without manually tracking cells exhibiting active reporters. On the other hand, fluorescent reporters offer variable activation times, introducing a time lag that can span minutes. To address these limitations, CAR could generate a detailed profile of the apoptotic dynamic. In turn, this information could elucidate the complex spatial and temporal dynamics occurring within the tumor microenvironment and the immune system.

AIM AND RELEVANCE

AIM AND RELEVANCE

Two-photon intra-vital microscopy has become the reference technology to study in real time interactions between host immune defenses and pathogens. However, analytical tools dedicated to this platform are scarce, and quantitative measurements are prevalently based on trajectory analysis. Therefore, to consolidate the analytical framework in live-cell imaging, the aim of this thesis is the development of methodologies that enable the quantitative studies *in vitro* and *in vivo*, with an eye of attention dedicated to the implications on the immune system. To accomplish this objective, I will adopt two main strategies. The first one consists in developing track-based CAR techniques to segregate cell behaviors into distinct classes that present specific motility patterns. This approach is meant to utilize modern DL techniques to maximize the information extracted from trajectories.

The second strategy consists in developing vision-based CAR methods to detect and classify different cellular activities based on morphology and temporal cues displayed by cells. Specifically, we are interested in characterizing cell death, which has relevant implications within the context of the immune response and immunotherapy. The exploration of video-based CAR is meant to provide alternatives to trajectory analysis, whose cell tracking pre-requisite represent a major bottleneck. To develop and test our tools, we will design tailored architectures for supervised learning. Hence, we will generate relevant 2P-IVM datasets which will be used to train and test the predictive models.

1. Aim 1: Track-based cellular activity recognition

The first aim of this thesis lays the groundwork for the future employ of CAR in live-cell imaging. Following a track-based approach, we want to show that we can use the information embedded within spatial trajectories to predict the dynamics and behavior of cells. Our focus pertains interactions and activities occurring between key players of the immune system, such as neutrophils, T cells, natural killers, and eosinophils.

Before addressing this aspect, however, it was necessary for us to have a consensus of the main cellular activities displayed by immune cells. Therefore, we grouped the major immune activities that were associated with clear and unique motility patterns, as described in the literature, generating an exhaustive ontology[26] that I partially cited in the introduction. The resulting atlas enabled us to characterize different aspect of the immune response, such as the role of neutrophils upon vaccine inflammation explored in manuscript 1.

In manuscript 2, I explored instead the potential of cell tracks to predict cellular identities using the sequential information contained in their spatial-temporal coordinates.

2. Aim 2: Video-based cellular activity recognition

The second aim of this thesis represent a shift from a track-based approach to a vision-based paradigm in CAR. We want to bridge live-cell imaging and CV, demonstrating that the unexpressed potential of vision techniques in microscopy can be promptly conveyed by designing sound DL architectures and appropriate datasets Therefore, using video-based CAR, we decided to characterize cell death as a prototypical activity that displayed clear and unique morphology traits. As a pre-requisite for this goal, in manuscript 3 I first curated a time-lapse dataset depicting apoptotic cells. After fulfilling this requisite, in manuscript 4 I designed and deployed different solutions for spatial-temporal detection of cell death in live-cell imaging.

RESULTS

1. Aim 1: Track-based cellular activity recognition

1.1. Manuscript 1: Characterization of the dynamic behavior of neutrophils following influenza vaccination

The present manuscript represents my first contribution to a peer-reviewed article achieved within the first year of my doctoral training. The project aimed to characterize the role of neutrophils during the inflammatory process induced by inactivated influenza in an unconventional yet innovative manner. By combining traditional immunological investigations with computational track-based analysis, the primary authors of the study, Dr. Latino and Dr. Pizzagalli, demonstrated varying phenotypic behaviors of neutrophils throughout the inflammatory process.

Although I am a co-author, I included this article in the thesis as it defines an important milestone that allowed me to gain a solid understanding over both experimental and analytical aspects that laid the basis for my following work. The practical contributions I provided consisted in supporting the authors with part of the analysis displayed, as well as during the writing and revision of the article.

Status: published in Frontiers in immunology

Characterization of the dynamic behavior of neutrophils following influenza vaccination

Diego Ulisse Pizzagalli[1,2&], Irene Latino[1&], Alain Pulfer[1], Miguel Palomino-Segura[1], Tommaso Virgilio[1], Yagmur Farsakoglu[3], Rolf Krause[2], Santiago F. Gonzalez[1¶].*

[1]Institute for Research in Biomedicine, Università della Svizzera italiana, via Vincenzo Vela 6, CH-6500 Bellinzona, Switzerland.

[2]Institute of Computational Science, Università della Svizzera italiana, via G. Buffi 13, Lugano, Switzerland.

[3]Salk Institute, San Diego, USA.

[&]These authors contributed equally to this work.

[¶]These authors shared the last authorship of this work

Abstract

Neutrophils are amongst the first cells to respond to inflammation and infection. Although they play a key role in limiting the dissemination of pathogens, the study of their dynamic behavior in immune organs remains elusive. In this work, we proposed a novel image-based systems biology approach to characterize *in vivo* the activities of neutrophils in the mouse popliteal lymph node (PLN) after influenza vaccination with UV-inactivated virus. We described a prominent and rapid recruitment of neutrophils to the LN following vaccination, which is dependent on the secretion of the chemokine CXCL1 and the alarmin molecule IL-1α. In addition, we observed that the initial recruitment occurred mainly via high endothelial venules located in the paracortical and interfollicular regions of the LN. The analysis of the spatial-temporal patterns of neutrophil migration demonstrated that, in the initial stage, the majority of neutrophils display a patrolling behavior, followed by the formation of swarms in the subcapsular sinus of the LN, which are associated with macrophages in this compartment. Finally, we observed using multiple imaging techniques, that neutrophils phagocytize and transport influenza virus particles. These processes might have important implications in the capacity of these cells to present viral antigens.

Introduction

The innate immune system plays a critical role in protecting the host during the first hours that follow a new insult[75]. This process involves complex cell-to-cell and cell-to-pathogen interactions that are essential for the early recognition of the pathogen and the initiation of the adaptive immune response[103]. Although several advances have been made in linking the behavior of innate immune cells to the efficiency of the immune response[166], many questions remain open. This is mainly due to the dynamic nature of the aforementioned interaction patterns, which change over time and are distributed in space[167].

The lymph node (LN) has been the preferred organ to investigate *in vivo* the complexity of cell behavior and cell dynamics in relation to immune functions [18]. This organ is highly compartmentalized and is composed of specific regions, which facilitate the coordination of the innate and adaptive immune responses. Indeed, the architecture of the LN further promotes the dynamics of immune cell interactions, such as antigen trafficking between macrophages from different regions, which is critical for the final effector response[36,116,142,168,169], and the capture and presentation of antigen by LN resident dendritic cells (DC) [170,171]. The migration of different cell populations to the specific regions of the LN follows a complex balance of chemokine gradients that orchestrate its architecture. For instance, CCL21 and CXCL12 act on the vascular endothelium to promote the recruitment of leukocytes via high endothelial venules (HEV)[172,173]. After the extravasation process, CXCL13 and CCL19-21 direct B and T cells towards the B-cell follicle and the T-cell zone, respectively[174–179].

Among the innate cells that migrate to the LN in inflammatory conditions, neutrophils constitute the first line of defense against pathogens[140,180]. These cells have important immunological functions, such as the secretion of antimicrobial compounds[181], and play a key role in tissue cleaning and remodeling [88]. Neutrophils are abundant in the circulation in their mature form and are rapidly recruited from the bone marrow upon inflammation[102,182] via post-capillary vessels[183,184] or lymphatics[184–187]. Neutrophil recruitment to the site of infection is a highly regulated process that involves the initial secretion of pro-inflammatory factors, released by activated macrophages and DC, which regulate the expression of adhesion molecules from vascular endothelial cells[80,88]. Among the different inflammatory

cytokines that have shown to be involved in this process, the interleukin-1 (IL-1) family[188–190] and the tumor necrosis factor (TNF) are some of the best-characterized[185]. In addition, many other chemokines and receptors are known to be involved[26,191].

Once recruited to the inflamed tissue, neutrophils can interact with lymphocytes and antigen-presenting cells (APC) influencing the adaptive immune response[88,192,193]. This was demonstrated in different inflammatory conditions in which neutrophils released B cell-stimulating molecules, such as BAFF or CD40L[194], or induced T cell proliferation and activation[192,193,195]. T cell response can further be orchestrated by neutrophils influencing both DC priming and T cell function via NETosis or release of granules[196]. Moreover, recent evidence has indicated that neutrophils can cooperate with DC, transporting antigens to the site of T cell activation or acting as APC[180,197,198].

While the initial recruitment of neutrophils from blood has been extensively characterized[199], their post-recruitment behavior remains widely unknown. One of the few activities previously described regards the formation of aggregates or swarms[140]. This process involves the coordinated migration of cells towards a common target[131,140,200]. During the formation of swarms, the first neutrophils that are recruited can trigger a cascade of secondary chemoattractants, which amplify the recruitment of other neutrophils in a feed-forward manner[201]. The main signals triggering neutrophil influx and swarm formation were associated with tissue injury[98,202]. However, in microbial infection models other factors such as pathogen-derived compounds[136] or other molecules released by dying neutrophils[132] can trigger swarm formation. The role of neutrophil swarms has been linked with microbicidal activity, tissue cleaning and remodeling and protection of uninfected tissues. However, it is unclear how individual neutrophils behave in the swarming environment. Recent evidences in infection model show that neutrophil swarm growth correlates with the removal of subscapular sinus macrophages[140], suggesting an interplay between the two populations and a possible involvement of the resident cell population in the initiation and regulation of the process.

To better investigate the behavior of neutrophils following influenza vaccination, imaging techniques are of paramount importance. Among the available imaging methods, 2-photon intravital microscopy (2P-IVM), allows the long-term observation

of cells in organs and tissues of living animals. For this reason, in the last two decades, 2P-IVM has become an essential tool for the observation of immune-related mechanisms *in vivo,* highlighting unprecedented mechanisms related to cell migration and cell-to-cell interaction [203]. However, an interdisciplinary approach is required to analyze the imaging data generated by this technique. Indeed, the recently established image-based systems biology approach[204] combines microscopy data with computational methods to describe, quantify, and interpret complex biological processes, from imaging data This combination of methods allowed for instance to uncover different T cell receptor signaling patterns[205] or different types of migration patterns[206] from the tracks of immune cells.

In this work, we employ a cutting-edge imaging analysis methodology to characterize *in vivo* the dynamics of neutrophil recruitment and their migratory patterns following vaccination with UV-inactivated influenza virus. Thus, we highlight the interaction of early recruited neutrophils with the resident macrophage population involved in antigen capturing. Finally, we report how neutrophil behavior changes over time, using a new mathematical model that maps recurrent motility patterns of neutrophils to biological functions.

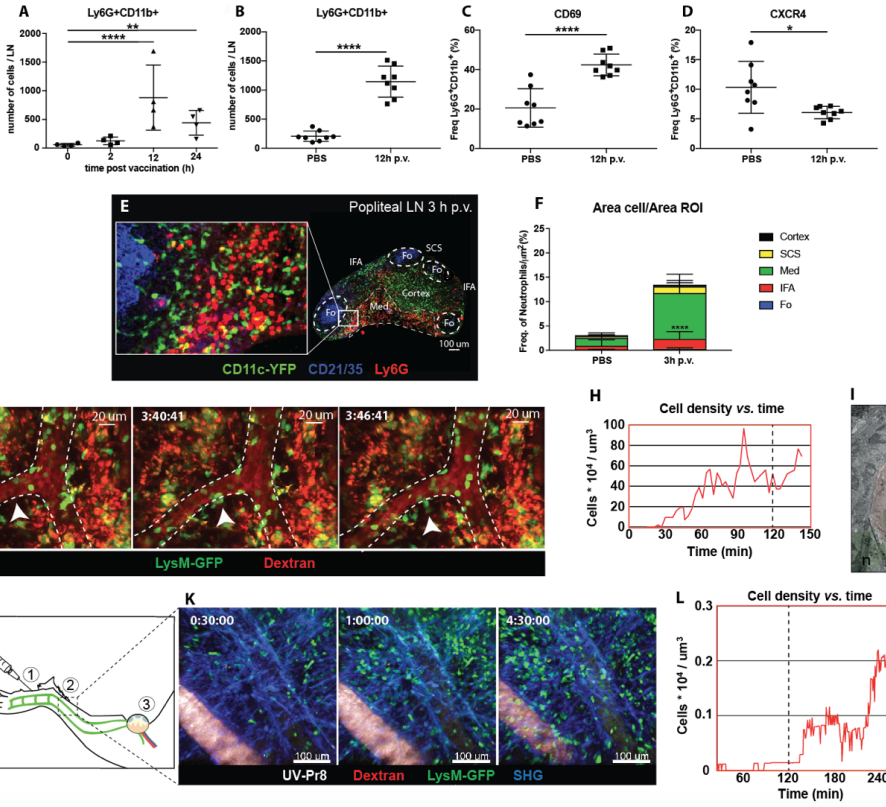
A
Ly6G+CD11b+
number of cells / LN
time post vaccination (h)
B
Ly6G+CD11b+
PBS
12h p.v.
C
CD69
Freq Ly6G+CD11b+ (%)
D
CXCR4
E
Popliteal LN 3 h p.v.
SCS
IFA
Cortex
Med
Fo
100 um
CD11c-YFP CD21/35 Ly6G
F
Area cell/Area ROI
Freq. of Neutrophils/um² (%)
3h p.v.
Cortex
SCS
Med
IFA
Fo
G
3:33:09
3:40:41
3:46:41
20 um
LysM-GFP Dextran
H
Cell density vs. time
Cells * 10⁴ / um³
Time (min)
I
HEV LN 2 h p.v.
n
5 um
J
K
0:30:00
1:00:00
4:30:00
100 um
UV-Pr8 Dextran LysM-GFP SHG
L
Cell density vs. time
Cells * 10⁴ / um³
Time (min)

Figure 1. Neutrophil recruitment and distribution into the popliteal lymph node (PLN) after influenza vaccine administration. ***A****) Kinetic of neutrophil recruitment into the LN during the first 24 h following UV-inactivated influenza virus injection (UV-PR8).* ***B****) Flow cytometric analysis showing the recruitment of neutrophils (Ly6G+ CD11b+) at 12 h post vaccination (p.v.). Percentages of CD69+ (****C****) and CXCR4+ (****D****) cells out of all neutrophils at 12 h p.v. compared with non-vaccinated controls.* ***E****) Representative confocal microscopy of LN section showing the distribution of Ly6G+ neutrophils (red) in the LN at 3 h p.v. in a CD11c-YFP animal.* ***F****) Quantification plots showing the distribution of neutrophils in the medullary (Med), interfollicular area (IFA), T cell zone (Cortex), follicle (Fo) and subcapsular sinus (SCS) areas of the LN at 3 h p.v.,* ***G****) Sequential 2-photon intravital (2P-IV) micrographs showing the recruitment of LysM-GFP neutrophils (green). Blood vessels (red) are labeled by i.v. injection of Rhodamine B isothiocyanate-Dextran and arrow indicated hotspot of neutrophil recruited.* ***H****) Time series showing the increasing density of neutrophils inside high endothelial venules (HEVs) of the PLN following vaccination.* ***I****) Scanning electron micrograph showing an association between neutrophils (n) and HEV at 2 h p.v.. The lumen of the blood vessel is marked in red.* ***J****) Schematic drawing of the mouse footpad showing the injection site (1), the imaged area (2) and the lymphatic drainage towards the PLN.* ***K****) Sequential 2P-IV micrographs showing the recruitment of LysM-GFP inside the lymphatic vessel in the injection site following UV-PR8 administration.* ***L****) Time series showing the density of neutrophils inside the draining lymphatic vessel. In all figures, the presented data are representative of at least three independent experiments. Results are given as mean ± SD. ns p>0.05; *p<0.05; **p<0.01; ***p<0.001; ****p<0.0001.*

Results

Neutrophils are recruited to the draining lymph node via blood following influenza vaccination. To study the dynamics of neutrophil recruitment to the popliteal lymph node (LN) we evaluated the total number of Ly6G+/CD11b+ cells by flow cytometry during the first 24 h following footpad administration of influenza vaccine (UV-inactivated influenza virus, strain A/Puerto Rico/8/34). We observed a rapid increase in the number of neutrophils, reaching a peak at 12 h post vaccination (p.v.) (Figures 1A, B). Moreover, we found that the recruitment coincided with an increase in the expression of the early activation marker CD69 in these cells (Figure 1C). However, we found that, once in the LN, neutrophils downregulate the expression of the chemokine receptor CXCR4, one of the key regulators of leukocyte trafficking (Figure 1D). In addition, we also detect loss and shedding of the receptors CD44, CD62L, and CD49d, which are constitutively expressed in resting neutrophils (Supplementary Figure 1A-D). To better characterize the recruitment process, we performed confocal micros-

copy and quantified the presence of these cells in different areas of the PLN at 3 h p.v. (Figure 1E). We observed that, at this early time, neutrophils accumulate in the medullary and interfollicular areas (Figure 1F). Next, to evaluate if the recruitment occurs via the blood vessels or the lymphatic system, we monitored *in vivo* the process using intravital 2-photon and electron microscopy. Quantitative analysis of the 2-photon movies acquired in the paracortical blood vessels of LysM-GFP mice showed a prominent increase in the number of neutrophils during the first 2 h p.v. (Figure 1H). In addition, we observed the presence of multiple hotspots [207] in the wall of high endothelial venules (HEVs), suggesting a relevant role of these areas in the observed recruitment (Figure 1G, Supplementary Movie 1). To confirm this observation, we performed electron microscopy in a PLN HEV, which clearly showed neutrophils associated with the blood vessel endothelium as early as 2 h p.v. (Figure 1I). Interestingly, intravital imaging of the lymphatic vessels, which drain the area in which the vaccine was administered (Figure 1J), showed a progressive increase in the number of neutrophils inside the lymphatic vessels during the first 4 h p.v. (Figure 1K, Supplementary Movie 2). However, this process appeared to be slower than the recruitment that occurs via the blood vessels, as we could not detect any neutrophil in the lumen of the lymphatic vessels during the first 2 h p.v. (Figure 1L).

The recruitment of neutrophils to the LN involves the cytokine IL-1α and the chemokine CXCL1.

In a previous study, we observed that the necrotic death of the LN macrophages after the administration of influenza vaccine was followed by the release of the potent inflammatory cytokine IL-1α[36]. In this work, we confirmed that IL-1α reaches an early peak (6 h) following vaccination and returns to basal levels at 24 h p.v. (Figure 2A). Moreover, we found that IL-1RKO animals show a significant inhibition of neutrophil recruitment in the PLN (Figure 2B). To confirm that IL-1α was involved in neutrophil recruitment, we injected a dose of 1 μg of recombinant IL-1α in the mouse footpad, and observed that the injection of this cytokine alone was able to induce the recruitment of neutrophil in the draining PLN at 12 h p.v. (Figure 2D). In a previous work, we also observed that influenza vaccination induced a fast increase of the chemokine CXCL1[36], a well-known inducer of neutrophil recruitment[208]. Therefore, to investigate whether the production of this chemokine was associated with LN

macrophages (LNM), we measured the secretion of CXCL1 in animals in which LNM (CD169DTR + Diphtheria toxin) or monocytes (CCR2KO) had been depleted. We observed that, in both cases, the levels of CXCL1 were significantly reduced at 12 h p.v. compared to the control group (Figure 2C). However, CXCL1 levels were not completely abrogated. Interestingly, we also observed that the type-I interferon response following vaccination was necessary for the secretion of this chemokine, as IFNAR-KO animals showed a prominent inhibition of the levels of CXCL1 at 12 h p.v. (Figure 2C). As internal control for the knockout strains, we confirmed that mutant mice do not exhibit complete defects in resident macrophages population (***Supplementary Figure 1F-G)***. By contrast, DTX-treated CD169-DTR mice exhibited a complete depletion of LN macrophages after the administration of the toxin (***Supplementary Figure 1E***). Moreover, footpad administration of recombinant CXCL1 (0.5 μg/fp) alone was able to induce a significant recruitment of neutrophils in the popliteal LN (Figure 2D). However, we observed significant differences in the effect that both molecules had on the activation of neutrophils. Based on the expression of the receptor CD69, recombinant CXCL1, but not IL-1α, was able to induce the expression of the early activation marker CD69 in the recruited neutrophils (Figure 2E). However, neutrophils recruited after IL-1α administration showed higher levels of MHC II compared to the ones recruited following treatment with CXCL1 (Figure 2F).

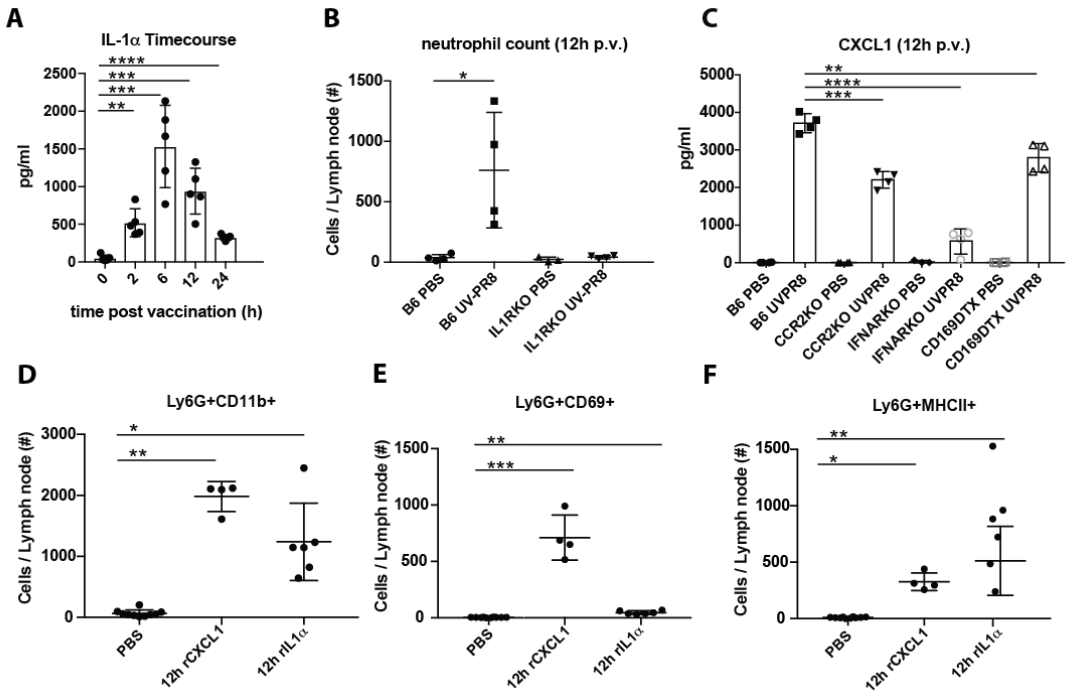

Figure 2. Production of CXCL1 and IL-1α induce recruitment of neutrophils to the lymph node in response to vaccination. ***A****) Time course showing the secreted IL-1α in the lymph from the LN at 0, 2, 6, 12 and 24 h following vaccination.* ***B****) Flow cytometric analysis showing the recruitment of neutrophils in the LN in B6 and IL-1R-deficient mice at 12 h p.v..* ***C****) Cytoplex analysis showing the production of CXCL1 in the LN at 12 h p.v. in CCR2 KO, IFNAR KO, and CD169DTR mice compared to B6 controls. Flow cytometric analysis showing the total neutrophils count (****D****), and the expression of CD69 (****E****) and MHCII (****F****) after administration of recombinant IL-1α and CXCL1. In all figures, the presented data are representative of at least three independent experiments. Results are given as mean ± SD. ns p>0.05; *p<0.05; **p<0.01; ***p<0.001; ****p<0.0001.*

Neutrophils phagocytize and transport influenza virus. To examine the capacity of neutrophils to phagocytize UV-inactivated influenza virus (UV-PR8), we performed electron microscopy. Indeed, results showed that a number of neutrophils phagocytized necrotic vesicles containing the UV-PR8 particles (Figure 3A). To quantify the percentage of neutrophils that phagocytized the virus, we labeled inactivated

influenza virus with the lipophilic dye DiO and performed flow cytometric analysis. We found that 15 % of the neutrophils were positive at 12 h p.v. (Figure 3B). Finally, to assess the capacity of neutrophils to transport phagocytized influenza particles, we performed 2P-IVM in LysM-GFP mice. The dual tracking of DiD-UV-PR8 and LysM-GFP neutrophils confirmed that, after phagocytosis, neutrophils were able to transport the phagocytized virus within the LN during 7 h (Figure 3C, representative track, Supplementary Movie 3). A volumetric reconstruction further confirmed that viral particles were internalized, with a distance from the cell centroid smaller than the cell radius (Figure 3D).

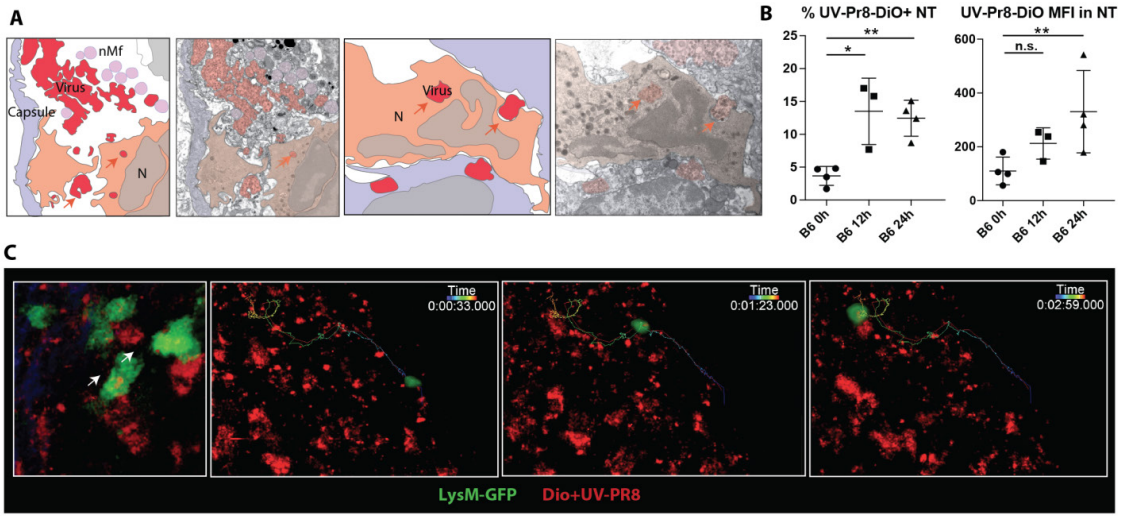

Figure 3. Neutrophils phagocyte and transport influenza virus. A*) Schematic drawing (left) of an electron micrograph (right) showing neutrophils in the SCS phagocytizing UV-inactivated influenza virus at 2 h p.v.. **B**) Flow cytometric analysis indicating the percentage of neutrophils positive for influenza vaccine (DiO labeled, left) and the corresponding MFI analysis (right). **C**) (Left) Intravital 2-photon micrograph showing a LysM-GFP neutrophil (green) phagocytizing DiD labeled UV-PR8 (red) (Right). Intravital 2-photon timelapse showing the correlation between the tracks from a UVPR8-positive vesicle and the neutrophil. In all figures, the presented data are representative of at least three independent experiments. **D**) Distance of the viral particles from the cell centroid (black line), compared to the cell radius (red line). Results are given as mean ± SD. ns p>0.05; *p<0.05; **p<0.01.*

Neutrophils change their motility soon after being recruited to the LN. To identify the areas of the LN with higher activity, we acquired low-magnification 2P-IVM movies (Figure 4A). Moreover, to visualize the vasculature and the LNM, we administered fluorescein isothiocyanate-dextran (200 kDa) and CD169-PE antibody, respectively. Initially, we imaged an area located in the paracortex of the LN (Figure 4A, dashed line), characterized by a high vascularization and active recruitment of neutrophils. Representative snapshots of the acquired movies are shown in Figure 4B-D, while the tracks of the analyzed cells are plotted in Figure 4E-G. A qualitative analysis of cell migration showed that at 30 min p.v. neutrophils generated long tracks in four main directions, which were associated with their movement inside the blood vessels (Figure 4E, Supplementary Movie 4). Once outside the blood vessel (75 min p.v.), neutrophils did not follow any preferential direction (Figure 4F, Supplementary Movie 4), while at later time points (135 min p.v.) they displayed a collective migration directed towards an area in which cells started to cluster (Figure 4G, Supplementary Movie 4). Next, we quantified cell migration by computing measures based on entire tracks (Figure 4H). We observed a significant change in neutrophil motility occurring within 30-75 minutes p.v. Indeed, neutrophils at 30 min p.v. were faster, more directional and traveled longer distances with a lower arrest coefficient, compared to later time points. However, no significant difference was observed between 75 and 135 min. These findings, using track-based measures, confirmed a change in the overall motility only after recruitment. Nevertheless, the analysis of the instantaneous speed of neutrophils showed a high variance (Figure 4I, left), which was associated with a variable mean over time (Figure 4I, right, black line). The observed variability in speed arises from both the differences between distinct cells at the changes of speed that a single neutrophil undergoes over time. An example is provided in Figure 4J, where the track of a neutrophil (left) and the plot of the instantaneous speed (right) over time are shown. This example shows the transition between two distinct behaviors that are characterized by low speed and high speed, respectively.

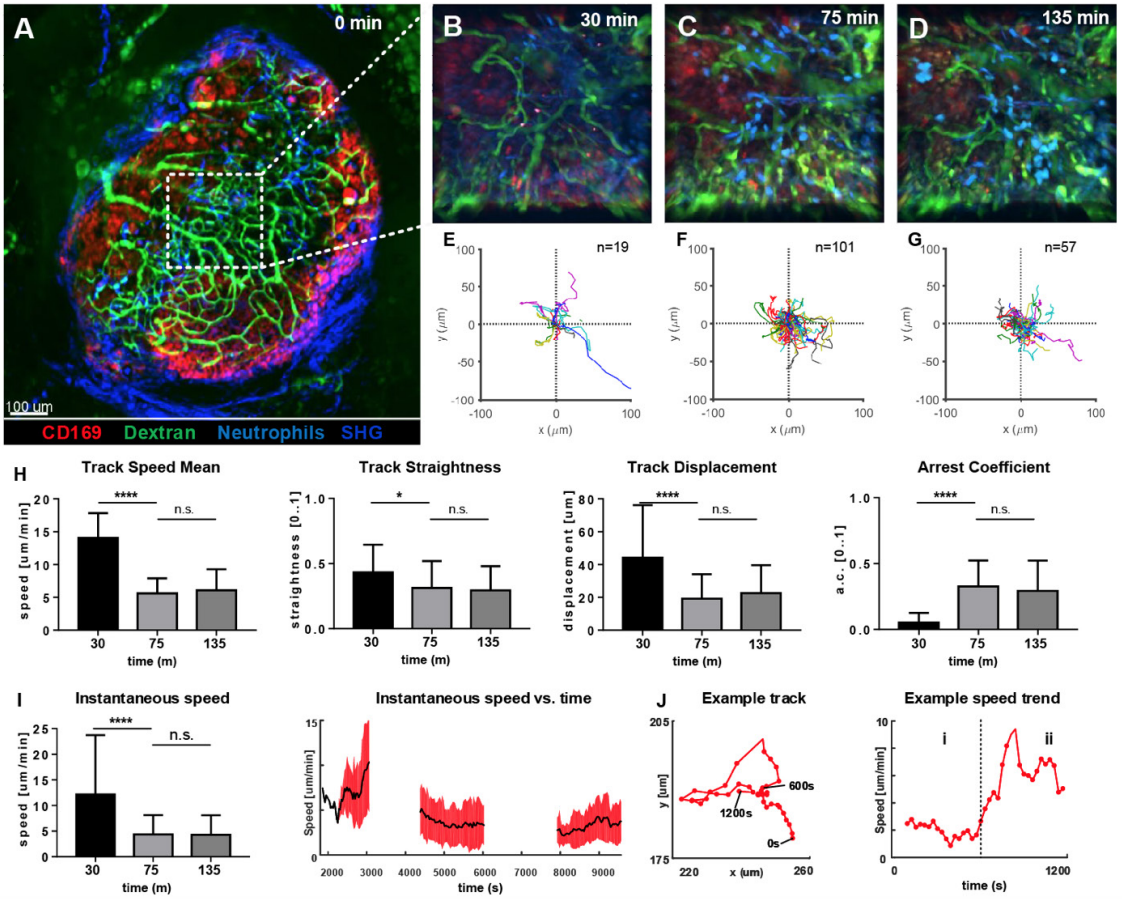

***Figure 4. Time-course of neutrophil motility. A**). Low-magnification 2P-IVM micrograph showing the structure of the PLN including vascular network (Fluorescein isothiocyanate-Dextran), CD169+ macrophages (red), collagen scaffold (Second Harmonic Generation - blue) and neutrophils (light-blue) adoptively transferred from a CK6/ECFP animal. Image was acquired immediately after vaccine injection. **B-D**) Snapshots of representative lymph node areas at different time points. **E-G**) Plots of cell tracks with common origin showing four preferential migratory directions at 30 min, more equally distributed directionalities at 75 minutes and a tendency towards the 1st and 4th quadrants at 135 minutes. The number of tracks is 19, 101, 57 respectively. **H**) Cell motility quantification using tracks mean speed, straightness, displacement and arrest coefficient. **I**) Boxplots of Instantaneous speed (left) exhibiting high variance at early time points. Instantaneous speed time series (right) showing distinct trends at different time points. **J**) Representative track (left) acquired at 135 min and the associated time series of the instantaneous speed. The same cell exhibits two different trends characterized by low speed (i) and high speed (ii). Results are given as mean ± SD. ns p>0.05; *p<0.05; **p<0.01; ***p<0.001; ****p<0.0001.*

Neutrophils change activities over time. To describe the long-term and time-varying behavior of each individual neutrophil, we defined, according to a previous study[26], five distinct cellular activities based on the motility patterns visually identifiable in the videos (Figure 5A). We named them as flowing, arresting, patrolling, directed migration and swarming (Figure 5A). To detect these activities from imaging data, we divided the track of each neutrophil into multiple fragments (tracklets). Then, we computed morphological and motility measures on each of them. By defining a gating strategy on these measures, each tracklet was associated with an activity (Figure 5B). Considering each tracklet as a data-point, the proposed gating strategy identified five distinct populations corresponding to the different activities (Figure 5C). Following this analysis, we observed that neutrophils perform different activities at different time points (Figure 5D). At homeostasis, neutrophils were mostly circulating within blood vessels, moving with high speed and directionality (Supplementary Figure 2**,** Supplementary Movie 8). Then, during the first 30 min p.v. neutrophils were mostly associated with capillaries. This behavior changed when neutrophils started to migrate within the LN (30 to 75 min p.v.), displaying primarily patrolling, directed and arrest behaviors. Other neutrophils exhibited a temporarily directed migration. Finally, at 2 h p.v., cluster formation was the predominant neutrophil behavior. This was associated with temporarily directed migration of neutrophils either towards a swarm under formation or from a previously formed swarm to another target. In addition, a small population of neutrophils was arrested (Figure 5D). These results confirmed that the time-varying motility of neutrophils can be represented as a sequence of distinct activities which, in turn, are associated with distinct biological processes.

Following vaccination neutrophils form swarms in the SCS associated with SCS macrophages (SSM). To identify the areas in the LN with high cell motility we performed low magnification (10X) 2P-IVM, which allowed the visualization of the whole organ (Figure 6A, Supplementary Movie 5). Cells were tracked for a period of 30 min and the percentage of cells migrating from one region to another was computed. We found that at early time p.v. most of the neutrophil migration occurred between the interfollicular (IF) and the SCS areas (Figure 6B). To evaluate the presence of areas associated with high neutrophil motility,

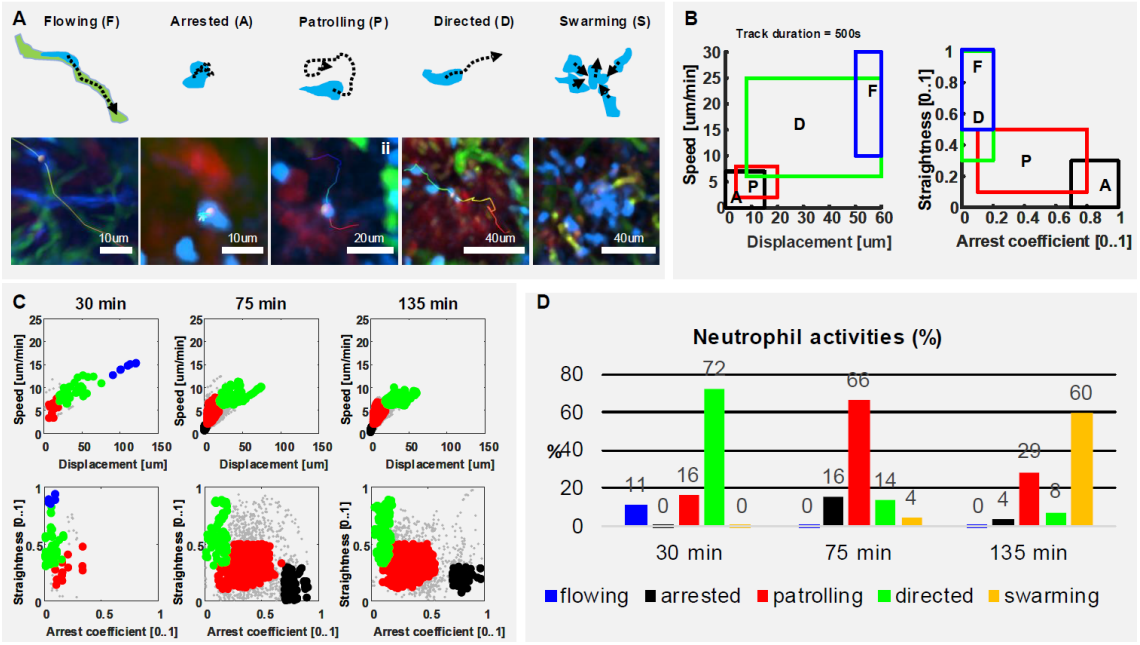

Figure 5. Neutrophils exhibit different activities in the early response to vaccination. **A**) Graphic representation (up) and 2P-IVM micrographs showing different neutrophil activities in response to influenza vaccination: flowing “F” neutrophils moving inside blood vessels, with long and straight following the vessel structure. Arrested neutrophils “A” exhibit confined tracks and short displacement. Patrolling neutrophils “P” have long, non-straight tracks associated with extensive tissue monitoring. Directed neutrophils “D” exhibit straight tracks with lower migration speed compared to flowing neutrophils. Swarming neutrophils (S) form cell aggregates with high density and large volume. **B**) Gating strategies used to define and identify the activities according to cell speed, displacement, straightness and arrest coefficient on track fragments of fixed length (500s). **C**) Classification of track fragments at different time intervals (arrested: black, patrolling: red, directed: green, flowing: blue). **D**) Time-course plot showing how neutrophil activities change over time according to our gating strategy.

we measured the average pixel velocity by optical flow, a computer vision method that does not require cell tracking[209]. The results showed the presence of hotspots with high motility, which are depicted as lighter areas in the pixel velocity heat map (Figure 6C). These hotspots were localized in the SCS and IF area. Interestingly, the hotspots were associated with the regions where swarms were formed (Figure 6D-E).

To fully characterize neutrophils swarming behavior, we recorded movies in the SCS region of the LN using different magnifications. Low magnification movies from LysM-GFP mice showed that neutrophils formed large and multiple swarms in association with regions enriched with macrophages (Figure 6F, *Supplementary Movie 6*). Such swarms grew in size over time (Figure 6G). Furthermore, these swarms competed for nearby neutrophils, which often changed their directionality from one cluster to another (Figure 6F). In mathematical terms, the average dynamic of the observed swarms was best described by a sigmoidal function (Figure 6H), suggesting that swarm formation undergoes an initial steady state, a growing phase and a plateau before its resolution. Moreover, we observed that the decreasing swarms showed a resolution period of approximately 30 min.

To better visualize individual neutrophil behavior, as well as possible interactions with resident macrophages, we acquired high-magnification videos starting from 5-7 h p.v. These videos confirmed that swarm formation occurs in proximity to SSM (Figure 6I, *Supplementary Movie 7*), with highly directed and skewed trajectories (Figure 6J), and the majority of the cells approaching the center of the swarm (Figure 6K). Moreover, using high-magnification 3D reconstruction and EM, we confirmed that neutrophils were located in close proximity to SSM clusters (Figure 6L-M). To investigate the involvement of SSM in the formation of swarms we quantified the accumulation of neutrophils in areas proximal or distal to SSM. Interestingly, the number of neutrophils fluctuated over time outside the SCS area (Figure 6N). By contrast, it constantly increased in areas rich in macrophages (Figure 6O) exhibiting the sigmoidal growth rate observed during swarm formation.

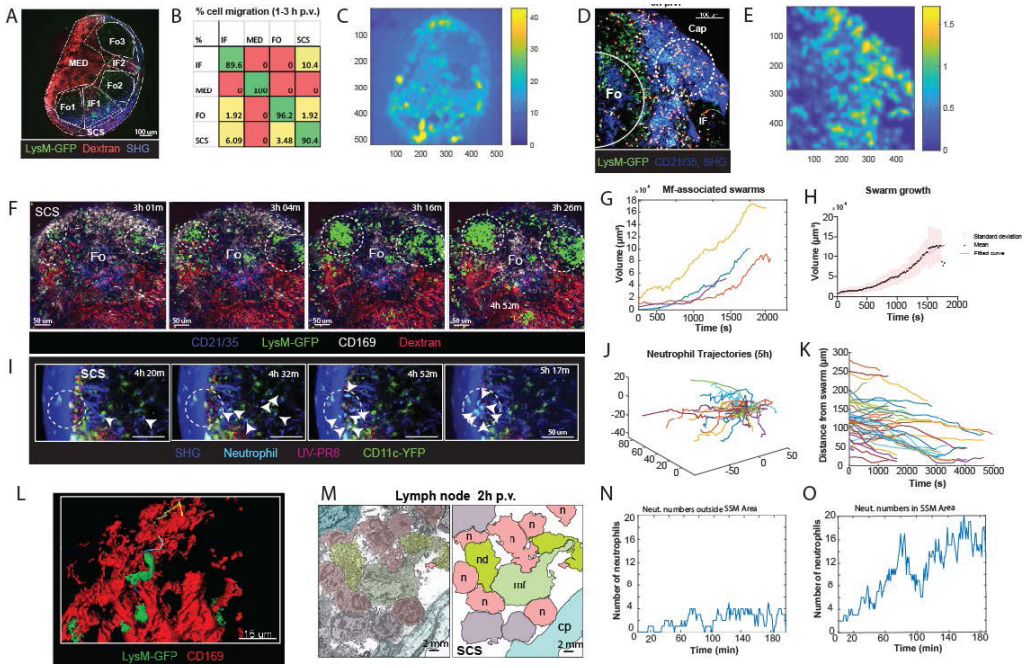

Figure 6: Characterization of neutrophils swarm formation in the lymph node after influenza vaccination. A) *Low magnification 2P-IVM micrograph showing the PLN of a LysM-GFP animal at 3 h p.v. Seven different areas are identified according to their anatomical structure and cell populations: SCS, follicles (Fo1-3), interfollicular areas (IF1-2) and medullary area (MED).* ***B)*** *Transition matrix showing the migration of cells across different areas. The value at the i-th row and j-th column refers to the percentage of cells that migrated from the i-th to the j-th area. Values on the diagonal refer to the percentage of cells that remained in the same area. The IF and the SCS areas exhibited the major communication with the neighboring regions.* ***C****) Pixel velocity heatmap, showing hotspots with high motility.* ***D-E****) 2P-IVM micrograph (****D****) and pixel velocity heatmap (****E****) showing the IF and SCS areas at 6 h p.v. Cap refers to the collagen capsule. Dashed lines indicate hotspots toward which cells migrate with high motility.* ***F****) Micrographs acquired with 25x magnification at 4 h p.v. showing the formation of multiple LysM-GFP neutrophils swarms in the SCS in close proximity to CD169+ macrophages* ***G****) Swarm volumes over time observed at 4 h p.v.. Volumetric data built according to fluorescence intensity thresholding.* ***H****) Sigmoid fit to previous swarm volume (R = 0.652) showing their averaged growth phase.* ***I****) Snapshots (25x) in the SCS showing CFP-expressing neutrophils initiating a swarm at 5 h p.v.* ***J)*** *Trajectories of 5h p.v. swarm plotted from the same origin* ***K)*** *Time-course distances from the swarm center at 5h p.v.* ***L)*** *High magnification 3D reconstruction of LysM-GFP neutrophils interacting with CD169 macrophage network in the SCS region.* ***M****) Colored transmission electron micrograph (left) and schematic drawing (right) showing the interaction of different neutrophils (n) with a macrophage (mf) in the SCS of the LN at 2h p.v..* ***N,O****) Number of neutrophils vs. time showing an oscillatory trend in an area without macrophages (****N****), and an increasing trend indicative of swarming in an area associated with macrophages (****O****).*

Discussion

In this study, we investigated *in vivo* the behavior of neutrophils that are recruited to the draining LN following influenza vaccine administration. Neutrophil recruitment has been previously described in several infection models[132,140,186,199,210]. However, despite the critical role of these cells in pathogen clearance and the initiation of the inflammatory response, their specific behavior upon vaccination remains poorly studied. In this work, we observed a rapid recruitment of activated and mature neutrophils in response to vaccination with an inactivated influenza virus. Although the role of neutrophils against influenza has been extensively studied in the lung[211], this is the first time that an *in vivo* response is characterized in response to an influenza vaccine administration.

The way neutrophils enter the LN remains controversial. Different studies have suggested that neutrophils get recruited mainly via the HEV[100,199]. However, other authors have stated that neutrophils access the LN mainly via the lymphatic vessels[185–187]. Our data suggested that influenza vaccination induces an initial recruitment of neutrophils via HEV, followed by a minor, secondary wave through the lymphatics that drain directly from the injection site to the sentinel LN. It is tempting to speculate that the type of recruitment might influence the function of the recruited cells in the LN. However, future experiments need to be performed to study differences in the behavior and the function of neutrophils that arrive through these two different routes. In addition, we found that a percentage of neutrophils downregulate the expression of CXCR4, a marker known to be involved in neutrophil mobilization from the bone marrow and trafficking through the circulation to the site of inflammation[212,213]. Moreover, consistently with neutrophils activation, we detected a downregulation in multiple cell surface-receptor linked with leucocyte trafficking and accumulation[214,215] or express at high level in resting neutrophils[216].

Neutrophil localization within the LN after pathogen challenge is tightly linked to their specific function. In a previous study we observed that macrophages, located within the subcapsular sinus (SCS) and the medullary area of the LN, capture and retain influenza virus following vaccination. Interestingly, in both the areas, macrophages undergo necrosis-like cell death after viral capture that leads to their progressive decline[36]. Our study demonstrated that neutrophils migrate towards the SCS pro-

gressively, probably in response to chemoattractant signals released by the necrotic macrophages, as suggested by other models based on infection[100,140]. Among the different signals released by the necrotic macrophages, IL-1α is one of the most potent[36]. In this work, we have demonstrated that IL-1α and its receptor IL-1R are involved in the initial recruitment of neutrophils to the LN. Other authors have previously confirmed the role of IL-1β and IL-1R in the recruitment of neutrophils to the infection site[188,217,218]. However, we could not observe any significant secretion of IL-1β or activation of the inflammasome pathway in the LN following influenza vaccine administration[36]. Therefore, we can conclude that the observed absence of neutrophil recruitment in the IL-1R-defective mice was associated with the macrophage-associated release of IL-1α.

Moreover, we confirmed that CXCL1, a mouse homolog of human IL-8, was also involved in the recruitment of neutrophils to the LN. The source of this chemokine needs to be further investigated but we speculate that DC and activated macrophages could be the main producers[219,220]. Indeed, the secretion of CXCL1 was almost abolished in mice lacking type-I interferon (IFN) receptors, suggesting an important role of LN macrophages and DC, the main producers of IFN, in this process. Thus, absence of IFN-I signaling in IFNARKO mice partially reduce the total number of CD169+ macrophages compared to the control, although it not impair the number of medullary macrophages. However, the specific elimination of macrophages reduced only partially the expression of CXCL1. Interestingly, our findings demonstrated that subcutaneous administration of IL1-α and CXCL1 induced the mobilization of neutrophils toward the LN. Nevertheless, we showed that CXCL1 induced the expression of CD69, a marker associated with the early activation, while IL-1α administration increased the expression of MHCII, suggesting a potential role of neutrophils in antigen presentation, as previously described in other models[195,221].

In the early phases of recruitment, we found that neutrophils exhibited significant differences, resulting in reduced speed, directionality, and displacement, while increased arrest coefficient. These findings suggest that the recruited neutrophils actively migrate and increase cell-to-cell interactions[26]. Previous studies have associated the increase in the arresting of neutrophils with the oxidative burst in which reactive oxygen species (ROS) are generated. Antigen presentation might also influence the

speed of neutrophils. Indeed, other authors have reported that neutrophils can serve as antigen presenting cells (APC) during influenza infection in mice[103,222,223]. In support of the notion that neutrophils might act as APC in the context of influenza vaccination, we observed that they actively phagocytize influenza particles, which were previously associated with necrotic macrophages. Moreover, they elevated their expression of MHCII after exposure to IL-1α which is released by the dying macrophages[36]. However, it is not clear if the APC function of neutrophils might occur in the LN or, as suggested by other authors[224], in other immune-relevant organs, such as the spleen. In support of the former, we observed that neutrophils are able to transport influenza particles for long distances in the lymph node[225]. This suggests that neutrophils can carry viral particles to specific areas as described for other infection models[226–228]. Therefore, a more detailed study regarding the potential capacity of the neutrophils to transport viral particles to other immune relevant organs as well as the capability of these cells to function as APC need to be further investigated.

Little is known regarding the behavior of early recruited neutrophils in the LN after influenza vaccination. Our findings supported that neutrophil behavior is a dynamic process, with significant differences observed already within the first 3 h p.v. These findings were in agreement with previous *in vitro* studies in which the motility of neutrophils was found to change within minutes in response to both external (i.e. chemical gradients) and internal factors (i.e. directional memory)[111].

Among the different activities that occur within the first few hours after vaccination, we identified the formation of swarms, which is a process previously associated with tissue injury[98,132]. In this study, we showed that neutrophils swarms are formed in the SCS, co-localizing with the resident SSM population. The characterization of the swarm dynamics showed consistent growth rates, suggesting that they are comparable to smaller transient swarms observed in other infection models[140]. Regarding the factors that generate this behavior, tissue injury, neutrophil secondary cell death and the release of the chemoattractant LTB4 have been previously proposed as triggers of swarming formation[132]. Although LTB4 is mainly secreted by neutrophils, macrophages can also produce this molecule[132]. These observations, along with our *in vivo* evidence of swarms association with SSM, suggest a close as-

sociation between the two populations. In previous studies, swarm formation in the SCS was linked with the removal of resident SSM. We speculate that macrophage death contributes to the initiation, amplification, and stabilization of neutrophil swarming and recruitment via the release of different chemo attractants, such as IL-1 . However, the redundancy in the recruitment process of neutrophils, with the involvement of more than 30 chemokine receptors[191], makes the effect of a single molecule difficult to be distinguished from other cues that regulate neutrophil chemotaxis.

Regarding the swarm dynamics, a direct correlation between swarm size and tissue injury severity has previously been shown[229]. Furthermore, the number of neutrophil secondary death is also proportional to the swarm size[132]. It would be compelling to determine whether influenza vaccination induces the death of neutrophils in a way similar to the previously described macrophage death[36].

The quantification of the spatio-temporal migration and interaction patterns of cells from 2P-IVM data presents specific challenges. These arise from the difficulties both in cell tracking and in describing a complex biological system by means of numerical values. The difficulties in cell-tracking, arise from both the textureless appearance and the complex biomechanical properties of neutrophils, including high plasticity and formation of contacts. These problems are amplified by the high number of cells that need to be tracked. To facilitate individual tracking, the number of fluorescently-labeled cells can be reduced by performing an adoptive transfer of a limited number of fluorescently labeled cell to a non-fluorescent recipient animal. This justifies the differences in cell number between the experimental setup using LysM-GFP transgenic model or the adoptive transfer of CFP-neutrophils into wild type animals prior to imaging shown in Figures 1, and 6, respectively.

In this study, we described an alternative way to analyze cell motility in 2P-IVM videos were single cells cannot be tracked. Indeed, by computing pixel velocity, we identified the areas in the LN, called hotspots, in which cells were more active. The advantage of pixel-based measures with respect to track-based measures is that neither manual nor automatic single-cell tracking is required. Therefore, this allows the analysis of videos with a high number of cells. The quantification of neutrophil behavior from 2P-IVM data is further challenged by the lack of mathematical models that

make their motility patterns interpretable. Although optical probes can be used to transform a biological function into a light signal, their application for 2P-IVM remains challenging[230].

To address this issue, we developed a new method of analysis that brings two main advantages with regard to the previously used methods: capturing the time-varying motility of cells and making results interpretable. Indeed, the available methods to assess cell motility can lose information during the averaging process[111]. Additionally, although several measures of cell motility were defined[28], the connection of their values to a biological meaning remains to be addressed by the investigator. When applied to our data, the standard track-based measures did not capture significant differences between neutrophils from 75 to 135 min p.v. (Figure 4). However, the new method of analysis, proposed in Figure 5, identified distinct activities, which changed over time, indicating clear differences in the functions of the analyzed cells. Although in this study we defined five distinct activities of neutrophils, alternative activities could be also defined in future studies, such as apoptosis or netosis[226] amongst others.

The proposed method allowed to perform a dynamic *in situ* cytometry analysis as proposed in a previous study[205,230] where distinct phenotypes of cells were identified in 2P-IVM data. However, a set of gates correlating phenotypes to actions were not defined. By contrast, our definition of activities allowed to define a precise set of gates to interpret the results. It would be compelling to define an extended list of activities that neutrophils can perform or automatically unravel populations of cells expressing distinct phenotypes using data mining methods such as clustering algorithms[231,232]. Additionally, advanced computer vision methods can be applied to detect more complex behaviors, both on shorter and longer periods of time considering other parameters such as cell morphology, context, and history. This is in line with recent works that aim to recognize cellular motion phenotypes in *in vitro* cultures[233] or human activities using deep machine learning methods[234].

In conclusion, to analyze the complex dynamics of neutrophils in intravital imaging data, an interdisciplinary effort is required. By combining different imaging methodologies, molecular techniques, and pattern recognition methods, we identified distinct behaviors of neutrophils in the early response to influenza vaccination. These behaviors

are the expression, of the biological mechanisms that follow influenza vaccination. In addition, we identified an interaction between neutrophil and macrophages, which might be important in terms of the capacity of the former to capture and present antigen.

Acknowledgments

We would like to thank David Jarrossay and Diego Morone for the provision of technical support, and Profs Mariagrazia Uguccioni and Marcus Thelen for critical discussion of the manuscript. This work was supported by the Swiss National Foundation (SNF) grants, 176124, R'equipt (145038) and Ambizione (148183), the European Commission Marie Curie Reintegration Grant (612742), the Center for Computational Medicine in Cardiology (CCMC) and SystemsX.ch for a grant to D.U.P. (2013/124). The authors declare no competing financial interests.

Authors Contributions

S.F.G. directed the study; S.F.G., D.U.P., I.L., A.P. designed and performed experiments, analyzed and interpreted the results and wrote the manuscript. R.K. supervised the computational aspects of the data analysis. S.F.G. and M.P.S. performed 2P-IVM. T.V. performed experiments.

1.2. Manuscript 2: vAbs: virtual antibodies for immune cell identification

The concept of a classifier capable of predicting cell type identity based on their motility is not entirely novel and it has been explored to some extent in the past. Nevertheless, drawing an explicit analogy with immune-specific antibodies holds compelling implications in microscopy, as it opens the door to identifying immune cells without the need for traditional staining methods.

With this premise in mind, the concept of a 'virtual antibody' that could potentially eliminate the requirement for fluorescent probes had been circulating within our laboratory for several years as a promising project. Finally, during the last months of my PhD, Prof. Santiago proposed that we bring this project to life as a brief communication. As a result, the following manuscript represents a personal take on the concept of virtual antibodies and their potential applications.

Far from complete, the present manuscript serves as draft that outlines the direction we will pursue over the course of the final months of my tenure in the lab.

vAbs: virtual antibodies for immune cell identification

Alain Pulfer[1,2], Tommaso Virgilio[1], Louis Renner[1], Diego U. Pizzagalli[3], Elisa Palladino[1], Santiago F. Gonzalez[1,*]

[1] Institute for Research in Biomedicine, Faculty of Biomedical Sciences, USI - Switzerland.

[2] Department of Information Technology and Electrical Engineering, ETH Zurich – Switzerland

[3] Faculty of informatics, USI - Switzerland

***Corresponding Author/ Lead contact:** *Santiago Fernandez Gonzalez*

Status: manuscript in preparation

Abstract

Cell tracks have long been a valuable source of information in live-cell imaging; proving to be instrumental to chatacterize immune cell processes under varying experimental conditions. However, cell trajectories retain an amount of embedded information that has not been fully explored yet. Different cell types display unique characteristic and motilities which in the present study we sought to use to predict cellular identity and migratory mode. Inferring the cell type solely based on spatial coordinates is a significant challenge, given that different populations of cells could exhibit similar motility patterns. However, recent developments in activity recognition have proven effective in forecasting human behavior, are they could be viable for identifying and classifying cellular activity in live-cell imaging. To further explore this direction, we applied natural language processing for the analysis of tracks depicted as temporal signals. This approach led us to introduce the concept of “virtual antibodies” (vAbs) – deep learning-based classifiers tailored to identify specific cell populations with varying affinity. Resulting vAbs were trained with more than 9000 cellular trajectories obtained from 4D time-lapses generated in vivo. Following this approach, and based solely on their trajectories, we successfully T cells, neutrophils, and natural killers. Moreover, we demonstrate potential use-case-scenarios for label-free staining of time-lapse acquisitions, as well as for generating an array of affinity profiles describing the motility state of the cells.

Introduction

Live-cell imaging has become a fundamental technology in immunological studies, facilitating real-time visualization of dynamic processes and interactions at the cellular level. A consolidated approach for translating the visual information within imaging time-lapses into quantitative measurements is cell track analysis[26,28]. Trajectory analysis has played a pivotal role in describing various immunological functions and cell behaviors, ranging from the homing of B and T cells[175,235,236], to antigen scanning and contact formation initiated by dendritic cells[237]. In these scenarios, cell tracks have served as experimental readouts capturing the transient states of cells in complex physiological environments. Consequently, trajectory analysis has proven instrumental in characterizing variations of motility in response to diverse experimental conditions within unique cell population. Nonetheless, these approaches relied on simple motility metrics such as cell speed or directionality, thereby only capturing limited aspects of cell dynamicity. In contrast, recent studies have demonstrated that multiple features related to cell migration can successfully identify discrete cell populations and behaviors[238]. Consequently, these findings

Live-cell imaging has become a fundamental technology in immunological studies, facilitating real-time visualization of dynamic processes and interactions at the cellular level. A consolidated approach for translating the visual information within imaging time-lapses into quantitative measurements is cell track analysis26,28. Trajectory analysis has played a pivotal role in describing various immunological functions and cell behaviors, ranging from the homing of B and T cells175,235,236, to antigen scanning and contact formation initiated by dendritic cells237. In these scenarios, cell tracks have served as experimental readouts capturing the transient states of cells in complex physiological environments. Consequently, trajectory analysis has proven instrumental in characterizing variations of motility in response to diverse experimental conditions within unique cell populations. Nonetheless, these approaches relied on simple motility metrics such as cell speed or directionality, thereby only capturing limited aspects of cell dynamicity. In contrast, recent studies have demonstrated that multiple features related to cell migration can successfully identify discrete cell populations and behaviors238. Consequently, these findings have raised a fundamental question: do cell tracks alone

contain sufficient information to predict cellular identity and behavior?

Given that the information embedded within trajectories requires tailored processing techniques for extraction, addressing this question is not straightforward. Furthermore, the complexity introduced by varying experimental conditions can result in a highly entangled feature space, causing two different cell types to exhibit identical motilities under specific circumstances27. For this reason, relying solely on individual cell tracks to achieve unequivocal predictions of cellular identities is a challenging and unlikely milestone. Nonetheless, we pose that individual tracks can serve as a reliable indicator of the corresponding cellular identity in a non-specific manner. Analogous to non-specific antibodies capable of binding a broad spectrum of cells, cell trajectories may indicate the presence of one or more populations of cells exhibiting similar motilities. Building on this concept, we introduce in this work the notion of virtual antibodies (vAbs), deep learning (DL) classifiers designed to target cell tracks and predict their identities. Drawing an explicit analogy with traditional antibodies, vAbs are mean to identify uniquely a specific motility pattern in the same way that an antibody identifies the specific expression of the target protein. Consequently, the combination of multiple vAbs has the potential to provide a comprehensive characterization of individual trajectories by capturing distinct facets of their motility.

To create a set of vAbs, we obtained more than 9000 cell tracks using 2-Photon intravital microscopy158,239 (2P-IVM) across various inflammatory conditions. These tracks were created and saved within the Immunemap platform, a collective effort from the intravital communities aimed at centralizing and make accessible 2P-IVM data (see chapter 8). Successively, we employed natural language processing (NLP) techniques to train the vAbs, specialized classifiers designed to predict distinct cell identities based on their movement patterns. In our research we demonstrate that vAbs possess remarkable versatility; serving as a label-free alternative for cellular staining and generating affinity profiles that offer valuable insights into cell behavior. In the future, vAbs might find diagnostic applications in predicting aberrant cell behavior as well as in monitoring the effect of various drugs on cell motility.

Results

Track analysis using averaged features. We established a comprehensive dataset for the analysis of cell tracks using time-lapses data acquired through 2PIVM (Fig. 1A, left). Imaging was conducted under inflammatory conditions in the spleen and lymph nodes of anesthetized mice. Subsequently, we performed manual tracking of each cell in the recordings annotating their spatial coordinates across time (x, y, z, t). During the annotation process, each track was associated with a label ID indicating the cell type, which encompassed CD4 T cells (TCs), natural killers (NKs), and neutrophils (Fig. 1B).

The resulting dataset comprised 9523 tracks with a balanced representation across the three classes of cells (Fig. 1C). To ensure the reliability of the dataset, we examined and processed the dataset with the primary goal of standardizing the sampling rate of the acquisitions and the track durations. This evaluation is crucial given that large discrepancies in these two parameters can exert significant influence on the estimation of derivative metrics such as cell displacement and speed28,237, introducing inherent biases into the dataset. Consequently, tracks characterized by substantial differences in duration or sampling rate might not be directly comparable. To address this aspect, we cleaned the dataset to remove outliers and ensured that both the sampling rates and track durations were comprised within comparable ranges (Fig. 1D); thereby enabling the subsequent comparison of trajectories.

Furthermore, we inspected the trajectories to assess their suitability for predicting cell class labels. To achieve this, we computed an array of motility-derived features (see material and methods) which we used to compute a hierarchical cluster grouping tracks according to their similarity (Fig. 1E). Notably, the resulting dendrogram showed a distinct structure partitioning tracks into three primary clusters, two of which exhibited predominant abundance of a single cell type (top green, bottom red). This observation suggests that motility-related features effectively facilitated the differentiation and aggregation of these particular cell populations. In contrast, the third and larger cluster displayed a more intricate composition, lacking specific enrichment for a single cell type.

We observed similar results after feature reduction with Uniform manifold approximation and projection (UMAP) technique

(Fig. 1F). Accordingly, we demonstrated that an increased number of motility features enabled a clear separation of tracks, leading to the formation of clusters highly representative of the cell types. Notably, the last dimensionality reduction showed three distinct regions prevalently populated by a unique cell type (Fig. 1F, left). However, outside these boundaries, the distributions were overlapping. Altogether, these findings suggests that multiple averaged features partially enable the distinction of cell types, but their motility attributes can exhibit large interconnections and overlaps. Consequently, the precise classification of cell types based on motility attributes represent a significant challenge. We expect that the inclusion of the temporal dimension in our analysis will further improve the distinction of cell based on their motility.

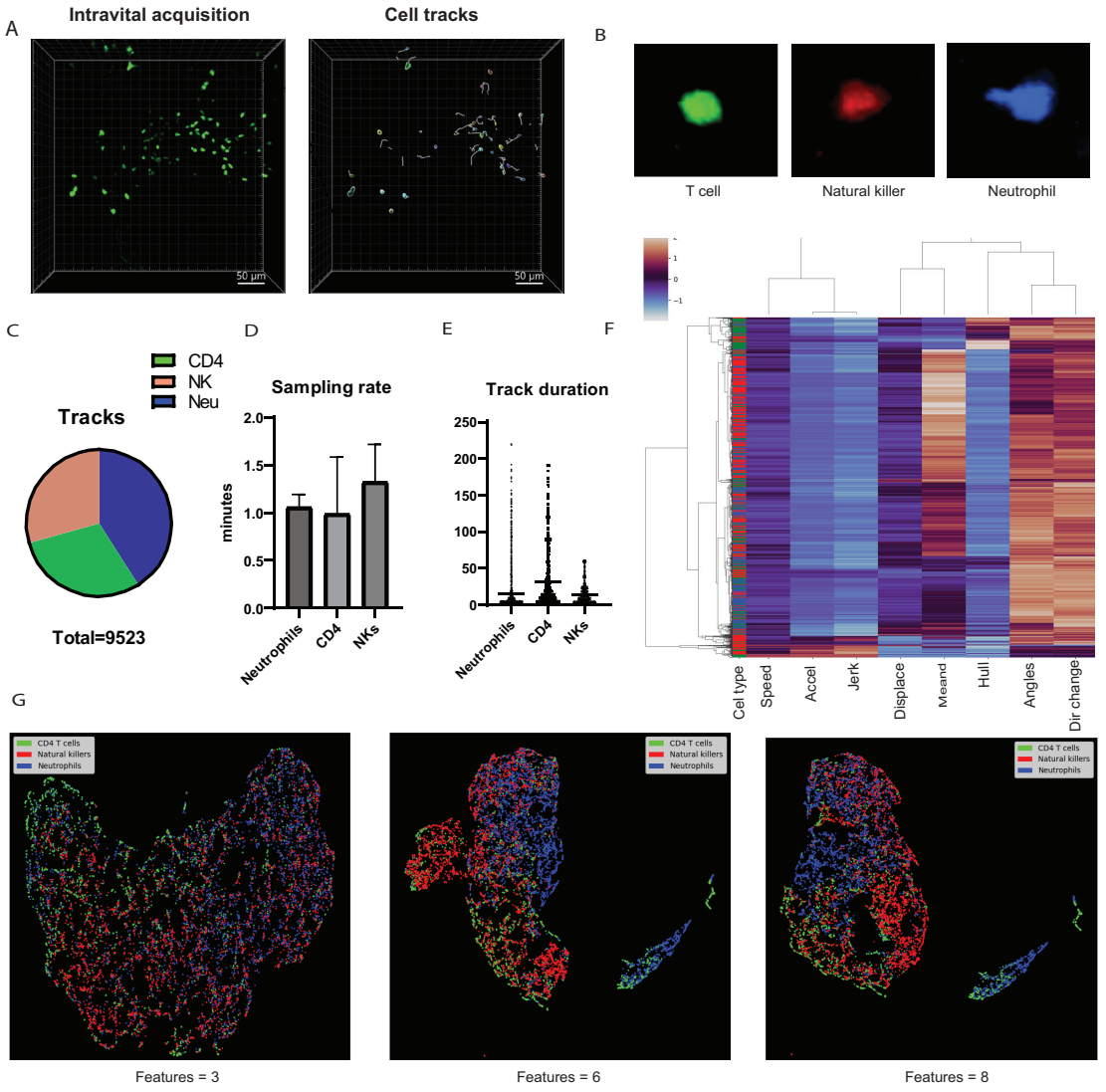

Figure 1. Dataset generation workflow. *A. Micrograph representation depicting intravital surgery and acquisition of T cells in the lymph node (left), and subsequent tracking (right).* ***B.*** *Cropped snapshots showing a T cell, natural killer, and neutrophil with cytoplasmic staining.* ***C.*** *Pie chart showing abundances of immune cells in the dataset.* ***D.*** *Plot showing the sampling rates (minutes/frame) of the imaging acquisitions from which the respective tracks are derived.* ***E.*** *Distribution of track duration per cell type.* ***F.*** *Hierarchical clustering of different motility features labelled per cell type.* ***G.*** *UMAP analysis of tracks with increasing number of featues.*

Classification of temporal cell tracks. To address the temporal aspect of cell tracking and for classification purposes, we utilized DL and NLP, as they proved promising approaches in recent works aiming to classify cell motility[50,240,241]. Initially, we standardized each track by centering it at the origin axis (Fig. 2A, left) and subsequently aligned the tracks along the direction of the average displacement vector (Fig. 2A, right). This procedure ensured that significant changes in motility occurred consistently along the same axis for all tracks, facilitating the detection of common patterns.

We then computed eight motility-derived features, combined with the spatial-temporal coordinates of the cells, to create our training set (Fig. 2B). In order to determine the most suitable classification approach, we implemented and evaluated various deep learning architectures with increasing numbers of parameters: a 1D convolutional network (Conv1D), a long short-term memory network[70] (LSTM), and LSTM and bidirectional LSTM models preceded by Conv1D feature extraction (Conv1D-LSTM, Conv1D-biLSTM). The results of this comparison are illustrated in Figure 2C, demonstrating a positive correlation between model complexity and predictive accuracy (Fig. 2D). Notably, the largest model, Conv1D-biLSTM, achieved the highest predictive accuracy at 0.902. Surprisingly, the Conv1D model ranked as the second best model amongst those tested despite having the smaller number of trainable parameters. This finding highlights the importance of Conv1D as a feature extractor, as indicated by the improved accuracy seen in networks utilizing this module in combination with recurrent components.

Subsequently, we assessed the performance of the Conv1D-biLSTM model on a dataset comprising 953 tracks equally distributed among neutrophils, TCs, and NKs. The results, visualized in a confusion matrix, indicated that the model had high sensitivity and relatively few false positives (Fig. 2E). Notably, most misclassifications occurred between TCs and NKs, suggesting that these two cell types exhibit greater similarity in motility compared to neutrophils. This observation was further supported by examining the receiver-operating curves (ROC) obtained after transforming the predictions into a binary output. Accordingly, the neutrophil curve exhibited the highest area under the curve (AUC), indicating a more favorable tradeoff between true positive rate (TPR) and false positive rate (FPR) compared to TCs and NKs (Fig. 2F-G).

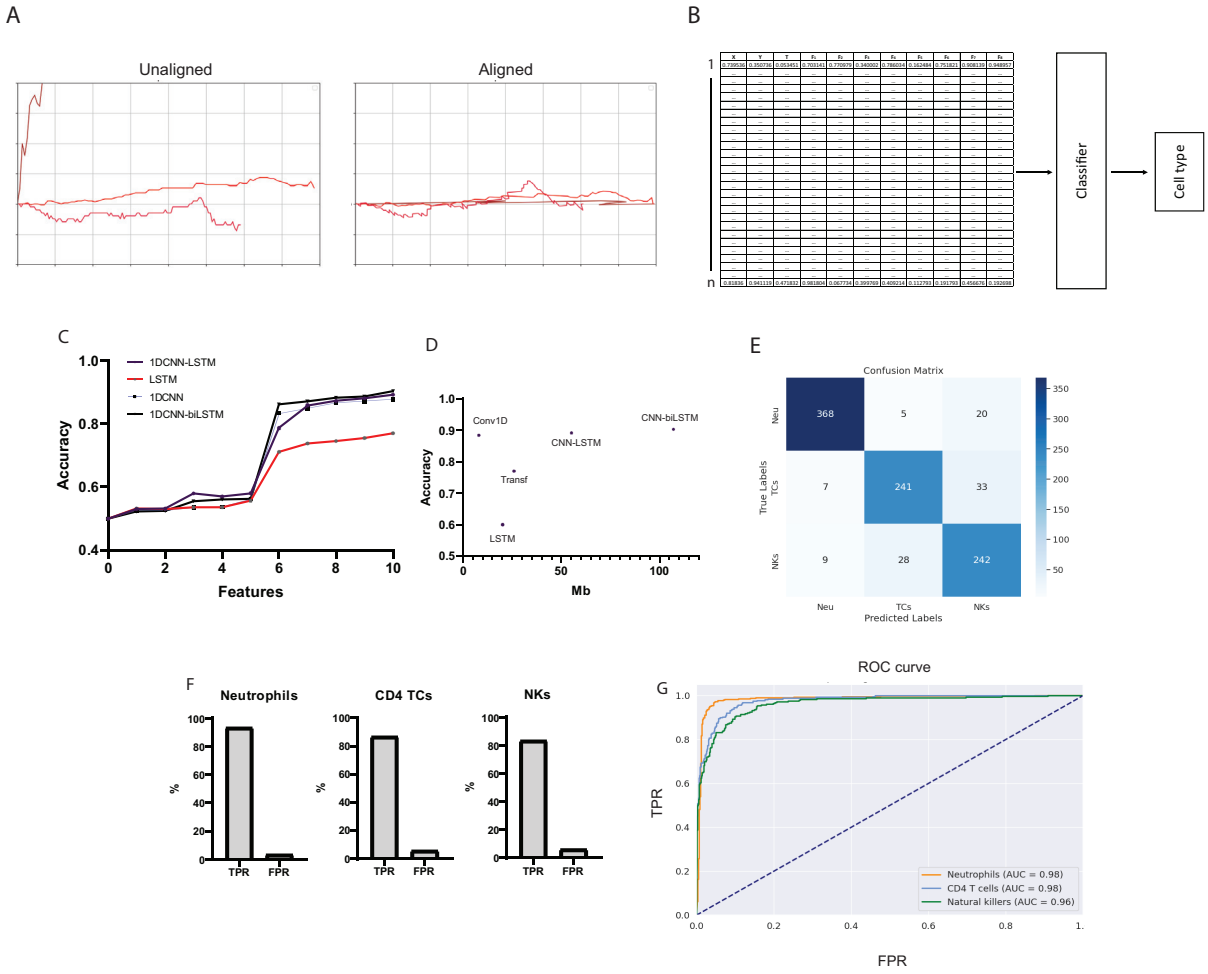

Figure 2. Dataset generation workflow. *A. Sampled tracks plotted at the common origin before being processed (left) and after being rotated to align in the direction of the average displacement vector B. Schematic representation of the motility-derived feature vector that is passed into a classifier for cell type prediction. C. Plot representing the predictive accuracy of different deep learning classifiers as a function of the number of features considered D. Scatterplot depicting a correlation between the predictive accuracy and the number of parameters of the classifiers (mB) E. Confusion matrix for three-class label classification of cell tracks F. True positive and false positive rates for binary classification (1 cell type vs all) G. Receiver operating curves for binary classification (1 cell type vs all).*

vAbs to assess different motility patterns. Following the assessment of vAbs theoretical capabilities, we decided to test them within an in vivo model application. For this, we acquired intravital movies depicting adoptively transferred neutrophils in the popliteal lymph-node of anesthetized mice. After tracking the cells (Fig. 3A), we compared vAbs with traditional motility estimates to assess the most effective approach to identify changes in cellular motility.

As previously observed, traditional metrics did not produce an evident hierarchical cluster of cell tracks (Fig. 3B). By contrast, testing the same tracks against a panel of 6 vAbs (see material and methods) generated an affinity profile that segregated cell tracks in two distinct major clusters (Fig. 3C). The larger cluster showed high affinity for vAbs1 and vAbs2, which were designed to specifically target neutrophils. At the same time, these tracks did not exhibit affinity for the other vAbs in the panel, as they were tailored for TCs and NKs respectively. The second and smaller cluster, however showed a notably different binding profile, with surprisingly low affinity for neutrophils.

Compelled by this observation, we decided to inspect the tracks within the cluster to screen for potential artefacts, abnormal behaviors, or biological insights. Surprisingly, we discovered that many tracks were the result of tracking mistakes (Fig 3D), hence explaining the existence of a different and anomalous group of tracks. Although this finding did not underlie a biological observation, we posit that such approach could enable the detection tracking errors and, possibly, different migratory modes within the same experimental condition. Moreover, we believe that vAbs screening might also highlight different cellular behavior under different stimuli and experimental conditions.

To sustain the latter hypothesis, we compared the affinity profiles of neutrophils in mice anesthetized with ketamine/xylazine (KX) and isofluorane (Iso). As we wanted to investigate whether the two anesthetics affected differently cell behavior, we ensured to eliminate other experimental variables by standardizing all acquired videos (2 x condition) to have identical duration (30 min), sampling rate (30s), and number of tracks (115). Then we successfully applied the panel of vAbs to the trajectories in the two experimental conditions, finding an affinity profile that was comparable in cells treated with ketamine and isoflurane (Fig. 3E-F). Despite this similarity, isoflurane treated

cells exhibited tracks with higher affinities for vAbs6, associated with NKs motility. These patterns were consistently observed in replicate videos, and therefore unlikely due to artifacts. Consequently, we conclude that vAbs might have elucidated a slightly difference in the motility of neutrophils due to the use of different anesthetics.

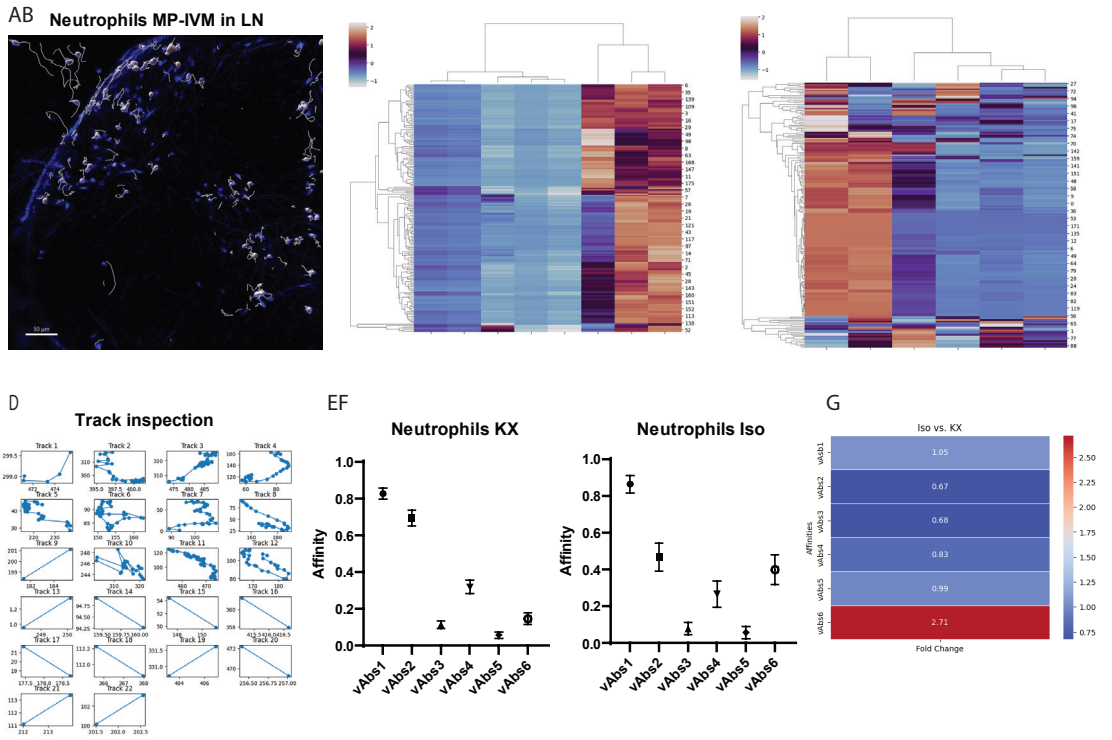

Figure 3. Dataset generation workflow. *A. Micrograph showing neutrophils imaged with 2P-IVM in the popliteal lymph node in a mouse anesthetized with ketamine and xylazine. Cell motility has been registered by means of cell tracking. B. Hierarchical clustering performed using motility features (left) compared to a cluster employing vAbs predicted affinity (right). The second cluster shows a better group segregation which highlights an anomalous group of racks. C. Plot inspection of the track from (D) showing an enrichment of anomalous tracking errors. E. Specificity fingerprint of neutrophil tracks against a panel of 6 vAbs in ketamine/xylazine (left) and isoflurane (right) conditions. F. Fold change ratio of vAbs specificity (videos per conditions =2, n tracks per video = 115).*

Discussion

The present study provided insights into challenges and solutions relating to cell track analysis. The motility information of cells is concealed within the spatial coordinates of cell tracks, and is mainly accessed using tailored processing techniques. In turn, extracted features enhance cell track separation and classification into distinct niches. Nevertheless, the abundance and complexity of these features can hinder their interpretation. To address this challenge, we introduced the idea of vAbs, computational models designed to interpret and classify cell tracks based on their motility traits. vAbs offer a concise and interpretable representation of the feature space embedded within tracks. Unlike traditional classification approaches, vAbs do not strive for a binary and exclusive prediction of cell types. Instead, they provide a nuanced quantification of the similarity between a track and a reference cell population. Consequently, this approach enables interpretable profiling of tracks across diverse experimental settings and conditions.

Among the potential applications of vAbs, label-free staining marks a significant paradigm shift in experimental design. Overcoming the need for fluorescent probes, vAbs have the potential to reduce experimental manipulation and associated costs. Most importantly, they have the potential to minimize experimental artifacts caused by dyes that can alter cell behavior, thus maintaining a physiological environment and cell dynamics. In turn, the unused acquisition channels could serve multiplexing purposes, maximizing the insights gained from each acquisition. Another compelling application of vAbs relates to behavioral studies. By testing multiple cell tracks against a panel of vAbs, resulting affinity profiles could become a behavioral fingerprint and experimental readout. Therefore, vAbs could find application in monitoring the effects of different therapies as well as the toxicity associated with different compounds.

In conclusion, vAbs represent a novel approach to cell track analysis with the potential to transform the way we conduct live-cell imaging. The concept of vAbs holds potential due to its flexibility and room for refinement. The integration morphological cues could further improve the design vAbs, as tracks and images are complementary in depicting different facets of cell motility. Therefore, future endeavors might expand the concept of vAbs by including morphological information and different cell types.

2. Aim 2: video-based cellular activity recognition in live-cell imaging

2.1. Manuscript 3: a microscopy dataset of apoptotic immune cells for algorithmic advancement in vivo

The third manuscript marks the initiation of the 'cell death detection project,' which required the creation of an annotated dataset comprising dying cells. In this project, I curated the design and implementation of a dataset which encompassed various cell death events. My responsibilities included selecting dataset entries and performing all manual annotations and data processing. I also wrote the initial draft of the text, which was subsequently reviewed by Dr. Pizzagalli and Dr. Carrillo, which contributions significantly enhanced the final quality of the text.

Beyond establishing the foundation of our following project, this manuscript holds significance as it represents my first independent research project within the lab.

Status: submitted to Scientific Data

Capturing cell death: a microscopy dataset of apoptotic immune cells for algorithmic advancement in vivo

Alain Pulfer[1,3,&], Diego Ulisse Pizzagalli[1,2,&], Pau Carrillo Barbera[1], Paola Antonello[1,5], Marcus Thelen[1], Rolf Krause[2], Santiago F. Gonzalez[1,*]

[1] Institute for Research in Biomedicine, Faculty of Biomedical Sciences, USI - Switzerland.

[2] Institute of Computational Science, USI - Switzerland.

[3] Department of Information Technology and Electrical Engineering, ETH Zurich - Switzerland

[5] Graduate School for Cellular and Biomedical Science, University of Bern - Switzerland

[&] Contributed equally to this work

***Corresponding Author/ Lead contact:** *Santiago Fernandez Gonzalez*

Abstract

Programmed cell death is pivotal for tissue homeostasis, embryological development, and host defense. Among the various forms of programmed cell death, apoptosis is characterized by distinct morphological traits such as cell shrinkage, membrane blebbing, and the formation of apoptotic bodies. Intravital microscopy (IVM) have revolutionized the study of apoptotic dynamics within living animals, enabling investigations under diverse and physiological experimental conditions. However, the analysis of resulting data poses significant challenges, necessitating the development of computational tools which requires curated datasets. Therefore, in this paper, we present an Intravital Microscopy (IVM) dataset specifically designed to advance the field of apoptosis classification and detection. Each movie within the dataset displays immune cells undergoing apoptosis and annotated by imaging scientists based on the formation of apoptotic bodies. Our dataset offers precise spatial coordinates and 3D reconstructions of each apoptotic cell, accompanied by semantic annotations that characterize the morphology of the cells at each time step. This richly annotated dataset serves as a valuable resource for comparative studies and the development of algorithms encompassing cell death classification, detection, and segmentation.

Background and summary

Apoptosis, a critical form of programmed cell death242, plays a pivotal role in multiple physiological processes243,244. In physiological conditions, damaged or dysfunctional cells undergo apoptosis to accommodate new healthy cells, an essential mechanism in development and tissue homeostasis245246. From a morphological perspective, apoptosis presents prototypical hallmarks that facilitate its identification. At the onset of the morphological change, dying cells are characterized by chromatin condensation, shrinkage, membrane blebbing, and the formation of apoptotic bodies247, which are membrane vesicles that encapsulate the cytoplasm to prevent the leakage of different molecules into the extracellular space248. In response, phagocytic cells are locally recruited to clear the resulting apoptotic bodies in a process known as efferocytosis249, which outline the end of the process.

This type of cell death plays a central role in the homeostasis of the immune system250. Traditionally apoptotic clearance of active leukocytes has been associated with reduced inflammation and host self-harm251, enforcing the idea that the process is immunologically silent247. Nonetheless, recent evidences suggest that apoptosis might promote an immune response252–254. Additionally, it orchestrates the development of adaptive immune progenitors, clearing self-reacting lymphocytes or those unable to recognize antigens255. Moreover, cytotoxic lymphocytes can induce apoptosis in infected or transformed cells to prevent the spread of pathogens and tumors164.

Considering these implications, maintain a balanced apoptotic rate is essential246,256, and measurement of the apoptotic process is of paramount importance in immunology research. Immunologist rely on experimental tools to measure the apoptotic rate of immune cells and assess its implications in physiological and pathological conditions. One pivotal approach to gain insights on cell death dynamics can be imaging. Different imaging techniques, such as in vivo or in vitro, can be used to monitor apoptosis of immune cells. In vitro imaging allows control over multiple experimental conditions257,258, including cell density and migratory cues. However, it cannot capture the complex behavior of the immune system within physiological conditions. In contrast, intravital techniques, in particular two-photon intravital microscopy (2P-IVM), enable the imaging of cells

within their physiological environment158. 2P-IVM delivers in real time, multidimensional imaging data (x,y,z,t,c) of living cells in vivo up to several hours of acquisition, thus representing a central technology for the study of the immune system16,259.

Following the FAIR principles260,261, the generation of public datasets becomes crucial for enhancing the reusability and reproducibility of experimental data. To date, however, there are only few examples of available dataset of @P-Microscopy (refer to LTDB), preventing thus the development of computational tools. Therefore, to foster the development of computational analysis, we created a comprehensive 2P-IVM dataset of apoptotic immune cells. This dataset encompasses 2P-IVM movies (Fig. 1 A-B) featuring neutrophils, eosinophils and dendritic cells undergoing apoptotic cell death in various experimental settings associated with inflammation. In addition to the raw data, we provide meticulously curated trajectories of apoptotic cells annotated by multiple operators trained to detect the morphological hallmarks of the process. Each entry in the dataset is enriched with 3D volumetric reconstructions and frame semantic annotations that describe the cell morphology (Fig. 1C). The resulting in vivo catalogue is a resource for comparative studies, cell segmentation, apoptosis detection and activity recognition in vivo.

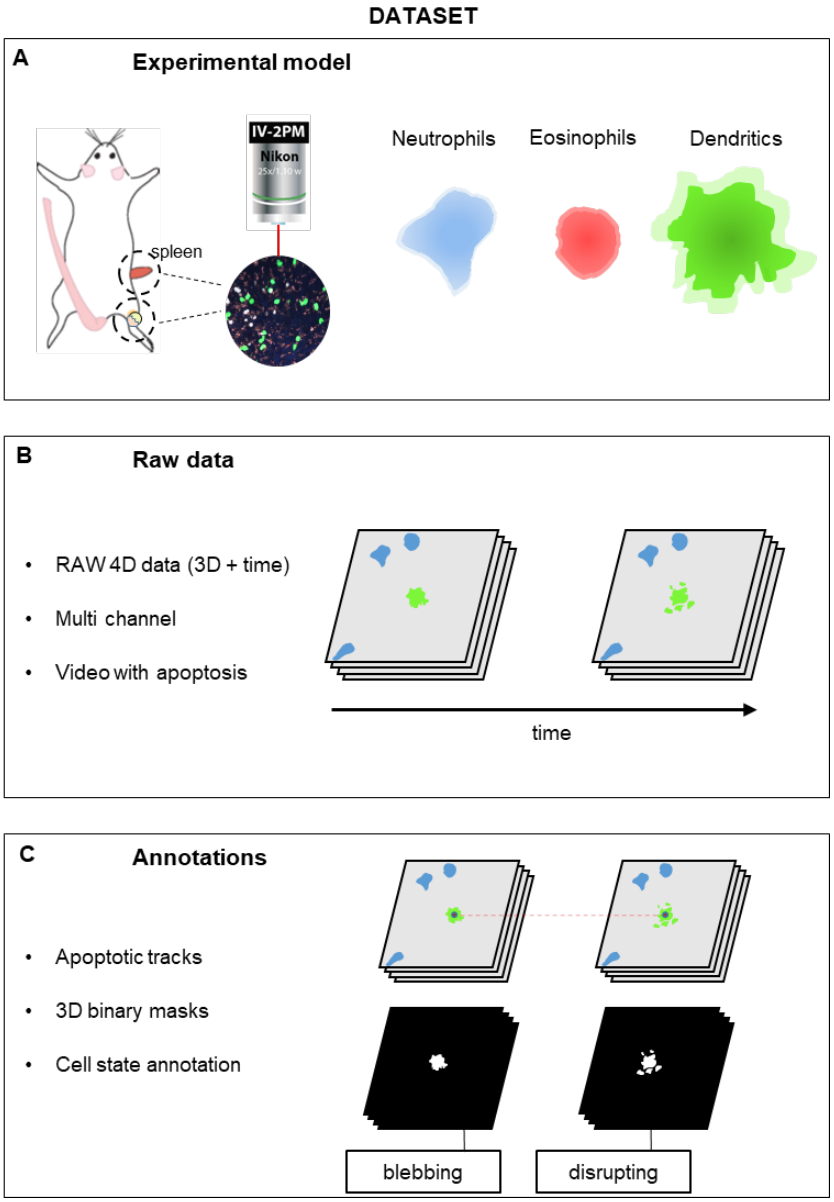

Figure 1. Dataset generation workflow. *(a) In vivo acquisition. Tissues from an anaesthetized mouse are surgically exposed and subjected to 2P-IVM. Resulting in vivo acquisitions (b) are 4D sequential data composed of multiple focal planes per time point and multiple channels. Raw data are annotated by three individual operators tracking apoptotic cells and generating a 3D mask. Apoptotic cells are associated with a cell state between "blebbing" and "disrupting" that defines the phase of the ongoing process.*

Methods

Mice. Before imaging, mice were anesthetized with xylazine (10 mg/Kg) and ketamine (100 mg/Kg)l, as previously reported[259]. Mice were stored in a sterile animal facility at the Institute for Research in Biomedicine (Bellinzona, CH). All experiments were conducted in compliance with the regulations set by the local authorities and were approved by the Swiss Federal Veterinary Office.

***In vivo* settings of the intravital microscope.** For intravital two-photon microscopy, we adopted a well-established surgical preparation method to access the popliteal lymph node. Subsequently, the exposed organs were subjected to imaging using a custom-made upright two-photon microscope (TrimScope, LaVision BioTec) specifically designed to capture 4D data, encompassing multiple stacks, channels, and time points (Table1, Fig. 1. A).

Our imaging system employed two Ti:sapphire lasers (Chameleon Ultra I, Chameleon Ultra II, Coherent) and an optical oscillator that emitted light within the 1,010–1,340 nm range (Chameleon Compact OPO, Coherent). The output wavelength ranged between 690–1,080 nm, serving dual purposes for probe excitation and tissue second-harmonic generation (SHG).

Neutrophil isolation from mouse bone marrow. Bone marrow was extracted via flushing with PBS from the long bones of UBC-GFP mice (https://www.jax.org/strain/004353). Then, the bone marrow was filtered through a 40um strainer and suspended in PBS. Primary bone marrow neutrophils were isolated with Ficoll gradient and resuspended in PBS.

Data processing. The microscopy data acquired from the videos were stored in HDF5 files, comprising uint8 or uint16 TIFFs. Prior to image analysis, the raw data underwent no preprocessing. For cell detection, tracking, and volumetric reconstruction of the microscopy videos, we employed Imaris (Oxford Instruments, v9.7.2), a versatile software suite. Subsequently, the data obtained from Imaris underwent further analysis using customized Matlab and Python scripts (refer to the code availability section for details).

Table 1: Experimental Conditions. *Table reporting channel specification and experimental settings for each movie entry included in the dataset. Channel specifications include the cell types visible in each channel among neutrophils (Neu), dendritic cells (DCs), eosinophils (Eos) and T-cells (TCs). Moreover, whenever visible, channel specification include the second harmonic generation (SHG) and the vaccine. Experimental settings include the imaging site, stimuli, cell markers, and microscope magnification.*

Video ID	CH1	CH2	CH3	CH4	Organ	Stimuli	Markers	Objective
Den1	DCs	WT-Eos	KO Eos		spleen	PR8	CD21/35,CXCR3,CD11c	40x
Den2	DCs	WT-Eos	KO Eos		spleen	PR8	CX3CR1, C57BL/6J-Tg(Il5)1638Jlee	40x
Den3	FDCs	DCs	Neu	SHG	spleen	PR8	CD21/35,CXCR3,CD11c	40x
Den4	DCs-EGFP				spleen	PR8	CXCR3	20x
Eos1	DCs	WT Eos	KO Eos		spleen	PR8	C57BL/6J-Tg(Il5)1638Jlee	16x
Eos2	DCs	WT Eos	KO Eos		spleen	PR8	C57BL/6J-Tg(Il5)1638Jlee, CX3CR1	40x
Eos3	DCs	WT Eos	KO Eos		spleen	PR8	C57BL/6J-Tg(Il5)1638Jlee, CX3CR1	40x
Eos4	DCs	WT Eos	KO Eos		spleen	PR8	C57BL/6J-Tg(Il5)1638Jlee, CX3CR1	40x
Eos5	DCs	WT Eos	KO Eos		spleen	PR8	C57BL/6J-Tg(Il5)1638Jlee, CX3CR1	40x
Neu1	Neu	Nk-GFP	SHG		lymphnode	PR8	CD21/32, Ncv1	20x
Neu2	Neu	TCs	TCs	SHG	lymphnode	PR8	CD11c	40x
Neu3	Neu	FDCs	vaccine		lymphnode	PR8	Cd21/35,CD11c	10x
Neu4	Neu	Neu	SHG		lymphnode	PR8	CD11c	16x
Neu5	Neu	Neu	SHG		lymphnode	PR8	CD11c	16x
Neu6	Neu	vaccine	SHG		spleen	PR8	CD11c	16x
Neu7	Neu	TCs	SHG		spleen	PR8	CD11c	16x
Neu8	Neu		vaccine	SHG	lymphnode	PR8	CD11c	40x
Neu9	Neu	vaccine			speen	PR8	CD11c	16x
Neu10	Neu				lymphnode	PR8	CD11c	16x
Neu11	Neu		Neu		spleen	PR8	CD11c	16x
Neu12	Neu	Neu			lymphnode	PR8	CD11c	16x
Neu14	Neu	vaccine	SHG	vaccine	spleen	PR8	CD11c	16x
Neu15	Neu	vaccine	SHG		spleen	PR8/laser ablation	CD11c	16x
Neu16	Neu		SHG	vaccine	spleen	PR8/laser ablation	CD21/32,CD11c	16x
Neu17	Neu			SHG	spleen	PR8	CD11c	40x
Neu18	Neu	Vaccine	SHG		spleen	PR8/laser ablation	CD11c	16x
Neu19	Neu		SHG		lymphnode	PR8/laser ablation	CD11c	40x
Neu20	Neu		vaccine		lymphnode	PR8	CD11c	40x
Neu21	Neu				spleen	PR8	CD11c	16x
Neu22	Neu				spleen	PR8	CD11c	16x
Neu23	Neu				spleen	PR8	CD11c	16x
Neu24	Neu	DCs	SHG		lymphnode	PR8	CD11c	16x
Neu25	DCs	Neu		SHG	lymphnode	PR8	CD11c	40x

Manual tracking. The centroids of cells over time were manually annotated and tracked using the "Spots drawing" tool in Imaris (Bitplane). To ensure robustness, three operators independently and redundantly performed tracking without knowledge of reciprocal results.

During the tracking process, the operators adhered to strict morphological criteria to identify apoptotic cells. Specifically, they focused on sequences exhibiting the characteristic hallmarks of apoptosis: 1) membrane blebbing, 2) subsequent formation of apoptotic bodies, and 3) eventual cell

disruption (Fig. 2 B). For each frame within the apoptotic sequences, the operators placed a centroid at the cell's center using the Imaris "Spots" function, resulting in a connected track representing the apoptotic event (x, y, z, t, ID). Subsequently, the trajectories generated by each operator were consolidated into a ground truth using a majority consensus scheme that considered the duration and location of the events. The starting and ending time points were determined by identifying overlaps among at least two of the three annotators' tracks. For each time point, the two closest spatial coordinates were selected and averaged to create a final ground truth. Once the ground

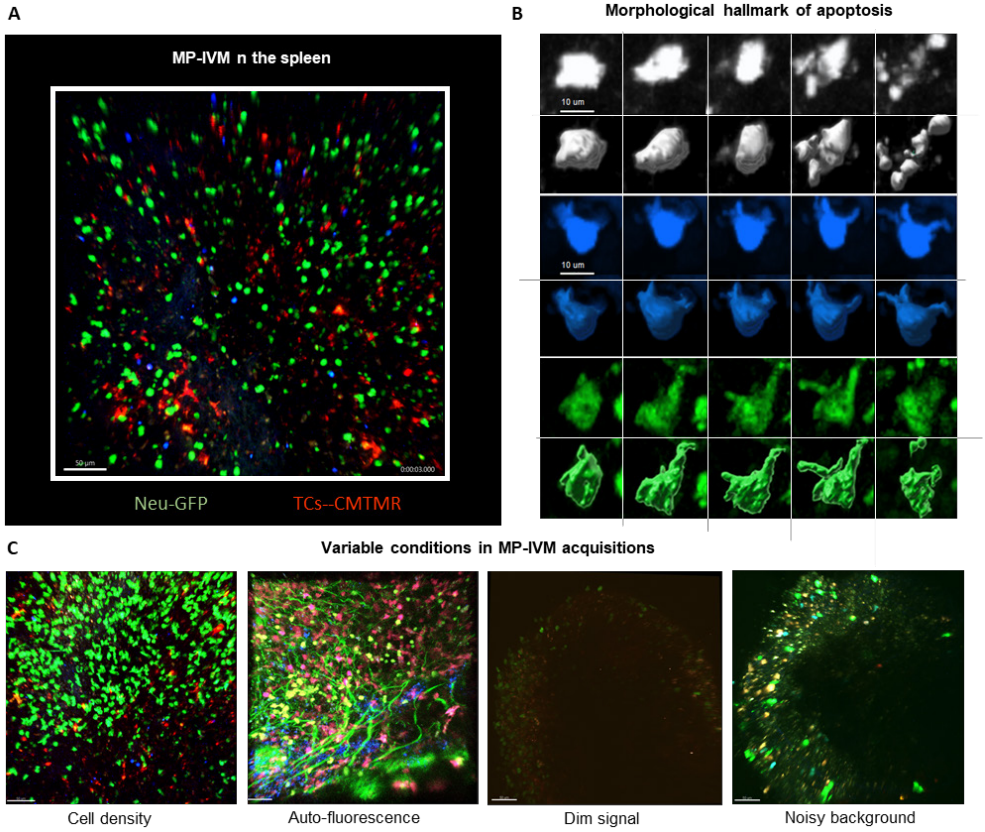

Figure 2. A. *Micrograph depicting a MP-IVM acquisition in the spleen of an anesthetized mouse. Neutrophils are stained with GFP (green) and T cells are stained with CMTCMR (red).* ***B.*** *Prototypical apoptotic sequences depicting the morphological hallmarks of cells undergoing apoptosis. The dataset encompasses neutrophils (**top**), eosinophils (**middle**), and dendritic cells (**bottom**). A 3D mask complements each raw sequence. .*

truths for each apoptotic event were established, volumetric 3D reconstruction was performed using the Imaris "Surface" function. This reconstruction process generated precise 3D masks of each cell undergoing apoptosis, enhancing the accuracy and reliability of the dataset.

Semantic annotation. Three annotators meticulously labeled the morphological state of the cells basing their annotations on specific morphological criteria. For each frame within the ground truth sequence, they assigned to each cell one of two apoptotic semantic labels: "membrane blebbing" or "cell disruption." The goal was to accurately annotate the interval and dynamics of apoptosis, capturing crucial moments in the cell's life cycle. To ensure robustness and consistency, a majority consensus scheme was employed to establish the final cell state. This scheme considered the overlap of annotations from at least two of the annotators, promoting a unified and reliable consensus on the apoptotic semantic label for each cell at every time point. Hence, by employing a consensus-driven approach, we minimized potential biases and variations in the annotations. The resulting ground truth dataset provides a comprehensive and accurate representation of the cellular behavior during apoptosis, setting the stage for in-depth analyses and advanced algorithm development.

Computation of quality metrics. To compute the SNR of the entries of the dataset, for each frame of the movies we computed a reference denoised image using a median filter. Successively, we used the snr function of matlab to compare the reference image to the original one, computing an estimate of the SNR. This procedure has been applied for each channel separately.

Computation of density metrics. The density metrics are computed by using adaptive thresholding and morphological operations to separate foreground objects from the background in each channel. The number of cells visible at each time point in each individual channel is then counted. By averaging these numbers over time, an estimate of the number of cells over the course of the movies is generated. The average shortest distance between cells and a coefficient of clustering can also be estimated by knowing the spatial coordinates of the cells.

Statistical analyses. Statistical analysis and plot visualization were performed using GraphPad Prism 8 (Graphpad, La Jolla, USA). All statistical tests were performed using non-parametric Kruskal-Wallis test or

Mann-Witney test. Significance of p value is described as * when $p < 0.05$, ** when $p < 0.005$ and *** when $p < 0.0005$.

Table 2: apoptotic phases annotation. *Table reporting the semantic annotations of the apoptotic events. For each video, apoptotic events are characterized by a unique identifier and frame level semantic annotations. The morphological state of cells undergoing apoptosis were categorized as "blebbing" or "disrupting", each defined by a starting and ending frame. Furthermore, the table indicates weather if apoptotic elicit a local immune response ("response").*

Video ID	blebbing start (frame)	blebbing end (frame)	disruption start (frame)	disruption ends (frame)	response (yes/no)	Channel
Neu1	3	5	6	10	yes	ch1
Neu2	18	20	21	22	no	ch1/ch4
Neu2	27	29	30	30	no	ch1
Neu2			24	30	no	ch1
Neu3			6	7	yes	ch1
Neu3	11	11	12	13	no	ch1
Neu4	9	11	12	15	no	ch1
Neu4	10	30	31	43	yes	ch1
Neu4	99	104	105	111	yes	ch1
Neu4			24	26	yes	ch1
Neu5	41	44	45	50	yes	ch1/ch3
Neu5	98	105	106	112	yes	ch1/ch3
Neu5	90	106	107	112	no	ch1/ch3
Neu6	17	18	19	23	no	ch1
Neu6			25	33	no	ch1
Neu6	37	53	54	60	no	ch1
Neu7			4	7	no	ch1
Neu7	21	24	25	26	no	ch1
Neu7	31	33	34	34	no	ch1
Neu7	43	43	44	51	no	ch1
Neu7	52	53	54	56	no	ch1
Neu7			53	57	no	ch1
Neu8	3	5	6	8	no	ch1/ch4
Neu9	25	25	26	30	no	ch1
Neu10			49	54	no	ch1/ch3
Neu11			1	3	no	ch1
Neu11			3	5	no	ch1
Neu11	20	21	22	24	no	ch1
Neu11			23	26	no	ch1
Neu11	24	24	25	29	yes	ch1
Neu11			26	28	no	ch1
Neu11	34	35	36	37	no	ch1
Neu11	36	37	38	40	no	ch1
Neu11	45	46	47	47	no	ch1
Neu11	51	52	53	55	no	ch1
Neu12	1	4	5	14	yes	ch1/ch3
Neu12			10	15	yes	ch1/ch3
Neu12	27	33	34	50	no	ch1/ch3
Neu12	46	49	50	54	no	ch1/ch3
Neu12	63	66	67	74	no	ch1/ch3
Neu12	104	129	121	124	yes	ch1/ch3
Neu12	145	146	147	150	no	ch1/ch3
Neu12	153	155	156	159	yes	ch1/ch3
Neu13	198	204	205	209	no	ch4
Neu13	247	252	253	255	no	ch4
Neu14	24	28	29	34	yes	ch1
Neu15	1	10	11	19	no	ch1
Neu16	2	6	7	14	yes	ch1
Neu16			19	22	yes	ch1
Neu16	28	41	42	45	yes	ch1
Neu17	111	111	112	114	yes	ch1
Neu18			1	12	yes	ch1
Neu18			28	33	no	ch1
Neu19	8	12	13	15	yes	ch1/ch3
Neu20	8	12	13	17	no	ch4/ch1
Neu20	22	25	26	34	no	ch4/ch1
Neu20			73	82	no	ch4/ch1
Neu20	103	104	105	108	yes	ch4/ch1
Neu21	1	5	6	12	no	ch1
Neu22			1	15	no	ch1
Neu23			11	17	no	ch1
Neu23			1	4	no	ch1
Neu24	7	8	9	12	no	ch1
Neu25	19	20	21	26	no	ch2
Eos1	1	34	35	52	no	ch3
Eos2	1	11	12	19	yes	ch1
Eos2			11	20	yes	ch3
Eos2	16	19	20	35	no	ch1
Eos2	15	29	30	47	no	ch1
Eos2	25	30	30	37	no	ch1
Eos2	1	5	6	10	yes	ch3
Eos3	1	6			yes	ch2
Eos3	18	31	32	40	yes	ch2
Eos3	24	33	34	36	no	ch2
Eos3	25	50	51	55	yes	ch2
Eos3	36	56	57	80	yes	ch2
Eos4	45	67	68	75	no	ch1
Eos4	49	71	72	81	no	ch1
Eos5	21	26	27	45	no	ch1
Den1	1	10	18	28	no	ch1
Den1	64	66	67	72	no	ch1
Den2			83	88	no	ch1
Den2	42	44	45	72	no	ch1
Den2	86	91	92	103	no	ch1
Den2	68	78	79	86	no	ch1
Den2	24	27	28	32	no	ch1
Den3			15	17	no	ch1
Den3	19	20	21	26	no	ch2
Den4			1	20	no	ch1
Den4	11	12	13	40	no	ch1

Data record

The proposed dataset is structured hierarchically, as illustrated in Figure 3. At the top level, it comprises a collection of videos featuring apoptotic cell death. These videos consist of unprocessed raw microscopy footage, each assigned a unique identifier (ID) and accompanied by essential metadata and acquisition settings. The videos contain multiple channels and span five dimensions: spatial coordinates (x, y, z), time (t), and multiple channels (c). The raw videos are available in HDF5 format.

Within each video, researchers will find three types of annotations providing insights into the apoptotic process. The first type includes tracks of apoptotic and non-apoptotic cells, available in the same HDF5 file or separate excel tables. These tracks enable comprehensive analysis of cellular behavior. The second type comprises 3D reconstructions of apoptotic cells, allowing researchers to visualize cell death in three dimensions. Finally, semantic annotations are provided in excel format, describing the state of the cells at different stages of the apoptotic process.

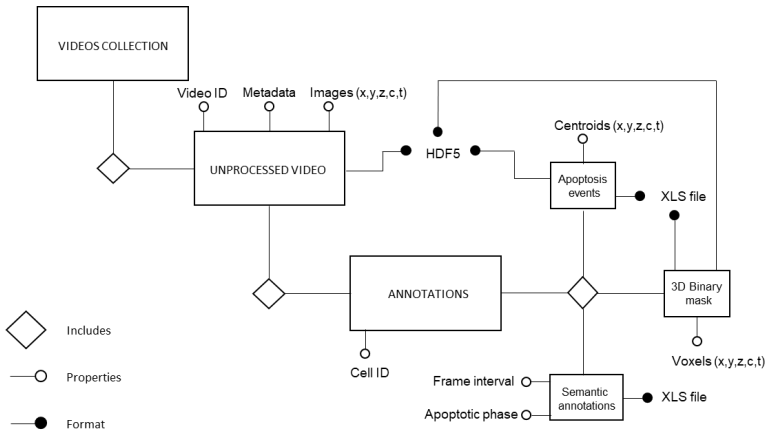

Figure 3. Dataset structure and format. *Diagram depicting the hierarchic organization of the dataset. The highest conceptual block of the dataset is the video collection depicting apoptotic cells. Each unprocessed video is characterized by its ID, the acquisition data, the metadata and the images stack with structure x, y, z, channel, time. Videos are available in HDF5. For each video, the dataset provides multiple annotations that are cell ID specific. Apoptotic cell tracks and binary masks are composed of centroids and voxels with properties x, y, z, c, t. Both annotations are in the same HDF5 of the acquisition or in xlsm format. Semantic annotations link a semantic information to a frame interval for each cell ID in a separate xlsm file. Annotations are always performed on the channel where apoptotic cells are more visible.*

Technical validation

Imaging raw data. Movies in the dataset were imaged with different microscopy settings. These included different voxel size, sampling rates, duration and volume (Table 3). As these parameters can influence the overall quality of the movies, we estimated the image-quality of our dataset by computing the signal-to-noise (SNR) ratio for each acquisition (Fig. 4 A). Higher SNR indicate better image quality, and reportedly values above 5 are considered sufficiently good to distinguish foreground objects from background. Hence, the measured average SNR of 10 can assert the overall quality of the dataset and guarantees that their entries provide reliable and interpretable results

The sampling rate of the movies in our dataset varied between 15s, 30s, 45s, and 60s (Fig 4B). This aspect holds relevance when evaluating dynamic processes in time-lapses. Specifically, estimations of general cell motility, such as speed and straightness, as well as cell tracking, can be significantly influenced by the selected sampling rate[28].

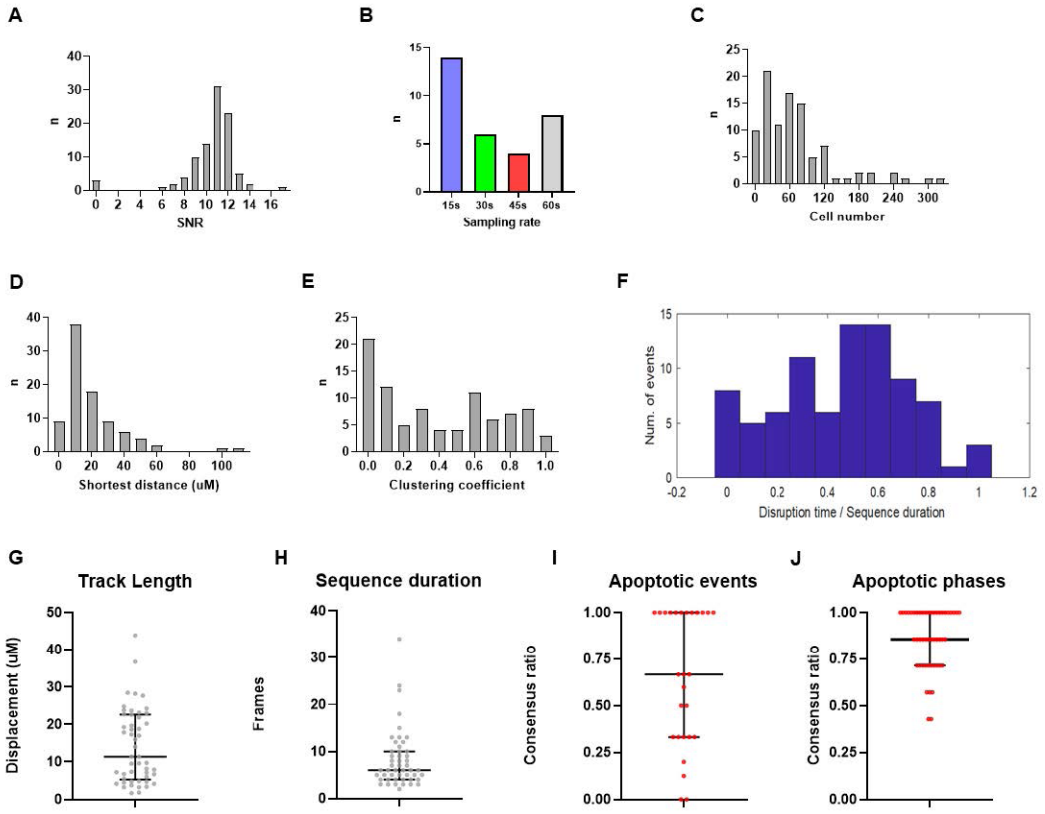

Figure 4: Data quality and validation. *To evaluate the quality of each video, different image related metrics, such as signal to noise ratio and the blur, are computed and combined into a final quality score. Similarly, a complexity score is computed by considering metrics related to cell density and local cell clusters. B) The inter operator variability is estimated by a consensus ratio, that is the ratio of individual annotations overlapping between at least two operators out of three.*

Higher sampling rates may result in the loss of critical information, especially in highly dynamic processes like cell death, where rapid and short-lived changes in the morphology of the cell occur. To address this concern and ensure accurate depiction of fast and transient processes, our dataset encompasses movies with low sampling rates. This guarantees robustness in detecting essential temporal dependencies, such as membrane blebbing, without overlooking critical features of the apoptotic process.

Aside from the acquisition settings, the interpretability of imaging data can be influenced by the biological content and complexity of the acquisitions. A prominent parameter in this regard is cell density, which has a significant impact on the analysis. In time-lapses with high cell density, potential side effects such as cluttering, cell merging, and cell splitting, may arise. These factors pose challenges to cell detection efforts and may hinder crucial information within the data. Consequently, excessive cell density may render certain algorithms incapable of extracting meaningful insights from the imaging data.

Thus, in light of these considerations, we estimated crucial parameters related to cell density and aggregation for each channel in the dataset. These parameters encompass the overall cell number, the shortest distance between cells, and a clustering coefficient that indicates the percentage of cells in close proximity to at least three other cells (Table 3, Fig. 4C-E). These measurements underscore the variability in the dataset, with movies ranging from 20 cells to up to 300 and exhibiting a clustering coefficients near 1. By analyzing such diverse time-lapses, researchers can effectively benchmark their detection algorithms on increasingly complex scenarios, ensuring the robustness and applicability of their methods across a wide range of biological conditions and cell densities.

Table 3: video quality and complexity. *For each video, we computed the following imaging metrics: image resolution (x, y, z), voxel size (x, y, z), and sampling rate (seconds/frame). In addition, we computed the following quality metrics: signal to noise ratio, peak signal to noise ratio, standard deviation of the mean intensity and power spectrum of the signal. To account for each video complexity, we calculated the total cell number, the average shortest distance between cells and a clustering coefficient that evaluates the percentage of cells in a cluster of at least four cells. Quality and complexity metrics were computed for all the separate channels.*

Video	resolution	resolution	resolution	vox size	vox size	vox size	Sampling (s/fr)	SNR	SNR	SNR	SNR	Cell number	Cell number	Cell number	Cell number	Shortest distance	Shortest distance	Shortest distance	Shortest distance	Clustering	Clustering	Clustering	Clustering
	X	Y	Z	X	Y	Z		CH1	CH2	CH3	CH4	CH1	CH2	CH3	CH4	CH1	CH2	CH3	CH4	CH1	CH2	CH3	CH4
EOS1	520	520	26	1.3346	1.3346	3	60	9	11	10	0	195	77	86		14.6	29.68	37.08		0.325	0.315	0	
EOS2	521	521	25	0.5336	0.5336	3	30	10	11	10	0	60	41	28		13.98	16.61	23.54		0.357	0.561	0.072	
EOS3	521	521	21	0.5336	0.5336	3	60	9	9	11	0	23	27	17		23.48	21.81	31.95		0.242	0.218	0.156	
EOS4	521	521	10	0.5336	0.5336	2	13	11	12	12	0	76	53	9		5.95	10.33	39.2		0.824	0.79	0.55	
EOS5	521	521	11	0.5336	0.5336	3	15	11	12	11	0	128	88	39		5.86	7.65	16.31		0.802	0.658	0.371	
Den3	556	556	7	0.5	0.5	3	15	12	14	13	13	50	9	1	63	4.2	15.36		7.85	0.892	0.279	0	0.576
Den4	439	406	26	0.801	0.801	3	30	10	11	17	0	73	53			7.34	12.34			0.723	0.603		
Den2	521	521	13	0.534	0.534	3	15	11	11	11	0	79	21	15		6.63	16.22	37.86		0.696	0.278	0.291	
Den1	512	512	18	0.533	0.533	2	30	11	14	9	0	43	0	21		4.13		8.13		0.908	0	0.768	
Neu1	555	555	24	0.8	0.8	3	60	11	11	10	0	147	15	60		11.84	34.05	5.81		0.281	0	0.882	
Neu2	189	173	25	0.9047	0.9842	3	60	8	9	10	9	23	7	4		21.42	42.73		1.00E+06	0.062	0	0	
Neu3	555	555	15	0.8	0.8	3	14	11	12	12	0	63	74	39		7.1	9.76	8.95		0.807	0.618	0.581	
Neu4	555	555	15	0.8	0.8	3	15	11	11	12	0	66	69	52		8.34	9.31	8.65		0.728	0.649	0.56	
Neu5	520	520	15	0.8538	0.8538	3	15	8	8	9	0	172	317	111		19.71	14.72	9.99		0.01	0.089	0.584	
Neu6	555	555	14	0.8	0.8	3	15	8	9	10	0	231	157	28		14.97	9.73	51.11		0.096	0.45	0	
Neu7	1041	930	19	0.2401	0.24	3	60	11	13	11	14	97	54	65	38	1.76	2.3	4.29	2.53	0.989	0.957	0.729	0.914
Neu8	555	555	14	0.8	0.8	3	30	12	9	0	0	22	106			37.54	17.04			0	0.06		
Neu10	555	555	15	0.8	0.8	3	15	12	11	12	0	79	95	62		11.54	9.61	10.94		0.395	0.46	0.338	
Neu11	555	555	14	0.8	0.8	3	60	7	10	10	0	178	190	54		10.7	10.53	27.99		0.487	0.459	0.021	
Neu12	555	555	13	0.8	0.8	3	46	12	11	12	0	94	125	84		15.41	11.75	22.19		0.086	0.225	0.046	
Neu13	320	320	21	0.867	0.867	3	45	11	12	12	9	18	8	1	29	6.27			7.16	0.902			0.872
Neu14	520	520	15	0.8538	0.8538	3	45	10	10	10	0	71	87	66		23.48		26.09		0.016		0.052	
Neu15	520	520	8	2.1346	2.1346	3	14	11	11	12	0	81	119	37		58.4	49.75	96.83					
Neu16	520	520	15	0.8538	0.8538	3	15	11	11	12	0	46	60	21		27.14	21.37	34.87		0.022	0.061	0.059	
Neu17	521	521	14	0.5336	0.5336	3	60	11	11	11	11	20	61	13	26	24.33			20.89	0.186			0.128
Neu18	361	300	8	2.14	2.14	3	14	12	10	11	0	31	40	13		63.77	47.22	113.49		0	0	0	
Neu19	556	556	18	0.5	0.5	2	60	13	13	12	0	13	0	14		12.57		5.69		0.308	0	0.639	
Neu20	555	555	19	0.8	0.8	3	19	13	12	11	11	80	11	9	88	11.23	38.42	54.07	10.19	0.437	0.048	0	0.584
Neu21	555	555	14	0.8	0.8	3	30	12	9	0	0	37	299			30.77	15.21			0	0.077		
Neu22	555	555	14	0.8	0.8	3	30	12	9	0	0	37	299			30.77	15.21			0	0.077		
Neu23	555	555	14	0.8	0.8	3	19	12	10	0	0	38	259			30.32	15.51			0	0.058		
Neu24	512	512	13	0.7106	0.7106	4	37	6	7	9	0	121	124	73		8.29	6.99	7.24		0.652	0.755	0.798	
Neu25	1040	1040	16	0.4269	0.4269	2	15	12	11	12	18	232	96	117		3.81	3.4	3.75		0.927	0.992	0.928	

Apoptotic events. Apoptotic events are inherently diverse, exhibiting variability that can affect classification and detection algorithms. One major challenge arises from the distinct morphologies of apoptotic cells, leading to a class heterogeneity[262,263] task that makes it difficult to identify consistent patterns within the same label in supervised classification. Additionally, the variable duration of apoptotic sequences can pose a challenge to algorithms aimed at classifying the entire apoptotic process over time.

Finally, the residual motility of apoptotic cells, caused by drifting, can further complicate the accurate identification of cell coordinates during the apoptotic process. To address these challenges and aid practitioners in designing effective algorithms, we estimated the variability between apoptotic events in our dataset. We quantified the mean timing of cell disruption (Fig. 4F), which provides insights into the typical occurrence of this critical phase. Additionally, we assessed the average displacement of cells (Fig. 4G) and the overall duration of

the apoptotic process (Fig. 4H), offering essential information to guide algorithmic solutions for apoptosis classification and detection. Hence, by considering these variabilities, researchers and practitioners can better design and fine-tune their algorithms for accurate classification and detection of apoptotic immune cells.

Operator annotations. To assess the inter-operator variability during the annotation process, we introduced a consensus ratio, which quantifies the proportion of annotations that achieved agreement between at least two out of the three operators involved. The mean consensus ratio for annotating apoptotic events (Fig. 4I) was 0.6, indicating a moderate level of agreement among the operators and the intrinsic challenge of visually detecting apoptotic events based on morphological cues. However, when annotating the specific apoptotic phases (Fig. 4J), the mean consensus ratio significantly increased to 0.9. This high consensus ratio displays strong agreement between the operators in identifying the distinct phases of apoptosis. Together, these metrics convey the challenge in identifying apoptotic cells, where some instances might be overlooked. However, once entries are established in the dataset, the subsequent annotation demonstrated high consensus, ensuring a consistent and reliable dataset.

Usage notes

The proposed database represents a valuable resource for researchers seeking to develop and validate algorithms targeted at identifying the apoptotic process. With access to the raw data and annotations in excel format, users can tailor training datasets to suit their specific tasks of cell classification, detection, or segmentation. To generate datasets for supervised-learning tasks, users can access the raw microscopy videos and their corresponding annotations provided in Excel format. By utilizing the annotations, it is possible to locate and track the centroids of individual apoptotic events over time (x, y, z, t). Users can then define a suitable region around each cell centroid to capture the information of the cells. Subsequently, single-cell crops can be extracted at each frame using the defined regions, and labels (0 for healthy, 1 for apoptotic) can be assigned based on the provided annotations. Users can create personalized training datasets to train custom classifiers to predict the apoptotic state of cells based on their morphology using various deep learning architectures or traditional machine learning

techniques (Fig. 5A left). To accomplish supervised classification on static frames, a wide array of deep learning architectures, such as convolutional networks (CNNs)[54], capsule networks[264], and vision transformers[72,265] among others, are available. Accordingly, recent studies demonstrated the successful classification of a variety of cell deaths in static images[160,266].

Moving towards a higher level of complexity, users can undertake the classification of complete apoptotic sequences of images (Fig. 5A right). To this end, deep learning architectures tailored for activity recognition[69], such as 3DCNNs[68], recurrent networks[267], or optical flow-based methods[268], can be employed. Recurrent architectures, in particular, have demonstrated effectiveness in classifying apoptotic sequences acquired *in vitro*[244], showcasing their potential for this task. To achieve whole sequence classification, users can extract consecutive frames as cropped time-lapses, thus preserving the temporal dependencies of the apoptotic events. Each resulting sequence would encapsulate a specific time window capturing the dynamic behavior of a cell throughout its apoptotic process. With this information, users can train models capable of effectively analyzing the temporal dependencies and patterns exhibited by cells during apoptosis.

***Figure 5. Dataset usage for deep learning applications**. **A.** Schematic representation of the classification task applied to single image crops depicting apoptotic cells (**left**) and to apoptotic sequences (**right**). Single image crops can be classified with the aid of convolutional networks, mapping an image to a corresponding binary value labelling healthy (0) or apoptotic (1) cells. Similarly, sequences of apoptotic images can be classified with activity recognition architectures. **B.** Schematic depiction of a detection routine applied to full microscopy images containing healthy and apoptotic cells. Input images are processed with a detector that predicts the spatial coordinates of apoptotic cells (red bounding boxes). **C.** Schematic representation of the image segmentation task applied to full microscopy images depicting apoptotic cells. Input microscopy images are processed with an auto encoder-decoder architecture which learns to map the input into a binary mask that highlights apoptotic cells only.*

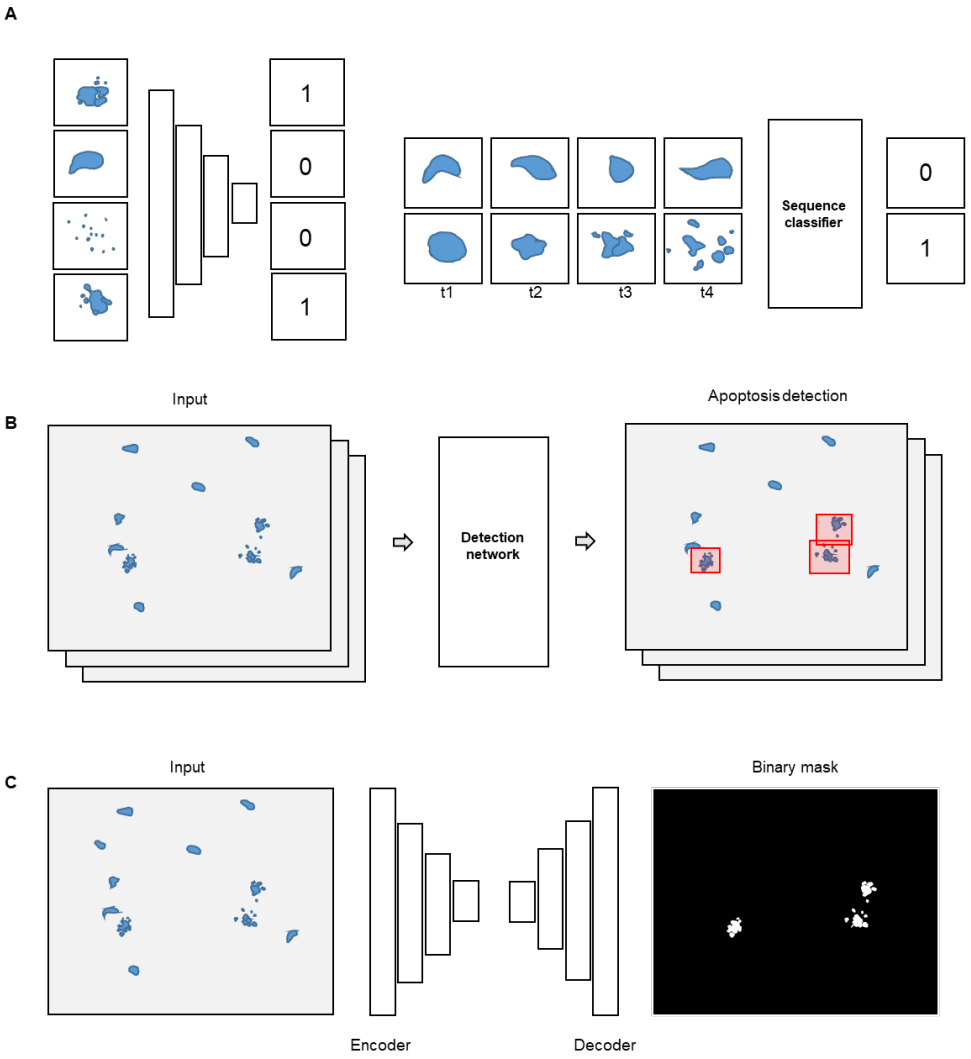

Users can also add complexity to the classification problem by venturing into detecting apoptotic cells in uncropped microscopy time-lapses (Fig. 5B). Unlike classification, the detection task poses greater challenges as it involves identifying the precise spatial and time interval of candidate apoptotic events. While specialized architectures can handle detection tasks effectively in static images, apoptosis detection in time-lapses remains a particularly demanding and open challenge. In static images, the detection of apoptotic events can be hampered by variations in cell appearance, overlapping cells,

or background clutter. However, in live-cell imaging, additional complexities arise from the dynamic motility of cells, including changes in shape and movement over time. This temporal dimension introduces new difficulties that requires tailored algorithmic solutions. To this end, researchers can leverage the presented dataset to explore novel approaches for tracking and detecting apoptotic events in time-lapse microscopy.

The dataset is also suitable for cell segmentation (Fig. 5C) through the utilization of encoder-decoder approaches[61]. These architectures have demonstrated to be effective in several bio-imaging segmentation tasks. Hence, they hold promising potential for the segmentation of apoptotic cells based on their distinct morphology. Our dataset enables the task of cell segmentation by providing 3D segmentation data of apoptotic cells over time. To train segmentation models, the dataset provides inputs 2D (single planes) and 3D (whole volume) images, as well as the ground truth annotations binary masks of each individual apoptotic cell. Consequently, researchers can design and apply segmentation techniques either in 2D or 3D settings, and each individual frames from the time-lapse videos can be used as an independent training sample.

Acknowledgements

Fundings

Suisse National Science Foundation grant 176124 (AP, DU, MP, SG)

SystemsX.ch grant iPhD2013124 (DU, RK, SG)

Biolink grant 189699 (DUP, PC)

Authors contributions

Conceptualization: SG, AP, DU

Methodology: AP, DU

Experiments: PA, MP

Data annotation: AP, DU, PC

Data analysis and visualization: AP

Figures: AP

Writing—original draft: AP, PC, DU, SG

2.2. Manuscript 4: Transformer-based spatial-temporal detection of apoptotic cell death in live-cell imaging.

This project initiated concurrently with the creation of the aforementioned dataset, as we decided to promptly experimenting with different computational techniques. Upon selecting deep learning methods, we established an ongoing communication with the group led by Prof. Gambardella, a renowned expert in the field. Our discussion mainly revolved around the scope and feasibility of the project, and Dr. Giusti, which already developed classifiers for mitosis, provided invaluable suggestions to direct our study toward the communities of pattern recognition and computer vision.

The hybrid nature of the project, however, demanded sound performances in real-world biological applications. Therefore, after realizing that the data in our possession would not suffice to generalize the proposed methodology, we decided to expand the scope of our dataset. Fortuitously, during a symposium on cell death and autophagy, we had the chance to meet Dr. Gagliardi, which had incidentally annotated an extended dataset of apoptotic cells *in vitro*. After briefly discussing, we decided to establish a collaboration with the common goal of integrating their data in the framework that we had already developed, leading to the present manuscript. Reflecting on the history of the project, the significance of this manuscript lies in the interdisciplinary collaborations which made it possible.

Status: accepted at eLife

Transformer-based spatial-temporal detection of apoptotic cell death in live-cell imaging.

Alain Pulfer[1,2,&], Diego Ulisse Pizzagalli[1,3,&], Paolo Armando Gagliardi[4,&], Lucien Hinderling[4], Paul Lopez[5], Romaniya Zayats[5], Pau Carrillo-Barberà[1,6], Paola Antonello[1,4], Miguel Palomino-Segura[7], Alessandro Giusti[8], Marcus Thelen[1], Luca Maria Gambardella[8], Thomas T. Murooka[5], Olivier Pertz[4], Rolf Krause[3], Santiago Fernandez Gonzalez[1,*]

[1] Institute for Research in Biomedicine, Faculty of Biomedical Sciences, USI—Switzerland
[2] Department of Information Technology and Electrical Engineering, ETH Zurich—Switzerland
[3] Euler Institute, USI—Switzerland
[4] Institute of Cell Biology, University of Bern—Switzerland
[5] University of Manitoba, Winnipeg—Canada
[6] Instituto de Biotecnología y Biomedicina (BioTecMed), Universitat de València—Spain.
[7] Centro Nacional de Investigaciones Cardiovasculares—Spain
[8] Dalle Molle Institute for Artificial Intelligence, IDSIA—Switzerland

[&] Contributed equally

***Corresponding Author/ Lead contact:** *Santiago Fernandez Gonzalez*

Abstract

Intravital microscopy has revolutionized live cell imaging by allowing the study of spatial-temporal cell dynamics in living animals. However, the complexity of the data generated by this technology has limited the development of effective computational tools to identify and quantify cell processes. Amongst them, apoptosis is a crucial form of regulated cell death involved in tissue homeostasis and host defense. Live-cell imaging enabled the study of apoptosis at the cellular level, enhancing our understanding of its spatial-temporal regulation. However, at present, no computational method can deliver label-free detection of apoptosis in microscopy time-lapses. To overcome this limitation, we developed ADeS, a deep learning-based apoptosis detection system that employs the principle of activity recognition. We trained ADeS on extensive datasets containing more than 10,000 apoptotic instances collected both *in vitro* and *in vivo*, achieving a classification accuracy above 98% and outperforming state-of-the-art solutions. ADeS is the first method capable of detecting the location and duration of multiple apoptotic events in full microscopy time-lapses, surpassing human performance in the same task. We demonstrated the effectiveness and robustness of ADeS across various imaging modalities, cell types, and staining techniques. Finally, we employed ADeS to quantify cell survival *in vitro* and tissue damage *in vivo*, demonstrating its potential application in toxicity assays, treatment evaluation, and inflammatory dynamics. Our findings suggest that ADeS is a valuable tool for the accurate detection and quantification of apoptosis in live-cell imaging and, in particular, intravital microscopy data, providing insights into the complex spatial-temporal regulation of this process.

Introduction

In the last two decades, Intravital microscopy (IVM) has revolutionized live-cell imaging by enabling microscopy acquisitions *in situ* across different organs, making it one of the most accurate model to describe cellular activities within a living host[259]. In particular, multiphoton intravital microscopy (MP-IVM) generates in-depth 3D data that encompass multiple channels for up to several hours of acquisition (x, y, z + t)[16,269,270], thus providing unprecedented insights into cellular dynamics and interactions[26]. The resulting MP-IVM data stream is a complex and invaluable source of information, contributing to enhance our understanding of several fundamental processes[28,259].

Apoptosis is a form of regulated cell death[247,271] which plays a crucial role in several biological functions, including tissue homeostasis, host protection, and immune response[255]. This process relies on the proteolytic activation of caspase-3-like effectors[250], which yields successive morphological changes that include cell shrinkage, chromatin condensation, DNA fragmentation, membrane blebbing[243,248,272], and finally, apoptotic bodies formation[273]. Due to its crucial role, dysregulations of apoptosis can lead to severe pathological conditions, including chronic inflammatory diseases and cancer[163,274]. Consequently, precise tools to identify and quantify apoptosis in different tissues are pivotal to gain insights on this mechanism and its implications at the organism level.

Traditional techniques to quantify apoptosis rely on cellular staining on fixed cultures and tissues[275–279] or flow cytometry[278,280]. However, these methods do not allow the temporal characterization of the apoptotic process. Moreover, they potentially introduce artifacts caused by sample fixation[281]. Live-cell imaging can overcome these limitation by unraveling the dynamic aspects of apoptosis with the aid of fluorescent reporters, such as Annexin staining[277] or the activation of Caspases[282]. However, the use of biochemical reporters *in vivo* could potentially interfere with physiological functions or lead to cell toxicity[283]. For these reasons, label-free detection of apoptosis represent a critical advancement in the field of cell death.

Computational methods could address this need by automatically detecting individual apoptotic cells with high spatial and temporal accuracy. In this matter, deep learning (DL) and activity recognition (AR) could provide a playground for the classification and

detection of apoptosis based on morphological features[284]. Accordingly, recent studies showed promising results regarding the classification of static frames[160,285] or time-lapses[244] portraying single apoptotic cells. However, none of the available methods can apply for the detection of apoptosis in microscopy movies depicting multiple cells. Therefore we developed ADeS, a novel apoptosis detection system which employs a transformer DL architecture and computes the location and duration of multiple apoptotic events in live-cell imaging. Here we show that our architecture outperforms state-of-the-art DL techniques and efficiently detects apoptotic events in a broad range of imaging modalities, cellular staining, and cell types.

Results

An *in vitro* and *in vivo* live-cell imaging data. Curated and high-quality datasets containing numerous instances of training samples are critical for developing data-hungry methods such as supervised DL algorithms[286]. To this end, we generated two distinct datasets encompassing epithelial cells (*in vitro*) and leukocytes (*in vivo*) undergoing apoptotic cell death. In addition, the two datasets include different imaging modalities (confocal and intravital 2-photon), biological models, and training-set dimensionalities. A meaningful difference between the datasets pertains to the staining methods and the morphological hallmarks, which define the apoptotic process in both models. In the *in vitro* model, the expression of nuclear markers allowed us to observe apoptotic features such as chromatin condensation and nuclear shrinkage[248], whereas in the *in vivo* model, cytoplasmic and membrane staining highlighted morphological changes such as membrane blebbing and the formation of apoptotic bodies[248]. Accordingly, we have manually annotated these datasets based on the presence of the specific hallmarks, ensuring that each dataset includes two class labels depicting either apoptotic or non-apoptotic cells. These two datasets constitute the first step toward creating, testing, and validating our proposed apoptosis detection routine.

To generate the *in vitro* dataset we used epithelial cells because, among the human tissues, they have the highest cellular turnover driven by apoptosis[287]. Nevertheless, from the bioimaging perspective, the epithelium is a densely packed tissue with almost no extracellular matrix, making it extremely challenging to analyze. As such, in epithelial research, there is a pressing need for com-

putational tools to identify apoptotic events automatically. To this end, we imaged and annotated the human mammary epithelial cells expressing a nuclear fluorescent marker (Fig.1A), obtaining 13120 apoptotic nuclei and 301630 non apoptotic nuclei image sequences (Fig. 1B-C, Supplementary 1A). Nuclear shrinkage and chromatin condensation, two of the most prototypical hallmarks of apoptosis (Fig. 1C), formed our criteria for manual annotation. We confirmed that non-apoptotic nuclei had constant area and chromatin density from the generated time-lapses. In contrast, apoptotic nuclei underwent a decrease in area and an increase in chromatin condensation (Fig. 1D). The resulting dataset captured the heterogeneity of apoptotic cells in epithelial tissue, including early nuclear fragmentation, a rapid shift along the x and y axes, and extrusion through the z dimension (Supplementary Fig. 1B–C). Moreover, our dataset incorporates the typical difficulties of automatically annotating apoptotic events from live microscopy of a densely packed tissue (Supplementary Fig. 1D) with the accumulation of apoptotic bodies (Supplementary Fig. 1E) and across multiple microscope hardware settings (Supplementary Fig. 1F).

To generate an *in vivo* dataset, we focused on polymorphonucleated leukocytes (neutrophils and eosinophils) that expressed a fluorescent marker. In these early immune responders, apoptosis is a crucial process that orchestrates their disposal, consequently determining the duration of the inflammation[288]. To acquire instances of apoptotic leukocytes, we performed MP-IVM in anesthetized mice by surgically exposing either the spleen or the popliteal lymph node (Fig. 1E-F). The resulting time-lapses (Fig. 1G) provided 3D imaging data encompassing consecutive multi-focal planes (3D) and multiple imaging channels. Then, from the generated MP-IVM movies, we generated cropped sequences of fixed size that tracked apoptotic cells for the duration of their morphological changes (59x59 pixels + time; Fig. 1H-I). This procedure was applied to 30 MP-IVM movies, generating 120 apoptotic sequences (supplementary Fig. 1G). Furthermore, we annotated random instances of non-apoptotic events, generating 535 cropped samples. To characterize the heterogeneity of the movies, we manually quantified the cell number per field of view (87 ± 76), the shortest distance between cells (21.2 μM ± 15.4), and the signal-to-noise ratio (8.9 ± 3.6; supplementary Fig. 1 H–J). We assumed that the morphological changes associated with apoptosis occur within defined time windows for detection purposes.

Hence, we estimated the median duration of the morphological changes corresponding to 8 frames (supplementary Fig. 1K–L, respectively). In addition, to classify apoptotic cells within defined spatial regions, we considered them to be non-motile. This assumption was confirmed when we found that apoptotic cells exhibited a displacement and speed that were not significantly different from those of arrested cells (supplementary Fig. 1M).

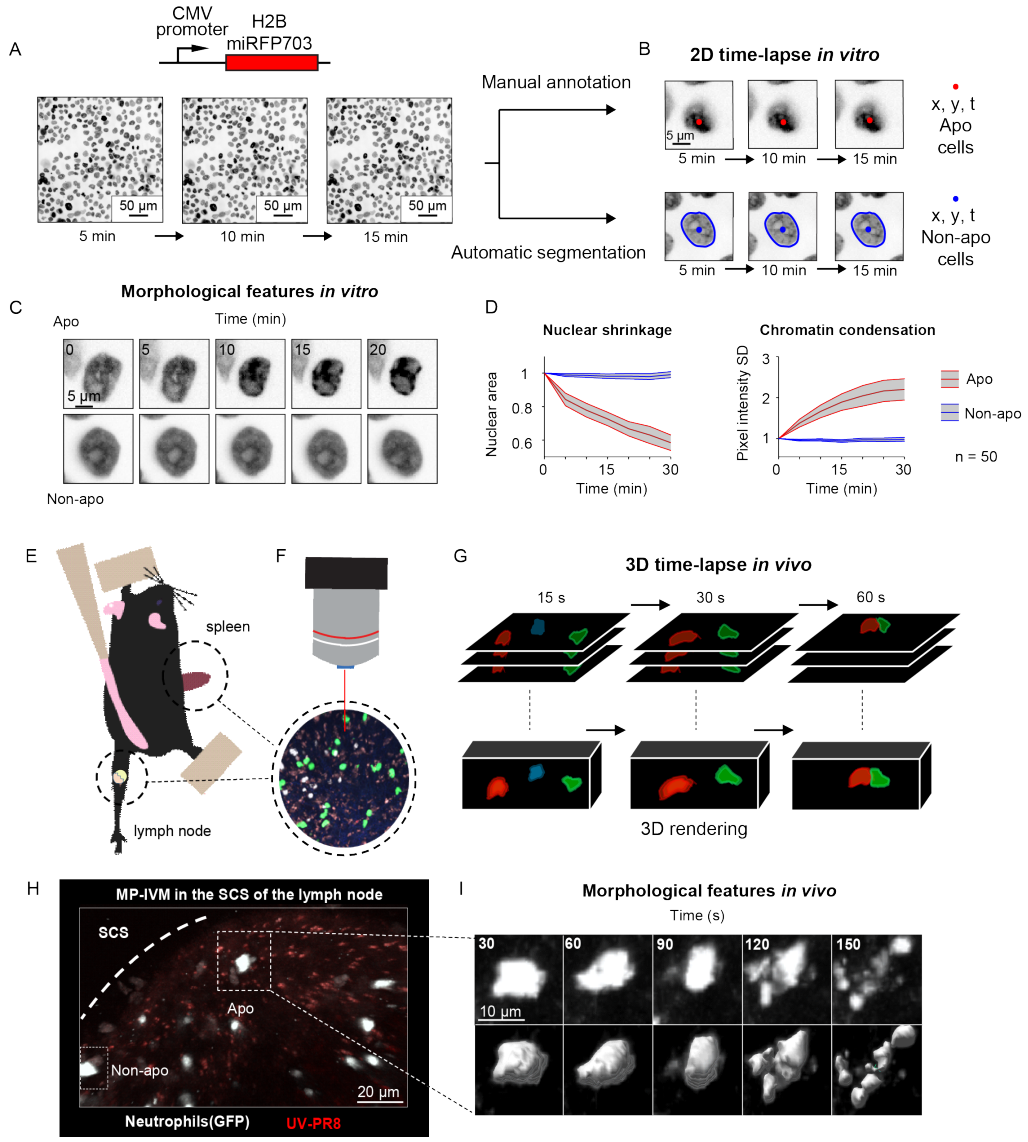

Figure 1: Generation of* in vitro *and* in vivo *live-cell imaging data. A. *Micrographs depicting mammary epithelial MCF10A cells transduced with H2B-miRFP703 marker and grown to form a confluent monolayer. The monolayer was acquired with a fluorescence microscope for several hours with 1-, 2- or 5-min time resolution.* ***B.*** *The centroid (x, y) and the time (t) of apoptotic events were annotated manually based on morphological features associated with apoptosis. Non-apoptotic cells were identified by automatic segmentation of nuclei.* ***C.*** *Image time-lapses showing a prototypical apoptotic event (**upper panels**), with nuclear shrinkage and chromatin condensation, and a non-apoptotic event (**bottom panels**).* ***D.*** *Charts showing the quantification of nuclear size (**left**) and the standard deviation of the nuclear pixel intensity (right) of apoptotic and non-apoptotic cells (n = 50). Central darker lines represent the mean, gray shades bordered by light colored lines represent the standard deviation.* ***E.*** *Simplified drawing showing the surgical set-up for lymph node and spleen.* ***F-G****. Organs are subsequently imaged with intravital 2-photon microscopy (IV-2PM, **F**), generating 3D time-lapses (**G**).* ***H.*** *Representative IV-2PM micrograph and* ***I.*** *selected crops showing GFP-expressing neutrophils (white) undergoing apoptosis. The apoptosis sequence is depicted by raw intensity signal (**upper panels**) and 3D surface reconstruction (**bottom panels**).*

ADeS, a pipeline for apoptosis detection. Detecting apoptosis in live-cell imaging is a two-step process involving the correct detection of apoptotic cells in the movies (x, y) and the correct estimation of the apoptotic duration (*t*). To fulfill these requirements, we designed ADeS as a set of independent modules assigned to distinct computational tasks (Fig. 2). As an input, ADeS receives a 2D representation of the microscopy acquisitions (Fig. 2A) obtained from the normalization of 2D raw data or the maximum projection of 3D data[289]. This processing step ensures the standardization of the input, which might differ in bit depth or acquisition volume. After that, we employ a selective search algorithm[55,290] to compute regions of interest (ROIs) that might contain apoptotic cells (Fig. 2B). For each ROI at time (*t*), ADeS extracts a temporal sequence of *n* frames ranging *from t - n*/2 to *t* + *n*/2 (Fig. 2C). The resulting ROI sequence is standardized in length and passed to a DL classifier (Fig. 3), which determines whether it is apoptotic or non-apoptotic. Finally, each apoptotic sequence is depicted as a set of bounding boxes and associated probabilities (Fig. 2D) generated from the predicted trajectories (x, y, t, ID; Fig. 2E). From this readout, ADeS can generate a heatmap representing the likelihood of apoptotic events throughout a movie (Fig. 2F, left), together with a cumulative sum of the predicted cell deaths (Fig. 2F, right).

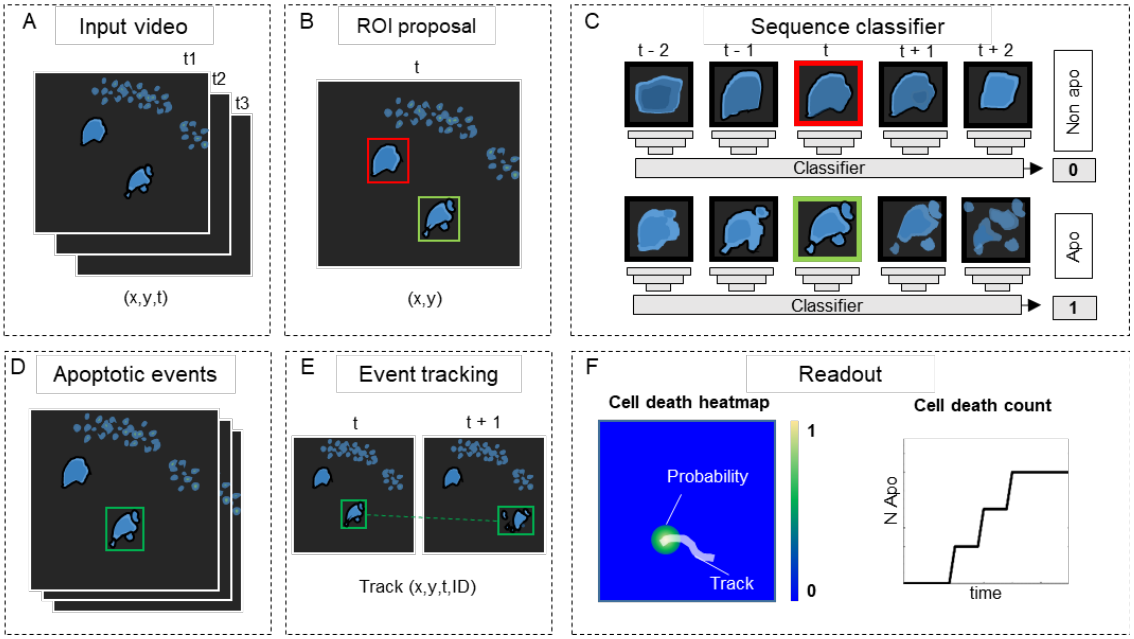

Figure 2. ADeS, a pipeline for apoptosis detection. A. *ADeS input consists of single channel 2D microscopy videos (x, y, t)* ***B.*** *Each video frame is pre-processed to compute the candidate Regions of Interest (ROI) with a selective search algorithm.* ***C.*** *Given the coordinates of the ROI at time t, ADeS extracts a series of snapshots ranging from t-n to t + n. A deep learning network classifies the sequence either as non-apoptotic (0) or apoptotic (1).* ***D.*** *The predicted apoptotic events are labelled at each frame by a set of bounding boxes which,* ***E.*** *are successively linked in time with a tracking algorithm based on Euclidean distance.* ***F.*** *The readout of ADeS consist of bounding boxes and associated probabilities, which can generate a probability map of apoptotic events over the course of the video (**left**) as well as providing the number of apoptotic events over time (**right**).*

For the classification of apoptotic sequences, we proposed a Conv-Transformer architecture (Fig. 3). In the proposed architecture, a convolutional module extracts the spatial features of the apoptotic cells, whereas attention-based networks evaluates the temporal relationship between consecutive frames.

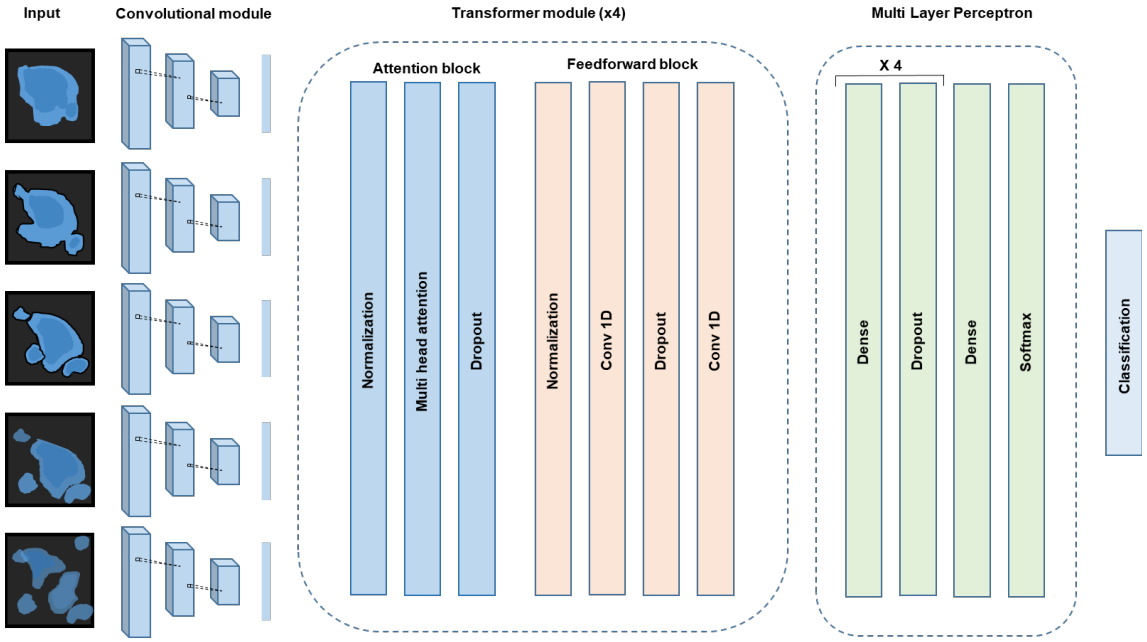

Figure 3. Conv-Transformer architecture at the chore of ADeS. *Abstracted representation of the proposed Conv-Transformer classifier. The input sequence of frames is processed with warped convolutional layers, which extract the features of the images. The extracted features are passed into the 4 transformer modules, composed of attention and feedforward blocks. Finally, a multi-layer perceptron enables classification between apoptotic and non-apoptotic sequences.*

Training and deployment *in vitro*. As previously described, ADeS is a multiple-block pipeline, and its application and validation to detect apoptotic cells in live-cell imaging follow two main steps: (1) the training of the DL classifier with a target dataset and (2) its deployment on live-cell imaging acquisitions. As opposed to *in vivo* acquisitions, *in vitro* time-lapses are more homogeneous in their content and quality, thus representing the first dataset in order of complexity for the training of ADeS. For this reason, we formulated the learning problem as a binary classification task that assigned non-apoptotic sequences to the class label 0 and apoptotic sequences to the class label 1 (Supplementary Fig. 2A). The class label 0 included instances of healthy nuclei and nuclei undergoing mitotic division (which can resemble apoptotic events).

To validate the proposed Conv-Transformer architecture for apoptosis classification, we compared it with the performances of a CNN, a 3DCNN, and a Conv-LSTM. To this end, the four models were trained on a dataset containing 13.120 apoptotic and 13.120 non-apoptotic events, using a 0.12 validation split (Table 1). Results show that the frame accuracy of the CNN is low, possibly due to morphological heterogeneity over consecutive frames, and therefore unsuitable for the task. By contrast, the 3DCNN and the Conv-LSTM displayed high sequence accuracy, F1 score and AUC, confirming that the temporal information within frames is pivotal to correctly classifying image sequences containing apoptotic cells. Nonetheless, the proposed Conv-Transformer outperformed both the 3DCNN and the Conv-LSTM, establishing itself as the final DL architecture at the chore of ADeS.

Table 1. Comparison of deep learning architectures for apoptosis classification. *Comparative table reporting accuracy, F1 and AUC metrics for a CNN, 3DCNN, Conv-LSTM, and Conv-Transformer. The classification accuracy is reported for static frames or image-sequences. N.A. stands for non-applicable. The last column shows which cell death study employed the same baseline architecture displayed in the table.*

Classifier architecture	Frame accuracy	Sequence accuracy	F1	AUC	Study
CNN	74 % ± 1.3	N.A.	0.77	0.779	[160,291]
3DCNN	N.A.	91.22 %± 0.15	0.91	0.924	-
Conv-LSTM	N.A.	97.42 % ± 0.09	0.97	0.994	[244,292]
Conv-Transformer	N.A	98.27 % ± 0.25	0.98	0.997	Our

Successively, we deployed a preliminary trained network on control movies without apoptotic events to collect false positives that we used to populate the class label 0, thus ensuring a systematic decrease in the misclassification rate (Supplementary Fig. 2B). Using the latter generated dataset, we trained the Conv-Transformer for 100 epochs using an unbalanced training set with a 1:10 ratio of apoptotic to non-apoptotic cells (Fig. 4A). After deploying the trained model on 1000 testing samples, the confusion matrix (Fig. 4B) displayed a scant misclassification rate (2.68%), similarly distributed between false positives (1.04%) and false negatives (1.64%). Accordingly, the receiver operating characteristic (ROC) of the model skewed to the left (AUC = 0.99, Fig. 4C). This skew indicates a highly favorable tradeoff between the true positive rate (TPR) and false positive rate (FPR), which the overall predictive accuracy of 97.32% previously suggested (Fig. 4B). Altogether, these metrics suggest an unprecedented accuracy of the DL model in the classification of apoptotic and non-apoptotic sequences. However, they only reflect the theoretical performances of the classifier applied to cropped sequences depicting a single cell at a time.

To validate ADeS on full-length microscopy acquisitions, we deployed it on six testing movies that were not part of the training set. Each testing movie had been annotated manually and contained a variable number of ground-truth apoptosis (98 ± 21) and

a comparable cell density (1705 ± 124). Moreover, all movies had identical magnification (20x), duration (21 h), and sampling rate (5 min). In order to test ADeS on these movies, we adopted an unbiased approach and we did not hard-tune the hyper-parameters of the model (see Material and Methods), specifying only a stringent confidence threshold (0.995) and a temporal window based on the average duration of the nuclear hallmarks (9 frames). As a result, ADeS could predict the location and timing of the apoptotic nuclei (Fig. 4D, Supplementary Movie 1), enabling the detection of multiple apoptosis in a densely packed field of view (Fig. 4E–F).

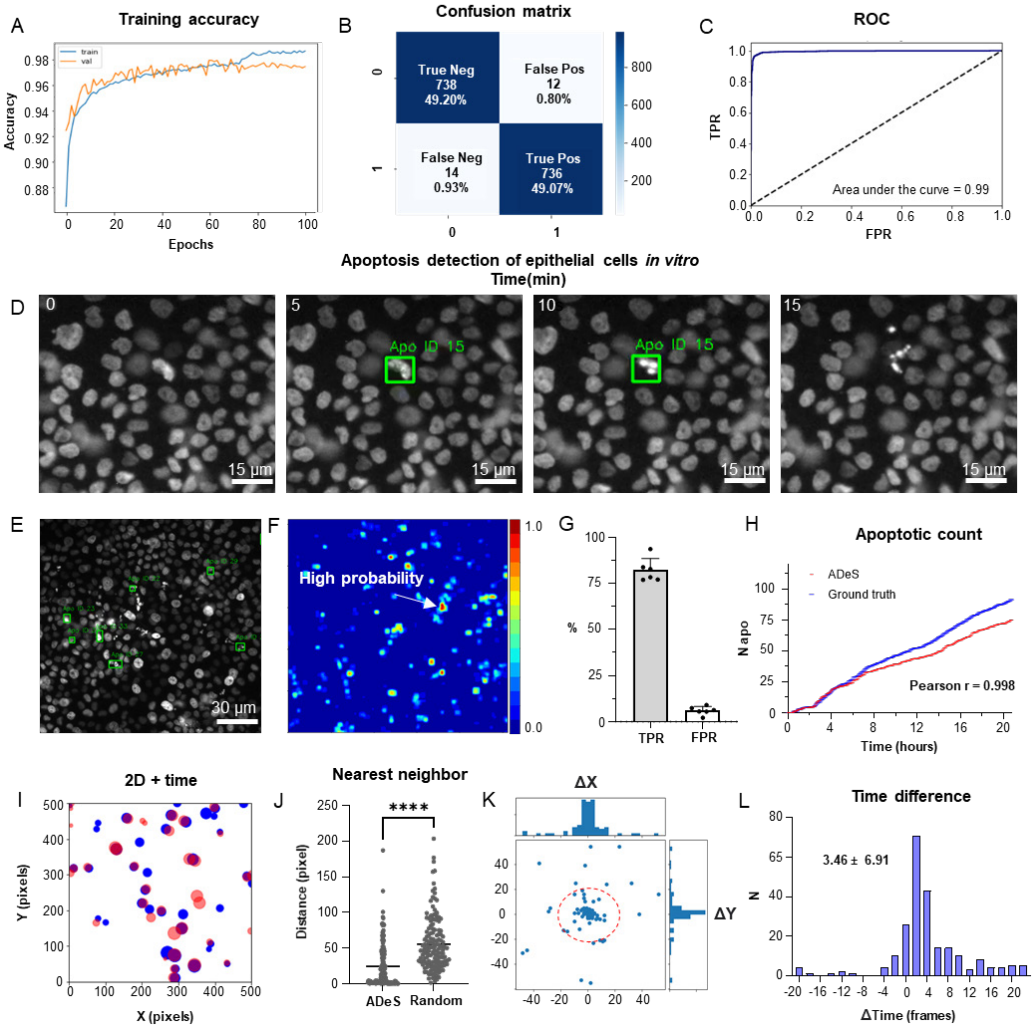

Figure 4. Training and performance in vitro. A. *Confusion matrix of the trained model at a decision-making threshold of 0.5.* ***B.*** *Receiver operating characteristic displaying the false positive rate (specificity) corresponding to each true positive rate (sensitivity).* ***C****. Training accuracy of the final model after 100 epochs of training.* ***D.*** *Representative example of apoptosis detection in a time-lapse acquired in vitro.* ***E.*** *Multiple detection of nuclei undergoing apoptosis displays high sensitivity in densely packed field of views.* ***F.*** *Heatmap representation depicting all apoptotic events in a movie and the respective probabilities.* ***G.*** *Bar plots showing the true positive rate (TPR) and false positive rate (FPR) of ADeS applied to five testing movies, each one depicting an average of 98 apoptosis.* ***H.*** *Time course showing the cumulative sum of ground truth apoptosis (blue) and correct predictions (red).* ***I.*** *2D visualization of spatial-temporal coordinates of ground truth (blue) and predicted apoptosis (red). In the 2D representation, the radius of the circles maps the temporal coordinates of the event.* ***J.*** *Pixel distance between ADeS predictions and the nearest neighbor (NN) of the ground truth (left) in comparison with the NN distance obtained from a random distribution (right). The plot depicts all predictions of ADeS, including true positives and false positives.* ***K.*** *Scatterplot of the spatial distance between ground truth and true positives of ADeS. Ground truth points are centered on the X = 0 and Y = 0 coordinates.* ***L.*** *Distribution of the temporal distance (frames) of the correct predictions from the respective ground truth nearest neighbor. Statistical comparison was performed with Mann-Whitney test. Columns and error bars represent the mean and standard deviation respectively. Statistical significance is expressed as: $p \leq 0.05$ (*), $p \leq 0.01$ (**), $p \leq 0.001$ (***), $p \leq 0.0001$ (****).*

To quantify these performances, we compared the prediction of ADeS to the annotated ground truths (x, y, t). By doing this, we found that the average TPR, or sensitivity, was 82.01% (ranging from 77% to 92%), while the average FPR was 5.95% (Fig. 4G). The undetected apoptotic events were likely a consequence of the heterogeneity of nuclear fragmentation, which can vastly differ in signal intensity, size, focal plane, and duration (Supplementary Fig.1). Nonetheless, hard tuning the model could further increase the sensitivity without additional training data, such as by adjusting the temporal interval or by lowering the confidence threshold. With respect to the false positives, most were mitotic cells, due to their morphological similarities with apoptotic nuclei. Nevertheless, the FPR was contained, translating into a new false positive every 4 frames (or 20 minutes of acquisition). This rate confirmed that ADeS is overall robust, especially in light of movies depicting 1700 cells per frame.

Concerning the spatial-temporal dynamics, the apoptotic count over time highlighted a tight relationship between ground truth apoptosis and correct detections of ADeS (Fig. 4H). Accordingly, the two curves were divergent but highly correlative (Pearson r = 0.998), proving that ADeS can successfully

capture cell death dynamics. A 2D scatterplot (x, y, t = radius; Fig. 4I) visually depicted the spatial-temporal proximity between ADeS and the ground truth, indicating overlap between the two scatter populations. Nearest neighbor (NN) analysis further captured this relationship; the average distance between all ADeS predictions (true positives + false positives) and the NN in the ground truth was 30 pixels. In contrast, randomly generated predictions had a ground truth NN within a 52-pixel radius (Fig. 4J). Considering instead the true positives only, we observed that they were in close spatial proximity to the ground truth, with most predictions falling within a 20-pixel radius (Fig. 4K). The difference between the predicted timing of apoptosis and the one annotated in the ground truth was also slight, with an average discard of 3.46 frames (Fig. 4L). Interestingly, ADeS showed a bias toward late detections, which is explained considering that operators annotated the beginning of the apoptosis, whereas ADeS learned to detect nuclear disruption, occurring at the end of the process. Altogether, these quantifications indicate that ADeS detects apoptotic nuclei with high spatial and temporal accuracy, establishing a novel comparative baseline for this task.

3D rotation of the *in vivo* dataset. Upon the successful application of ADeS *in vitro*, the next step in complexity was detecting apoptosis *in vivo* time lapses. The latter is inherently more challenging due to different factors, including high background signal, autofluorescence, and the presence of collagen[25], among others. For this purpose, we re-trained ADeS using the *in vivo* data described in Figure 1. However, one of the main limitations of supervised DL is the need for large datasets, and the finite number of MP-IVM acquisitions and apoptotic instances represented a bottleneck for the training of ADeS. To overcome this limitation, we implemented a custom data augmentation strategy that exploits 3D volumetric rotations, as previously performed in other studies [293,294]. Accordingly, each 3D apoptotic sequence underwent multiple spatial rotations and was successively projected in 2D (Fig. 5A). This procedure enabled us to increase the dataset of a 100 fold factor without introducing imaging artifacts, as each volume rotation was a physiological representation of the cell (Fig. 5B).

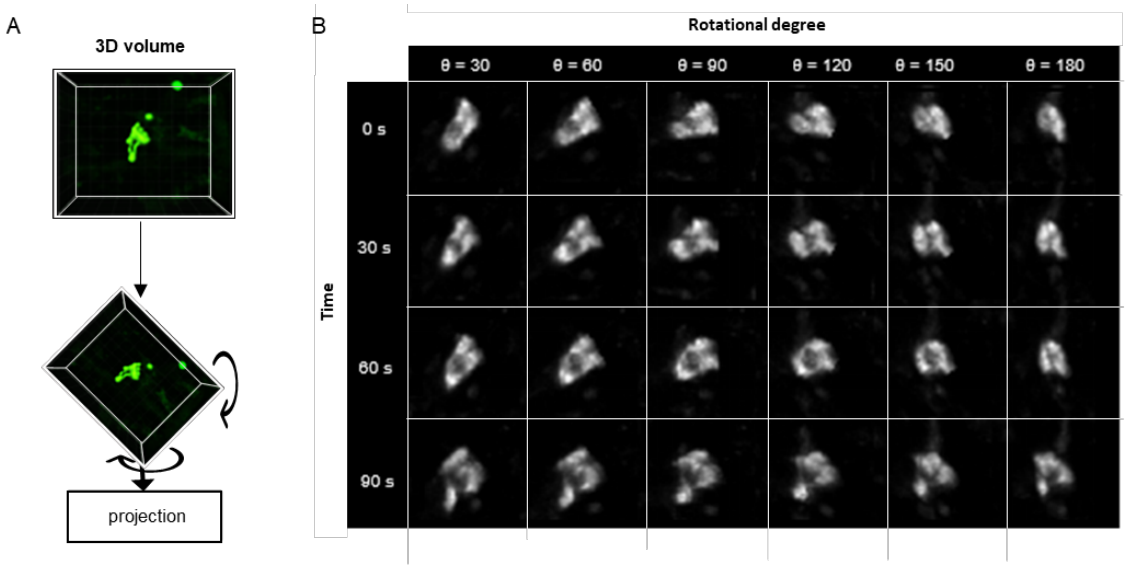

Figure 5. 3D rotation of the* in vivo *dataset. A *Depiction of a 3D volume cropped around an apoptotic cell. Each collected apoptotic sequence underwent multiple 3D rotation in randomly sampled directions. The rotated 3D images were successively flattened in 2D.* ***B.*** *Gallery showing the result of multiple volume rotations applied to the same apoptotic sequence. The vertical axis depicts the sequence over time, whereas the horizontal describes the rotational degree applied to the volumes.*

Training and deployment *in vivo*. To train ADeS using the latter rotated *in vivo* dataset, we defined a binary classification task in which ROIs containing apoptotic cells were assigned to the class label 1. In contrast, all remaining ROIs, including healthy cells and background elements, were assigned to the class label 0 (Supplementary Fig. 3A). Subsequently, we trained the DL classifier for 200 epochs. Finally, we performed 5-fold cross-validation according to the ID of the movies (Fig. 6A). The resulting confusion matrix demonstrated a classification accuracy of 97.80% and a 2.20% misclassification rate that is primarily due to type II error (1.80% false negatives) (Fig. 6B). Analogous to the tests *in vitro*, classification *in vivo* proved highly effective in predicting apoptotic and non-apoptotic instances. The ROC of the model, which indicated high sensitivity and a low FPR, supported this favorable result (Fig. 6C).

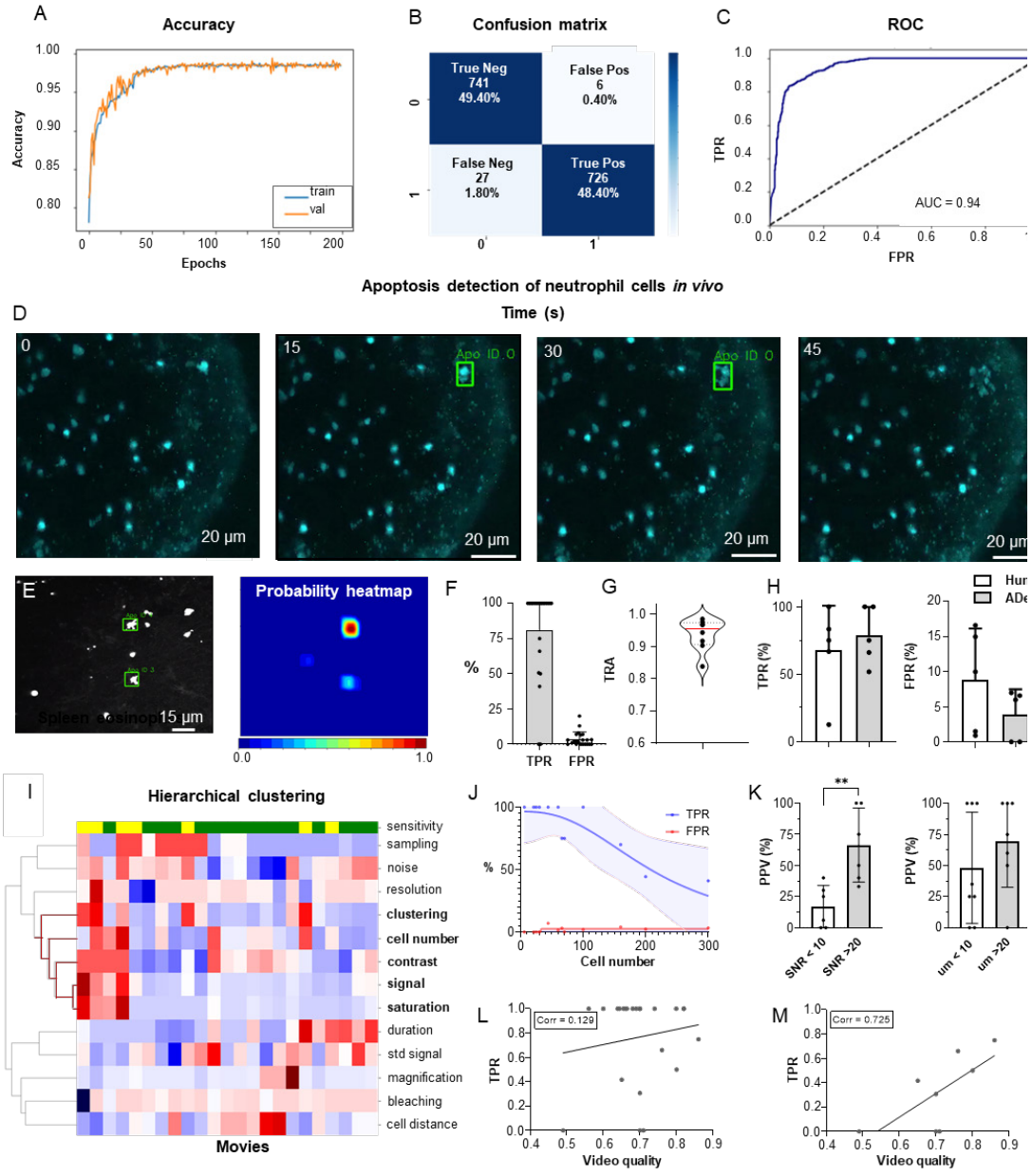

Figure 6. Training and performance in vivo. A*. Confusion matrix of the trained model at a decision-making threshold of 0.5.* ***B****. Receiver operating characteristic displaying the false positive rate (FPR) corresponding to each true positive rate (TPR).* ***C****. Training accuracy of the final model trained for 200 epochs with data augmentations.* ***D.*** *Image gallery showing ADeS classification to sequences with different disruption timing. The generated heatmap reaches peak activation (red) at the instant of cell disruption* ***D.*** *Representative*

snapshots of a neutrophil undergoing apoptosis. Green bounding boxes represents ADeS detection at the moment of cell disruption ***E.*** *Representative micrograph depicting the detection of two eosinophil undergoing cell death in the spleen (****left****) and the respective probability heatmap (****right****).* ***F.*** *ADeS performances expressed by means of true-positive rate (TPR) and false-positive rate (FPR) over a panel of 23 videos.* ***G****. TRA measure distribution of the trajectories predicted by ADeS with respect to the annotated ground truth (n = 8)* ***H****. Comparison between human and ADeS by means of TPR and FPR on a panel of 5 randomly sampled videos* ***I.*** *Hierarchical clustering of several video parameters producing two main dendrograms (n = 23). The first dendrogram includes videos with reduced sensitivity and is enriched in several parameters related to cell density and signal intensity.* ***J.*** *Graph showing the effect of cell density on the performances expressed in terms of TPR and FPR (n = 13).* ***K****. Comparison of the positive predictive value between videos with large and small signal to noise ratio (****left****), and videos with large and small shortest cell distance (****right****).* ***L-M.*** *Selected video parameters are combined into a quality score that weakly correlates with the TPR in overall data (****M, n = 23****) and strongly correlates with the TPR in selected underperforming data (****N, n = 8****). Statistical comparison was performed with Mann-Whitney test. Columns and error bars represent the mean and standard deviation respectively. Statistical significance is expressed as: p ≤ 0.05 (*), p ≤ 0.01 (**), p ≤ 0.001 (***), p ≤ 0.0001 (****).*

We then benchmarked ADeS in the detection task performed on a set of 23 MP-IVM acquisitions of immune cells undergoing apoptosis. Unlike *in vitro* settings, *in vivo* acquisitions displayed high variability in cell number, auto-fluorescence, signal intensity, and noise levels (Supplementary Fig. 3B). Still, ADeS correctly predicted the location and timing of cells undergoing apoptosis (Fig. 6H, Supplementary Movie 2), indicating its robustness to increasingly populated fields of view (Supplementary Fig. 3C). In addition, we successfully applied the pipeline to neutrophils imaged in the lymph node (Fig. 6D) and eosinophils in the spleen (Fig. 6E). By comparing ADeS predictions with the annotated ground truths, we found that our pipeline detected apoptotic events with a TPR of 81.3% and an FPR of 3.65% (Fig. 6F). The detections, provided in the form of bounding boxes and trajectories, indicated the coordinates and duration of the events. Hence, to measure how close they were to the annotated trajectories, we employed the tracking accuracy metric (TRA), a compound measure that evaluates the similarities between predicted and ground truth trajectories. The average TRA was above 0.9, indicating the high fidelity of the trajectories predicted by ADeS (Fig. 6G).

Next, we compared ADeS to human annotation performed by three operators on five testing movies. As a result, ADeS displayed an upward trend of the TPR and a downward trend of the FPR. However, we found

no significant difference in the TPR and FPR (Fig. 6H). Regardless, ADeS performances appeared to be distributed across two distinct groups: a large group with an average sensitivity of 100% and a smaller group with an average sensitivity of 53% (Fig. 6H). To understand this discrepancy, we applied hierarchical clustering to the testing videos according to their imaging properties and biological content (Fig. 6I), thus generating two major dendrograms. The first dendrogram mostly contained videos with reduced sensitivity (yellow) and was defined by a high cell number, high noise levels, short cell distance, and a saturated and fluctuating image signal. Most notably, the cell number played a crucial role in overall performance, as reflected in the fact that an increment of this parameter resulted in a pronounced decrease in the TPR and a moderate increase in the FPR (Fig. 6J). Incidentally, the positive predictive value (PPV) was significantly lower in videos with poor SNR and, although not statistically significant, the PPV was lower when the signal standard deviation was higher (Fig. 6K). Following these observations, we hypothesized that the quality of a movie predicts ADeS performance. Hence, we combined the parameters highlighted by the clustering analysis (Fig. 6I) into a single score ranging from zero to one (one indicating the highest and ideal score) and, in doing so, found there to be a weak correlation between the video quality and the sensitivity of ADeS (Fig. 6L). However, this trend was evident only when we considered videos with suboptimal sensitivity; indeed, in these cases, we found a strong correlation (0.72), confirming that the video quality partially explains the observed performances (Fig. 6M).

Finally, we evaluated how the biological variability *in vivo* could affect the readout of ADeS, defining nine distinct biological categories, including apoptotic cells, healthy cells, and background elements. For all biological categories, the classification accuracy was above 80%, except for overlapping cells and cells with high membrane plasticity (Supplementary Fig. 3D).

Comparison with the state-of-the-art. To compare the performance of ADeS with other state-of-the-art algorithms for cell death quantification, we conducted a comprehensive literature review. For each study, we reported the attained classification accuracy, the experimental setup, the architecture of the classifier, the capability of detecting cell death events in movies, and the number of cell deaths in the training set (Table 2). Initial results indicate that ADeS achieved the highest classification accuracy, but a direct comparison in terms of accuracy is not meaningful due to the differences in datasets, including distinct cell types, different types of cell death, and varying dataset sizes. For a more appropriate benchmark, we refer to Table 1, which shows that our classifier outperformed the baseline re-implementations of the main classifiers used in other studies.

From Table 2, we observe that ADeS is the only algorithm for cell death quantification that has been applied *in vivo*. Additionally, only ADeS and the study by Vicar and colleagues[295] effectively detected apoptotic cells in fully uncropped microscopy movies, which is a significant achievement given the computational challenge associated with the task. However, Vicary and colleagues relied on the temporal analysis of cell trajectories, while ADeS used vision-based methods to directly analyze consecutive frames of a movie. As a result, ADeS offers a comprehensive and pioneering pipeline for effectively applying vision-based classifiers to detect cell death in imaging time-lapses.

Applications for toxicity assay *in vitro*. A common application of cell death staining is the evaluation of the toxicity associated with different compounds[277,297] or the efficacy of an apoptotic-inducing treatment. Here, we show that ADeS has analogous purposes and can effectively quantify the toxicity of different compounds *in vitro*. For this application, we grew epithelial cells *in vitro*, treating them with PBS and three increasing concentrations of doxorubicin, a chemotherapeutic drug that elicits apoptosis in the epithelium[298]. Epithelial cells were seeded with the same density of cells per well, and all four conditions had the same confluence before the treatment. However, at 24 h. post-acquisition, the number of survivor cells was inversely proportional to the doxorubicin concentration (Fig. 7A). We confirmed this trend using ADeS (Supplementary Movies 3–6), which measured the lowest mortality after 24 h. in PBS (62 cells), followed by doxorubicin concentrations of 1.25 μM (95 cells), 2.50 μM (167 cells), and 5.00 μM (289 cells). Moreover,

Table 2. Comparison of cell death identification studies. *Table reporting all studies on cell death classification based on machine learning. For each study, we included the reported classification accuracy, the experimental conditions of the studies, the target input of the classifier, and the capability of performing detection on static frames or microscopy time-lapses. Met conditions are indicated with a green check. Moreover, for each study we reported the architecture of the classifier and the number of apoptotic cells in the training set. N.A. stands for not available and indicates that the information is not reported in the study.*

Study	Input of the classifier	Reported classification accuracy	*In vitro*	*In vivo*	Detection In frame	Detection in movies	Classifier architecture	N cell death
Our	Frame sequence	98.27 %	✓	✓	✓	✓	Conv-Transformer	13'120
[266]	Frame	93 %	✓	✗	✗	✗	Logistic regression	N.A.
[160]	Frame	87 %	✓	✗	✗	✗	VGG-19	19'339
[292]	Frame sequence	93 %	✓	✗	✗	✗	ResNet101-LSTM	3'172
[291]	Frame	96.58 %	✓	✗	✗	✗	ResNet50	11'036
[244]	Frame sequence	93.8 %	✓	✗	✗	✗	CapsNet-LSTM	41'000
[285]	Frame	93.2 %	✓	✗	✗	✗	CAE-RandomForest	27'224
[295]	Frame sequence	N.A.	✓	✗	✓	✓	biLSTM	1'745
[296]	Frame	N.A.	✓	✗	✓	✗	R-CNN	255'215

ADeS predicted distinct pharmacodynamics (Fig. 7B), which can define the drug concentration and experimental duration required to reach a specific effect in the apoptotic count. To this end, each time point in Figure 7B also defines a dose-response relationship. Here we provide two dose-responses curves at 5 h. and 24 h. post-treatment, showing different pharmacodynamics (EC50 5h = 2.35, Hill slope 5h = 3.81, EC50 24h = 4.47, Hill slope 24h = 1.93, Fig. 7C–D). Notably, the fit can project the dose-responses for higher drug concentrations, predicting the maximum effect size at a given time. For instance, at 24 h. post treatment, a 10 μM titration attains 86% of the maximum effect (456 apoptotic cells), whereas a further increase in the concentration of the drug leads only to a moderate increase of the toxicity (Fig. 7E). We argue that this approach helps to maximize the effect of a drug on a designated target, while minimizing collateral damage done to non-target cells. For instance, in chemotherapies employing doxorubicin, apoptosis of epithelial cells is an undesired effect. Therefore, researchers can select a titration of the drug and a duration of the treatment that does not affect the epithelium yet still positively affects the tumor. Finally, we also demonstrated the reproducibility of the toxicity assay by targeting another cell type (T-cells) treated with a different apoptotic inducer (staurosporine, Supplementary Fig. 4).

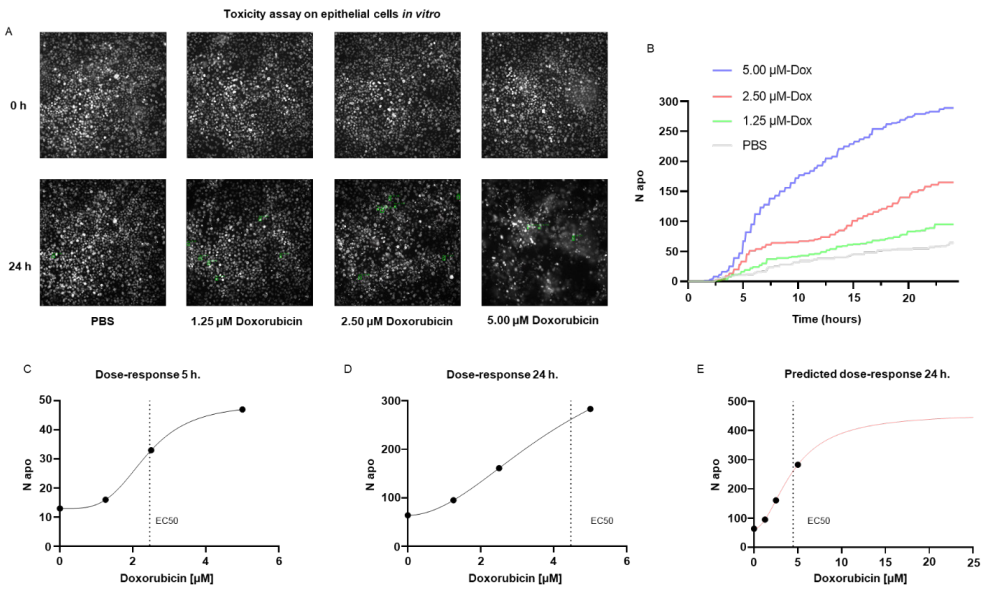

Figure 7. Applications for toxicity assay* in vitro.** ***A*. Representative snapshots depicting epithelial cells* in vitro *at 0 and 24 hours after the addition of PBS and three increasing doses of doxorubicin, a chemotherapeutic drug and apoptotic inducer* ***B****. Plot showing the number of apoptotic cells detected by ADeS over time for each experimental condition.* ***C-D****. Dose-response curves generated from the drug concentrations and the respective apoptotic counts at 5 h. and 24 h.post-treatment. Vertical dashed lines indicates the EC50 concentration.* ***E.*** *Dose-response curve projected from the fit obtained in (****D****). The predicted curve allows to estimate the response at higher drug concentrations than the tested ones.*

Measurement of tissue dynamics *in vivo*. To test the application of ADeS in an *in vivo* setting, we applied it to study the response of bystander cells following apoptotic events in the lymph nodes of mice treated with an influenza vaccine. We computed the spatial and temporal coordinates of a neutrophil undergoing apoptosis (Fig. 8A), which, combined with the tracks of neighboring cells, allowed us to characterize cellular response patterns following the apoptotic event. Among other parameters, we observed a sharp decrease in the distance between the neighboring cells and the apoptotic centroid (Fig. 8B) in addition to a pronounced increase in the instantaneous speed of the cells (Fig. 8C).

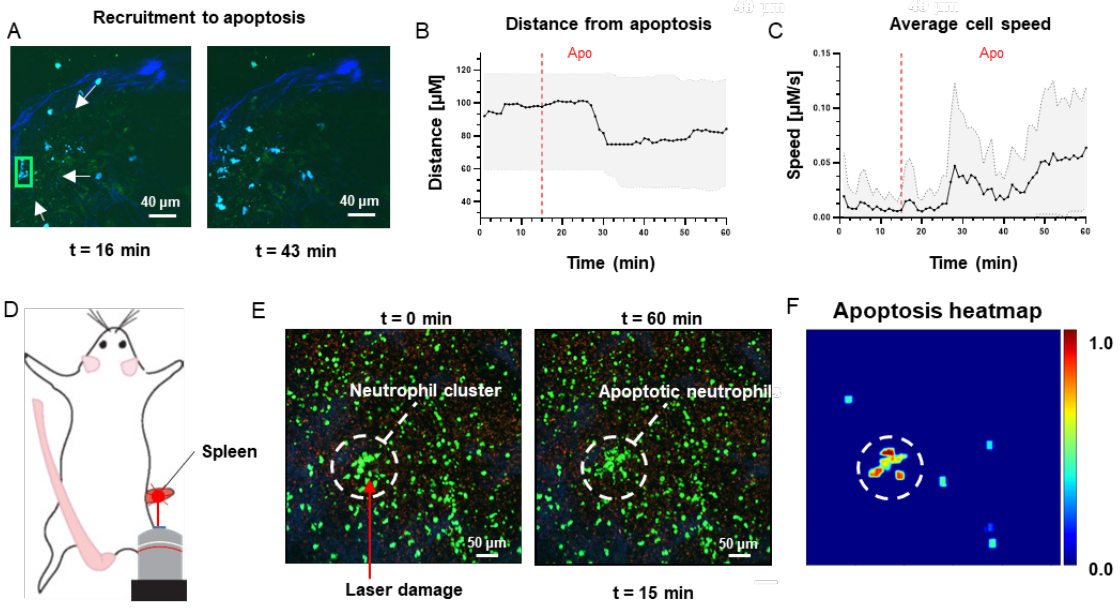

Figure 8. Measurement of tissue dynamics* in vivo.** ***A*. Intravital 2-photon micrographs showing ADeS detection of an apoptotic neutrophil (Blue, left) and the subsequent recruitment of neighboring cells (right) in the popliteal LN at 19 h. following influenza vaccination.* ***B****. Plot showing the distance of recruited neutrophils with respect to the apoptotic coordinates over time (n = 22)* ***C.*** *Plot showing the instantaneous speed of recruited neutrophils over time (n = 22). The dashed vertical lines indicate the instant in which the apoptotic event occurs.* ***D****. Schematic drawing showing the intravital surgical set up of a murine spleen after inducing a local laser ablation.* ***E****. Intravital 2-photon micrographs showing the recruitment of GFP-expressing neutrophils (Green) and the formation of a neutrophil cluster (red arrows) at 60 min after photo burning induction.* ***F****. Application of ADeS to the generation of a spatiotemporal heatmap indicating the probability of encountering apoptotic events in the region affected by the laser damage. The dashed circle indicates a hot spot of apoptotic events.*

Successively, we evaluated the detection of apoptotic cells following laser ablation in the spleen of an anesthetized mouse (Fig. 8D). Previous research has employed this method to study immune cell responses to tissue damage[299]. The insult caused prompt recruitment of neutrophils, leading to the formation of a local swarm (Fig. 8E, left). After that, the neutrophils within the swarm underwent apoptotic body formation in a coordinated manner (Fig. 8E, right). To quantify this event, we processed the generated time-lapse with ADeS, resulting in a probability map of apoptotic events throughout the acquisition (x, y, t, p; Fig. 8F). Accordingly, the location with the highest probability corresponded to the area damaged by the laser, while the visual representation of the probability map enabled us to infer the morphology and location of the swarm. This result demonstrates the potential application of ADeS in digital pathology, showing how the distribution of apoptotic events throughout the tissue can identify areas enriched by cell death events.

Discussion

Automated bio-image analysis obviates the need for manual annotation and avoids bias introduced by the researcher. In this regard, recent studies showed the promising usage of DL to classify static images[160,285,296] or time-lapses containing single apoptotic cells[244]. However, these approaches are unsuitable for microscopy time-lapses because they do not address two fundamental questions: the location, over the whole field of view, at which an event occurs, and its duration. These questions define a detection task[300] in space and time, which has a computational cost that can rapidly grow with the size and length of a movie. Moreover, live-cell imaging data present specific

challenges which further increase the difficulty of detection routines, including densely packed fields of view, autofluorescence, and imaging artifacts[25].

Consequently, computational tools to effectively detect apoptotic events in live-cell imaging remained unavailable. Thus, we created an apoptosis detection pipeline that could address the abovementioned challenges *in vitro* and *in vivo*. In this regard, ADeS represents a crucial bridge between AR and bioimaging analysis, being the first apoptosis detection routine with demonstrated applicability to full microcopy time-lapses. In addition, we presented two comprehensive and curated datasets encompassing multiple cell types, fluorescent labels, and imaging techniques to encourage reproducibility and foster the development of apoptosis detection routines.

In human activity recognition benchmark, 3DCNNs[68], two-streams networks[73], and RNNs[267] have proved to score the highest accuracy on most kinetic datasets[74]. However, in most studies for the classification of apoptosis, authors unanimously employed RNNs such as Conv-LSTMs. This choice, although produced valid results, is not necessarily optimal for the task. In this regard, Ullah and colleagues highlighted that the performances of different DL architectures are highly dependent on the AR dataset[74]. Therefore, selecting the most suitable one is only possible after an extensive benchmark. In our comparison, we demonstrated for the first time that attention-based networks are suitable for the classification and detection of apoptotic events. Accordingly, our Conv-Transformer network outperformed DL architectures previously employed in other studies, including 3DCNNs and RNNs. This result established a landmark in the application of attention-based networks in AR for live-cell imaging. Moreover, it suggests the possible benefits of employing transformers for the classification of different biological activities other than cell death.

Similar to most diagnostic tools, ADeS displayed a tradeoff between sensitivity (TPR) and specificity (1 - FPR), which is a known challenge in binary classification[263]. This tradeoff can be attributed to the fact that apoptosis is rare in normal physiological conditions, leading to a high degree of class imbalance during training. As a result, the choice of the training set had a significant impact on the performances of ADeS. For instance, we highlighted the importance of a training and validation set that included challenges related to real live-cell imag-

ing acquisitions, such as overlapping cells and low signal-to-noise samples. Including these challenges instances enabled ADeS to attain low misclassification rate and robust real-life performances. Nonetheless, we observed residual misclassifications due to shared similarities between healthy and apoptotic cells. For instance, *in vitro* mitotic divisions could mislead the detection of apoptotic nuclei, while *in vivo*, overlapping cells were sometimes mistaken for apoptotic cells. Therefore, to effectively address these challenges, it is crucial to implement strategies to increase the representativeness of the dataset, such as integrating multiple data sources and data augmentation techniques.

From a biological perspective, ADeS has multiple applications in fundamental and clinical research. Among other advantages, it can provide insights into pivotal cell death mechanisms, monitor the therapies used to modulate apoptosis in various diseases and characterize the toxicity of different compounds. In this regard, ADeS readout is analogous to standard fluorescent probes for apoptosis detection, with the advantage that it can be applied directly to nuclear or cytoplasmic staining without the need of additional fluorescent reporters. Therefore, ADeS avoids using any additional acquisition channel, which can be used for multiplexing purposes. Moreover, common probes[275–279] flag early apoptosis stages, activated up to several minutes before the point at which morphological changes in the cell[282,301]; meanwhile, these cells can reverse the apoptotic process [302–304]. By contrast, ADeS indicates the exact instant of cell disruption, thus adding specificity to the spatial-temporal dimension. For these reasons, we suggest that ADeS can complement the information provided by classic apoptotic biomarkers, which will prove advantageous in experimental assays where the temporal resolution delivers more information than the sole apoptotic count. Moreover, ADeS can be usefully applied in processing high-throughput live-cell imaging, minimizing annotation time and research bias.

Finally, in tissue dynamics the spatial-temporal activity of cells can reveal connections between signaling pathways and the fate decision of individual cells, such as mitosis or apoptosis[305]. These intricate systems can display complex dynamics, which can be better comprehended incorporating spatial and temporal coordinates provided by ADeS. Consequently, we propose that integrating these spatial-temporal characteristics with experimental observations could

lay the groundwork for understanding the mechanism governing complex signaling pathways. Furthermore, we contend that this information has the potential to facilitate the development of predictive models, establishing a correlation between specific cell death dynamics and the underlying stimuli. This, in turn, could serve as the foundation for innovative diagnostic tools capable of inferring the cause of cell death.

In conclusion, ADeS constitutes a novel solution for apoptosis detection that combines state-of-the-art microscopy and DL. Its successful implementation represents a step towards the general application of AR methods to live-cell imaging. By bridging these two distinct fields, ADeS leverages successfully the benefits of automated routines. Further work could expand the proposed pipeline to encompass diverse cell populations, various types of cell death, and potentially broader cellular activities.

Acknowledgements

We would like to thank Dr. Coral Garcia (IQS, Barcelona, Spain) for the support in generating graphical content. Moreover, we would like to acknowledge Gabriele Abbate (IDSIA, Lugano, Switzerland) for his help during an early implementation of the DL classifier.

Funding

Suisse National Science Foundation grant 176124 (AP, DU, MP, SG)

Swiss Cancer League grant KLS-4867-08-2019, Suisse National Science Foundation grant Div3 310030_185376 and IZKSZ3_62195, Uniscientia Foundation (PG, LH, OP)

SystemsX.ch grant iPhD2013124 (DU, RK)

Novartis Foundation for medical-biological Research, The Helmut Horten Foundation, SwissCancer League grant KFS-4223-08-2017-R (PA, MT)

Canadian Institute for Health Research (CIHR) Project grants PJT-155951 (RZ, PL, TM)

NCCR Robotics program of the Swiss National Science Foundation (AG, LG)

Biolink grant 189699 (DU, PC)

Authors contributions

Conceptualization: SG, DU, AP

Methodology: AP, DU

Experiments: PG, PA, MP, RZ, PL

Data annotation: PG, AP, LH, DU, PC

Data analysis and visualization: AP, LH, AG

Figures: AP, PG, LH

Testing and validation: AP, LH, AG

Supervision: SG, DU, RK, LG, OP, TM, MT

Writing—original draft: AP, PC, DU, PG

Writing—review & editing: AP, SG

Competing interests

Authors declare that they have no competing interest.

Supplementary figures

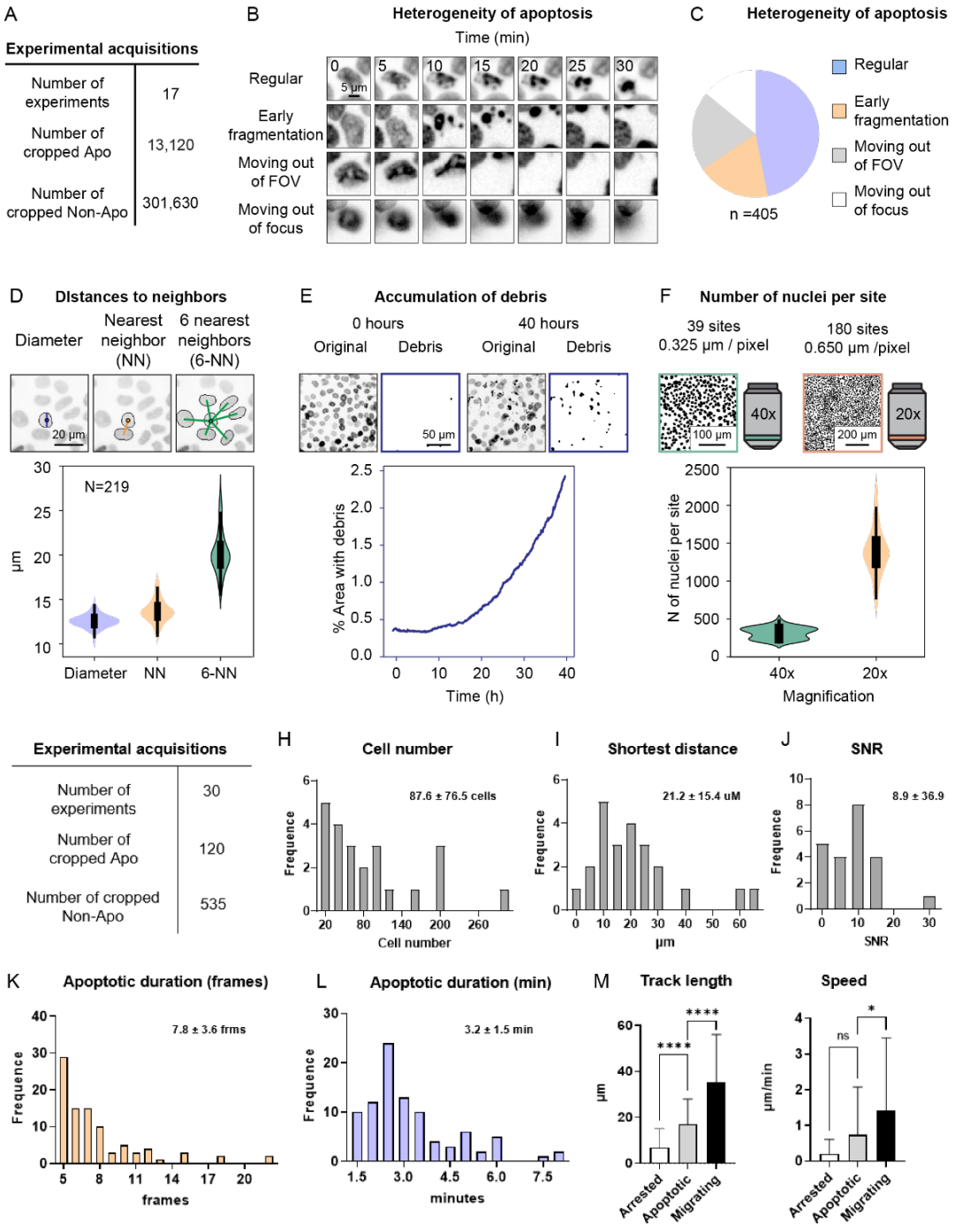

Supplementary figure 1. Generation of* in vitro *and* in vivo *microscopy data. A. *Table reporting the number of entries of the dataset* in vitro. ***B.*** *Time-lapses showing the heterogeneity of the morphological appearance of apoptotic events.* ***C.*** *Pie chart representing the frequency of the classes of morphological appearance in the entire dataset.* ***D.*** *The density of the epithelium is quantified by comparing the diameter of the nuclei versus the distance to the nearest neighbor (NN), and to the 6 nearest neighbors (6-NN). Violin plot showing the mean of all cells of the first frame from (n = 219 FOVs).* ***E.*** *Data from a single FOV shows the accumulation of apoptotic debris over time, making the identification of newer apoptotic events difficult. In this experiment, MCF10A cells were treated with 1.25 μM Doxorubicin for 40 hours. The image crops show the original nuclear channel and the binary images with identification of debris with a machine learning approach (Ilastik) and thresholding. The Chart represents the area occupied by debris over time.* ***F.*** *Two imaging modalities were used (40x, 20x), representative nuclear masks are shown in the left images. Violin plots show the mean number of nuclei in the first frame per FOV (40x: n = 39, 20x: n = 180).* ***G.*** *Table reporting the number of entries of the dataset* in vivo. *Neu and Eos stand for neutrophils and eosinophils, respectively.* ***H-J.*** *Quantification of cell numbers, shortest distance, and signal to noise ratio (SNR) in the generated IV-2PM movies (n = 30).* ***K-L.*** *Histograms representing the duration of the apoptotic events expressed in frames (**K**) and minutes (**L**).* ***M.*** *Quantification of the track length (**left**) and cell speed (**right**) of apoptotic cells before disruption, compared to arrested and migrating cells. Statistical comparison was performed with non-parametric Kruskal-Wallis test. Columns and error bars represent the mean and standard deviation respectively. Significance is expressed as: p ≤ 0.05 (*), p ≤ 0.01 (**), p ≤ 0.001 (***), p ≤ 0.0001 (****).*

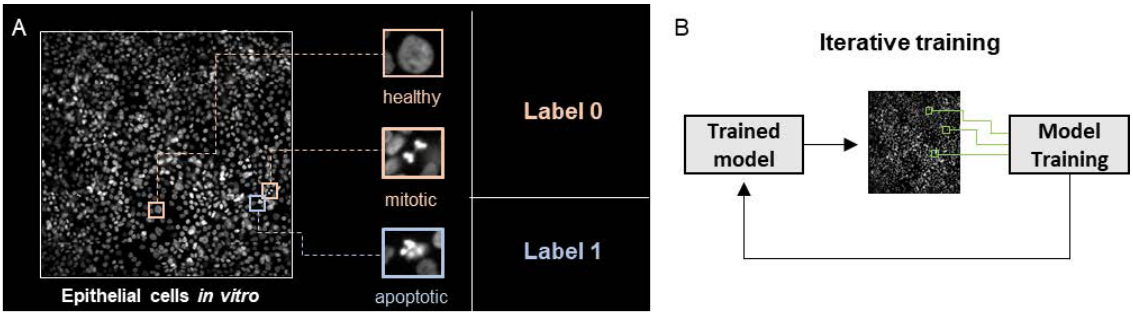

Supplementary figure 2. Training and performance* in vitro*. A. *The training set describes a binary classification task in which the class label 1 contains the nuclei of epithelial cells undergoing apoptosis, while the class label 0 includes healthy and mitotic nuclei.* ***B.*** *The class label 0 has been further expanded by iteratively including false positives generated by a trained network and applied to movies which contained no apoptotic events*

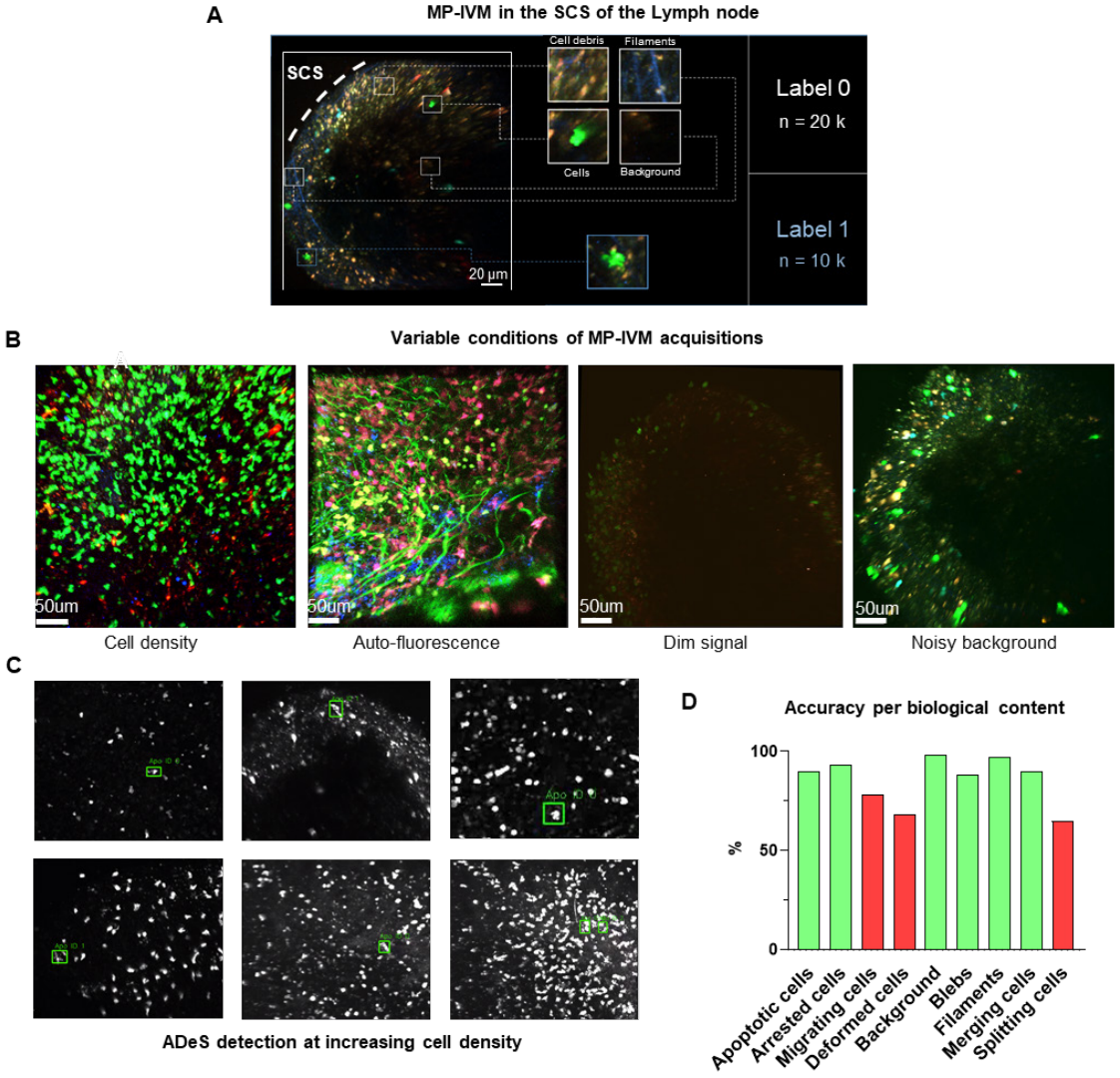

Supplementary figure 3. Training and deployment* in vivo*. A. *The designed training set describes a binary classification task in which the class label 1 contains only apoptotic cells and the class label 0 encompasses all non-apoptotic content, including healthy cells, filaments, background, and cell debris.* ***B.*** *Representative snapshots of variable and potentially challenging conditions in multi-photon intravital microscopy (MP-IVM), including high cell density, auto-fluorescence, dim signal, and noisy background.* ***C.*** *Representative micrographs depicting the detection of apoptotic cells at increasing cell densities.* ***D.*** *Graph showing the accuracy of ADeS in predicting the class label (0 or 1) of sequences containing different biological content. Red bars represent an accuracy below 80%.*

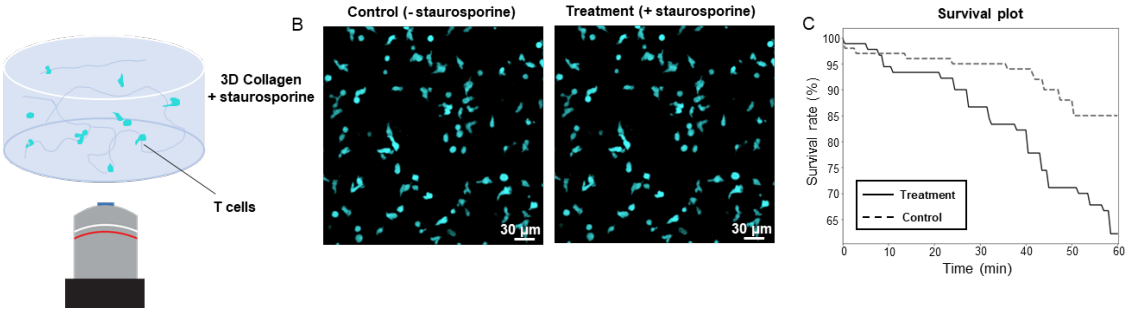

Supplementary figure 4. Applications for toxicity assay* in vitro*. A*. Schematic drawing representing in vitro-cultured T cells treated with staurosporine. **B**. Confocal micrograph snapshot showing T cells at 60 min after treatment with staurosporine (**left**) compared to the untreated control group (**right**). **C**. Survival assay plot of control (dotted lined) and treated samples (solid line) during the first 60 min post treatment with staurosporine.*

DISCUSSION

1. Establishing the basis of cellular activity recognition

1.1. Cell activity recognition requires distinct morpho-dynamics

The application of CAR techniques presupposes that cellular activities display well-defined and unique morpho-dynamics. However, at present, there is no consensus on the motility and morphological phenotypes of different cells engaged in distinct activities. For this reason, in our review[26] partially cited in the introduction, we created an atlas of known cellular activities grouped by morphological phenotype and function. As a pioneer study in this direction, our review examined and collected only those activities that exhibited a phenotype extensively supported by the literature. Specifically, we grouped distinct biological processes by function, appearance, and the available metrics used for quantification. The inclusion of the latter metrics was meant to highlight the possibilities and limitations of existing quantification methods, suggesting new directions to improve and automatize the identification of biological activities. In this regard, we assessed that existing analyses are limited to simple heuristics applied to motility parameters, such as cell speed and directionality. For this reason, we argued that DL methods have the potential to improve the quality and robustness of analytical routines, while creating a bridge between the fields of image analysis, cell biology and activity recognition. The proposed atlas of cellular activities represents thus a starting point and a playground to achieve this aim.

In this regard, we treated cells as active agents performing activities with a measurable effect on the environment, thus neglecting all the homeostatic activities occurring within the cell. This approach, although highly reductive, had a clear advantage for track-based and vision-based models: treating cells as active agents makes them comparable to humans performing distinct activities, for which human activity recognition (HAR) already proved successful.

1.2. Track-based cellular activity recognition and limitations

In the first manuscript presented in this thesis[27], we investigated whether the set of biological activities previously postulated could find application in the context of a biological characterization. Our approach was simple yet effective. The entire inflammatory response post-vac-

cine was abstracted and reduced to a sum of individual immunological activities that we detected by means of motility parameters and gating strategies. Therefore, our study carried two main contributions. The first one was the proof that discrete cellular activities are detectable by combining motility parameters and gating strategies that define the range of motility for each behavior. The second and most important contribution was observing that the proportion of cellular activities captured different phases of inflammation in agreement with experimental observations.

2. CAR for cell death identification

From a biological perspective, automatic apoptosis detection offers multiple advantages, including the label-free identification of events without the need for fluorescent staining. This approach would reduce the need for experimental manipulation, eliminate researcher bias, and facilitate multiplexing studies. Additionally, given that apoptosis occurs within various physiological and pathological conditions, understanding the precise location and duration of individual apoptotic events could elucidate the mechanisms behind several diseases involving apoptosis. Consequently, automated detection could enhance the comprehension of therapeutics that modulate apoptosis in target cells, such as those used in tumor treatments.

Due to these reasons, one of the main goals of this thesis was to establish a framework for the application of video-based CAR to automatically detect apoptosis in live-cell imaging. As mentioned earlier, the first prerequisite for achieving this task in AR is the existence of morphological hallmarks associated with the target activity. In our case, this requirement had already been met, given that apoptosis is one of the most extensively characterized forms of cell death at the morphological level. Hence, there was no need to establish a consensus morphology for the apoptotic process during our review of cellular activities. In turn, this allowed me to immediately address the challenge of creating a pipeline for apoptosis detection.

To this end, two components were still missing: a dataset with high-quality annotations, and a robust predictive model. To address the first requirement, in the third manuscript I presented a dataset of apoptotic leukocytes acquired *in vivo*. The creation of this dataset presented the typical challenges encountered when performing man-

ual labelling for supervised learning tasks. For instance, I highlighted that although the morphological cues of apoptosis were defined, they could extensively vary from event to event, making the annotation process difficult. To address this aspect, I defined a strict annotation criteria and I successively merged the annotations of three independent operators into a consensus ground truth. This precaution ensured the quality of the dataset by limiting the bias associated with a single operator.

Regarding the selection of a predictive model, I had to identify first the framework that was best suited for apoptosis detection in live-cell imaging. Previous studies demonstrated that DL networks could successfully classify cell death events in static images[295] and time-lapses[244] with high accuracy. Given these premises, I decided to use supervised DL to tackle the detection of apoptosis. However, this particular domain was relatively unexplored, and several questions were yet unaddressed. Among these, the question of how different DL architectures would compare in the classification of apoptotic events was not clear, as most authors employed the same networks in their studies. However, performances of DL architectures can be task and dataset dependent, for which reason it is pivotal to benchmark multiple networks. Considering this aspect, the first scientific contribution of my third manuscript was to provide an extensive benchmark of various DL architectures. In turn, this showed that a DL architecture based on attention mechanisms attained the highest task-specific classification accuracy.

After selecting the DL model, the second contribution of my manuscript was the creation of a pipeline for the effective detection of apoptosis in live-cell imaging. This achievement was realized through ADeS, a modular pipeline compatible with different DL classifiers. Despite its simple implementation, ADeS represents the first use of DL classifiers for the detection of apoptosis in real-world microscopy movies. Consequently, this result is a significant proof-of-concept for implementing CAR in microscopy, demonstrating that competitive predictive accuracy can be attained even in light of imaging-related challenges. In terms of competitive accuracy, our goal was to achieve a predictive accuracy of at least 80%. Once ADeS surpassed this arbitrary threshold, I halted its algorithmic enhancement and I deployed it to showcase real-world applications across various experimental scenarios. However, it is important to note that there is substantial potential for technical

improvements in apoptosis detection, both in the near and distant future.

2.1 Technical implementation and future design of apoptosis detection in live-cell imaging

One of the primary challenges I encountered during the implementation of ADeS was the complexity of the imaging data. Microscopy time-lapses can exhibit large spatial depth, incorporate multiple acquisition channels, and span several hours in duration. As a result, conducting detection on this data incurs a significantly higher computational cost compared to the classification or detection of 2D images, for which most CV routines are designed. Consequently, the initial step I took to enable apoptosis detection in live-cell imaging involved mitigating the computational cost by reducing and standardizing the input data. To achieve this goal, I devised a pipeline tailored for 2D single-channel time-lapses, rather than 3D volumes. This approach not only helped in limiting computational demands, but also proved effective in standardizing the input data by removing variations stemming from different acquisition depth sizes.

Even so, the computational cost of processing 2D movies can be significant, especially considering their potential for large size and extended acquisitions. The latter aspect posed a constraint on the depth of our DL classifier, which I had to confine to a fixed number of representative frames to prevent abrupt growth in model parameters. This tradeoff affected the design of our detection pipeline, which ultimately encompassed a region proposal block defining cell crops for classification, a sliding-window deployment of the classifier over time, and a tracking module assigning a unique identifier to each apoptotic event. As a result, this pipeline enabled effective apoptosis detection utilizing a simple and modular framework.

However, this implementation included some of the pitfalls associated with supervised DL classifiers. Namely, a classifier that evaluates only one cell at a time might require a larger training set compared to a DL architecture that comprehends the entire field of view along with its contextual information. In our case, this choice led to a trial-and-error process in which I iteratively adjusted the training set until the model achieved competitive performance. Although this procedure was successful, it was arguably not time-efficient. Therefore, future methods for apoptosis detection should ensure a more systematic training procedure that does not require

extensive tuning of the training set to converge toward an optimal solution.

To address this aspect and overcome the aforementioned limitations, I suggest the utilization of an end-to-end DL architecture rather than a modular pipeline. One characteristic of such an architecture should be the ability to process entire fields of view sequentially, replacing the region proposal module and enabling training with fewer samples. Additionally, predictions should encompass the class of the cells, regression boxes, and a unique identifier. This format would eliminate the need for region proposal and tracking modules, as the predictive network would infer the coordinates and identifiers of the apoptotic cells. This approach offers the advantage of optimizing all routines that previously relied on heuristics according to a common cost function. This cost function would be based on metrics such as the distance from the ground truth apoptotic trajectories and bounding boxes. As a result, with a representative dataset, the final network is expected to generalize better across various real-world scenarios and require less parameter tuning.

2.2. Comparison of automated cell death detection with fluorescent reporters

In this study, I argued that utilizing CV for the detection of apoptosis offers advantages over traditional staining techniques that rely on fluorescent markers[276,277,306]. Specifically, while fluorescent staining measures the cumulative apoptosis occurrence over time, it may lack the precision to pinpoint the exact moment when a cell undergoes apoptosis. In this regard, automated detection based on morphological features has the potential to predict the temporal and spatial coordinates of apoptosis. Furthermore, employing CV for apoptosis detection facilitates the incorporation of an additional imaging channel to enable multiplexing, while also minimizing experimental costs and manipulations.

Despite these theoretical advantages, vision-based methods reliant on human supervision may be susceptible to errors, for examples due to morphological similarities shared between healthy and apoptotic cells. Therefore, at present fluorescent biomarkers remain the most reliable approach to identify cell death. To address this concern and improve the accuracy of vision-based techniques, it is imperative to ensure that

the training datasets exclusively comprises instances of apoptosis. This could can be achieved by selecting data according to apoptotic biomarkers or adhering to strict and specific morphological criteria.

In the second and third manuscript, we adopted rigorous morphological criteria generate *in vitro* and *in vivo* datasets that contained exclusively apoptotic cells. This precaution increased the likelihood that the model learned only features specific to apoptotic cells. Nonetheless, it is unclear to which degree ADeS could misclassify other forms of cell death for apoptosis and vice-versa. Consequently, a limitation of our investigation is the lack of specificity assessment of our model. Future studies in this direction could include a broader array of cell deaths, along with a multi-class labeling model that generates outputs for each distinct type of cell death. This framework would enable a quantitative evaluation of the specificity of the model in predicting each type of cell death.

2.3. Experimental relevance of CAR-based apoptosis detection

In this work, my aim was to establish the groundwork for CAR in apoptosis detection. Concurrently, I aimed to showcase the immediate potential of this approach in both fundamental and clinical research. Notably, the disruption of apoptosis regulation is involved in a range of conditions spanning from autoimmune diseases to different cancers[246,256]. Consequently, the ability to detect apoptosis can have crucial clinical implications for the diagnosis and treatment of several diseases. In cancer, for instance, abnormally low apoptotic rates contribute to the uncontrolled proliferation of tumor cells. Thus, quantifying apoptosis within tumors not only provides insights into fundamental disease mechanisms, but also paves the way for targeted therapies capable of inducing apoptosis in cancerous cells. Particularly, I believe that automatic apoptosis detection holds great potential in assessing the efficacy of novel therapies against tumors. To demonstrate this perspective, I applied ADeS to detect apoptosis in lymphoma B cells induced by chimeric antigen receptor T cells[164] (data kindly provided by Professor Philippe Bousso from the Pasteur Institute, Fig. 1). Although the results were preliminary and unpublished, it is compelling to note that our method was capable of predicting the apoptosis of lymphoma cells coinciding with the activation of the caspase reporter (shown in blue). Therefore, future endeavors in this direc-

tion could validate similar methods with a direct comparison with fluorescent probes for apoptosis.

Apoptosis plays also a major role within the immune system[255]. For instance, one way in which dysregulated apoptosis can

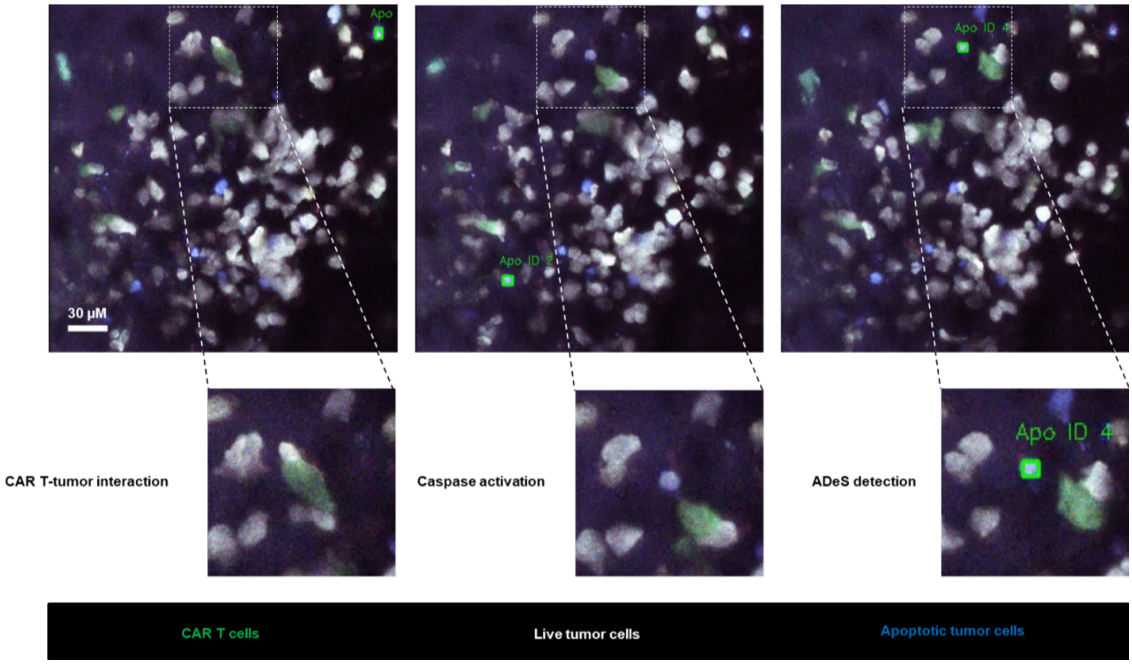

Figure 1. Detection of CAR T induced apoptosis on lymphoma cells*. Intravital 2-photon micrographs depicting tumor B cells in the bone marrow (white), CAR T cells (green) and apoptotic tumor cells (blue). Upon interaction with CART cells, live tumor cells undergo caspase activation, reported by fret, and they turn blue. ADeS can detect the instant in which cells become apoptotic. Movies kindly provided by Prof. Philippe Bousso from Pasteur Institute.*

contribute to autoimmune diseases is by leading to the accumulation of self-antigens that are not cleared by the immune system. When self-antigens accumulate, the immune system may mistakenly recognize them as foreign and initiate an immune response against them, leading to tissue damage and inflammation. Dysregulated apoptosis can also lead to the accumulation of immune cells that are not properly activated or regulated, which can equally contribute to autoimmune diseases. The

interplay between apoptosis and immune diseases is therefore complex and partially unknown, hence the need for tools that enables quantification of apoptosis in targeted cell populations.

Finally, the detection of apoptosis can prove pivotal in understanding cellular responses to diverse external stimuli. For instance, the identification of apoptosis in healthy cells can highlight the potential side effects of drugs and aid in the recognition of potential toxic substances. In this thesis, I showcased that automated apoptosis detection can be particularly effective in quantifying the toxicity linked to various drugs *in vitro*, revealing promising avenues for drug-response characterization and survival assays.

3. CAR in biology: from individual activities to process understanding

3.1. Application to other cellular activities

In our work, apoptosis has served as the prototypical activity through which we demonstrated the application of CAR principles. However, a multitude of other cellular processes could benefit from CAR. A natural extension of our work would target additional types of regulated cell death, such as autophagy, ferroptosis, necroptosis, and pyroptosis, among others[246,247,272]. Distinguishing between different types of cell death based on morphological cues would be highly relevant for studying individual processes and for comprehending cell death from a holistic perspective. For instance, a tool capable of predicting various types of cell death could enhance our understanding of the fate-decision process of cells in response to diverse environmental triggers and diseases. Such a tool would also eliminate the need for experimental manipulation required to label the signaling pathways specific to each type of cell death.

Other than apoptosis, mitosis also presents distinct and characteristic morphological hallmarks. Furthermore, mitosis plays a critical role in tissue homeostasis; diminished mitotic activity might serve as a senescence marker, while elevated mitotic rates can indicate the pace of tumor growth. Consequently, a video-based mitotic detector could serve multiple purposes, such as monitoring tissue health in various scenarios.

Finally, from an immunological perspective, several other activities are candidates

for automatic detection. Among these, the immunological synapse[118] presents a distinct and characteristic morphology that can act as a fingerprint for its identification in vision-based methods. One of the main functions of immunological synapses is to ensure the integration of adaptive and innate signals that modulate the immune response. Additionally, immunological synapses initiate effector programs upon antigen recognition, including cell killing. For this reason, having access to the spatial-temporal coordinates of immunological synapses can provide an unprecedented understanding of the regulation of the immune system.

3.2 Understanding biological processes

Cell behavior is one of the last manifestations of effector functions. One compelling advantage of CAR applied to microscopy is the generation of several biological readouts in terms of cell behavior. Following this approach, the monitoring of a large number of cells performing different activities will generate a behavioral landscape in agreement with internal and external stimuli.

In turn, the information retrieved from this large ensemble of behaviors will enrich the current phenotypical characterization of cell populations, unveiling behavioral associations with underlying experimental conditions or . As such, behavioral landscapes could represent a novel entry in omics science. Following the principles of genomics or proteomics, it would be possible to find relationships between cell actions, their underlying gene regulation and effector proteins. Recently, this hypothesis has been partially supported by Palomino and colleagues[238], in which the authors characterized and stratified the behavior of immune cells to highlight key regulatory genes. This result, although a first take on the approach, represents a promising venture for the inclusion of cell behavior in the domain of “big data”.

Concretely, there is more than one way in which behavioral landscapes could provide biological insights. Traditional data mining approaches could evaluate statistical association between enriched cell behaviors and experimental conditions such as diseases, gene expression and drug delivery. Conversely, we propose that knowing the occurrence of individual actions is useful to characterize and visualize biological processes. For instance, in tissue dynamics, the spatial-temporal activity of cells can reveal interplays between signaling pathways

and the fate decision of individual cells. A prototypical example reported from *in vitro* and *in vivo* epithelial systems is the extracellular signal-regulated kinase (ERK) wave triggered by single apoptotic events, a signal which expands radially to neighboring cells and prevents them from undergoing further apoptosis[305]. Hence, integrating spatial-temporal cues with experimental observations could enhance our understanding of complex signaling pathways, whereas predictive models could establish a link between behavioral dynamics and underlying stimuli.

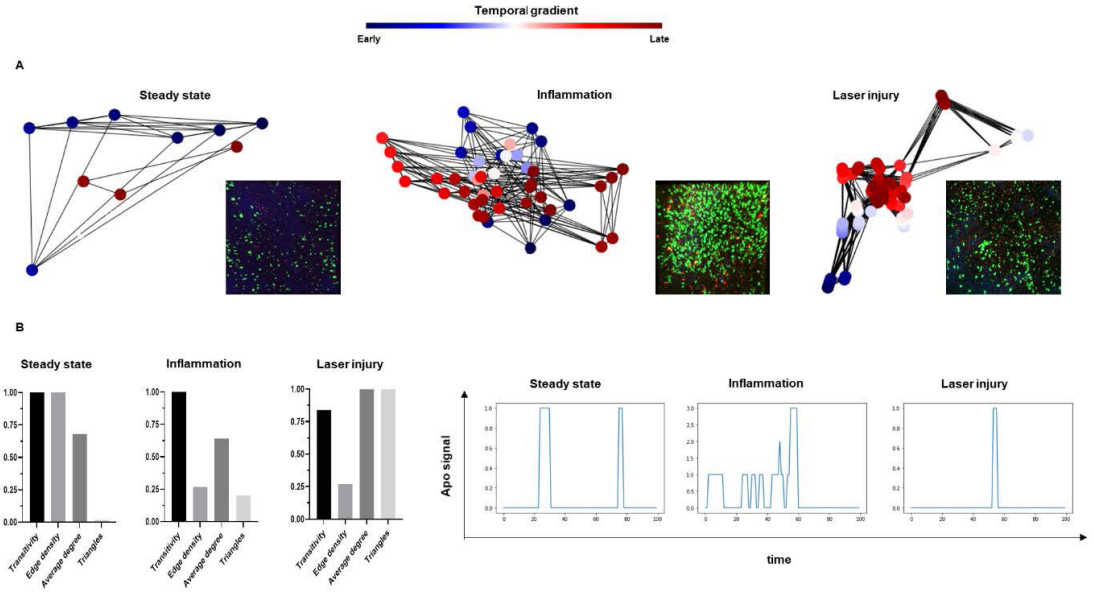

Figure 2. Measurement of tissue dynamics in vivo. A. *Graph representation of the spatial-temporal distribution of apoptotic events in steady state (**left**), inflammatory (**middle**) and laser injury (**right**) conditions. Nodes of the graph describe apoptotic events (x, y, t), whereas the color gradient indicates the timing of occurrence. B. Distribution of graph properties (**left**) and signal representation of the graphs over time (**right**).*

Following this premise, I wanted to demonstrate that the spatial-temporal distribution of apoptotic events may differ due to experimental conditions. Comparing steady-state, infection, and laser ablations condition in the lymph-node, I quantified the apoptotic events in each condition and successively created a graph representative of the spatial-temporal distribution of apoptosis (Fig. 2). Although preliminary and unpublished, results showed a clear difference in the connectivity of the graphs. These unique dynamics could be employed as unique identifiers that defines the underlying triggers and experimental cues associated with apoptosis, with relevant implications in the development of diagnostic models.

4. Concluding remarks and future perspectives

In this thesis, I extensively discussed the potential benefits of activity recognition in live-cell imaging using both track-based and video-based approaches. During this work, I also noticed a significant gap between the fields of computer vision and live-cell imaging. This led me to consider the possible reasons behind this disparity. Computer vision has evolved into a mature discipline, as evidenced by its growth during the last 40 years, and the same holds for microscopy technologies. Given these premises, one might expect computer vision to be more prevalent and effective in the context of live-cell imaging. However, this interdisciplinary bridge is not yet consolidated, as academic researchers do not possess yet the tools to maximize the outcome of vision-based techniques.

The training of robust and large deep learning models, which can encompass billions of parameters, is a costly investment which does not only include hardware requirements, but it extends to server storage and data curation too, without forgetting the invaluable contributions of the engineers who design, test, and validate the different models. Therefore, the costs associated with large-scale models can be a burden that is often unsustainable within academic research, and the consequences of these constraints are evident. Academic researchers are typically tasked with overseeing the entire process underlying the generation of a predictive model, spanning from from the data generation and curation, to the development and deployment of the network. These tasks are often carried out with limited computational resources, further highlighting the challenges faced in bridging computer vision and live-cell imaging.

Consequently, the application of computer vision in live-cell imaging is primarily directed toward the creation of proof-of-concept solutions. These solutions are often groundbreaking, but they frequently lack the capacity to generalize beyond the laboratory where they were conceived. Consequently, numerous studies conclude that their methods could potentially apply to different datasets through fine-tuning or further refinement. But this leads to a proliferation of custom solutions for each individual laboratory, which not only proves inefficient, but also lacks sustainability in the long term. Most importantly, I think that this strategy hampers methodological, as time and resources that could be allocated

to this end are instead diverted to re-adapt existing solutions.

For these reasons, I believe that a shift in the current paradigm would require changes in two crucial aspects: datasets availability, and effective learning methods. In my view, the first bottleneck revolves around data, which at present do not align with established FAIR[260] (Findable, Accessible, Interoperable, Reusable) principles prevalent in other scientific disciplines. This inadequate situation arises from several factors. First, not all studies openly share their datasets, consequently hindering advancement and reproducibility. Furthermore, the limited availability of publicly accessible datasets limits the development of powerful and robust models. Compounding this issue, shared dataset frequently lack metadata information, such as details about imaging acquisition and experimental settings, which are crucial to prevent biases in imaging analyses. Additionally, public datasets are fragmented and lack centralized repositories, preventing researchers from discovering and accessing these resources. To exacerbate the situation, the absence of standardized data formats further complicates the development of universally applicable models. In my opinion, these last two points hold the most significant consequences, as they prevent collaborative efforts.

To draw a direct analogy, in the field of omics sciences rapid progress has been achieved through collaborative efforts that have upheld two critical aspects: data centralization and standardized formats. Genome and protein sequence databases provided a unified reference platform for data access and upload, fully aligning with the FAIR principles. Furthermore, standardized formats ensured that any developed algorithms was compatible with data in the intended format, eliminating the need for further data curation.

Considering these factors, I believe that the key to advance computer vision in live-cell imaging relies on establishing centralized platforms and standardized data formats. Given the multiplicity of cellular activities and microscopy platforms, achieving complete standardization is unrealistic. Nevertheless, prescribing standardized data formats and guidelines for data acquisition and processing could immensely benefit the field. For example, capturing consecutive microscopy time-lapses with consistent sampling rates and magnifications, coupled with a predefined sequence of pro-

cessing steps, would enhance the uniformity and comparability of the data. In this regard, pre-trained deep learning networks could be leveraged to simplify and accelerate the automated data curation and feature extraction. Ultimately, the objective is to convert raw live-cell imaging movies into a structured and standardized format that enables meaningful analysis, while ensuring comparability across diverse datasets.

The second major bottleneck in current computer vision applied to live-cell imaging, is the heavy reliance on supervised learning techniques. As I mainly employed supervised deep learning during my PhD, I became aware that they might not be viable in the long term. Supervised deep learning is currently the leading approach for tasks demanding high predictive accuracy, like image recognition and natural language processing, and for good reasons: it works extremely well.

However, supervised techniques become increasingly costly when dealing with the growing stream of data and model parameters. This trend exacerbates the need for manual data annotation, which quickly becomes impractical for large real-world applications. To address this limitation, alternative approaches have recently gained attention. Semi-supervised learning[307] combines labeled and unlabeled data, making more efficient use of resources and reducing the need for extensive manual labeling. On the other hand, few-shot[308,309] learning techniques aim at recognizing new patterns and classes with the provision of minimal labeled examples. Finally, reinforcement-learning[310] eliminates the need for extensive annotations by simulating an environment in which an agent operates to find the optimal policy. Altogether, these approaches offer promising avenues for an efficient use of available data, addressing effectively the limitations posed by extensive manual annotation. Therefore, I believe that the future of computer vision and CAR in live-cell imaging revolves around the exploration of these alternative paradigms.

COLLABORATIONS

1. Manuscript 5

CANCOL: A computer-assisted annotation tool to facilitate colocalization and tracking of immune cells in intravital microscopy

Diego Ulisse Pizzagalli,[1,2,&] Joy Bordini,[1,&] Diego Morone,[1] Alain Pulfer,[1,3] Pau Carrillo-Barbera,[1] Benedikt Thelen,[1] Kevin Ceni,[1] Marcus Thelen,[1] Rolf Krause,[2,*] Santiago Fernandez Gonzalez[1,*]

[1] Institute for Research in Biomedicine, Faculty of Biomedical Sciences, USI—Switzerland

[2] Institute of Computational Science, USI—Switzerland

[3] Department of Information Technology and Electrical Engineering, ETH—Switzerland

[&] Contributed equally

[*] Co-last authors

Abstract

2-photon intravital microscopy (2P-IVM) has become a widely used technique to study cell-to-cell interactions in living animals. 2P-IVM generates 4D videos (3D images over time), which are classically analyzed by performing cell tracking, a procedure that computes the trajectories followed by each cell. However, technical artifacts associated with the imaging procedure, such as brightness shifts, presence of autofluorescent objects, and channel crosstalking, often generate imaging channels that are not specific for the cells of interest, thus hampering automatic tracking. Recently, machine learning has been applied to overcome a variety of obstacles in biomedical imaging. However, existing methods are not tailored to the specific problems of intravital imaging of immune cells. Moreover, results are highly dependent on the quality of annotations provided by the user. Therefore, we developed CANCOL, a tool designed to assist the user during the annotation process. CANCOL guides the user in this process by identifying specific objects that are problematic for cell tracking if not properly annotated. It then uses this information to generate a virtual channel that is specifically tailored to the cells of interest. This process facilitated the analysis of challenging 2P-IVM videos, significantly improving the accuracy of automatic tracking.

2. Manuscript 6

IMMUNEMAP, an intravital microscopy imaging platform to enable Spatial-Temporal Dynamic studies in Immunology.

Diego Ulisse Pizzagalli[&,1,2,3], Pau Carrillo-Barberà[&,1,4], Kevin Ceni[1,5], Elisa Palladino[1], Benedikt Thelen[2], Alain Pulfer[1,6], Joy Bordini[1], Florentino Caetano-Santos[1,7], The IMMUNEMAP project consortium[§], Rolf Krause[2,], Santiago Fernandez Gonzalez[1,]*

[1]*Institute for Research in Biomedicine, Università della Svizzera Italiana, Bellinzona, Switzerland.*

[2]*Euler Institute, Università della Svizzera Italiana, Lugano, Switzerland.*

[3]*Faculty of Biomedical Sciences, Università della Svizzera Italiana, Lugano, Switzerland.*

[4] *Instituto de Biotecnología y Biomedicina (BioTecMed), Universitat de València, València, Spain.*

[5]*Institute for Diagnostic and Interventional Neuroradiology, Inselspital, Bern University Hospital, Bern, Switzerland.*

[6]*Department of Information Technology and Electrical Engineering, ETH Zurich, Switzerland.*

[7]*Maria Sklodowska-Curie National Research Institute of Oncology, Warsaw, Mazowieckie, Poland.*

Abstract

In vivo imaging technologies, such as intravital 2-photon microscopy (IV-2PM), are a valuable tool for studying immune cell behavior, providing detailed insights into the spatiotemporal dynamics of the immune response. IV-2PM generates rich, multidimensional data in the form of 3D videos with multiple acquisition channels. IV-2PM videos are classically analyzed by performing cell tracking and by computing measures of cell motility and interaction. However, these data are often stored in locally inaccessible repositories, limiting their use for the scientific community. Conversely, there is a growing need for publicly available IV-2PM to ensure reproducibility and facilitate large-scale investigations. Hence, the absence of such resource the advancement of data-mining methods in immunological research.

Here we introduce IMMUNEMAP, a cloud-based platform that centralizes storage, retrieval, and analysis of IV-2PM videos of immune cells. Adhering to the FAIR principle, IMMUNEMAP promotes open data research and maximizes data reuse. To date, the platform features more than 400 videos from various experimental settings and over 20,000 single-cell tracks. IMMUNEMAP also provides sample applications to identify diverse migration patterns and evaluate the effect of different imaging protocols on cell motility. As a result, IMMUNEMAP promotes collaboration between immunologists and computer scientists, fostering an interdisciplinary approach in biomedical research.

3. Manuscript 7

Intravital microscopy reveals a distinct biodistribution pattern in neoplastic lesions of the L19 antibody depending on the administration route.

Tommaso Virgilio[1], Alain Pulfer[1,2], Kamil Chahine[1], Chiara Pizzichetti[1], Louis Luca Renner[1], Dario Neri[3], Emanuele Puca[4], Roberto De Luca[4], Santiago F. Gonzalez[1*]*

1: Institute for Research in Biomedicine, Università della Svizzera Italiana, Bellinzona, Switzerland.

2: Department of Information Technology and Electrical Engineering, Swiss Federal Institute of Technology (ETH Zürich), Zürich, Switzerland.

3: Philogen S.p.A., Piazza La Lizza 7, 53100 Siena, Italy

4: Philochem AG, Otelfingen, Switzerland.

Abstract

Antibody-based targeted delivery of pharmaceuticals has emerged as a promising approach for selective and effective cancer therapy. The Extra Domain B (EDB) of Fibronectin, expressed in the neo-vasculature of aggressive tumors, has been identified as a promising cancer marker. The L19 antibody, specific for EDB, has demonstrated efficient accumulation in tumor tissues and selective delivery of therapeutic agents to cancer cells. L19 has been conjugated with radionuclides for imaging studies in cancer patients, showing high sensitivity and specificity in detecting various solid and liquid tumors. Biodistribution studies, characterizing the spatio-temporal dissemination *in vivo*, are essential to fully exploit the potential of L19 for diagnosing and treating cancer. Macroscopic imaging methods, such as MRI, PET, CT scan, or IVIS, provide information on the overall spread of a product, while microscopic techniques, such as 2-photon intravital microscopy (2P-IVM), allow real-time assessment of drug delivery time and cellular distribution. In this work, we aim to investigate the biodistribution of the L19 antibody *in vivo* using a combination of macroscopic and microscopic imaging techniques. The results of this study provide a better understanding of the mechanisms underlying the targeting and accumulation of L19 in tumor tissues, with potential implications for optimizing administration protocols and improving cancer diagnosis and therapy.

METHODS

1. Charaterization of the dynamic behavior of neutrophils following influenza vaccination

Mice. All animals were bred in-house or acquired from Janvier labs (C57BL/6). Mice were maintained under specific pathogen-free conditions at the Institute for Research in Biomedicine, Bellinzona and used in accordance with the Swiss Federal Veterinary Office guidelines. The following transgenic mice were used: LysM-GFP[311], IL-1R KO[312], TLR3 KO, Myd88 KO[313], CCR2 KO, IFNAR KO[314], CD169DTR[76], CD11c-YFP[108], CK6/ECFP [315], UBC-GFP [316]. All strains had C57BL/6 background. All animal experiments were performed in accordance with the Swiss Federal Veterinary Office guidelines and authorized by the relevant institutional committee (Commissione cantonale per gli esperimenti sugli animali, Ticino) of the Cantonal Veterinary with authorization numbers TI28/17, TI02/14 and TI07/13.

Virus production inactivation and labeling. Influenza virus strain A/PR/8/34 was grown for 3 days in the allantoic cavity of 10-day embryonated chicken eggs. To remove cellular debris the allantoic fluid was harvested and centrifuged at 3000 rpm for 30 min and virus was subsequently purified twice in a discontinuous sucrose gradient at 25,000 rpm for 90 min. Virus stocks were quantified by tissue culture infective dose assay (TCID50) and to inactivate, viral suspensions were placed under the UV lamp at a distance of 15 cm for 15 min. For the labeling of UV-inactivated influenza virus, 50 mg/ml of DiD or DiO dye was added to the viral suspension and incubated for 20 min at RT. After that, virus was subsequently purified by centrifugation as mentioned before.

Antigen administration and injections. 10^6 plaque-forming units (PFU) of inactivated virus per footpad in a final volume of 10 µL were injected into anesthetized mice at different time points prior to LN collection. Macrophage depletion from CD169DTR mice was established by intraperitoneal (i.p.) injection of 10µg/kg of diphtheria toxin (Sigma-Aldrich) a day before vaccination. Recombinant murine IL-1α (1 µg/fp) and murine CXCL1 (0.5 µg/fp) were reconstituted in sterilized PBS and injected in a final volume of 10 µl 12 h before LN collection. For *in vivo* labeling of cells, mice received subcutaneous injection of 1 µg of fluorescently-labeled αCD21/35, αF4/80 and αCD169/footpad (Biolegend), 3 h before image acquisition.

To label the blood vessel mice were injected intravenously with 70 kDa Rhodamin B isothiocyanate-Dextran or Fluorescein isothiocyanate-Dextran solution as described before[317].

Flow cytometry. Neutrophil influx to the popliteal LN was monitored using flow cytometry. LN were collected, disrupted with tweezers, and digested for 10 min at 37 °C in an enzyme mix composed of DNase I (0.28 mg/ml, Amresco), dispase (1 U/mL, Corning), and collagenase P (0.5 mg/mL, Roche) in calcium- and magnesium-free PBS (PBS-) followed by a stop solution composed of 2 mM EDTA (Sigma-Aldrich) and 2% heat-inactivated filter-sterilized fetal calf serum (Thermo Fisher Scientific) in PBS- (Sigma-Aldrich). Fc receptors were blocked (αCD16/32, Biolegend) followed by surface staining and analyzed by flow cytometry on a LSRFortessaTM (BD Biosciences). Dead cells were excluded using ZombieAcqua fixable viability dye (Biolegend) and data were analyzed using FlowJo software (TriStar Inc).

Antibodies. In this study cell suspension was isolated from harvested organs and immunostained with various combinations of the following fluorescence-conjugated antibodies: αB220 (RA3-6B2), αCD3 (17A2), αCD11b (M1/70), αCD69 (H1.2F3), αI-A/I-E (M5/114.15.2), αLy-6G (1A8), αCD21/CD35 (7E9), αF4/80 (BM8), αCD169 (3D6.112), αCD16/32 (93) (all from Biolegend.

Cytoplex assay. The concentration of various cytokines and chemokine in the lymph was determined by LEGENDPlex assays (Mouse Proinflammatory Chemokine Panel and Mouse Inflammation Panel; Biolegend) according to manufacturer's instructions. Briefly, popliteal LNs were collected and carefully disrupted in 75 mL ice-cold phosphate buffer, minimizing cell rupture. The suspension was centrifuged at 1,500 rpm for 5 min, and the supernatant was collected. 25 mL supernatant was used for the protocol following the manufacturer's instructions. Samples were analyzed by flow cytometry on an LSRFortessa (BD Biosciences), and data were analyzed using LEGENDPlex software (BioLegend).

Immunohistology and microscopy. Mice were euthanized, popliteal lymph nodes harvested and fixed in 4 % PFA at 4 °C for 4-6 h. Organs were embedded in 4 % low gelling agarose (Sigma-Aldrich) and 50 µm sections were cut with Leica VT1200S vibratome (Leica Microsystems), blocked with proper sera and stained with the indi-

cated antibodies in 0.05 % Tween-20 in 0.5 % BSA PBS- for two days at 4 °C shaking. More details are reported in the antibodies section. Immunofluorescence confocal microscopy was performed using a Leica TCS SP5 confocal microscope (Leica Microsystems). Micrographs were acquired in sequential scans and merged to obtain a multicolor image. Images were processed using Imaris software (Bitplane AG).

Electron microscopy. PLN were collected and fixed in 2 % formaldehyde 2.5 % glutaraldehyde in 0.1 M sodium cacodylate buffer (pH 7.4) overnight at 4 °C. LN were washed in 0.05 M maleate buffer (pH 5.15) and stained for 2 h in 1 % uranyl acetate in maleate buffer. The samples were dehydrated by incubation for 15 minutes in ethanol water (60 %, 90 %, 100 %) and embedded in Epon.

Intravital two-photon microscopy. Deep tissue imaging was performed on a customized up-right two-photon platform (TrimScope, LaVision BioTec). Two-photon probe excitation and tissue second-harmonic generation (SHG) were obtained with a set of two tunable Ti:sapphire lasers (Chamaleon Ultra I, Chamaleon Ultra II, Coherent) and an optical parametric oscillator that emits in the range of 1,010 to 1,340 nm (Chamaleon Compact OPO, Coherent), with output wavelength in the range of 690–1,080 nm.

Image analysis and data processing. Cell detection, tracking and volumetric reconstruction from 4D 2P-IVM data were performed using Imaris (Oxford Instruments, v7.7.2). Raw data generated from Imaris were further processed and analyzed with a custom Matlab script.

Cell tracks were generated semi-automatically and curated to correct errors (i.e. jumps or non detected cells). Tracks with a duration less than 5 points or 300 s were excluded from the analysis. Videos were stabilized using the drift correction functionality when needed, compensating for translational-drift only and by cropping the largest common area in the videos. Standard measures of cell motility were computed using Imaris. These include Track duration (time interval between the first and the last time points in which a cell is tracked), Track Length (total length of the cell trajectory), Track Speed Mean (Track length / Track duration), Track Displacement (length of the vector from the first to the latest centroid position of the cell), Track Straightness (Track Displacement / Track Length), Speed (instantaneous speed computed between adjacent time points).

Spectral unmixing. An additional imaging channel, specific for the cells of interest was generated by classifying each pixel as foreground or background. This was achieved using the Coloc functionality of Imaris in combination with a custom supervised machine learning method for pixel classification implemented in Matlab as described in [318]. This method trains a Supported Vector Machine (SVM) to classify pixels as background or background on the basis of examples provided by the user. A minimum of 20 and a maximum of 60 training points were provided for each video. To differentiate between background and foreground the following features were used: Local color, Gaussian-weighted average color in a neighborhood (sigma = 3 um, 7 um).

Quantification of cell density in High Endothelial Venules (HEV) and Lymphatic vessels (LV). The density of neutrophils in a vessel presented in Fig. 1 is defined as the ratio of the number of cells inside a vessel and the volume of the vessel itself. The density of neutrophils in HEV was computed at different time points inside a selected HEV which was visible for the entire duration of the acquisition (3 hours). HEV were labeled by the i.v injection of 70 kDa Rhodamine B isothiocyanate-Dextran. Cells inside the HEV were manually counted every 300s. The volume of the HEV was estimated as the volume of a cylinder, by measuring the average diameter in the xy plane and the average height along z and the length of the vessel.

The density of neutrophils in LV at the injection site were computed in a LV visible for the entire duration of the acquisition (4 hours). Draining LV were labeled by the subcutaneous injection of DiD-labeled virus and 70 kDa Rhodamine B isothiocyanate-Dextran. Cells were detected and counted automatically using the Spots function of Imaris. The volume of the LV was estimated via volumetric reconstruction using the Surfaces tool of Imaris.

Estimation of distance of the virus particle with respect to cell centroid. To confirm the internalization of the viral particles by neutrophils, the distance of the particles from the cell centroid was computed and compared to the cell radius. Cell radius was estimated via volumetric reconstruction of the cell surface and computed as the radius of a sphere having the same volume of the cell.

Pixel velocity. The average velocity of pixels presented in (Fig. 6, A) was estimated via a custom Matlab script that computes opti-

cal flow as described in [209]. Only the channel where the neutrophils were visible was used for optical flow estimation. To address the lack of texture of immune cells which leads to an aperture problem, Tikhonov regularization was used while computing the flow (Tikhonov constant = 40). Additionally, outliers were removed by Gaussian smoothing (sigma = 7) followed by the saturation of the bottom 1 % and the top 1 % of all pixel velocity values (set to the minimum and maximum values respectively).

Gating strategy for activity recognition. We mapped a biological meaning (activities) to specific ranges of instantaneous motility measures. This allowed both to describe the dynamic behavior of neutrophils as a series of activities and provided a suggestion on the biological function of each neutrophil at different time points. However, the problem of identifying one activity from a range of measures (gate) is an ill-posed problem which often arises when characterizing a complex biological system from experimental data [319]. Indeed, not all the possible activities are known and several activities might exhibit similar motility measures leading to an undetermined solution. To solve this issue, we defined gating thresholds that minimize the overlap between distinct activities and we selected one activity out of the multiple possible solutions, based on an arbitrary priority order. Although the gates used to detect activities are subjected to the bias of the investigator, these can be easily adapted according to the experimental settings and based on a priori knowledge.

Software implementation. A custom Matlab script (Supplementary Data File 1) was used to automatically compute instantaneous motility measures and detect activities.

This script decomposes each track into track fragments (tracklets) with a fixed duration of 500 s (approximated to 17 time points with a sampling interval of 30 s). From a track with total duration Td >= 17 time points, K = (Td - 17) + 1 tracklets were extracted by a sliding window. Then, it computes the following measures on each tracklet. For the analysis of neutrophils actions in homeostasis conditions, due to the high speed of cells flowing in large blood vessels, this window was reduced to 5 time points and the sampling interval of the microscope decreased to 20s.

Displacement: distance between the initial and the final points of the tracks. Speed: track length / track duration. Straightness:

displacement / track length.

Arrest coefficient is typically defined as the percentage of time in which a cell moves below a certain threshold. However, being the tracklets of short duration this results in a limited number of admissible percentages. Additionally, a sharp threshold may introduce artifacts. Therefore we computed arrest coefficient by using a sigmoidal thres ollows.

$$\mathrm{ac} = \frac{\sum_{i=1}^{k} 1 - \frac{1}{e^{1+s(k)-\tau}}}{\mathrm{ac}_0}$$

where τ = 2 μm/min is a speed threshold and $ac_0 = k - (k / e^{1-\tau})$ is the arrest coefficient of a cell having a constant speed of 0 μm/min. Based on the aforementioned parameters, each tracklet was associated with one of the following activities:

"Arrested": Cell which does not move (i.e. interacting / adhering / death), exhibiting low speed, low directionality, low displacement, and high arrest coefficient.

"Patrolling": Cell which moves, covering a large area of tissue, with medium speed and directionality.

"Directed": Cell which moves towards a target exhibiting high speed and directionality (high displacement and low arrest coefficient)

"Flowing": Cell which flows inside the capillaries of blood vessels in the LN. A flowing cell exhibits extremely high speed and directionality. This association was implemented by means of fixed thresholds corresponding to different gates defined in

parameters (columns). Values refer to tracklets with a duration of 500s.

The detection of cells involved in a swarm (swarming) was achieved via a volumetric reconstruction. For the videos in Figure 4 with adoptively transferred CK6/ECFP neutrophils, swarms were considered as surfaces with a minimum volume of $2*10^3$ um^3. The number of cells in a swarm was estimated by dividing the swarm volume by the volume of a single cell (assumed to $1*10^3$ um^3 without spaces between cells).

Swarm quantification. To quantify the size and growth rate of swarms we defined a both cell density and an overall directionality criteria. More precisely, we detected swarms in regions where cells accumulated and where most trajectories pointed to. The "surfaces" functionality of Imaris was

Table 1.

Table 1. Gating thresholds. *Each activity (row) is mapped to a specific range (min-max) of motility evaluated on 500 s*

		Arrested	Patrolling	Directed	Flowing	Swarming
speed [µm/min]	min	0	2	6	10	-
	max	7	8	25	300	-
straightness [0-1]	min	0	0.1	0.3	0.5	-
	max	0.3	0.5	1	1	-
arrest coefficient [0-1]	min	0.7	0.1	0	0	-
	max	1	0.8	0.2	0.2	-
displacement [0-1]	min	0	4	8	50	-
	max	15	20	80	300	-
volume [µm^3]	min	-	-	-	-	2000

used to reconstruct the volume of swarms, selecting the marching cube algorithm with either a user-defined brightness threshold in (low-magnification videos - Figure 6C) or by manually defining a region of interest around the swarm in (high magnification videos - Figure 6I). Neutrophils involved in the swarm were manually tracked until the end of the videos or when they merged to emerging swarms.

Statistics. Results were expressed as mean ± standard deviation (SD). All statistical analyses were performed in Prism8 (Graphpad Software, La Jolla, USA). Means among two groups were compared with two-tailed t-test and among three or more groups were compared with one-way ANOVA analysis of variance with Dunn's multiple comparison post-test.

Software availability and usage. The source code of the program to quantify the actions of immune cells from their tracks, is provided in Supplementary Data File 1. This program requires the tracks of the cells to be exported from Imaris to an Excel file. After this has been done, it is possible to open the program in Matlab, enter the location of Excel file, and executing the program. The plots counting the actions will be automatically created to facilitate this process, and to avoid the requirement of Matlab, after publication the software will be released as an open source plug-in for Imaris (Oxford Instruments) and will be available at

http://open.bitplane.com

2. vAbs: virtual antibodies for immune cell identification

Dataset curation. Tracks in our dataset were processed to extract features related to cell movement. The engineered features included displacement, meandering index, turning angles, speed, acceleration, jerk, directional change, and hull area. In addition, we rotated and aligned all tracks such that the average displacement vector was parallel to the X axis. Tracks coordinates and features were successively normalized between 0 and 1.

Hierarchical clustering of cell tracks. We employed hierarchical clustering to group cell tracks based on spatial coordinates and previously engineered features. The analysis was conducted in Python using the seaborn library. We employed correlation as distance metrics, applying z-score row normalization of the data. The resulting dendrogram was color-coded according to the cell type to highlight possible segregation patterns associated with motility.

UMAP analysis. We conducted UMAP analysis using the umap-learn library in Python. The analysis was performed on the same dataset used for hierarchical clustering. Before conducting UMAP analysis, we preprocessed the data by averaging the track features over time, resulting in a concise representation of cell behavior. The analysis was executed with a 15 nearest neighbors and a distance parameter of 0.1.

Deep learning models. All benchmarked models were generated with the keras python library. For training we set 80 epochs with a learning rate of 0.00001 and adam optimizer. Binary models were trained with binary cross entropy loss, while for multiclass models we employed categorical cross entropy.

Panel of vAbs. For each target cell population amongst neutrophils, TCs, and NKs, we tailored two vAbs meant to capture the respective motility. Three vAbs were obtained from a multiclass model trained to predict the labels of all cell populations. Three other vAbs were obtained from binary models trained to predict only a one class label in an anomaly detection fashion.

3. Transformer-based spatial-temporal detection of apoptotic cell death in live-cell imaging

MCF10A cell line and image acquisition. The normal-like mammary epithelial MCF10A cells (provided by Joan Brugge[320]), stably expressing the nuclear marker, were generated as previously described[305]. Briefly, the nuclear marker H2B-miRFP703, provided by Vladislav Verkhusha (Addgene plasmid # 80001)[321], was subcloned in the PiggyBac plasmid pPBbSr2-MCS. After cotransfection with the transposase plasmid[322], cells were selected with 5 µg/ml Blasticidin and subcloned. For time-lapse imaging, the cells were seeded on 5 µg/ml fibronectin (PanReac AppliChem) coated 1.5 glass-bottom 24 well plates (Cellvis) at 1 x 10^5 cells/well density. After 48 hours, when the optical density was reached, the confluent cell monolayer was acquired every 1 or 5 minutes for several hours with a Nikon Eclipse Ti inverted epifluorescence microscope with 640nm LED light source, ET705/72m emission filter and a Plan Apo air 203 (NA 0.8) or a Plan Apo air 403 (NA 0.9) objectives. The collection of biological experiments used in this study includes different stimulation of apoptosis, such as growth factors, serum starvation and doxorubicin at various concentrations.

Apoptosis induction of MCF10A cells with doxorubicin. Normal-like mammary epithelial MCF10A cells were grown in 24 well glass coated with fibronectin with a seeding of 1x10^5 cells/well. After two days, cells were starved for three hours and treated with doxorubicin at 1.25, 2.50, and 5.00 µM concentrations.

Mice. Prior to imaging, mice were anesthetized with a cocktail of Ketamine (100 mg/Kg) and Xylazine (10 mg/Kg) as previously described[259]. All animals were maintained in specific pathogen-free facilities at the Institute for Research in Biomedicine (Bellinzona, CH). All the experiments were performed according to the regulations of the local authorities and approved by the Swiss Federal Veterinary Office.

Intravital Two-Photon Microscopy. Surgery in the popliteal lymph node was performed as previously reported[35]. The exposed organs were imaged on a custom up-right two-photon microscope (TrimScope, LaVision BioTec). Probe excitation and tissue second-harmonic generation (SHG) were achieved with two Ti:sapphire lasers (Cha-

maleon Ultra I, Chamaleon Ultra II, Coherent) and an optical oscillator that emits in the 1,010–1,340 nm range (Chamaleon Compact OPO, Coherent) and has an output wavelength between 690–1,080 nm.

Neutrophil isolation from mouse bone marrow. Bone marrow samples were extracted via flushing with PBS from the long bones of UBC-GFP mice (https://www.jax.org/strain/004353). Then, the bone marrow was filtered through a 40um strainer and resuspended in PBS. Primary bone marrow neutrophils were isolated with Ficoll gradient and resuspended in PBS.

T-cell culture in a 3D collagen matrix. Human CD4+ T cells were isolated from the PBMC fraction of healthy donors obtained from NetCAD (Canadian Blood Services). Cell purity was above 95%. Naïve CD4+ T cells were activated by adding Dynabeads coated with anti-human CD3e/CD28 antibody (1:1 bead:cell ratio, Life Technologies Cat #11131D) in RPMI1640 supplemented with 10% FBS (VWR Seradigm Cat #1500-500), 2 mM GlutaMAX (Gibco Cat #3050-061), 1mM sodium pyruvate (Corning Cat #25-000-CI) and 10mM HEPES (Sigma-Aldrich Cat #H4034). After two days, beads were removed and cells were cultured for another 4-6 days in a medium containing 50 IU/mL human rIL-2 (Biotechne Cat #202-IL-500), keeping cell density at 2 x 10^5 cells/mL. Cells were used for all experiments between days 6 to 8. All work with human blood has been approved by the University of Manitoba Biomedical Research Ethics Board (BREB).

Apoptosis live-cell imaging of T-cells in 3D collagen chambers. T cells were labeled at day 6-8 using CMAC (10μM) cell tracker dye (Invitrogen) and glass slide chambers were constructed as previously described[323,324]. Briefly, 2 x 10^6 cells were mixed in 270μL of bovine collagen (Advanced Biomatrix cat #5005-100ML) at a final concentration of 1.7 mg/mL. Collagen chambers were solidified for 45 minutes at 37°C / 5% CO2 and placed onto a custom-made heating platform attached to a temperature control apparatus (Werner Instruments). For the induction of apoptosis, 1μM of Staurosporine (Sigma Cat #569397-100UG) and 800ng of TNF-a (Biolegend Cat #570104) in 100μL RPMI were added on top of the solidified collagen. Cells were imaged as soon as the addition of apoptosis inducers using a multiphoton microscope with a Ti:sapphire laser (Coherent), tuned to 800 nm for optimized excitation of CMAC. Stacks of 13 optical sections (512 x 512 pixels) with 4 mm z-spacing were acquired every 15 sec-

onds to provide imaging volumes of 44mm in depth (with a total time of 60 - 120 minutes). Emitted light was detected through 460 / 50nm, 525 / 70 nm, and 595 / 50 nm dichroic filters with non-descanned detectors. All images were acquired using the 20 x 1.0 N.A. Olympus objective lens (XLUMPLFLN; 2.0mm WD).

Data Processing and Image Analysis. The raw video data, composed by uint8 or uint16 TIFFs, were stored as HDF5 files. No video pre-processing was applied to the raw data before image analysis. Cell detection, tracking, and volumetric reconstruction of microscopy videos were performed using Imaris (Oxford Instruments, v9.7.2). The resulting data were further analyzed with custom Matlab and Python scripts (see code availability section).

Apoptosis annotation of epithelial MCf10A cells *in vitro*. We manually annotated apoptotic events of MCF10A cells by visual inspection of the movies. The annotation was done by observing the morphological changes associated with apoptosis (e.g. nuclear shrinkage, chromatin condensation, epithelial extrusion, nuclear fragmentation) across multiple consecutive frames. Using a custom Fiji[325] macro, we automatically stored x and y centroids of the apoptotic nucleus. The time t of each apoptotic annotation was defined as the beginning of nuclear shrinkage.

Generation of the *in vitro* training dataset. The 16-bit raw movies were min-max scaled to the 0.001 and 0.999 quantiles and downsampled to 8-bit resolution. Using the database of manually labeled coordinates of apoptotic events (x, y, t), we extracted crops with 59 x 59 pixels resolution (2x scaling for the FOVs acquired with the 20x objective). Seven time-steps of the same location were extracted, with linear spacing from -10 minutes to +50 minutes relative to the apoptosis annotation. This time frame was chosen to capture the cell before the onset of apoptosis, and the morphological changes associated with apoptosis (nuclear shrinkage, decay into apoptotic bodies, and extrusion from epithelium). The resulting image cube has dimensions of 59 x 59 x 7. To create the training data for the non-apoptotic class, we excluded areas with an annotated apoptotic event with a safety margin from the movies. From the remaining regions without apoptoses, we extracted image cubes from cells detected with StarDist[326] and from random locations. The random crops also included debris, apoptotic bodies from earlier apoptotic events, empty regions, and out-of-focus nuclei.

Apoptosis annotation of leukocyte cells *in vivo*. Three operators independently annotated the videos based on selected morphological criteria. To label apoptotic cells, the annotators considered only the sequences of cells that displayed membrane blebbing followed by apoptotic bodies formation and cell disruption (Fig. 2B). For each frame in the apoptotic sequence, the operators placed a centroid at the center of the cell with the Imaris "Spots" function, generating an apoptotic track. Successively, ground truth tracks were generated according to a majority voting system, and 3D volume reconstruction was performed on ground truth cells using the Imaris "Surface" function. Nearby non-apoptotic cells were also tracked. In addition, other non-apoptotic events were automatically sub-sampled from regions without apoptotic cells.

3D rotation of the *in vivo* annotations. *In vivo* annotations presented a class unbalance in favor of non-apoptotic cells, with a relative few apoptotic instances. Hence, to compensate for this bias, we produced several representations of the raw data by interpolating the raw image stacks in 3D volumes and rotating them in randomly sampled directions, with rotational degrees between 0° and 45°. After each manipulation, the rotated volume underwent flattening by maximum projection and symmetric padding to preserve the original dimension. The 2D images were successively resized and cropped to match the 59 x 59 pixels input of the classifier. Finally, the training sequences were saved as uint8 gray-scale TIFFs files.

Generation of the *in vitro* and *in vivo* training datasets. To detect apoptotic cells in microscopy acquisitions, we defined a 2D binary classification task in which apoptotic events are labeled with class 1, while non-apoptotic events belonged to the class label 0. The resulting unprocessed data consisted of frame sequences composed of 3D crops. The content of the class label 0 in vitro included: healthy nuclei, background, cell debris and mitotic cells. The content of the class label 0 *in vivo* included: motile cells, arrested cells, highly deformed cells, overlapping cells, cell debris or blebs, empty background, noisy background, and collagen.

Data augmentation and data loader. Given the varying length of the training sequences contained in the TIFFs, upon training, we used a custom data loader that uniformly samples the input data and produces sequences with a fixed number of frames. The

fixed number of frames was set to 5, corresponding to the frame-length of the shortest apoptotic sequence. During training, each sample underwent horizontal shift, vertical shift, zoom magnification, rotation, and flipping. All data augmentations were performed in python using the Keras library.

Deep learning architecture. As a deep learning classifier, we employed a custom architecture relying on time-distributed convolutional layers stacked on top of a transformer module (Conv-Transformer). The input size consists of 5 single-channel images with 59x59 pixel size. The convolutional network has three layers of size 64, 128, and 256 length. Each layer has a 3x3 kernel, followed by RELU activation, batch normalization, and a dropout set to 0.3. The inclusion of padding preserves the dimension of the input, while 2D max-pooling is at the end of each convolutional block. After 2D max pooling, the output is passed to a transformer module counting 6 attention heads, and successively to a fully connected decision layer. The fully connected network has four layers with 1024, 512,128, and 64 nodes, each one followed by RELU activation and a 0.3 dropout layer. The last layer is a softmax activation, which predicts a decision between the two classes.

Training and hyper-parameters. Our model was trained in tensorflow with Adam optimizer, using binary cross-entropy loss and an initial learning rate of 0.0001. The optimal mini-batch size was 32, and the number of training epochs was 200. In training mode, we set a checkpoint to save the model with the best accuracy on the validation dataset, and a checkpoint for early stopping with patience set to 15 epochs. In addition, the learning rate decreased when attending a plateau.

ADeS deployment. For the deployment of the classifier on microscopy videos, we generative region proposals using the selective search algorithm, obtaining a set of ROIs for each candidate frame of the input movie. For each ROI computed by the region proposal at time t, a temporal sequence is cropped around t and classified with the Conv-Transformer. The resulting bounding boxes are filtered according to a probability threshold and processed with the non-maxima suppression utils from Pytorch. Consecutive bounding boxes classified as apoptotic are connected using a custom multi-object tracking algorithm based on Euclidean distance. The generated trajectories are filtered by discarding those with less than two objects.

Default and user-defined parameters. ROIs detected with the region proposal are filtered according to their size, discarding the ones with edges below 20 pixels and above 40 pixels. Furthermore, a threshold on intensity is applied to exclude uint8 patches with an average brightness below 40. Upon classification, a temporal window corresponding to the expected duration of the apoptotic event is set by the user (9 frames by default). This temporal window is subsampled to match the number of input frame of the classifier (5). The filtering of the predictions depends on a user-specified threshold, which by default corresponds to 0.95 *in vivo* and 0.995 *in vitro*. Non-maxima suppression is based on the overlapping area between bounding boxes, set to 0.1 by default. The centroid tracking has the following adjustable parameters: gap and distance threshold. The "gap" parameter, set to three frames, specifies for how long a centroid can disappear without being attributed a new ID upon reappearance. A threshold on the distance, set by default to 10 pixels, allows the connection of centroids within the specified radius. All the reported quantifications had default parameters.

Statistical analyses. Statistical comparisons and plotting were performed using GraphPad Prism 8 (Graphpad, La Jolla, USA). All statistical tests were performed using non-parametric Kruskal-Wallis test or Mann-Witney test For significance, p value is represented as * when $p < 0.05$, ** when $p < 0.005$ and *** when $p < 0.0005$.

REFERENCES

1. Walker-Daniels, J. Live Cell Imaging Methods Review. *Mater. Methods* **2**, (2012).
2. Conchello, J. A. Fluorescence microscopy - Nature Methods. *Nat. Methods* (2005).
3. Ettinger, A. & Wittmann, T. Fluorescence live cell imaging. in *Methods in Cell Biology* vol. 123 (2014).
4. Pujadas, A. B., Manich, M., Guillén, N., Olivo-Marin, J.-C. & Dufour, A. C. BIOPHYSICAL MEASUREMENTS IN 2D AND 3D LIVE CELL IMAGING USING FLUID DYNAMICS AND OPTICAL FLOW. (2016) doi:10.0/Linux-x86_64.
5. Toomre, D. K., Langhorst, M. F. & Davidson, M. W. Introduction to Spinning Disk Confocal Microscopy. *Carl Zeiss Microsc. Online Campus Digit. Imaging Considerations* (2012).
6. Kamada, T. *et al.* Low-invasive 5D visualization of mitotic progression by two-photon excitation spinning-disk confocal microscopy. *Sci. Rep.* **12**, (2022).
7. Movsisyan, N. & Pardo, L. A. Measurement of microtubule dynamics by spinning disk microscopy in monopolar mitotic spindles. *J. Vis. Exp.* **2019**, (2019).
8. Demchenko, A. P. Photobleaching of organic fluorophores: Quantitative characterization, mechanisms, protection. *Methods and Applications in Fluorescence* vol. 8 (2020).
9. Pijuan, J. *et al.* In vitro cell migration, invasion, and adhesion assays: From cell imaging to data analysis. *Front. Cell Dev. Biol.* **7**, (2019).
10. Kramer, N. *et al.* In vitro cell migration and invasion assays. *Mutation Research - Reviews in Mutation Research* vol. 752 (2013).
11. Corrò, C., Novellasdemunt, L. & Li, V. S. W. A brief history of organoids. *Am. J. Physiol. - Cell Physiol.* **319**, (2020).
12. Shanti, A., Hallfors, N., Petroianu, G. A., Planelles, L. & Stefanini, C. Lymph Nodes-On-Chip: Promising Immune Platforms for Pharmacological and Toxicological Applications. *Frontiers in Pharmacology* vol. 12 (2021).
13. Jorch, S. K. & Deppermann, C. Intravital Imaging Allows Organ-Specific Insights Into Immune Functions. *Front. Cell Dev. Biol.* **9**, (2021).
14. Ricard, C. *et al.* Two-photon probes for in vivo multicolor microscopy of the structure and signals of brain cells. *Brain Structure and Function* vol. 223 (2018).
15. Shaner, N. C., Steinbach, P. A. & Tsien, R. Y. A guide to choosing fluorescent proteins. *Nat. Methods* **2**, (2005).

16. Secklehner, J., Celso, C. Lo & Carlin, L. M. Intravital microscopy in historic and contemporary immunology. *Immunology and Cell Biology* vol. 95 (2017).

17. Pittet, M. J., Garris, C. S., Arlauckas, S. P. & Weissleder, R. Recording the wild lives of immune cells. *Science Immunology* vol. 3 (2018).

18. Stein, J. V., Gonzalez, S. F., F. Gonzalez, S. & Gonzalez, S. F. Dynamic intravital imaging of cell-cell interactions in the lymph node. *J. Allergy Clin. Immunol.* **139**, 12–20 (2017).

19. Rakhilin, N. *et al.* An intravital window to image the colon in real time. *Nat. Commun.* **10**, (2019).

20. Jahromi, N. H. *et al.* A novel cervical spinal cord window preparation allows for two-photon imaging of T-cell interactions with the cervical spinal cord microvasculature during experimental autoimmune encephalomyelitis. *Front. Immunol.* **8**, (2017).

21. Zhang, W. *et al.* In vivo two-photon characterization of tumor-associated macrophages and microglia (TAM/M) and CX3CR1 during different steps of brain metastasis formation from lung cancer. *Neoplasia (United States)* **23**, (2021).

22. Mulazzani, M. *et al.* Long-term in vivo microscopy of CAR T cell dynamics during eradication of CNS lymphoma in mice. *Proc. Natl. Acad. Sci. U. S. A.* **116**, (2019).

23. Dunn, K. W. & Sutton, T. A. Functional studies in living animals using multiphoton microscopy. *ILAR Journal* vol. 49 (2008).

24. Soulet, D., Lamontagne-Proulx, J., Aubé, B. & Davalos, D. Multiphoton intravital microscopy in small animals: motion artefact challenges and technical solutions. *Journal of Microscopy* vol. 278 (2020).

25. Pizzagalli, D. U. *et al.* Data Descriptor: Leukocyte Tracking Database, a collection of immune cell tracks from intravital 2-photon microscopy videos. *Sci. Data* **5**, 1–13 (2018).

26. Pizzagalli, D. U., Pulfer, A., Thelen, M., Krause, R. & Gonzalez, S. F. A review on activities of immune cells observed via intravital microscopy. *Prep.*

27. Pizzagalli, D. U. *et al.* Characterization of the Dynamic Behavior of Neutrophils Following Influenza Vaccination. *Front. Immunol.* **10**, 1–17 (2019).

28. Beltman, J. B. *et al.* Analysing immune cell migration. *Nat. Rev. Immunol.* **9**, 789–798 (2009).

29. Vladymyrov, M., Haghayegh Jahromi, N., Kaba, E., Engelhardt, B. & Ariga, A. VivoFollow

2: Distortion-Free Multiphoton Intravital Imaging. *Front. Phys.* **7**, (2020).

30. Pizzagalli, D. U., Thelen, M., Gonzalez, S. F. & Krause, R. Semi-supervised machine learning facilitates cell colocalization and tracking in intravital microscopy. *bioRxiv* (2019) doi:10.1101/829838.

31. Maška, M. *et al.* The Cell Tracking Challenge: 10 years of objective benchmarking. *Nat. Methods* **20**, (2023).

32. Pizzagalli, D. U. *et al.* Leukocyte Tracking Database, a collection of immune cell tracks from intravital 2-photon microscopy videos. *Sci. Data* **5**, 1–13 (2018).

33. Maška, M. *et al.* A benchmark for comparison of cell tracking algorithms. *Bioinformatics* **30**, (2014).

34. Hunter, M. C. *et al.* Dendritic cells and T cells interact within murine afferent lymphatic capillaries. *Front. Immunol.* **10**, (2019).

35. Miller, M. J., Hejazi, A. S., Wei, S. H., Cahalan, M. D. & Parker, I. T cell repertoire scanning is promoted by dynamic dendritic cell behavior and random T cell motility in the lymph node. *Proc. Natl. Acad. Sci. U. S. A.* **101**, (2004).

36. Chatziandreou, N. *et al.* Macrophage Death following Influenza Vaccination Initiates the Inflammatory Response that Promotes Dendritic Cell Function in the Draining Lymph Node. *Cell Rep.* **18**, (2017).

37. Horn, B. K. P. & Schunck, B. G. Determining optical flow. *Artif. Intell.* **17**, 185–203 (1981).

38. Baker, S. & Matthews, I. Lucas-Kanade 20 years on: A unifying framework. *Int. J. Comput. Vis.* **56**, (2004).

39. Sommer, C., Straehle, C., Köthe, U. & Hamprecht, F. A. Ilastik: Interactive learning and segmentation toolkit. in *2011 IEEE international symposium on biomedical imaging: From nano to macro* 230–233 (2011).

40. Wiley, V. & Lucas, T. Computer Vision and Image Processing: A Paper Review. *Int. J. Artif. Intell. Res.* **2**, (2018).

41. Hubel, D. H. & Wiesel, T. N. Receptive fields of single neurones in the cat's striate cortex. *J. Physiol.* **148**, (1959).

42. Blake, R. The visual system of the cat. *Percept. Psychophys.* **26**, (1979).

43. Hochstein, S. & Ahissar, M. View from the top: Hierarchies and reverse hierarchies in the visual system. *Neuron* vol. 36 (2002).

44. Herzog, M. H. & Clarke, A. M. Why vision is not both hierarchical and feedforward. *Frontiers in Computational Neuroscience* vol. 8 (2014).

45. Paolanti, M. & Frontoni, E. Multidisciplinary Pattern Recognition applications: A review. *Computer Science Review* vol. 37 (2020).

46. Viola, P. & Jones, M. Rapid object detection using a boosted cascade of simple features. in *Proceedings of the IEEE Computer Society Conference on Computer Vision and Pattern Recognition* vol. 1 (2001).

47. Viola, P. & Jones, M. J. Robust Real-Time Face Detection. *Int. J. Comput. Vis.* **57**, (2004).

48. Tsai, C.-F. Bag-of-Words Representation in Image Annotation: A Review. *ISRN Artif. Intell.* **2012**, (2012).

49. Burges, C. J. C. A tutorial on support vector machines for pattern recognition. *Data Min. Knowl. Discov.* **2**, (1998).

50. Kimmel, J. C., Brack, A. S. & Marshall, W. F. Deep Convolutional and Recurrent Neural Networks for Cell Motility Discrimination and Prediction. *IEEE/ACM Trans. Comput. Biol. Bioinforma.* **18**, (2021).

51. Dhillon, A. & Verma, G. K. Convolutional neural network: a review of models, methodologies and applications to object detection. *Progress in Artificial Intelligence* vol. 9 (2020).

52. Del Real, A. J., Dorado, F. & Durán, J. Energy demand forecasting using deep learning: Applications for the French grid. *Energies* **13**, (2020).

53. Tian, D. *et al.* Review of object instance segmentation based on deep learning. *J. Electron. Imaging* **31**, (2021).

54. Bhatt, D. *et al.* Cnn variants for computer vision: History, architecture, application, challenges and future scope. *Electronics (Switzerland)* vol. 10 (2021).

55. Girshick, R. Fast R-CNN. in *Proceedings of the IEEE International Conference on Computer Vision* (2015). doi:10.1109/ICCV.2015.169.

56. Suzuki, K. Overview of deep learning in medical imaging. *Radiological Physics and Technology* vol. 10 (2017).

57. Brinker, T. J. *et al.* Skin cancer classification using convolutional neural networks: Systematic review. *Journal of Medical Internet Research* vol. 20 (2018).

58. Urban, G. *et al.* Deep Learning Localizes and Identifies Polyps in Real Time With 96% Accuracy in Screening Colonoscopy. *Gastroenterology* **155**, (2018).

59. Nketia, T. A., Sailem, H., Rohde, G., Machiraju, R. & Rittscher, J. Analysis of live cell images: Methods, tools and opportunities. *Methods* vol. 115 (2017).

60. Salvi, M., Acharya, U. R., Molinari, F. & Meiburger, K. M. The impact of pre- and post-image processing techniques on deep learning frameworks: A comprehensive review for digital pathology image analysis. *Computers in Biology and Medicine* vol. 128 (2021).

61. Ronneberger, O., Fischer, P. & Brox, T. U-net: Convolutional networks for biomedical image segmentation. in *Lecture Notes in Computer Science (including subseries Lecture Notes in Artificial Intelligence and Lecture Notes in Bioinformatics)* (2015). doi:10.1007/978-3-319-24574-4_28.

62. Aggarwal, J. K. & Ryoo, M. S. Human activity analysis: A review. *ACM Computing Surveys* vol. 43 (2011).

63. Vrigkas, M., Nikou, C. & Kakadiaris, I. A. A review of human activity recognition methods. *Frontiers Robotics AI* vol. 2 (2015).

64. Zhang, S. *et al.* A Review on Human Activity Recognition Using Vision-Based Method. *J. Healthc. Eng.* **2017**, (2017).

65. Gupta, N. *et al.* Human activity recognition in artificial intelligence framework: a narrative review. *Artif. Intell. Rev.* **55**, (2022).

66. Al-Faris, M., Chiverton, J., Ndzi, D. & Ahmed, A. I. A review on computer vision-based methods for human action recognition. *Journal of Imaging* vol. 6 (2020).

67. Logacjov, A., Bach, K., Kongsvold, A., Bårdstu, H. B. & Mork, P. J. Harth: A human activity recognition dataset for machine learning. *Sensors* **21**, (2021).

68. Vrskova, R., Hudec, R., Kamencay, P. & Sykora, P. Human Activity Classification Using the 3DCNN Architecture. *Appl. Sci.* **12**, (2022).

69. Yeole, C., Singh, H., Waykole, H. & Deshpande, A. Deep Neural Network Approaches for Video Based Human Activity Recognition. *Int. J. Innov. Sci. Res. Technol.* **6**, (2021).

70. Hochreiter, S. & Schmidhuber, J. Long Short-Term Memory. *Neural Comput.* (1997) doi:10.1162/neco.1997.9.8.1735.

71. Zhu, Y., Zhao, J. K., Wang, Y. N. & Zheng, B. B. A review of human action recognition based on deep learning. *Zidonghua Xuebao/Acta Automatica Sinica* vol. 42 (2016).

72. He, K. *et al.* Transformers in medical image analysis. *Intelligent Medicine* vol. 3 (2023).

73. Ye, W., Cheng, J., Yang, F. & Xu, Y. Two-Stream Convolutional Network for Improving Activity Recognition Using Convolutional Long Short-Term Memory Networks. *IEEE Access* **7**, (2019).

74. Ullah, H. A., Letchmunan, S., Zia, M. S., Butt, U. M. & Hassan, F. H. Analysis of Deep Neural Networks for Human Activity Recognition in Videos - A Systematic Literature Review. *IEEE Access* vol. 9 (2021).

75. Alberts, B. *et al.* Innate immunity. in *Molecular Biology of the Cell. 4th edition* (Garland Science, 2002).

76. Miyake, Y. *et al.* Critical role of macrophages in the marginal zone in the suppression of immune responses to apoptotic cell–associated antigens. *J. Clin. Invest.* **117**, 2268–2278 (2007).

77. Luster, A. D., Alon, R. & von Andrian, U. H. Immune cell migration in inflammation: Present and future therapeutic targets. *Nature Immunology* vol. 6 (2005).

78. MD, B. B. Systemic Response to Inflammation. *Nutr. Rev.* **65**, S170–S172 (2008).

79. Voisin, M. B. & Nourshargh, S. Neutrophil transmigration: Emergence of an adhesive cascade within venular walls. *Journal of Innate Immunity* vol. 5 (2013).

80. Ley, K., Laudanna, C., Cybulsky, M. I. & Nourshargh, S. Getting to the site of inflammation: The leukocyte adhesion cascade updated. *Nature Reviews Immunology* vol. 7 (2007).

81. Teixidó, J., Hidalgo, A. & Fagerholm, S. Editorial: Leukocyte Trafficking in Homeostasis and Disease. *Frontiers in Immunology* vol. 10 (2019).

82. Nowarski, R., Gagliani, N., Huber, S. & Flavell, R. A. Innate immune cells in inflammation and cancer. *Cancer immunology research* vol. 1 (2013).

83. Barton, G. M. A calculated response: Control of inflammation by the innate immune system. *Journal of Clinical Investigation* vol. 118 (2008).

84. Auffray, C. *et al.* Monitoring of Blood Vessels and Tissues by a Population of Monocytes with Patrolling Behavior. *Science (80-.).* **317**, 666–670 (2007).

85. Buscher, K., Marcovecchio, P., Hedrick, C. C. & Ley, K. Patrolling Mechanics of Non-Classical Monocytes in Vascular Inflammation. *Frontiers in Cardiovascular Medicine* vol. 4 (2017).

86. Audoy-Remus, J. *et al.* Rod-Shaped Monocytes Patrol the Brain Vasculature and Give Rise to Perivascular Macrophages under the Influence of Proinflammatory Cytokines and Angiopoietin-2. *J. Neurosci.* **28**, 10187–10199 (2008).

87. Carlin, L. M. *et al.* Nr4a1-dependent Ly6Clow monocytes monitor endothelial cells and orchestrate their disposal. *Cell* **153**, (2013).

88. Kolaczkowska, E. & Kubes, P. Neutrophil recruitment and function in health and inflammation. *Nature Reviews Immunology* (2013) doi:10.1038/nri3399.

89. Nourshargh, S. & Alon, R. Leukocyte Migration into Inflamed Tissues. *Immunity* **41**, 694–707 (2014).

90. Chojnacki, A. *et al.* Intravital imaging allows real-time characterization of tissue resident eosinophils. *Commun. Biol.* **2**, (2019).

91. Cyster, J. G. & Allen, C. D. C. B Cell Responses: Cell Interaction Dynamics and Decisions. *Cell* vol. 177 (2019).

92. Beuneu, H. *et al.* Dynamic behavior of NK cells during activation in lymph nodes. *Blood* **114**, (2009).

93. Katakai, T. & Kinashi, T. Microenvironmental control of high-speed interstitial T cell migration in the lymph node. *Front. Immunol.* **7**, (2016).

94. Hanna, R. N. *et al.* Patrolling monocytes control tumor metastasis to the lung. *Science (80-.).* **350**, (2015).

95. Garrod, K. R., Wei, S. H., Parker, I. & Cahalan, M. D. Natural killer cells actively patrol peripheral lymph nodes forming stable conjugates to eliminate MHC-mismatched targets. *Proc. Natl. Acad. Sci.* **104**, 12081–12086 (2007).

96. Arasa, J. *et al.* Upregulation of VCAM-1 in lymphatic collectors supports dendritic cell entry and rapid migration to lymph nodes in inflammation. *J. Exp. Med.* **218**, (2021).

97. Singer, A. J. & Clark, R. A. Cutaneous wound healing. *N.Engl.J.Med.* **341**, 738–746 (1999).

98. Ng, L. G. *et al.* Visualizing the neutrophil response to sterile tissue injury in mouse dermis reveals a three-phase cascade of events. *J. Invest. Dermatol.* **131**, 2058–2068 (2011).

99. Chatziandreou, N. *et al.* Macrophage Death following Influenza Vaccination Initiates the Inflammatory Response that Promotes Dendritic Cell Function in the Draining Lymph

Node. *Cell Rep.* (2017) doi:10.1016/j.celrep.2017.02.026.

100. Kamenyeva, O. *et al.* Neutrophil Recruitment to Lymph Nodes Limits Local Humoral Response to Staphylococcus aureus. *PLoS Pathog.* **11**, (2015).

101. de Oliveira, S., Rosowski, E. E. & Huttenlocher, A. Neutrophil migration in infection and wound repair: going forward in reverse. *Nat. Rev. Immunol.* **16**, 378–391 (2016).

102. Mayadas, T. N., Cullere, X. & Lowell, C. A. The multifaceted functions of neutrophils. *Annu. Rev. Pathol. Mech. Dis.* **9**, (2014).

103. Leliefeld, P. H. C., Koenderman, L. & Pillay, J. How neutrophils shape adaptive immune responses. *Frontiers in Immunology* vol. 6 (2015).

104. Zhang, Y. *et al.* In Vivo Interstitial Migration of Primitive Macrophages Mediated by JNK-Matrix Metalloproteinase 13 Signaling in Response to Acute Injury. *J. Immunol.* **181**, 2155–2164 (2008).

105. Zinselmeyer, B. H., Lynch, J. N., Zhang, X., Aoshi, T. & Miller, M. J. Video-rate two-photon imaging of mouse footpad - A promising model for studying leukocyte recruitment dynamics during inflammation. *Inflamm. Res.* **57**, (2008).

106. De Filippo, K. & Rankin, S. M. The Secretive Life of Neutrophils Revealed by Intravital Microscopy. *Frontiers in Cell and Developmental Biology* vol. 8 (2020).

107. Hampton, H. R. & Chtanova, T. Lymphatic migration of immune cells. *Frontiers in Immunology* vol. 10 (2019).

108. Lindquist, R. L. *et al.* Visualizing dendritic cell networks in vivo. *Nat. Immunol.* **5**, 1243–1250 (2004).

109. Bougherara, H. *et al.* Real-time imaging of resident T cells in human lung and ovarian carcinomas reveals how different tumor microenvironments control T lymphocyte migration. *Front. Immunol.* **6**, (2015).

110. Friedl, P. & Weigelin, B. Interstitial leukocyte migration and immune function. *Nat. Immunol.* **9**, 960–969 (2008).

111. Hallett, M. B. *The neutrophil: Cellular biochemistry and physiology*. *The Neutrophil: Cellular Biochemistry and Physiology* (2018). doi:10.1201/9781351077200.

112. Qi, H., Cannons, J. L., Klauschen, F., Schwartzberg, P. L. & Germain, R. N. SAP-controlled T-B cell interactions underlie germinal centre formation. *Nature* **455**, (2008).

113. Kawakami, N. & Flügel, A. Knocking at the brain□s door: Intravital two-photon imaging of

autoreactive T cell interactions with CNS structures. *Seminars in Immunopathology* vol. 32 (2010).

114. Boissonnas, A., Fetler, L., Zeelenberg, I. S., Hugues, S. & Amigorena, S. In vivo imaging of cytotoxic T cell infiltration and elimination of a solid tumor. *J. Exp. Med.* **204**, (2007).

115. Kreisel, D. *et al.* In vivo two-photon imaging reveals monocyte-dependent neutrophil extravasation during pulmonary inflammation. *Proc. Natl. Acad. Sci.* **107**, 18073–18078 (2010).

116. Farsakoglu, Y. *et al.* Influenza Vaccination Induces NK-Cell-Mediated Type-II IFN Response that Regulates Humoral Immunity in an IL-6-Dependent Manner. *Cell Rep.* **26**, (2019).

117. Mrass, P. *et al.* Random migration precedes stable target cell interactions of tumor-infiltrating T cells. *J. Exp. Med.* **203**, (2006).

118. Krummel, M. F. & Cahalan, M. D. The immunological synapse: A dynamic platform for local signaling. *J. Clin. Immunol.* **30**, 364–372 (2010).

119. Dustin, M. L., Chakraborty, A. K. & Shaw, A. S. Understanding the Structure and Function of the Immunological Synapse. *Cold Spring Harb. Perspect. Biol.* **2**, a002311–a002311 (2010).

120. Monks, C. R. F., Freiberg, B. A., Kupfer, H., Sciaky, N. & Kupfer, A. Three-dimensional segregation of supramolecular activation clusters in T cells. *Nature* (1998) doi:10.1038/25764.

121. Xie, J., Tato, C. M. & Davis, M. M. How the immune system talks to itself: the varied role of synapses. *Immunol. Rev.* **251**, 65–79 (2013).

122. Bousso, P. & Robey, E. Dynamics of CD8+ T cell priming by dendritic cells in intact lymph nodes. *Nat. Immunol.* **4**, (2003).

123. Mempel, T. R. *et al.* Regulatory T Cells Reversibly Suppress Cytotoxic T Cell Function Independent of Effector Differentiation. *Immunity* **25**, 129–141 (2006).

124. Kitano, M. *et al.* Imaging of the cross-presenting dendritic cell subsets in the skin-draining lymph node. *Proc. Natl. Acad. Sci.* **113**, 1044–1049 (2016).

125. Mempel, T. R., Henrickson, S. E. & Von Andrian, U. H. T-cell priming by dendritic cells in lymph nodes occurs in three distinct phases. *Nature* **427**, (2004).

126. Bajénoff, M. *et al.* Natural killer cell behavior in lymph nodes revealed by static and real-

time imaging. *J. Exp. Med.* **203**, (2006).

127. Dustin, M. L. & Long, E. O. Cytotoxic immunological synapses. *Immunol. Rev.* **235**, 24–34 (2010).

128. Beal, A. M. *et al.* Kinetics of Early T Cell Receptor Signaling Regulate the Pathway of Lytic Granule Delivery to the Secretory Domain. *Immunity* **31**, 632–642 (2009).

129. Trapani, J. A. & Smyth, M. J. Functional significance of the perforin/granzyme cell death pathway. *Nat. Rev. Immunol.* **2**, 735–747 (2002).

130. Chtanova, T. *et al.* Dynamics of Neutrophil Migration in Lymph Nodes during Infection (DOI:10.1016/j.immuni.2008.07.012). *Immunity* vol. 29 (2008).

131. Kienle, K. & Lämmermann, T. Neutrophil swarming: an essential process of the neutrophil tissue response. *Immunol. Rev.* **273**, 76–93 (2016).

132. Lämmermann, T. *et al.* Neutrophil swarms require LTB4 and integrins at sites of cell death in vivo. *Nature* **498**, (2013).

133. Gregory, C. D. & Pound, J. D. Cell death in the neighbourhood: Direct microenvironmental effects of apoptosis in normal and neoplastic tissues. *Journal of Pathology* vol. 223 178–195 (2011).

134. Ravichandran, K. S. Find-me and eat-me signals in apoptotic cell clearance: Progress and conundrums. *Journal of Experimental Medicine* vol. 207 (2010).

135. Kienle, K. *et al.* Neutrophils self-limit swarming to contain bacterial growth in vivo. *Science (80-.).* **372**, (2021).

136. Shannon, J. G., Bosio, C. F. & Hinnebusch, B. J. Dermal Neutrophil, Macrophage and Dendritic Cell Responses to Yersinia pestis Transmitted by Fleas. *PLoS Pathog.* **11**, 1–19 (2015).

137. Alex, H. *et al.* Neutrophil swarming delays the growth of clusters of pathogenic fungi. *Nat. Commun.* **11**, (2020).

138. Nguyen, W. N. T., Jacobsen, E. A., Finney, C. A. M., Colarusso, P. & Patel, K. D. Intravital imaging of eosinophils: Unwrapping the enigma. *Journal of Leukocyte Biology* vol. 108 (2020).

139. Coombes, J. L. *et al.* Motile invaded neutrophils in the small intestine of Toxoplasma gondii-infected mice reveal a potential mechanism for parasite spread. *Proc. Natl. Acad. Sci.* **110**, E1913–E1922 (2013).

140. Chtanova, T. *et al.* Dynamics of Neutrophil Migration in Lymph Nodes during Infection. *Immunity* **29**, (2008).

141. Louie, D. A. P. & Liao, S. Lymp node subcapsular sinus macrophages as the frontline of lymphatic immune defense. *Front. Immunol.* **10**, (2019).

142. Moseman, E. A. *et al.* B Cell Maintenance of Subcapsular Sinus Macrophages Protects against a Fatal Viral Infection Independent of Adaptive Immunity. *Immunity* **36**, (2012).

143. Coombes, J. L., Han, S. J., van Rooijen, N., Raulet, D. H. & Robey, E. A. Infection-induced regulation of natural killer cells by macrophages and collagen at the lymph node subcapsular sinus. *Cell Rep.* **2**, (2012).

144. Finsterbusch, M. *et al.* Patrolling monocytes promote intravascular neutrophil activation and glomerular injury in the acutely inflamed glomerulus. *Proc. Natl. Acad. Sci. U. S. A.* **113**, (2016).

145. Wang, H. *et al.* Intravital imaging of interactions between iNKT and kupffer cells to clear free lipids during steatohepatitis. *Theranostics* **11**, (2021).

146. Westhorpe, C. L. V. *et al.* Effector CD4+ T cells recognize intravascular antigen presented by patrolling monocytes. *Nat. Commun.* **9**, (2018).

147. Deguine, J. & Bousso, P. Dynamics of NK cell interactions in vivo. *Immunol. Rev.* **251**, (2013).

148. Celli, S., Lemaître, F. & Bousso, P. Real-Time Manipulation of T Cell-Dendritic Cell Interactions In Vivo Reveals the Importance of Prolonged Contacts for CD4+ T Cell Activation. *Immunity* **27**, (2007).

149. Shakhar, G. *et al.* Stable T cell-dendritic cell interactions precede the development of both tolerance and immunity in vivo. *Nat. Immunol.* **6**, (2005).

150. Hugues, S. *et al.* Distinct T cell dynamics in lymph nodes during the induction of tolerance and immunity. *Nat. Immunol.* **5**, (2004).

151. Waite, J. C. *et al.* Dynamic imaging of the effector immune response to listeria infection In Vivo. *PLoS Pathog.* **7**, (2011).

152. Peters, N. C. *et al.* In vivo imaging reveals an essential role for neutrophils in leishmaniasis transmitted by sand flies. *Science (80-.).* **321**, (2008).

153. Lee, S. H. *et al.* M2-like, dermal macrophages are maintained via IL-4/CCL24-mediated cooperative interaction with eosinophils in cutaneous leishmaniasis. *Sci. Immunol.* **5**,

(2020).

154. Park, S. A., Choe, Y. H., Park, E. & Hyun, Y. M. Real-time dynamics of neutrophil clustering in response to phototoxicity-induced cell death and tissue damage in mouse ear dermis. *Cell Adhes. Migr.* **12**, (2018).

155. Bajénoff, M. *et al.* Stromal Cell Networks Regulate Lymphocyte Entry, Migration, and Territoriality in Lymph Nodes. *Immunity* **25**, (2006).

156. Miller, M. J., Wei, S. H., Cahalan, M. D. & Parker, I. Autonomous T cell trafficking examined in vivo with intravital two-photon microscopy. *Proc. Natl. Acad. Sci. U. S. A.* **100**, (2003).

157. McDonald, B. *et al.* Intravascular Danger Signals Guide Neutrophils to Sites of Sterile Inflammation. *Science (80-.).* **330**, 362–366 (2010).

158. Wang, B. G., König, K. & Halbhuber, K. J. Two-photon microscopy of deep intravital tissues and its merits in clinical research. *Journal of Microscopy* (2010) doi:10.1111/j.1365-2818.2009.03330.x.

159. McComb, S., Mulligan, R. & Sad, S. Caspase-3 is transiently activated without cell death during early antigen driven expansion of CD8+ T cells in vivo. *PLoS One* **5**, (2010).

160. Verduijn, J., Van der Meeren, L., Krysko, D. V. & Skirtach, A. G. Deep learning with digital holographic microscopy discriminates apoptosis and necroptosis. *Cell Death Discov.* **7**, (2021).

161. Horobin, R. W., Stockert, J. C. & Zhang, H. Reactive dyes for living cells: Applications, artefacts, and some comparisons with textile dyeing. *Coloration Technology* vol. 138 (2022).

162. Lim, B., Greer, Y., Lipkowitz, S. & Takebe, N. Novel apoptosis-inducing agents for the treatment of cancer, a new arsenal in the toolbox. *Cancers* vol. 11 (2019).

163. Fesik, S. W. Promoting apoptosis as a strategy for cancer drug discovery. *Nature Reviews Cancer* vol. 5 876–885 (2005).

164. Graham, C., Hewitson, R., Pagliuca, A. & Benjamin, R. Cancer immunotherapy with CAR-T cells - Behold the future. *Clin. Med. J. R. Coll. Physicians London* **18**, (2018).

165. Perrin, L., Bayarmagnai, B. & Gligorijevic, B. Frontiers in intravital multiphoton microscopy of cancer. *Cancer Reports* vol. 3 (2020).

166. Hickman, H. D., Bennink, J. R. & Yewdell, J. W. Caught in the Act: Intravital Multiphoton

Microscopy of Host-Pathogen Interactions. *Cell Host Microbe* **5**, 13–21 (2009).

167. Medyukhina, A., Timme, S., Mokhtari, Z. & Figge, M. T. Image-based systems biology of infection. *Cytom. Part A* **87**, 462–470 (2015).

168. Carrasco, Y. R. & Batista, F. D. B Cells Acquire Particulate Antigen in a Macrophage-Rich Area at the Boundary between the Follicle and the Subcapsular Sinus of the Lymph Node. *Immunity* **27**, 160–171 (2007).

169. Iannacone, M. *et al.* Subcapsular sinus macrophages prevent CNS invasion on peripheral infection with a neurotropic virus. *Nature* **465**, 1079–1083 (2010).

170. Thomas, S. N., Rohner, N. A. & Edwards, E. E. Implications of Lymphatic Transport to Lymph Nodes in Immunity and Immunotherapy. doi:10.1146/annurev-bioeng-101515-014413.

171. Gonzalez, S. F. *et al.* Capture of influenza by medullary dendritic cells via SIGN-R1 is essential for humoral immunity in draining lymph nodes. *Nat. Immunol.* **11**, 427–434 (2010).

172. Förster, R., Davalos-Misslitz, A. C. & Rot, A. CCR7 and its ligands: balancing immunity and tolerance. *Nat. Rev. Immunol.* **8**, 362–71 (2008).

173. Muller, W. A. Mechanisms of Leukocyte Transendothelial Migration. *Annu. Rev. Pathol. Mech. Dis.* (2011) doi:10.1146/annurev-pathol-011110-130224.

174. Allen, C. D. C. & Cyster, J. G. Follicular dendritic cell networks of primary follicles and germinal centers: Phenotype and function. *Seminars in Immunology* vol. 20 14–25 (2008).

175. Gunn, M. D. *et al.* A B-cell-homing chemokine made in lymphoid follicles activates Burkitt's lymphoma receptor-1. *Nature* **391**, 799–803 (1998).

176. Gonzalez, S. F. *et al.* Trafficking of B cell antigen in lymph nodes. *Annu. Rev. Immunol.* **29**, 215–33 (2011).

177. Lian, J. & Luster, A. D. Chemokine-guided cell positioning in the lymph node orchestrates the generation of adaptive immune responses. *Current Opinion in Cell Biology* (2015) doi:10.1016/j.ceb.2015.05.003.

178. Cyster, J. G. Chemokines and cell migration in secondary lymphoid organs. *Science* **286**, 2098–102 (1999).

179. Förster, R., Braun, A. & Worbs, T. Lymph node homing of T cells and dendritic cells via

afferent lymphatics. *Trends Immunol.* **33**, 271–80 (2012).

180. Maletto, B. A. *et al.* Presence of neutrophil-bearing antigen in lymphoid organs of immune mice. *Blood* **108**, 3094–102 (2006).

181. Petri, B., Phillipson, M. & Kubes, P. The Physiology of Leukocyte Recruitment: An In Vivo Perspective. *J. Immunol.* (2008) doi:10.4049/jimmunol.180.10.6439.

182. Furze, R. C. & Rankin, S. M. Neutrophil mobilization and clearance in the bone marrow. *Immunology* (2008) doi:10.1111/j.1365-2567.2008.02950.x.

183. Miyasaka, M. & Tanaka, T. Lymphocyte trafficking across high endothelial venules: Dogmas and enigmas. *Nature Reviews Immunology* vol. 4 360–370 (2004).

184. Gorlino, C. V. *et al.* Neutrophils Exhibit Differential Requirements for Homing Molecules in Their Lymphatic and Blood Trafficking into Draining Lymph Nodes. *J. Immunol.* **193**, 1966–1974 (2014).

185. Arokiasamy, S. *et al.* Endogenous TNFα orchestrates the trafficking of neutrophils into and within lymphatic vessels during acute inflammation. *Sci. Rep.* (2017) doi:10.1038/srep44189.

186. Hampton, H. R., Bailey, J., Tomura, M., Brink, R. & Chtanova, T. Microbe-dependent lymphatic migration of neutrophils modulates lymphocyte proliferation in lymph nodes. *Nat. Commun.* **6**, 7139 (2015).

187. Rigby, D. A., Ferguson, D. J. P., Johnson, L. A. & Jackson, D. G. Neutrophils rapidly transit inflamed lymphatic vessel endothelium via integrin-dependent proteolysis and lipoxin-induced junctional retraction. (2015) doi:10.1189/jlb.1HI0415-149R.

188. Miller, L. S. *et al.* MyD88 mediates neutrophil recruitment initiated by IL-1R but not TLR2 activation in immunity against Staphylococcus aureus. *Immunity* (2006) doi:10.1016/j.immuni.2005.11.011.

189. Dinarello, C. A. Overview of the IL-1 family in innate inflammation and acquired immunity. *Immunological Reviews* vol. 281 8–27 (2018).

190. Mantovani, A., Dinarello, C. A., Molgora, M. & Garlanda, C. Interleukin-1 and Related Cytokines in the Regulation of Inflammation and Immunity. *Immunity* **50**, 778–795 (2019).

191. Lämmermann, T. In the eye of the neutrophil swarm-navigation signals that bring neutrophils together in inflamed and infected tissues. *J. Leukoc. Biol.* **100**, 55–63 (2016).

192. Mantovani, A., Cassatella, M. A., Costantini, C. & Jaillon, S. Neutrophils in the activation and regulation of innate and adaptive immunity. (2011) doi:10.1038/nri3024.

193. Mócsai, A. Diverse novel functions of neutrophils in immunity, infammation, and beyond. *Journal of Experimental Medicine* vol. 210 1289–1299 (2013).

194. Puga, I. *et al.* B cell-helper neutrophils stimulate the diversification and production of immunoglobulin in the marginal zone of the spleen. *Nat. Immunol.* **13**, 170–180 (2012).

195. Vono, M. *et al.* Neutrophils acquire the capacity for antigen presentation to memory CD4+ T cells in vitro and ex vivo. *Blood* **129**, 1991–2001 (2017).

196. Minns, D., Smith, K. J. & Findlay, E. G. Orchestration of Adaptive T Cell Responses by Neutrophil Granule Contents. *Mediators Inflamm.* **2019**, 1–15 (2019).

197. Duffy, D. *et al.* Neutrophils transport antigen from the dermis to the bone marrow, initiating a source of memory CD8+ T cells. *Immunity* **37**, 917–29 (2012).

198. Abdallah, D. S. A., Egan, C. E., Butcher, B. A. & Denkers, E. Y. Mouse neutrophils are professional antigen-presenting cells programmed to instruct T h1 and T h17 T-cell differentiation. *Int. Immunol.* **23**, 317–326 (2011).

199. Bogoslowski, A., Butcher, E. C. & Kubes, P. Neutrophils recruited through high endothelial venules of the lymph nodes via PNAd intercept disseminating Staphylococcus aureus. *Proc. Natl. Acad. Sci.* **115**, 2449–2454 (2018).

200. Lai, J. *et al.* In vivo two-photon imaging reveals monocyte-dependent neutrophil extravasation during pulmonary inflammation. *Proc. Natl. Acad. Sci.* **107**, 18073–18078 (2010).

201. Weninger, W., Biro, M. & Jain, R. Leukocyte migration in the interstitial space of non-lymphoid organs. *Nat. Rev. Immunol.* **14**, 232 (2014).

202. Kamenyeva, O., Boularan, C., Kabat, J., Cheung, G. Y. C. & Kehrl, J. H. Neutrophil Recruitment to Lymph Nodes Limits Local Humoral Response to Staphylococcus aureus. (2015) doi:10.1371/journal.ppat.1004827.

203. Stein, J. V. & F. Gonzalez, S. Dynamic intravital imaging of cell-cell interactions in the lymph node. *Journal of Allergy and Clinical Immunology* vol. 139 12–20 (2017).

204. Figge, M. T. & Murphy, R. F. Image-based systems biology. *Cytometry Part A* vol. 87 (2015).

205. Moreau, H. D. *et al.* Dynamic In Situ Cytometry Uncovers T Cell Receptor Signaling

during Immunological Synapses and Kinapses In Vivo. *Immunity* **37**, 351–363 (2012).

206. Mokhtari, Z. *et al.* Automated characterization and parameter-free classification of Cell tracks based on local migration behavior. *PLoS One* **8**, (2013).

207. Hyun, Y.-M., Choe, Y. H., Park, S. A. & Kim, M. LFA-1 (CD11a/CD18) and Mac-1 (CD11b/CD18) distinctly regulate neutrophil extravasation through hotspots I and II. *Exp. Mol. Med.* **51**, 39 (2019).

208. Pruenster, M. *et al.* The Duffy antigen receptor for chemokines transports chemokines and supports their promigratory activity. *Nat. Immunol.* **10**, 101–8 (2009).

209. Karlsson, S. M. & Bigun, J. Lip-motion events analysis and lip segmentation using optical flow. in *2012 IEEE Computer Society Conference on Computer Vision and Pattern Recognition Workshops* 138–145 (IEEE, 2012). doi:10.1109/CVPRW.2012.6239228.

210. Lopez, S., Marco, A. J., Prats, N. & Czuprynski, C. J. Critical Role of Neutrophils in Eliminating Listeria monocytogenes from the Central Nervous System during Experimental Murine Listeriosis. *Infect. Immun.* **68**, 4789–4791 (2000).

211. Ueki, H. *et al.* In vivo imaging of the pathophysiological changes and neutrophil dynamics in influenza virus-infected mouse lungs. *Proc. Natl. Acad. Sci.* **115**, E6622–E6629 (2018).

212. Martin, C. *et al.* Chemokines acting via CXCR2 and CXCR4 control the release of neutrophils from the bone marrow and their return following senescence. *Immunity* (2003) doi:10.1016/S1074-7613(03)00263-2.

213. Eash, K. J. *et al.* CXCR4 is a key regulator of neutrophil release from the bone marrow under basal and stress granulopoiesis conditions. *Blood* **113**, 4711–9 (2009).

214. Khan, A. I. *et al.* Role of CD44 and Hyaluronan in Neutrophil Recruitment. *J. Immunol.* **173**, (2004).

215. Kishimoto, T. K., Jutila, M. A., Berg, E. L. & Butcher, E. C. Neutrophil Mac-1 and MEL-14 adhesion proteins inversely regulated by chemotactic factors. *Science (80-.).* **245**, 1238–1241 (1989).

216. Tsuda, Y. *et al.* Three different neutrophil subsets exhibited in mice with different susceptibilities to infection by methicillin-resistant Staphylococcus aureus. *Immunity* **21**, 215–226 (2004).

217. Mayer-Barber, K. D. & Yan, B. Clash of the Cytokine Titans: counter-regulation of interleukin-1 and type I interferon-mediated inflammatory responses. *Cell. Mol. Immunol.*

14, 22–35 (2017).

218. Biondo, C. *et al.* The interleukin-1β/CXCL1/2/neutrophil axis mediates host protection against group B streptococcal infection. *Infect. Immun.* **82**, 4508–17 (2014).

219. De Filippo, K., Henderson, R. B., Laschinger, M. & Hogg, N. Neutrophil Chemokines KC and Macrophage-Inflammatory Protein-2 Are Newly Synthesized by Tissue Macrophages Using Distinct TLR Signaling Pathways. *J. Immunol.* (2008) doi:10.4049/jimmunol.180.6.4308.

220. Barry, K. C., Fontana, M. F., Portman, J. L., Dugan, A. S. & Vance, R. E. IL-1α Signaling Initiates the Inflammatory Response to Virulent Legionella pneumophila In Vivo . *J. Immunol.* (2013) doi:10.4049/jimmunol.1300100.

221. Voisin, M.-B. & Nourshargh, S. INVITED REVIEW Neutrophil trafficking to lymphoid tissues: physiological and pathological implications. *J. Pathol. J Pathol* **247**, 662–671 (2019).

222. Hufford, M. M. *et al.* Influenza-Infected Neutrophils within the Infected Lungs Act as Antigen Presenting Cells for Anti-Viral CD8+ T Cells. *PLoS One* **7**, (2012).

223. Tate, M. D., Brooks, A. G., Reading, P. C. & Mintern, J. D. Neutrophils sustain effective CD8 + T-cell responses in the respiratory tract following influenza infection. *Immunol. Cell Biol.* **90**, 197–205 (2012).

224. Nourshargh, S., Renshaw, S. A. & Imhof, B. A. Reverse Migration of Neutrophils: Where, When, How, and Why? *Trends Immunol.* **37**, 273–286 (2016).

225. Hashimoto, Y., Moki, T., Takizawa, T., Shiratsuchi, A. & Nakanishi, Y. Evidence for Phagocytosis of Influenza Virus-Infected, Apoptotic Cells by Neutrophils and Macrophages in Mice. *J. Immunol.* **178**, 2448–2457 (2007).

226. Naumenko, V., Turk, M., Jenne, C. N. & Kim, S.-J. Neutrophils in viral infection. *Cell Tissue Res.* **371**, 505–516 (2018).

227. Camp, J. V. & Jonsson, C. B. A role for neutrophils in viral respiratory disease. *Frontiers in Immunology* vol. 8 (2017).

228. Ratcliffe, D., Migliorisi, G. & Cramer, E. Translocation of influenza virus by migrating neutrophils. *Cell. Mol. Biol.* **38**, 63–70 (1992).

229. Peters, N. C. *et al.* In vivo imaging reveals an essential role for neutrophils in Leishmaniasis transmitted by sand flies. **321**, 970–974 (2009).

230. Bousso, P. & Moreau, H. D. Functional immunoimaging: the revolution continues. *Nat. Rev. Immunol.* **12**, 858–864 (2012).

231. Wiwie, C., Baumbach, J. & Röttger, R. Comparing the performance of biomedical clustering methods. *Nat. Methods* **12**, 1033–1038 (2015).

232. Pizzagalli, D. U., Gonzalez, S. F. & Krause, R. A shortest-path based clustering algorithm for joint human-machine analysis of complex datasets. *arXiv Prepr.* (2019).

233. Zhou, F. Y. *et al.* Motion sensing superpixels (MOSES) is a systematic computational framework to quantify and discover cellular motion phenotypes. *Elife* **8**, (2019).

234. Zhang, Y., Zhang, Y., Zhang, Z., Bao, J. & Song, Y. Human activity recognition based on time series analysis using U-Net. (2018).

235. Beltman, J. B., Allen, C. D. C., Cyster, J. G. & De Boer, R. J. B cells within germinal centers migrate preferentially from dark to light zone. *Proc. Natl. Acad. Sci. U. S. A.* **108**, (2011).

236. Iparraguirre, A. & Weninger, W. Visualizing T cell migration in vivo. *International Archives of Allergy and Immunology* (2003) doi:10.1159/000074896.

237. Beltman, J. B., Henrickson, S. E., von Andrian, U. H., de Boer, R. J. & Marée, A. F. M. Towards estimating the true duration of dendritic cell interactions with T cells. *J. Immunol. Methods* (2009) doi:10.1016/j.jim.2009.05.013.

238. Crainiciuc, G. *et al.* Behavioural immune landscapes of inflammation. *Nature* **601**, (2022).

239. Cahalan, M. D., Parker, I., Wei, S. H. & Miller, M. J. Two-photon tissue imaging: Seeing the immune system in a fresh light. *Nature Reviews Immunology* vol. 2 (2002).

240. D'Orazio, M. *et al.* Deciphering Cancer Cell Behavior From Motility and Shape Features: Peer Prediction and Dynamic Selection to Support Cancer Diagnosis and Therapy. *Front. Oncol.* **10**, (2020).

241. Mencattini, A. *et al.* Discovering the hidden messages within cell trajectories using a deep learning approach for in vitro evaluation of cancer drug treatments. *Sci. Rep.* **10**, (2020).

242. Jorgensen, I., Rayamajhi, M. & Miao, E. A. Programmed cell death as a defence against infection. *Nature Reviews Immunology* vol. 17 (2017).

243. Elmore, S. Apoptosis: A Review of Programmed Cell Death. *Toxicologic Pathology*

(2007) doi:10.1080/01926230701320337.

244. Mobiny, A., Lu, H., Nguyen, H. V., Roysam, B. & Varadarajan, N. Automated Classification of Apoptosis in Phase Contrast Microscopy Using Capsule Network. *IEEE Trans. Med. Imaging* **39**, 1–10 (2020).

245. Rathmell, J. C. & Thompson, C. B. Pathways of apoptosis in lymphocyte development, homeostasis, and disease. *Cell* vol. 109 (2002).

246. Hotchkiss, R. S., Strasser, A., McDunn, J. E. & Swanson, P. E. Mechanisms of disease: Cell death. *N. Engl. J. Med.* **361**, 1570–1583 (2009).

247. Tang, D., Kang, R., Berghe, T. Vanden, Vandenabeele, P. & Kroemer, G. The molecular machinery of regulated cell death. *Cell Research* vol. 29 (2019).

248. Saraste, A. & Pulkki, K. Morphologic and biochemical hallmarks of apoptosis. *Cardiovascular Research* vol. 45 (2000).

249. Doran, A. C., Yurdagul, A. & Tabas, I. Efferocytosis in health and disease. *Nature Reviews Immunology* vol. 20 (2020).

250. Shalini, S., Dorstyn, L., Dawar, S. & Kumar, S. Old, new and emerging functions of caspases. *Cell Death and Differentiation* vol. 22 (2015).

251. Yang, Y., Jiang, G., Zhang, P. & Fan, J. Programmed cell death and its role in inflammation. *Military Medical Research* vol. 2 (2015).

252. Green, D. R., Ferguson, T., Zitvogel, L. & Kroemer, G. Immunogenic and tolerogenic cell death. *Nature Reviews Immunology* vol. 9 (2009).

253. Yatim, N., Cullen, S. & Albert, M. L. Dying cells actively regulate adaptive immune responses. *Nature Reviews Immunology* vol. 17 (2017).

254. Vandenabeele, P., Vandecasteele, K., Bachert, C., Krysko, O. & Krysko, D. V. Immunogenic apoptotic cell death and anticancer immunity. in *Advances in Experimental Medicine and Biology* vol. 930 (2016).

255. Opferman, J. T. Apoptosis in the development of the immune system. *Cell Death and Differentiation* vol. 15 (2008).

256. Edelblum, K. L., Yan, F., Yamaoka, T. & Polk, D. B. Regulation of apoptosis during homeostasis and disease in the intestinal epithelium. *Inflammatory Bowel Diseases* vol. 12 (2006).

257. Nitschke, C., Garin, A., Kosco-Vilbois, M. & Gunzer, M. 3D and 4D imaging of immune

cells in vitro and in vivo. *Histochem. Cell Biol.* **130**, 1053–1062 (2008).

258. Martinez, N. J., Titus, S. A., Wagner, A. K. & Simeonov, A. High-throughput fluorescence imaging approaches for drug discovery using in vitro and in vivo three-dimensional models. *Expert Opinion on Drug Discovery* vol. 10 (2015).

259. Sumen, C., Mempel, T. R., Mazo, I. B. & Von Andrian, U. H. Intravital microscopy: Visualizing immunity in context. *Immunity* vol. 21 (2004).

260. Sinaci, A. A. *et al.* From Raw Data to FAIR Data: The FAIRification Workflow for Health Research. *Methods Inf. Med.* **59**, (2020).

261. Jacobsen, A. *et al.* A generic workflow for the data fairification process. *Data Intell.* **2**, (2020).

262. Van Valen, D. A. *et al.* Deep Learning Automates the Quantitative Analysis of Individual Cells in Live-Cell Imaging Experiments. *PLoS Comput. Biol.* **12**, (2016).

263. Pang, G., Shen, C., Cao, L. & Hengel, A. Van Den. Deep Learning for Anomaly Detection: A Review. *ACM Computing Surveys* vol. 54 (2021).

264. Kwabena Patrick, M., Felix Adekoya, A., Abra Mighty, A. & Edward, B. Y. Capsule Networks – A survey. *Journal of King Saud University - Computer and Information Sciences* vol. 34 (2022).

265. Han, K. *et al.* A Survey on Vision Transformer. *IEEE Trans. Pattern Anal. Mach. Intell.* **45**, (2023).

266. Jin, J. *et al.* Machine Learning Classifies Ferroptosis and Apoptosis Cell Death Modalities with TfR1 Immunostaining. *ACS Chem. Biol.* **17**, (2022).

267. Mohd Noor, M. H., Tan, S. Y. & Ab Wahab, M. N. Deep Temporal Conv-LSTM for Activity Recognition. *Neural Process. Lett.* **54**, (2022).

268. Weinzaepfel, P., Revaud, J., Harchaoui, Z. & Schmid, C. DeepFlow: Large displacement optical flow with deep matching. in *Proceedings of the IEEE International Conference on Computer Vision* (2013). doi:10.1109/ICCV.2013.175.

269. Helmchen, F. & Denk, W. Deep tissue two-photon microscopy. *Nature Methods* vol. 2 932–940 (2005).

270. Rocheleau, J. V. & Piston, D. W. Two□Photon Excitation Microscopy for the Study of Living Cells and Tissues. *Curr. Protoc. Cell Biol.* **20**, (2003).

271. D'Arcy, M. S. Cell death: a review of the major forms of apoptosis, necrosis and

autophagy. *Cell Biology International* vol. 43 (2019).

272. Galluzzi, L. *et al.* Molecular mechanisms of cell death: Recommendations of the Nomenclature Committee on Cell Death 2018. *Cell Death and Differentiation* vol. 25 (2018).

273. Coleman, M. L. *et al.* Membrane blebbing during apoptosis results from caspase-mediated activation of ROCK I. *Nat. Cell Biol.* **3**, (2001).

274. Hotchkiss, R. S. & Nicholson, D. W. Apoptosis and caspases regulate death and inflammation in sepsis. *Nature Reviews Immunology* vol. 6 813–822 (2006).

275. Loo, D. T. In situ detection of apoptosis by the TUNEL assay: An overview of techniques. *Methods Mol. Biol.* **682**, (2011).

276. Kyrylkova, K., Kyryachenko, S., Leid, M. & Kioussi, C. Detection of apoptosis by TUNEL assay. *Methods Mol. Biol.* **887**, (2012).

277. Atale, N., Gupta, S., Yadav, U. C. S. & Rani, V. Cell-death assessment by fluorescent and nonfluorescent cytosolic and nuclear staining techniques. *J. Microsc.* **255**, 7–19 (2014).

278. Vermes, I., Haanen, C., Steffens-Nakken, H. & Reutellingsperger, C. A novel assay for apoptosis Flow cytometric detection of phosphatidylserine expression on early apoptotic cells using fluorescein labelled Annexin V. *J. Immunol. Methods* **184**, (1995).

279. Sun, L., Chen, T., Wang, L. & Wang, H. Analysis of caspase3 activation in ChanSu-induced apoptosis of ASTC-a-1 cells by fluorescence techniques. in *Biophotonics and Immune Responses III* vol. 6857 (2008).

280. Darzynkiewicz, Z., Galkowski, D. & Zhao, H. Analysis of apoptosis by cytometry using TUNEL assay. *Methods* **44**, (2008).

281. Schnell, U., Dijk, F., Sjollema, K. A. & Giepmans, B. N. G. Immunolabeling artifacts and the need for live-cell imaging. *Nature Methods* vol. 9 (2012).

282. Takemoto, K., Nagai, T., Miyawaki, A. & Miura, M. Spatio-temporal activation of caspase revealed by indicator that is insensitive to environmental effects. *J. Cell Biol.* **160**, (2003).

283. Jensen, E. C. Use of Fluorescent Probes: Their Effect on Cell Biology and Limitations. *Anatomical Record* vol. 295 (2012).

284. Poppe, R. A survey on vision-based human action recognition. *Image Vis. Comput.* **28**, 976–990 (2010).

285. Kranich, J. *et al.* In vivo identification of apoptotic and extracellular vesicle-bound live cells using image-based deep learning. *J. Extracell. Vesicles* **9**, (2020).

286. Adadi, A. A survey on data□efficient algorithms in big data era. *J. Big Data* **8**, (2021).

287. Van Der Flier, L. G. & Clevers, H. Stem cells, self-renewal, and differentiation in the intestinal epithelium. *Annual Review of Physiology* vol. 71 (2009).

288. Fox, S., Leitch, A. E., Duffin, R., Haslett, C. & Rossi, A. G. Neutrophil apoptosis: Relevance to the innate immune response and inflammatory disease. *Journal of Innate Immunity* vol. 2 216–227 (2010).

289. Shi, X. *et al.* Convolutional LSTM network: A machine learning approach for precipitation nowcasting. in *Advances in Neural Information Processing Systems* vols 2015-Janua 802–810 (2015).

290. Uijlings, J. R. R., Van De Sande, K. E. A., Gevers, T. & Smeulders, A. W. M. Selective search for object recognition. *Int. J. Comput. Vis.* **104**, 154–171 (2013).

291. Damián La Greca, A. *et al.* celldeath: A tool for detection of cell death in transmitted light microscopy images by deep learning-based visual recognition. *PLoS One* **16**, (2021).

292. Kabir, M. A. *et al.* Automated detection of apoptotic versus nonapoptotic cell death using label-free computational microscopy. *J. Biophotonics* **15**, (2022).

293. Zhuang, X. *et al.* Self-supervised feature learning for 3d medical images by playing a rubik's cube. in *Lecture Notes in Computer Science (including subseries Lecture Notes in Artificial Intelligence and Lecture Notes in Bioinformatics)* vol. 11767 LNCS 420–428 (2019).

294. Xu, J., Li, M. & Zhu, Z. Automatic data augmentation for 3d medical image segmentation. in *Lecture Notes in Computer Science (including subseries Lecture Notes in Artificial Intelligence and Lecture Notes in Bioinformatics)* vol. 12261 LNCS 378–387 (2020).

295. Vicar, T., Raudenska, M., Gumulec, J. & Balvan, J. The Quantitative-Phase Dynamics of Apoptosis and Lytic Cell Death. *Sci. Rep.* **10**, (2020).

296. Jimenez-Carretero, D. *et al.* Tox_(R)CNN: Deep learning-based nuclei profiling tool for drug toxicity screening. *PLoS Comput. Biol.* **14**, (2018).

297. Schmid, I., Uittenbogaart, C. & Jamieson, B. D. Live-cell assay for detection of apoptosis by dual-laser flow cytometry using Hoechst 33342 and 7-amino-actinomycin D. *Nat. Protoc.* **2**, 187–190 (2007).

298. Eom, Y. W. *et al.* Two distinct modes of cell death induced by doxorubicin: Apoptosis and cell death through mitotic catastrophe accompanied by senescence-like phenotype. *Oncogene* **24**, (2005).

299. Uderhardt, S., Martins, A. J., Tsang, J. S., Lämmermann, T. & Germain, R. N. Resident Macrophages Cloak Tissue Microlesions to Prevent Neutrophil-Driven Inflammatory Damage. *Cell* **177**, (2019).

300. Zhao, Z. Q., Zheng, P., Xu, S. T. & Wu, X. Object Detection with Deep Learning: A Review. *IEEE Transactions on Neural Networks and Learning Systems* vol. 30 (2019).

301. Green, D. R. Apoptotic pathways: Ten minutes to dead. *Cell* vol. 121 (2005).

302. Masri, C. & Chandrashekhar, Y. Apoptosis: A potentially reversible, meta-stable state of the heart. *Heart Failure Reviews* vol. 13 (2008).

303. Geske, F. J., Lieberman, R., Strange, R. & Gerschenson, L. E. Early stages of p53-induced apoptosis are reversible. *Cell Death Differ.* **8**, (2001).

304. Tang, H. L., Yuen, K. L., Tang, H. M. & Fung, M. C. Reversibility of apoptosis in cancer cells. *Br. J. Cancer* **100**, (2009).

305. Gagliardi, P. A. *et al.* Collective ERK/Akt activity waves orchestrate epithelial homeostasis by driving apoptosis-induced survival. *Dev. Cell* **56**, (2021).

306. Tyas, L., Brophy, V. A., Pope, A., Rivett, A. J. & Tavaré, J. M. Rapid caspase-3 activation during apoptosis revealed using fluorescence-resonance energy transfer. *EMBO Rep.* **1**, (2000).

307. Yang, X., Song, Z., King, I. & Xu, Z. A Survey on Deep Semi-Supervised Learning. *IEEE Trans. Knowl. Data Eng.* **35**, (2023).

308. Li, X., Yang, X., Ma, Z. & Xue, J. H. Deep metric learning for few-shot image classification: A Review of recent developments. *Pattern Recognition* vol. 138 (2023).

309. Zhang, L. N., Zuo, X. & Liu, J. W. Research and Development on Zero-Shot Learning. *Zidonghua Xuebao/Acta Automatica Sinica* vol. 46 (2020).

310. Khetarpal, K., Riemer, M., Rish, I. & Precup, D. Towards Continual Reinforcement Learning: A Review and Perspectives. *J. Artif. Intell. Res.* **75**, (2022).

311. Clausen, B. E., Burkhardt, C., Reith, W., Renkawitz, R. & Förster, I. Conditional gene targeting in macrophages and granulocytes using LysMcre mice. *Transgenic Res.* **8**, 265–277 (1999).

312. Labow, M. *et al.* Absence of IL-1 signaling and reduced inflammatory response in IL-1 type I receptor-deficient mice. *J. Immunol.* **159**, 2452 LP – 2461 (1997).

313. Hou, B., Reizis, B. & DeFranco, A. L. Toll-like Receptors Activate Innate and Adaptive Immunity by using Dendritic Cell-Intrinsic and -Extrinsic Mechanisms. *Immunity* **29**, 272–282 (2008).

314. Muller, U. *et al.* Functional role of type I and type II interferons in antiviral defense. *Science (80-.).* **264**, 1918–1921 (1994).

315. Tran Cao, H. S. *et al.* Development of the transgenic cyan fluorescent protein (CFP)-expressing nude mouse for "Technicolor" cancer imaging. *J. Cell. Biochem.* **107**, 328–34 (2009).

316. Schaefer, B. C., Schaefer, M. L., Kappler, J. W., Marrack, P. & Kedl, R. M. Observation of Antigen-Dependent CD8+ T-Cell/ Dendritic Cell Interactions in Vivo. *Cell. Immunol.* **214**, 110–122 (2001).

317. Palomino-Segura, M. & Gonzalez, S. F. Two-Photon Intravital Imaging of Leukocytes in the Trachea During Pneumococcal Infection. in *Streptococcus pneumoniae* 183–194 (Springer, 2019).

318. Pizzagalli, D. U. *et al.* Semi-supervised colocalization facilitates detection and tracking of immune cells in 4D 2-photon intravital microscopy data. *Prep.*

319. Guzzi, R., Colombo, T. & Paci, P. Inverse Problems in Systems Biology: A Critical Review. in (ed. Bizzarri, M.) 69–94 (Springer New York, 2018). doi:10.1007/978-1-4939-7456-6_6.

320. Debnath, J., Muthuswamy, S. K. & Brugge, J. S. Morphogenesis and oncogenesis of MCF-10A mammary epithelial acini grown in three-dimensional basement membrane cultures. *Methods* vol. 30 (2003).

321. Shcherbakova, D. M. *et al.* Bright monomeric near-infrared fluorescent proteins as tags and biosensors for multiscale imaging. *Nat. Commun.* **7**, (2016).

322. Yusa, K., Zhou, L., Li, M. A., Bradley, A. & Craig, N. L. A hyperactive piggyBac transposase for mammalian applications. *Proc. Natl. Acad. Sci. U. S. A.* **108**, (2011).

323. Lopez, P., Koh, W. H., Hnatiuk, R. & Murooka, T. T. HIV Infection Stabilizes Macrophage-T Cell Interactions To Promote Cell-Cell HIV Spread. *J. Virol.* **93**, (2019).

324. Lopez, P. *et al.* T cell migration potentiates HIV infection by enhancing viral fusion and integration. *Cell Rep.* **38**, (2022).

325. Schindelin, J. *et al.* Fiji: An open-source platform for biological-image analysis. *Nature Methods* vol. 9 (2012).

326. Jacquemet, G. *et al.* Automated cell tracking using StarDist and TrackMate. *F1000Research* **9**, (2020).

PUBLICATIONS

Alain Pulfer, Tommaso Virgilio, Diego Ulisse Pizzagalli, Elisa Palladino. 2023."vAbs: virtual antibodies for immune cell identification" Manuscript in preparation

Diego Ulisse Pizzagalli, Pau Carrillo-Barberà, Kevin Ceni, Elisa Palladino, Benedikt Thelen, **Alain Pulfer**, Joy Bordini, Florentino Caetano-Santo, The IMMUNEMAP project consortium, Rolf Krauser,, Santiago Fernandez Gonzalez. 2023. "IMMUNEMAP, an intravital microscopy imaging platform to enable Spatial-Temporal Dynamic studies in Immunology." To be submitted.

Tommaso Virgilio, **Alain Pulfer**, Kamil Chahine, Chiara Pizzichetti, Louis Luca Renner, Dario Neri, Emanuele Puca, Roberto De Luca, Santiago F. Gonzalez. 2023."Intravital microscopy reveals a distinct biodistribution pattern in neoplastic lesions of the L19 antibody depending on the administration route." To be submitted.

Alain Pulfer, Diego Ulisse Pizzagalli, Pau Carrillo Barbera, Paola Antonello, Marcus Thelen, Rolf Krause, Santiago F. Gonzalez. 2023. "Capturing cell death: a microscopy dataset of apoptotic immune cells for algorithmic advancement in vivo." Submitted to Scientific Data.

Alain Pulfer, Diego Ulisse Pizzagalli, Paolo Armando Gagliardi, Lucien Hinderling, Paul Lopez, Romaniya Zayats, Pau Carrillo-Barberà, Paola Antonello, Miguel Palomino-Segura, Alessandro Giusti, Marcus Thelen, Luca Maria Gambardella, Thomas T. Murooka, Olivier Pertz, Rolf Krause, Santiago Fernandez Gonzalez. 2023."Transformer-based spatial-temporal detection of apoptotic cell death in live-cell imaging." eLife. https://doi.org/10.7554/eLife.90502.1.

Pizzagalli, Diego Ulisse, Joy Bordini, Diego Morone, **Alain Pulfer**, Pau Carrillo-Barberà, Benedikt Thelen, Kevin Ceni, Marcus Thelen, Rolf Krause, and Santiago Fernandez Gonzalez. 2022. "CANCOL, a Computer-Assisted Annotation Tool to Facilitate Colocalization and Tracking of Immune Cells in Intravital Microscopy." The Journal of Immunology 208 (6). https://doi.org/10.4049/jimmunol.2100811.

Alain Pulfer, Pizzagalli, Diego Ulisse, Marcus Thelen, Rolf Krause, and Santiago F. Gonzalez. 2022. "In Vivo Motility Patterns Displayed by Immune Cells Under Inflammatory Conditions." Frontiers in Immunology. https://doi.org/10.3389/fimmu.2021.804159.

Pizzagalli, Diego Ulisse, Irene Latino, **Alain Pulfer**, Miguel Palomino-Segura, Tommaso Virgilio, Yagmur Farsakoglu, Rolf Krause, and Santiago F. Gonzalez. 2019. "Characterization of the Dynamic Behavior of Neutrophils Following Influenza Vaccination." Frontiers in Immunology 10 (November): 1–17. https://doi.org/10.3389/fimmu.2019.02621.